Optically Triggered Superconducting Opening Switches

by

Deepnarayan Gupta

Submitted in Partial Fulfillment

of the

Requirements for the Degree

Doctor of Philosophy

Supervised by

Professor Alan M. Kadin

Department of Electrical Engineering

The College

School of Engineering and Applied Sciences

Reviewed for Classification 11/6/95
(Date)
UNCLASSIFIED
R. L. McCRORY, JR.
Authorized Derivative Classifier

University of Rochester

Rochester, New York

1995

To my Mother

Curriculum Vitae

Deepnarayan Gupta was born in Calcutta, India in the year 1969. He finished his Secondary and Higher Secondary education from Scottish Church Collegiate School and St. Xaviers College in Calcutta, in 1984 and 1986 respectively. From 1986 to 1990, he attended the Indian Institute of Technology at Kharagpur, India, where he obtained the Bachelor of Technology (Hons.) degree in Electronics and Electrical Communications Engineering. From 1984 to 1990, he received the National Talent Search Scholarship from the National Council for Educational Research and Training, Government of India. He joined University of Rochester in the Fall of 1990, to pursue a Ph.D. degree in Electrical Engineering. In the first year of his graduate study he held a teaching assistantship from the Department of Electrical Engineering. Next year he received a research assistantship from his thesis adviser Prof. Alan M. Kadin. University of Rochester awarded Mr. Gupta the Master of Science degree in Electrical Engineering in 1992. The Link Foundation awarded him a Fellowship in the academic year 1992-93 for an outstanding Energy Research Proposal submitted by Mr. Gupta. For the last two years, Laboratory for Laser Energetics has awarded him the Frank J. Horton Fellowship to pursue his research in the field of superconducting thin film switches under the supervision of Dr. Kadin and Dr. Donaldson.

Acknowledgments

I am deeply indebted to my thesis adviser Prof. Alan Kadin for his guidance in every aspect of my research. His door was always open to me and I have benefited from his prudent advice in academics as well as in matters concerning life in general. For the last five years, I have constantly imbibed from his vast, encyclopedic knowledge regarding a diverse range of subjects. It is a great privilege to have worked with Prof. Kadin, a person whom I hold in the highest esteem.

This research wouldn't have been possible without the supervision of Dr. William Donaldson. He always had a ready solution to every problem that I encountered in the lab. I was extremely fortunate to have a research supervisor who worked *with* me in the lab. He taught me how to be a rational experimentalist and I take this opportunity to express my sincerest gratitude to him.

Prof. Michael Wengler is a person I have always looked up to. He instilled in me a feeling of self-confidence which will have a lasting influence in my life. He also taught me the first course in superconductivity which deepened my interest in this field.

I am also indebted to a number of graduate students in the Electrical Engineering department. During the initial stages of my research, Sotiris Alexandrou and Derek Mallory helped me generously. I have also benefited a lot from discussions with Mark Johnson. I am much obliged to Linda Marchese for allowing me to use the MATLAB software on her computer, to run my first simulations on transient flux dynamics in superconducting disks. My friend Wei Xiong was a source of constant encouragement during all these years. I enjoyed the company and the sense of humor of my friend and office-mate José Nuñez-Regueiro inside and outside the lab. It was always nice to talk to Darren Brock, who always lent me his helping hand. I acknowledge the help and cooperation of Andrew Denysenko, Witold Kula, Marc Currie, Douglas Jacobs-Perkins, Kenton Green, Chia-Chi Wang, and Paul Rodney.

I had the pleasure of working with undergraduate students Mark Bernard, Ali Muhtaroglu, Benjamin Gannon, and Agnim Cole, during the summers of 1992, 93, 94 and 95. I am especially grateful to Ali for his help in the early experiments with the inductively-coupled switch.

I am very grateful to Mr. Robert Fellows at the Laser Lab machine shop for helping me and machining some of the finer components of my experimental set-up that I couldn't even dream of doing myself. I also thank Ms. Ladonna Black, Ms. Diane Hixson, Ms. Lisa Cliff, Ms. Kathie Freson, and Ms. Lena Cardone of the Laser Lab illustrations and word-processing.

I would also like to thank the Link Foundation for the Link Foundation Energy Fellowship in 1992-93 and the Laboratory for Laser Energetics for the Frank Horton Fellowship in 1993-95. Our research was funded through grants from BMDO through ONR Contract #N00014-92-J-1993, Rochester Gas and Electric, NSF grants #DMR89-13524 and #DMR91-22727 and New York State Energy Research and Development Authority.

The success of my graduate work is intimately related to the inspiration and encouragement from my wife Titania. Words cannot express the importance of her love and support during these difficult years in graduate school.

Abstract

This dissertation delineates the study of fast switching devices based on high temperature superconducting thin films. The research explores the prospects of a fast high-current opening switch utilizing the high current densities of $YBa_2Cu_3O_{7-x}$ thin films. Two different classes of devices, the *photoresistive switch* and the *inductively-coupled switch* , and their switching mechanisms have been investigated. In both cases, experimental design and implementation are complemented with analyses of the underlying physical phenomena. Short, near-infrared laser pulses provide a fast, efficient, and accurately controllable triggering mechanism for these switches.

The photoresistive opening switch is based on the transition to the resistive (*open*) state from a superconducting (*closed)* state following laser illumination. Zero closed-state resistance, relatively high normal state resistivity, and very fast switching times are the attractive features of this switch. We have studied the photoresponse of microbridges, under varying current bias, initial temperature, and laser fluence. The use of optically thick films, for enhanced current capacity, allowed us to separate a fast response from a delayed, slow bolometric response. The bolometric component of the observed response conforms with simulations based on a one-dimensional heat-diffusion model. Preliminary experiments with a larger switch exhibit high switching currents.

The inductively-coupled switch, invented to avoid problems associated with metallic contacts to the photoresistive switch, is a contactless design. The switching is performed by destroying screening currents in a thin YBCO film with an optical trigger, enabling rapid change in flux coupling between previously isolated, inductively-coupled source and load circuits. The switch was tested at low and high magnetic fields, corresponding to reversible and irreversible operating regimes of the superconductor respectively. Switching voltages with rise times as short as 2.5 ns and 75 V peak have been observed. A transient analysis of the screening current and magnetic field distributions, for the inductively-coupled switch configuration, has enabled us to develop an understanding of the mechanism governing the operation of this new device. This analysis has led to the development of efficient numerical algorithms adaptable to a variety of problems concerning macroscopic flux dynamics in superconductors.

TABLE OF CONTENTS

1. INTRODUCTION 1

2. OPENING SWITCHES FOR HIGH POWER APPLICATIONS 7
- 2.1 Opening Switches 8
- 2.2 An overview of opening switch technology 10
- 2.3 Applications of opening switches 16
- 2.4 Inductive Energy Storage Systems 21

3. PHYSICAL PROPERTIES OF SUPERCONDUCTORS 27
- 3.1 Introduction 28
- 3.2 Different Classes of Superconducting Materials 30
- 3.3 Electrical and Magnetic Properties 35
- 3.4 Thermal Properties 58
- 3.5 Optical Properties 63
- 3.6 Summary of material properties of YBCO 66

4. SUPERCONDUCTING PHOTORESISTIVE OPENING SWITCH 67
- 4.1 Principle of Operation 68
- 4.2 Switch Design 71
- 4.3 Experimental Results 73
- 4.4 Modeling and simulation of the bolometric component 80
- 4.5 Discussion 87
- 4.6 Scaling the photoresistive switch up to higher current 95
- 4.7 Disadvantages of the photoresistive switch design : Motivation for a contactless switch 97

5. SUPERCONDUCTING INDUCTIVELY COUPLED SWITCH 98
- 5.1 Principle of Operation 99
- 5.2 Experimental Results in low magnetic field 104
- 5.3 Experimental Results in high magnetic field with a multi-turn secondary coil 108
- 5.4 Experimental results in high magnetic field with single turn secondary coil 121
- 5.5 Discussion 126

6. ANALYSIS OF TRANSIENT FLUX DYNAMICS IN SUPERCONDUCTING INDUCTIVELY COUPLED SWITCH 130
- 6.1 Modeling the screening currents in a superconducting disk 131

6.2 Magnetostatic currents and fields of a single superconducting disk....137
6.3 The case of two superconducting disks (experimental configuration)....144
6.4 Transient analysis of current and magnetic field....148
6.5 Coupling of transient flux in an output (secondary) coil....152
6.6 Heating below T_c : Flux-flow regime....161
6.7 Comparison with experimental results....162

7. CONCLUSION....164

BIBLIOGRAPHY....168

APPENDICES....182
Appendix 1 : Elliptic Integrals and their properties....183
Appendix 2 : Two problems involving the logarithmic divergence....186
Appendix 3 : MATLAB Programs....190
Appendix 4 : The laser system....204
Appendix 5 : Operation of the superconducting magnet and the magnet cryostat....213

LIST OF TABLES

Table 2.2.1	Merits and demerits of existing and developing opening switch technologies	15
Table 2.4.1.1	Comparison of energy storage methods	21
Table 3.2.1	Critical temperature and magnetic field of some metallic superconductors	30
Table 3.6.1	Properties of YBCO	66
Table 4.5.1	Nature of nonbolometric photoresponse observed by different groups	91

LIST OF FIGURES

Figure 2.2.1	Comparison of opening switch technologies	10
Figure 2.2.3.1	Schematic representation of the operation of a plasma erosion opening switch.	14
Figure 2.3.1.1	Operation of fault current limiter.	16
Figure 2.3.1.2	Resistive fault current limiter.	17
Figure 2.3.1.3	Inductive fault current limiter	18
Figure 2.3.2.1	Pulse sharpening using an opening switch.	19
Figure 2.3.3.1	Energy extraction from an inductive energy storage system	20
Figure 2.4.1.1	A comparison of different storage methods in terms of their energy density and transfer time.	22
Figure 3.1.1	The J-H-T phase diagram showing the superconducting state	29
Figure 3.2.1	Manufacturing process of filamentary Nb-Ti copper composite wire	31
Figure 3.2.2	Crystal structure of $YBa_2Cu_3O_7$	33
Figure 3.3.1.1	Resistance of a thin YBCO film drops to zero at a transition temperature of 91.5 K.	36
Figure 3.3.2.1	The two-fluid model	38
Figure 3.3.3.1	Screening currents (J_S) are set up inside the superconducting half-space to screen the applied field B_0.	40
Figure 3.3.4.1	Magnetization of Type I superconductor	43
Figure 3.3.4.2	Critical field (H_C) as a function of temperature(T).	43

Figure 3.3.5.1	An ellipsoid of revolution with a magnetic field applied along the axis of revolution.	45
Figure 3.3.6.1	The ratio of lower critical field and the thermodynamic critical field as function of the Ginzburg-Landau k	48
Figure 3.3.6.2	Magnetization of type II superconductor	48
Figure 3.3.7.1	Current-voltage characteristics of type II superconductors.	52
Figure 3.3.8.1	The change in average flux density and current density as the applied field H_0 is increased from H_1 to H_{max} in two steps	53
Figure 3.3.8.2	The change in average flux density as H_0 is decreased from H_{max} of Fig. 3.3.8.1.	54
Figure 3.3.8.3	The flux density inside the superconductor and magnetization as the applied field is increased from zero to Hmax and then decreased from Hmax to zero	54
Figure 3.3.9.1	Variation of critical current density as a function of magnetic field.	57
Figure 3.3.9.2	$J_c(B)$ of $YBa_2Cu_3O_{7-x}$ films on $LaAlO_3$ substrates measured at 77K	57
Figure 3.4.1.1	C/T vs. T^2 for $YBa_2Cu_3O_{7-y}$	59
Figure 3.4.1.2	C vs. T of YBCO films obtained by various groups	60
Figure 3.5.1	Reflectance of YBCO.	64
Figure 3.5.2	Room temperature reflectivity of $YBa_2Cu_3O_{6+x}$ for varying x	65
Figure 4.2.1	The photoresistive switch.	71
Figure 4.3.1	Photoresponse for varying fluence at 70K with a 30 mA current bias shows two switching components. The slower component is bolometric in origin	74
Figure 4.3.2	Photoresponse for varying fluence at 80K with a 30 mA current bias.	74

Figure 4.3.3 Photoresponse for varying fluence at 70K with a 100 mA current bias..... 75

Figure 4.3.4 Photoresponse for varying fluence at 70K with a 10 mA current bias. 76

Figure 4.3.5 Photoresponse for varying fluence at 65K with a 100 mA current bias..... 76

Figure 4.3.6 Photoresponse for varying fluence at 65K with a 30 mA current bias. 77

Figure 4.3.7 Photoresponse depends on the bias current. (a) responses at 10 mA, 30 mA and 100 mA at a fluence of 10.5 mJ/cm^2 at 70K..... 78

Figure 4.3.8 Photoresponse at different initial temperatures (70K, 65K, and 60K) at a fixed current bias (100 mA) and laser fluence (10.5 mJ/cm^2)..... 78

Figure 4.3.9 Photoresponse at different initial temperatures (70K, 75K, and 80K) at a fixed current bias (10 mA) and laser fluence (7.35 mJ/cm^2). 79

Figure 4.4.1 Time variation of the temperature distribution across the thickness of the film..... 82

Figure 4.4.2 Simulated signals showing the variation of the response time. (a) response time increases with decreasing laser fluence, (b) response time increases for lower initial temperature and lower bias current..... 84

Figure 4.4.3 Thermal response time of the switch increases with decreasing fluence..... 85

Figure 4.5.1 Current redistribution in electrodes..... 94

Figure 4.6.1 New design of high current switch..... 96

Figure 5.1.1 Operation of the inductively-coupled switch..... 99

Figure 5.1.2 Flux exclusion and expulsion in the reversible (Meissner) regime for $H_{app} < H_{c1}$ 101

Figure 5.1.3 In the irreversible regime, $H_{c1} \leq H_{app} \leq H_{c2}$, the initially excluded flux is trapped once it penetrates the film.....102

Figure 5.2.1 Experimental set-up for the inductive switch.....104

Figure 5.2.2	The inductive switch configuration showing the use of pancake coils as the primary and secondary coils and the sample holder.	106
Figure 5.2.3	Photoinduced switching observed in the inductively coupled switch of Fig. 5.2.1	107
Figure 5.2.4	Peak of the photoinduced secondary voltage as a function of laser fluence.	107
Figure 5.3.1.1	The superconducting magnet system.	109
Figure 5.3.2.1	The high field experiments are performed with a superconducting magnet acting as the primary coil.	110
Figure 5.3.2.2	Torque on the film due to perpendicular magnetic field	111
Figure 5.3.3.1	YAG laser system used to produce 150-ps laser pulses of energy up to 30 mJ.	112
Figure 5.3.3.2	The experimental set-up for the high field experiments showing the laser illumination scheme and the data acquisition system.	113
Figure 5.3.3.3	The secondary voltage signal decreases exponentially with laser shots	115
Figure. 5.3.3.4	Anomalous charge signal in the inductive switch	116
Figure 5.3.4.1	Magnetic field lines bend around the superconducting films due to flux screening.	117
Figure 5.3.4.2	The dark region is not illuminated by laser and remains superconducting while the central illuminated region goes normal.	118
Figure 5.3.4.3	The film is supported only at the four corners. This modification will avoid any screening currents after the laser illumination.	118
Figure 5.3.4.4	The film is patterned into a circle in the region of illumination. The entire film is illuminated under this scheme	119

Figure 5.3.4.5 The film is patterned as a ring so that only a portion of the ring needs to be illuminated to allow flux entry.....120

Figure 5.4.1 Secondary voltage pulse taken at T=12K, and an applied magnetic field of 0.2 T. The rise time of the pulse is 2.5 ns.....122

Figure 5.4.2 Flux motion is faster for higher laser energies. The flux associated with each pulse is the same.....123

Figure 5.4.3 As laser energy is increased for the same flux, peak voltage rises sharply, indicating faster flux motion.....124

Figure 5.4.4 Larger critical current at lower temperature corresponds to a larger amount of excluded flux.....125

Figure 5.4.5 Peak secondary voltage and magnetic flux are essentially independent of magnetic field.....125

Figure 5.5.1 The Programmed inductive element (PIE) scheme.....128

Figure 6.1.1 A thin circular disk of radius R is divided into concentric strips of width w.....133

Figure 6.1.1.1 Vector potential due to a current loop of radius r in the z=0 plane.....134

Figure 6.2.1 The field is calculated at radial locations ri, halfway between two consecutive current loops.....137

Figure 6.2.1.1 Zero flux surface current distribution calculated by our model (solid line) with n = 25, and by the analytical expression (dotted line) of Eq. 6.2.3-1. The results are virtually identical.....139

Figure 6.2.2.1 Surface current distribution as a function of radial distance.....140

Figure 6.2.2.2 Magnetic field distribution as a function of radial distance.....140

Figure 6.2.4.1 (a) Surface current and (b) field distribution for constant $J_c(B)$ (solid line) and $J_c(B) = J_c(0)^{(1-|B|/B_0)}$ (dashed line).....143

Figure 6.3.1 Two identical coaxial disks of thickness d and radius R separated by a distance c. The external field is parallel to the axis of the disks.....145

Figure 6.4.2.1 (a) Surface current ($I_S(r,t)$), and (b) magnetic field ($B_Z(r,z=0,t)$) distributions at different instants of time.....151

Figure 6.5.1 A secondary coil, connected with the load circuit placed halfway between two superconducting disks.....152

Figure 6.5.1.1 Two coaxial circular loops of radii a and b, carrying currents I_a and I_b are separated along the axis ($\hat{z}$) by a distance c.....153

Figure 6.5.2.1 The inductance matrix L, for a film coupled to the secondary coil, is partitioned into four submatrices.....154

Figure 6.5.2.2 The inductance matrix L, for two films, is partitioned into nine submatrices.....156

Figure 6.5.2.3 The voltage pulse produced at a single-turn secondary coil for different values of output resistance.....158

Figure 6.5.2.4 A comparison of secondary voltage pulses in the one-film and two-film configurations.....159

Figure 6.6.1 Voltage pulse for superconducting films heated to flux-flow regime.....161

Figure 6.7.1 A comparison between the experimentally obtained voltage waveform (thick line) to one simulated by our model (thin line) , preserving the time integral of the output voltage.....163

Figure A2.1 A thin loop of width w and radius a. The self-inductance of the loop is calculated in the limit w << a.....188

Figure A4.1.1 The laser system.....205

Figure A4.2.1 Regenerative amplification and cavity dumping.....208

Figure A4.4.1 Laser beam profile is measured by scanning with a razor blade.....209

Figure A4.4.2 Measurement of laser beam profile for an elliptical beam. 211

Figure A5.2.1 A drawing of the magnet cryostat. The cryostat was built by Janis Research Co., Wilmington, MA and their drawing number is D02-12-93A. 220

CHAPTER 1

INTRODUCTION

The quest for knowledge is driven by the search for perfection. Perfect electrical conductors have always been an object of fantasy since the discovery of electric current. Therefore, it is natural that the discovery of superconductors, though accidental, proved to be one of the most significant achievements of this century. The superconductor is more than a perfect conductor. It exhibits a host of other properties, the most important being expulsion of magnetic flux (Meissner Effect), besides having zero dc electrical resistance.

The superconducting state and its properties have been a topic of active research since its discovery in 1911. Cryogenic temperatures are required to maintain the superconducting phase. This limits the use of superconductors to applications where the advantages of using superconducting devices exceed the cost of the associated cooling system. The early metallic superconductors had critical temperatures (T_c) below 10 K. Therefore, liquid helium, an expensive cryogen, was required to cool any superconducting device. The discovery of cuprate superconductors with critical temperatures above the boiling point of nitrogen (77 K) opened a new horizon in the field of superconducting devices. Since liquid nitrogen is much cheaper than liquid helium, many superconducting devices are expected to become economical in future. The superconductive devices are superior to others in both high power engineering (transmission lines, magnets, generators, and motors) and ultrafast, high performance electronics (microelectronics, microwave and millimeter wave electronics, and precision instrumentation).

In this thesis, we have chosen to investigate fast, high-current switching with high temperature superconducting films. There is a requirement for high quality solid-state opening switches in the field of electrical power engineering. Superconductors with zero closed-state resistance are ideal candidates for opening switches. The design of opening switches is a challenging problem, especially when both high speed and large current capacity are required. These thin film switches exhibit very high current densities and are compatible with the high power superconducting devices like magnets. Therefore, these superconducting switches may be utilized in various commercial applications like fault current limiters, energy extraction from inductive storage systems, production of fast rising current pulses, and flexible ac transmission lines.

In chapter 2, we discuss the present state of opening switch technology and their application. The superconducting switch, though in its inchoate stage of development, has bright prospects for very high speed (nanosecond) switches where other technologies fail. In section 2.2, we discuss the relative merits of different technologies and identify the operational regimes where superconductors hold a clear advantage over other established and developing technologies. In section 2.3, a few key applications of opening switches are discussed. Studying a suitable superconducting switch for energy extraction from superconducting magnetic energy storage (SMES) was a strong motivation for this research. A discussion of salient features of SMES technology (section 2.4) as a fast and compact energy storage device is therefore deemed necessary to identify the need for a lossless and a contactless switch.

We have studied two different types of superconducting opening switches. In both cases the switches were thin $YBa_2Cu_3O_{7-x}$ (YBCO) films and were triggered with short laser pulses. Optical triggering provide us accurate timing control. Besides, photoresponse of high-T_C superconducting materials (in our case thin YBCO films) is a subject of great interest. The first design, the photoresistive switch, operates by a transition from the zero-resistance superconducting state to a resistive normal state. The second design, the inductive switch, is based on flux screening in the superconducting state. While the two switches are based on two entirely different principles of operation, they produce the same switching action.

In chapter 3, we discuss the physical properties of superconductors that are relevant to our switches. Different classes of superconductors are described in section 3.2. We have discussed the electrical and magnetic properties in section 3.3. The concepts of critical magnetic fields, critical currents, flux exclusion and expulsion and flux pinning in type II superconductors are extremely important for the operation of our switch and are described in this section. Relevant thermal and optical properties are discussed in sections 3.4 and 3.5. Important material properties of YBCO are summarized in section 3.6.

The photoresistive switch is described in chapter 4. After a description of its principle of operation (section 4.1), the experimental set-up (section 4.2) and results(section 4.3) are described . The switching response (also called the

photoresponse) revealed a fast and a slow component. The fast component had short (~4-6 ns) rise and fall times. A slower signal (50-100 ns rise time) was superimposed on the fast signal component. The amplitudes of these two signals were of the same magnitude. The slower component showed a delay with respect to the laser trigger, referred to as the response time, and is bolometric in origin. The finite response time arises from our use of optically thick[1] films. Initially the incident laser energy is absorbed in the top part of the film, while the material at the bottom of the film remains superconducting, acting as a zero-resistance shunt. The temperature profile across the thickness of the film changes in time as heat diffuses down, heating up the entire bulk of the film.

A one-dimensional heat-flow model, incorporating thermal properties of the film and the substrate, was developed to simulate the bolometric component of the photoresponse. This is described in section 4.4. We follow this up with a discussion of the equilibrium and nonequilibrium processes in superconductors, outlining possible mechanisms responsible for the fast switching component (section 4.5). The origin of the fast component is still not understood clearly.

A new design (section 4.6) has tested high current operation of these thin film switches. Only preliminary results are available at the present time. However the results were encouraging as we switched currents up to 80 A in 1-cm wide, 500 nm thick switches. The last section (4.7) of this chapter describes some of the problems with the earlier design of the photoresistive switch. Due to poor metallic contacts to the superconductor and other problems associated with contacts, we were encouraged to look for other switching mechanisms. This lead to our invention of the contactless inductive switch.

The inductive switch is based on flux screening properties of a superconductor. It isolates the source (primary) and load (secondary) circuits which are magnetically coupled, by acting as a removable flux-screen. Upon optical triggering, the switch becomes resistive, and a decay of screening currents allows flux penetration through

---

[1]Films thicker than the optical penetration depth (~120 nm) were used to enhance current carrying capacity of the switch.

the film, enabling flux coupling between source and load circuits. Section 5.1 describes the principle of operation of this switch in different regimes. The following three sections discuss the experimental set-up and the results of three different sets of measurements : in low magnetic fields, in high magnetic fields using a multi-turn secondary coil, and in high magnetic fields using a single-turn secondary coil. The load voltage arises from temporal change of flux coupling in the secondary coil. Since this is a derivative effect, the faster the flux motion, the larger the peak voltage and the extracted energy. By minimizing secondary inductance with a single turn coil, we were, therefore, able to get shorter switching time and higher switching current.

The inductive switch involves transient flux motion in the superconducting films following laser irradiation in the critical state[2]. In the past three years, the critical-state current and field distributions in thin films of various geometries have been an area of active interest. While most of the work concentrates on static distributions and those for ac magnetic fields, the issue of transient effects on screening currents has remained neglected. In order to understand the underlying physical phenomena associated with the switching of thin film superconductors to the resistive state in magnetic field, we have investigated the critical state flux dynamics for the thin disk geometry (chapter 6). Section 6.1 describe the modeling of screening currents in the superconductor. The calculation of static current and field distributions is discussed in sections 6.2 and 6.3.

The transient analysis, utilizing a method based on temporal evolution of magnetic vector potential, is described in section 6.4. This novel technique leads to efficient computation of simulated switching signals (section 6.5). If nanosecond switching speed is not a requirement, a considerable saving in laser energy can be achieved by heating the cold thin film switch in the flux flow regime (section 6.6), instead of driving it fully normal. The dissipation associated with flux flow is expected to result in rapid thermal run-away driving the switch fully normal. A comparison of simulated signal with experimental results (section 6.7) shows good agreement. The thermal delay arising from heat diffusion in optically thick films was not incorporated in this simulation to avoid computational complexity. Therefore, the simulation, assuming

---

[2]See section 3.2.7

instantaneous transition of the film, estimates even shorter rise time and higher peak voltage than the experimental result.

Finally, a number of appendices are included. Appendices 1 and 2 describe properties of elliptic integrals and a novel method of treating logarithmic divergence. These are extremely useful for the analysis described in chapter 6. Appendix 3 lists the MATLAB codes used for computations described in chapter 6. These are very efficient and adaptable for other problems involving flux motion, and magnetostatics. The Nd:YAG laser system is an important component in all our experiments. Appendix 4 gives a description of the laser system. Appendix 5 describes the operation of the superconducting magnet and the custom-made cryostat that fits into its horizontal warm bore.

CHAPTER 2

OPENING SWITCHES FOR HIGH POWER APPLICATIONS

2.1 Opening Switches

Switches are indispensable in electrical circuits. Switches are characterized by two main parameters, the switching speed and the power handling ability. However, it is difficult to achieve high power switching at high speed. The switches can be categorized into two primary functional classes: closing switch and opening switch. There are three components of a switching circuit : the source, the load, and the switch. The function of a closing switch is to divert the current from components connected in parallel to the switch into the circuit branch containing the switch. On the other hand, an opening switch diverts current away from the circuit branch containing the switch to parallel circuit branches. In the absence of a parallel circuit branch the closing switch closes the current path through the switch, while the opening switch interrupts the current path.

In high power switching, fast solid-state closing switches are available using semiconducting devices. Fast high power opening switches are a challenging design problem. Most of the commercial high power opening switches are mechanical and are inherently slow. This is a field of active research and many plasma based and explosive opening switches are being developed. Semiconductor switching devices are mainly voltage driven, which is the normal mode of operation for closing switches. Opening switches are, on the contrary, current driven devices. Superconducting devices are current-driven and are natural candidates for opening switches. We have therefore focused our research towards superconducting opening switches.

The design of an opening switch depends on the specific application. These switches are required to carry high currents (100A–10MA) and operate with short switching times (10ms–10ns), with repetition rates ranging from 1 to 30,000 pulses per second. Moreover, before opening, the switch must conduct the source current as required. To accomplish current interruption, the opening switch must force the source current to transfer from the switch to a parallel circuit branch (a load) and then withstand the voltage generated across the load. If there is no load in parallel to the branch containing the switch, then the switch can interrupt the current only by absorbing all of the energy stored in the circuit inductance and recovering against the open circuit voltage of the current source. This makes the design of an opening switch a

difficult problem. The severity of the switching problem depends upon the circuit in which it operates. Therefore, opening switches must always be considered in the context of the circuit in which they are used.

There are various types of opening switches. In the next section, we shall briefly discuss various types of existing and developing technologies and discuss their relative merits and demerits.

Applications of opening switches range from fault current protection to transfer of energy from an inductive energy store to a load. In section 2.3 we shall discuss some key applications of opening switches. Our research on inductively-coupled switches mainly focused on energy extraction from superconducting magnetic energy storage systems (SMES). This emerging technology is becoming increasingly popular for power quality improvement and uninterruptible power supplies. In section 2.4, we shall discuss the advantages of inductive energy storage systems and briefly review the SMES technology. We shall also examine the benefit of using a superconducting switch to reduce the operating cost of a SMES system.

2.2 An overview of opening switch technology

There are several classes of opening switches. The oldest and the most widely used are the mechanical switches or circuit breakers. These can handle high power but are slow. The other popular varieties are solid state switches, and fuses. The advancement of semiconductor technology in the power electronics area has enabled the use of thyristor based switches at moderately high power. Fuses are one-shot switches, but can handle high power while operating very fast. There are many classes of plasma-based opening switches that are being currently developed. These are very promising but are expensive and less reliable. The superconducting switch is a solid state switch and uses nonlinear material properties to switch from the superconducting to the resistive state. Figure 2.2.1 shows the switching time and current of different opening switches. A brief description of different switching methods are described below. Table 2.2.1 summarizes their relative merits and demerits.

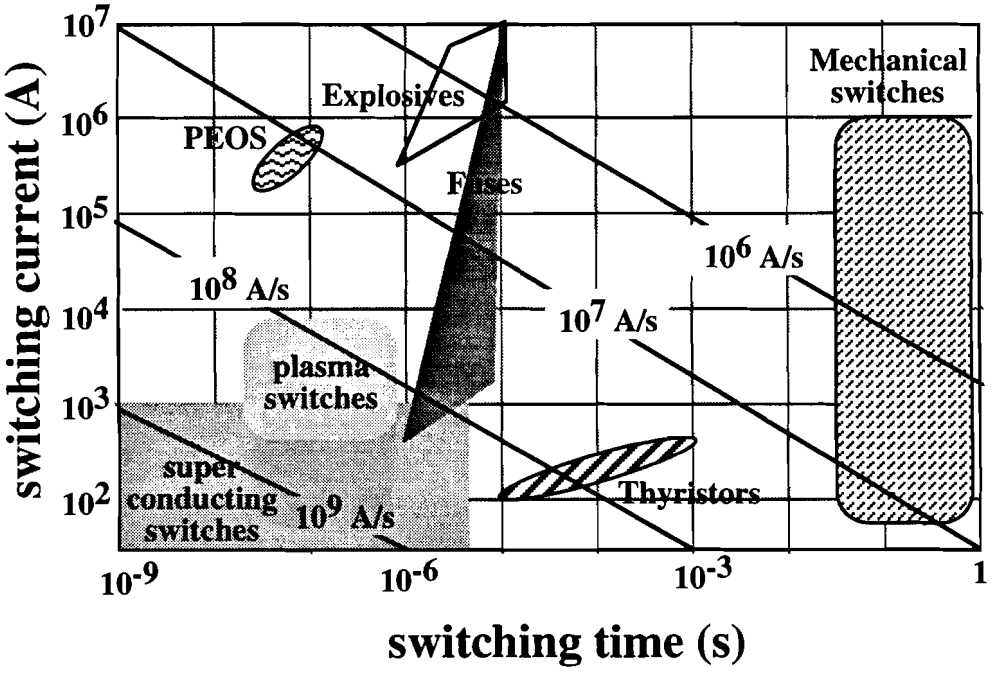

Figure 2.2.1 Comparison of opening switch technologies. The superconducting switches have the highest dI/dt, but have not demonstrated high current operation. The plasma switches, including the plasma erosion opening switch (PEOS) are in the experimental stages. Mechanical switches, thyristors and fuses are commercially available mature technologies.

2.2.1 Mechanical Switches

Mechanical switches have been used to control the flow of current since the 18th century. Commercial break switches in air medium by Westinghouse, Asea Brown Boveri and General Electric are rated in the range of 10 kA and a few thousand volts[1]. Those in oil medium (which has a higher dielectric strength than air) operate in the 10-200 kV range with 10-100 kA[1]. The gas-blast switch (usually employing SF_6) operates at somewhat higher voltage range (up to 800 kV). SF_6 has higher dielectric strength, greater thermal conductivity than air, and lack of oxygen in the system prevents oxidation of contact surfaces. However, these switches are slow compared to all the other switches discussed below. The "tripping" of the breakers is performed magnetically or thermally. This switching technology is well established and has very low production cost for large volume productions and is extremely reliable.

2.2.2 Solid state switches

Solid state switches are based on nonlinear material properties of the solid that are used to reduce the mobility and/or concentration of carriers. The resistivity changes may stem from semiconductor-insulator, metal-semiconductor, or superconductor–normal conductor transitions. The transition should preferably be reversible and controllable by suitable triggers. The semiconductor based switches are becoming increasingly popular since they have fast switching speeds and high repetition rates, even though they cannot handle very high power. Unlike mechanical switches, solid state switches are compatible with electronic control. They also have a long lifetime, unlike plasma based switches.

Thyristors and other semiconductor switches:

The most established solid state opening switches belong to the thyristor family[2]. Thyristors are four layer (p-n-p-n) semiconductor devices[3]. Thyristors can act as either closing or opening switches. The basic device of the thyristor family is the silicon controlled rectifier (SCR). The device is normally nonconducting and blocks the current flow of either polarity across it. The conducting or "on" state is achieved by using a gate voltage pulse. The SCR latches to the "on" state. To open the switch (to recover to the blocking state) the device current is reduced below the holding current. The opening time depends on the carrier recombination time of the central junction.

Therefore, if the junction width is made larger to increase power handling capacity the switching time also goes up.

The other thyristor used as an opening switch is the gate turn-off (GTO) thyristor. The SCR requires a counterpulse of the magnitude of the entire device current for opening. The GTO, on the other hand, can be opened by a reverse gate pulse. GTO's are effective for a few kV switches at a few 100 Hz repetition rate. Power bipolar transistors, power MOSFETs, and Insulated gate bipolar transistors (IGBT) are other semiconducting switches. All these switches are better as closing switches since the turn-on time is faster than the turn-off time.

Switches based on a positive temperature coefficient of resistance (PTCR) [4]

Many solid state materials exhibit sharp changes in their resistance at phase transitions and can be used as an opening switch. Usually, a temperature change effected by external heating is employed to cause the phase transition. Superconductors exhibit the sharpest resistance change at the superconductor–normal-conductor transition. Also, in the superconducting phase, the resistance is zero for dc and very small at power frequencies. The superconductors can also carry a very large current in the closed state. The photoresistive switch (chapter 4) is based on this effect. There are three methods of triggering the phase transition : heating above the critical temperature, exceeding the critical current, and applying an external magnetic field higher than the critical field of the superconductor.

Barium Titanate shows a sharp PTCR (more than 3 orders of magnitude) effect at ~125° C. This is an insulating polycrystalline material. It is made semiconducting by doping with La or Nb which provide donor sites. Following a low temperature annealing oxygen diffuses into the grain boundaries creating acceptor sites. Below 125°C, $BaTiO_3$ contains poled domains and charged domain walls. Since grain boundaries coincide with the domain walls, the negative charge on half of the grain boundaries neutralizes the space charge from oxygen acceptor states. This permits an easy flow of conduction electrons between grains and the resistance is low (10 Ω-cm). However, the domain walls and their charges disappear above 125° C greatly increasing the resistivity. Barium Titanate switches are used in 60 Hz motors as starter switches.

Other methods utilize the metal-semiconductor transition of Europium Oxide, reduction of carrier mobility in Indium Antimonide, and polymeric phase change in Carbon-filled polymers.

2.2.3 Plasma based switches

Different classes of Plasma opening switches are currently been studied[5]. We describe below three promising technologies.

Diffuse Discharge Opening Switch [6]

Here the switch medium is an externally sustained discharge. The external sustaining source is either a laser (usually CO_2) or an electron beam (e-beam). By e-beam or laser radiation the gas between the two electrodes becomes ionized and conductive. The switch is closed. When the external source is turned off the conductivity of the gas decreases and opens the switch. Usually the opening of the switch is performed by turning off the e-beam. However if the discharge is optically illuminated with a wavelength corresponding to the atomic or molecular transition of the gas, the conductivity can be controlled through optogalvanic effects. The most efficient scheme is therefore an e-beam sustained optically assisted discharge switch.

Low-pressure Plasma Opening Switch [7]

This is also a diffuse discharge switch. However, glow-discharge with cold cathodes, employing secondary electron emission, is used in this switch. The mechanism of glow discharge is Paschen breakdown. An example of such a switch is the Crossed Field Tube (XFT) which employs crossed magnetic field to produce high-density plasma.

Plasma Erosion Opening Switch (PEOS) [8]

This opening switch (Fig. 2.2.3.1) is operated by injection of plasma. The source is a suitable current source or a slow capacitor bank. The injection of plasma [Fig. 2.2.3.1(a)] allows the storage inductor to charge by isolating the load. When the requisite current level is reached in the storage inductor it opens by erosion of the plasma [Fig. 2.2.3.1(b)]. This can be used for pulse sharpening [section 2.3.2]. Like

all other plasma switches the main disadvantage of this switch is gradual erosion of the electrodes through repetitive operation. Characteristics of PEOS is a field of active research.

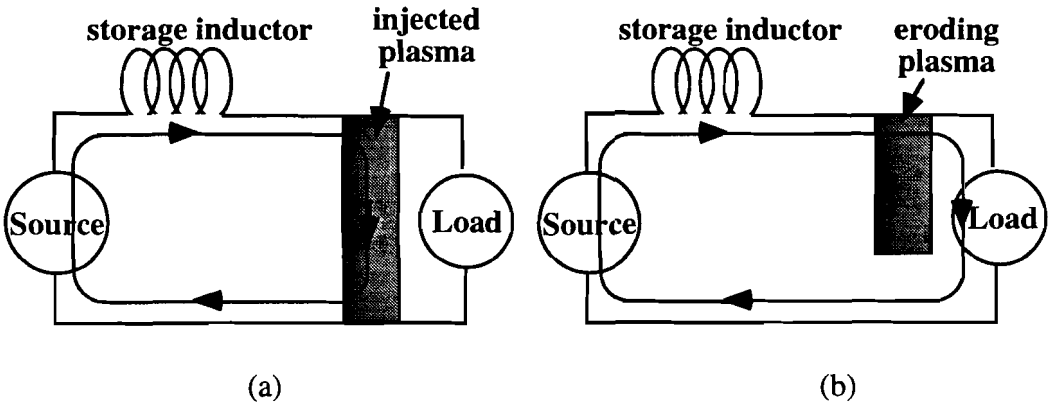

Figure 2.2.3.1 Schematic representation of the operation of a plasma erosion opening switch. (a) switch is closed. (b) switch is open.

2.2.4 Fuse Opening Switch

The fuse opening switch[9], as the name suggests, operates by melting of a foil or wire (the fuse) to interrupt current. The foils or wires of metals such as copper, silver, gold and aluminum are placed in a quench medium that can be granular (Glass, quartz, alumina, silicon carbide), solid (polythene, paraffin, mylar) or liquid (water). The foils in solid and granular medium exhibit currents of 300-400 kA but the foils and wires in water can be as low as 500 A and as high as 400 kA depending on the design. However, currents as high as 15-30 ṂA (peak) have been interrupted in 200-300 ns against 200-300 kV in the Shiva Star Inductive Pulse Compression System[9]. The fuse opening switches operate in single shot mode. However they are quite reliable.

2.2.5 Explosively-Driven Opening Switch

This switch uses a high pressure rapidly advancing detonation wave following an explosion[10]. A cylindrical geometry is used for high current switching. Opening of the switch, effected by a rise of resistance, is caused by the compression of the surrounding plasma channel as the detonation wave front reaches the outer surface of the explosive at the time when the generator current reaches its peak. Very high currents and very fast (~1 μs) switching times can be obtained. This switch can be used as a closing switch too[11].

An explosively driven HTS opening switch has been proposed[12]. Here a hollow cylindrical bulk HTS switch carries the current in the closed state. The switch is opened by shattering the cylinder as the pressure wave following an explosion inside moves outward. The ceramic HTS materials work better in this mode rather than the metallic superconductors which do not break uniformly.

Table 2.2.1 Merits and demerits of existing and developing opening switch technologies

Type of Switch	Merits	Demerits
Mechanical Switches	• High power operation • Excellent reliability • Low cost • Very low on-state resistance • Bi-directional	• Slow switching time • Not electronically compatible
Thyristors	• Moderate switching speed • Electronic compatibility • Good reliability	• Low power operation only • Faster as closing switch • High losses in closed state
Fuse Opening Switches	• Low on-state resistance • High power operation • good reliability	• Only single-shot operation • Not suited for low power • Expensive
Super-conducting opening switches	• Very high switching speed • Lossless in closed-state • Electronic compatibility • Repetitive operation for resistive switch • Compatible with super-conducting magnetic energy storage	• High power operation yet to be demonstrated • Only single-shot operation for inductive switch • Low normal state resistance for LTS • Developing technology
Explosively-driven switches	• Low on-state resistance • High power operation	• Only single-shot operation • Poor reliability • Expensive
Plasma Erosion Opening Switch	• High power operation • High switching speed • Repetitive operation	• Developing technology • Short life-time

2.3 Applications of opening switches

2.3.1 Fault Current Limiters

Fault current protection is required in electrical transmission and distribution systems. In the event of an accidental short circuit (or a *fault)* the current in a part of the circuit rises suddenly. Without protection the sudden increase in current will catastrophically destroy devices connected to that part of the circuit. An opening switch in series with such devices [Fig. 2.3.1.1(a)] can prevent the flow of large fault currents. To interrupt the fault current, the opening switch must absorb all the energy stored in the circuit's stray inductance and then withstand the high voltage remaining on the source as shown in Fig. 2.3.1.1(b). Fault-current limiters can also be designed so that the opening switch diverts any excess current away from the circuit while the load current stays constant.

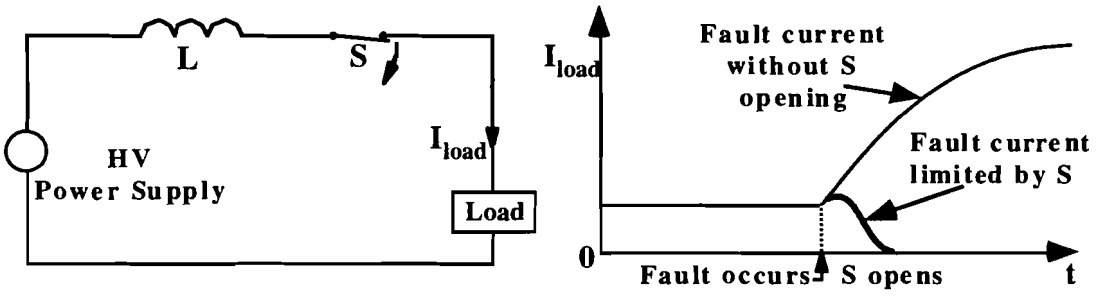

Figure 2.3.1.1 Operation of fault current limiter. (a) Opening switch used for fault-current protection. (b) Current waveform showing effectiveness of opening switch in limiting fault current magnitude. [13]

The present techniques in fault-current protection employs mechanical circuit breakers. However, these circuit-breakers operate at the zero-crossing of the alternating source current. Therefore, the components above the fault have to withstand the destructive effects of the short-circuit currents for 8.33 ms or 16.67 ms (for 60 Hz ac), depending on whether the fault is symmetric or asymmetric[14]. A much more attractive device is a current limiter that clips the fault currents and reduces damage to the circuit components. This will reduce the fault duration and improve the dynamic stability of the transmission system. Ultrafast fuses and thyristors are such devices.

These are not suitable for high voltages (above 10 kV). Superconducting fault current limiters (SFCL) are therefore being developed due to their superior speed and power handling prospects.

In its simplest form, the SFCL consists of a series superconducting element. However, to avoid excessive heating in the superconductor, a shunt resistor is placed in parallel with the switch. During normal operation the superconducting switch carries the current. When a fault occurs, the superconductor is switched to its resistive state and the shunt resistor offers the necessary impedance to limit the fault current (Fig. 2.3.1.2). The switching may be achieved by heating it above T_c. The superconducting element should have high current carrying capacity. In order to commutate most of the current to the shunt resistor, the normal state resistance of the superconductor has to be high. Important material parameters are therefore high normal state resistivity (ρ_N) and high critical current density (J_c)[15]. Uniform heating of the switch is also important. Non-uniform heating leads to local hot spots which result in large transient dissipation in the superconductor. Visible and IR radiation are considered the best choices for heating, whenever possible. It is also preferable to design the switch to be self sustaining. The heating of the superconductor in the normal state due to the residual current flow should maintain the superconductor above its transition temperature as long as the switch is required to stay open.

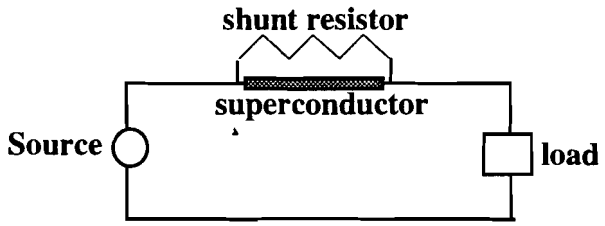

Figure 2.3.1.2 Resistive fault current limiter. The superconducting switch may be triggered thermally (e.g. a laser pulse) or by a pulsed magnetic field or by exceeding the critical current density.

There is also a self-triggered switching scheme based on exceeding the critical current density of the superconductor. This can be of two types : resistive and inductive. The same considerations regarding material properties discussed in the previous paragraph apply to this case. As shown in Fig 2.3.1.2 the superconductor is shunted by a resistor under normal operating conditions. When the fault occurs the critical current is exceeded and the superconductor becomes resistive. The resistance of

the superconductor increases from zero towards its normal state value as the quench occurs[1]. As before, the shunt resistor limits the fault current.

For the inductive design [16], a primary normal metallic coil is coupled to a shorted superconducting secondary (usually a hollow cylinder) through a ferromagnetic core. Under normal operating condition, the superconductor screens the primary field. At 60 Hz, the ac hysteretic losses in the superconductor are negligible compared to the inductive impedance[2]. When the fault occurs the superconductor quenches and develops a resistance R_n. The transformed impedance (N^2R_n) at the primary is very high[3] and limits the fault current. This configuration is fundamentally the same as our inductively-coupled switch (chapter 5). This type of SFCL is considered the most cost-effective [17]. Various elegant designs of the inductive fault-current limiter have been studied and implemented [18–23].

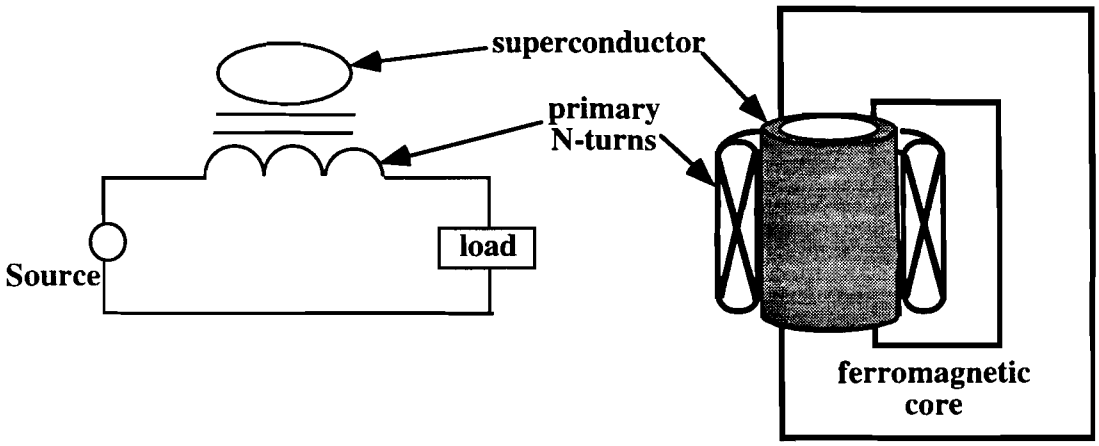

Figure 2.3.1.3 Inductive fault current limiter. The superconducting tube acts as a single-turn shorted secondary with a normal state resistance of R_n.

---

[1]Usually several normal zones start simultaneously and propagate. If the total normal state resistance is not achieved in a few milliseconds, the zones collapse as joule heating decreases following reduction of current.

[2]from the leakage flux in the gap between the core and the superconducting cylinder.

[3] Typical turns ratio is 100:1. So for a 50 A system a critical current of 5 kA is required.

2.3.2 Pulse Sharpening

Opening switches are used to sharpen a current pulse from a capacitive discharge[13]. A load requiring a fast rising current pulse is bypassed with a closed opening switch, during the initial part of a capacitive discharge [Fig. 2.3.2.1(a)]. Near peak current, the switch opens, forcing a rapid transfer of the current to the load [Fig. 2.3.2.1(b)]. These are required in applications such as weapons simulation, missile launching, and inertial confinement fusion.

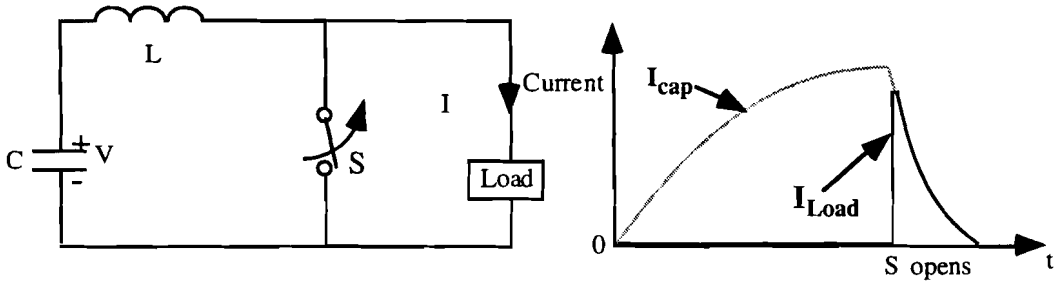

(a) (b)

Figure 2.3.2.1 Pulse sharpening using an opening switch. (a) Opening switch used for pulse-sharpening of the current from a capacitive discharge. (b) Wave forms of capacitive discharge current and load current[13].

2.3.3 Energy extraction from inductive storage

The standard inductive energy storage system [Fig. 2.3.3.1(a)] is used to supply power in the form of a large single pulse or a train of high power pulses. Energy is transferred from the inductive storage to the load each time the opening switch operates [Fig. 2.3.3.1(b)]. Such systems are widely used for pulsed particle accelerators and lasers, nuclear fusion, high power radar, induction heating systems and defense.

Many of the systems require repetitive operation and have a low output duty factor (ratio of pulse width to pulse interval). The average power is an equally low fraction of the peak power in a pulse. Therefore, instead of using a power supply rated at the peak pulse power, to drive the load directly, it is generally more practical to use a power supply rated at the average pulse train power, in conjunction with an energy storage system. The energy store is charged by the power supply during the interval

between pulses and then discharged to produce the output pulse. An alternative mode of operation is to use a larger energy store with the total energy of a train of pulses and recharging it from a much smaller power supply in between pulse trains. The advantage of using an energy storage increases as the repetition rate decreases. In the limit, a single shot operation, an energy storage is almost mandatory.

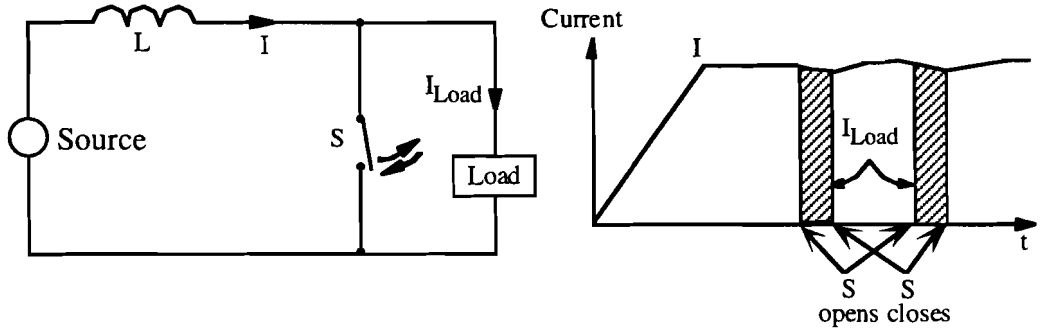

(a) (b)

Figure 2.3.3.1 Energy extraction from an inductive energy storage system. (a) Opening switch used in an inductive energy storage system to transfer energy to a load. (b) Simplified waveforms of the storage coil current and load current for an inductive energy storage system. The current through the power supply remains nearly constant. The cross-hatched area represents the current through the switch[13]

2.4 Inductive Energy Storage Systems

2.4.1 Why inductive energy storage?

Energy storage systems can be capacitive, inductive, chemical (batteries and high explosives), or inertial (rotating machines). The salient features in comparing these systems are energy storage density, storage losses, charging and discharging times, cost and size. Fig. 2.4.1.1 and Table 2.4.1.1 show a comparison of various energy storage methods. High explosives have the highest energy density and short energy release times (μs), but they are limited to single-shot operation and require expensive auxiliary equipment to convert the chemical energy to electrical energy. Chemical storage, such as batteries, have high energy storage density but have low power capability and long charging and discharging times (minutes). Inertial storage (flywheels) has moderate storage density and moderate power capability. Capacitors have the highest electrical discharge capability but relatively low energy storage density. Only inductive storage has both high energy density, a high electrical power capability, and short transfer times.

Table 2.4.1.1 Comparison of energy storage methods [13]

Storage Device	Energy Density (MJ/m^3)	Energy/Weight (MJ/kg)	Transfer time
Capacitors	0.01-1	300-500	μs
Inductors	3-40	100-1000	ms-μs
Batteries	2000	10^6	minutes
Explosives	6000	5.10^6	μs
Flywheels	400	10^4-10^5	seconds

Inductive storage also has a decreasing ratio of cost per unit energy as size increases. Superconducting inductors can be made essentially lossless and have higher energy density than normal metal inductors. For non-superconducting or normal coils, energy must be stored for times less than its L/R time constant to be practical. The need to charge a normal coil quickly requires a larger power supply than for other storage

systems. Superconducting inductive energy storage is therefore an economical and efficient method and is gaining popularity among the power engineering community.

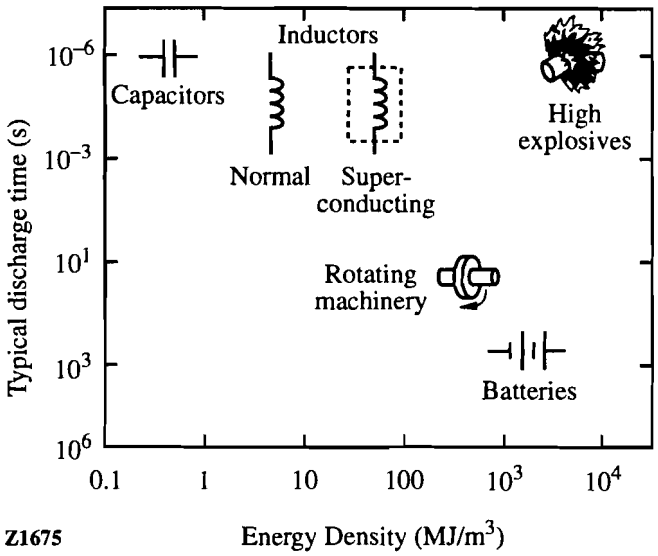

Figure 2.4.1.1 A comparison of different storage methods in terms of their energy density and transfer time[13].

2.4.2 Superconducting Magnetic Energy Storage (SMES)

Superconducting magnetic energy storage (SMES) was first proposed for use by utilities, to help them meet peak electricity demands[24, 25]. The SMES systems were to store gigawatts of electricity for several hours at a time. However, smaller units storing energy of the order of kWh with peak powers in the MW range, called μ-SMES (micro-SMES) have been commercialized before the larger units. The application of μ-SMES is for power quality improvement. American commerce and industry face a major problem with power quality which is estimated to cost $26 billion per year. This is caused by momentary (0.5-2 s) power sags and outages. Studies have shown that 85-90% of the time a sag, or a drop in the line voltage, is the cause of a failure. These problems mainly affect automated manufacturing processes such as semiconductor manufacturing, paper industry, chemical factories and assembly lines in the automobile industry, where the manufacturing process is controlled by digital electronic equipment. To provide an Uninterruptible Power Supply (UPS), small superconducting magnetic energy storage (μ-SMES) can be used. This consists of a superconducting magnet

(usually Nb-Ti or Nb_3Sn) connected to the load through a switch which opens in case of a line power failure. The advantages of SMES are the following[26]:

1) Many charge-discharge cycles implying longer life (~30 years, much longer than batteries).

2) Discharge times are very short (ms) and charging times are short compared to other devices (a few seconds).

3) It has no moving parts, except for the refrigerator.

4) Can be made more compact than other systems.

5) Even μ-SMES is very powerful. It can handle large carry-over requirements (750-1400 kVA-seconds)

6) No explosive gases, corrosive or toxic materials, or heavy moving masses.

Commercial μ-SMES units, made by Superconductivity Inc., are called Superconducting Storage Devices (SSD). Several of these units have now been installed and have performed admirably. A matter of concern for SMES is the strong static magnetic field. Usually there is a safety radius of 5 m. Outside this safety zone the field is less than 1 mT and does not pose any significant danger. The other danger is a failure in the cryogenic support system resulting in quenching of the magnet. This is extremely dangerous when the magnet is fully charged. However the possibility of this happening is very remote. Usually the refrigerator has 100% redundancy. If the refrigerator fails the other back-up refrigerator takes over. If that fails too, the magnet has a storage of liquid helium of 50 to 60 hours (usually enough time for repairs or replacement) and additional helium can be added in the cryostat hosting the magnet. If a situation requires emergency shut down, the magnet can be discharged in 3-5 seconds by placing a dump resistor in series with the coil. The SSD installed at an IBM plant in Fishskill, NY has performed admirably[26]. It has operated through more than 30 voltage dips preventing the tester units from tripping. The testers in the plant not supported by SSD did trip during those events.

The interest in large scale SMES system has recently been revived by a cooperative program between Babcock and Wilcox, Anchorage Municipal Light and

Power, and Advanced Research Projects Agency (ARPA) of the U.S. Department of Defense[27]. Bechtel Corp. has performed research on technical, economic, risk-reduction aspects of SMES in collaboration with a group of companies (including General Electric, General Atomics, and Martin-Marietta), and institutions (Houston Advanced Research Center, National High Magnetic Field Lab) for over a decade now[28]. In the near future a commercial demonstration of their 1MWh, 500MW SMES system will be operated on the San Diego Gas & Electric system. The Defense Nuclear Agency has conducted a dual-use SMES program for military and civilian applications, and concluded that the μ-SMES is now ready for commercial exploitation[29].

2.4.3 Need for a lossless opening switch : Motivation for our research

Ideally a SMES should operate in the lossless persistent current mode. After charging the magnet, the charging power supply can be removed and the magnet can be left in the stand-by mode as circulating currents flow without resistance in the superconducting winding. The stored energy is released by opening a switch connected in series with the magnet. Alternators and transformers are then used to deliver the released energy to a load, typically requiring ac power.

In commercial μ-SMES systems, this opening switch is a power semiconductor device. In the closed state, the opening switch carries the entire magnet current and dissipates energy through Joule heating. This is highly undesirable since this resistive switch does not allow true persistent current operation of the magnet. Consequently, the energy lost in the switch needs to be replenished constantly by keeping the magnet power supply connected at all times. This energy loss in the commercial μ-SMES, SSD, can be several kilowatts. A μ-SMES is used for power quality improvement, to provide back-up power to ride over the momentary sags and brown outs. These events, though detrimental to automated manufacturing processes are relatively rare – from once a week to once in a few months. Therefore, the μ-SMES is left off-line most of the time. Just to have the capability of supplying the extra energy at the occurrence of sags, several kilojoules of energy is wasted every second by the lossy series opening switch.

This energy loss can be prevented by using a superconducting opening switch. A superconducting switch, being lossless, allows the magnet to operate in the persistent current mode indefinitely before it is required to release the stored energy. The cryogenic system required for the superconducting magnet can also support the superconducting switch. Unlike other applications (e.g. a fault current limiter), in this case, the cryogenic requirement of the superconducting switch does not impose an additional operational expense. This provides a strong motivation towards development of a high current superconducting opening switch.

In the past, there have been some studies of a superconducting switch using both bulk and thin film low-temperature superconductors (LTS). The bulk LTS material, stabilized in a normal metal matrix, has small normal state resistance and is not suitable as an opening switch. Very long lengths are usually needed and the thermal recovery time is poor due to small surface to volume ratio. A group at Argonne National Laboratory studied 1 μm thick Nb thin film switches[30]. They used a pulsed magnetic field to trigger a transition of the switch to its normal state. As we have already mentioned in section 2.3.1, the main requirements of a superconducting opening switch are high critical current density and normal state resistivity. Although these Nb films had high critical currents (2.8 MA/cm^2), the normal state resistivity was low (12 μΩ-cm). The opening time for these switches was 3 μs. NbN has a higher normal state resistivity, and has been used for thin film switches[31]. Optical triggering was usually employed in these designs. The switching currents were typically 1–5 A and switching times were 10-100 ns.

While these results were promising, they did not lead to any commercial switch design. With the discovery of ceramic HTS materials, exhibiting high normal state resistivity, the interest in high power switching devices has been renewed[32, 33]. However, material problems and strong competition with highly developed power semiconductors, prevented active research in this area. The recent emergence of SMES technology and improvement of material parameters (especially critical current density) has created a new opportunity for HTS opening switches. Thin films of YBCO have current densities as high as 10–50 MA/cm^2 at 4.2 K and 1–5 MA/cm^2 at 77K. For a 1 cm wide 1 μm thick switch, this translates to switching currents in the 100 A to 5 kA range. These materials also absorb light efficiently and can be suitably triggered with a laser pulse. We, therefore, chose to explore an optically triggered thin film

superconducting opening switch. Our contactless design (chapter 5) of the inductively coupled switch is particularly attractive from the point of view of SMES technology. Here the stored energy is coupled out to a magnetically-coupled load by removing a superconducting flux screen that acts as the switch. Unlike most other cases, in this design the switch does not interrupt the source current and is particularly suited for energy extraction from a SMES magnet.

In the past five years, the critical current density of bulk HTS materials has increased by three orders of magnitude. Despite the very high current densities, thin films can not carry very large currents. For very high current switches, bulk HTS materials or thick films will be used in future.

CHAPTER 3

PHYSICAL PROPERTIES OF SUPERCONDUCTORS

3.1 Introduction

Superconductors are among the most interesting materials of the twentieth century. The enormous potential of superconductors in engineering, combined with their exotic physical properties, has stimulated the interest of scientists all over the world, throughout the century. In order to appreciate any superconducting device, such as our switch, it is therefore necessary to describe the physical properties of superconductors. Superconductors exhibit "perfect" conduction of electrical current (i.e., zero resistance) below a certain temperature (called the critical temperature, T_c), provided that the current density is smaller than a critical value, J_c .The absence of dc electrical resistance makes superconductors very attractive for application where high current carrying capacity is required. Commercial magnet wires (Nb-Ti or Nb_3Sn) can carry current densities of 10^{10} A/m^2 and higher. However, there are many other properties of superconductors that are unique and lead to novel applications. In section 3.2 we describe the different classes of superconducting materials with relevant examples.

The electrical and magnetic properties are intimately related and are discussed together in section 3.3. As shown in Fig. 3.1.1, the superconducting state exists in a parameter space bounded by three critical parameters : critical temperature (T_c), critical current density (J_c), and critical magnetic field (H_c). The superconducting state can be destroyed by exceeding any one of these critical values, each dependent on the other two parameters. Superconductors can be classified into two categories, type I and type II, according to their magnetic properties. Only type II superconductors can operate in (and produce) large magnetic fields. The material used in our switches, $YBa_2Cu_3O_{7-x}$ or YBCO, is a type II material. We have discussed the relevant thermal and optical properties of superconductors in sections 3.4 and 3.5. The useful material properties of YBCO are summarized in section 3.6.

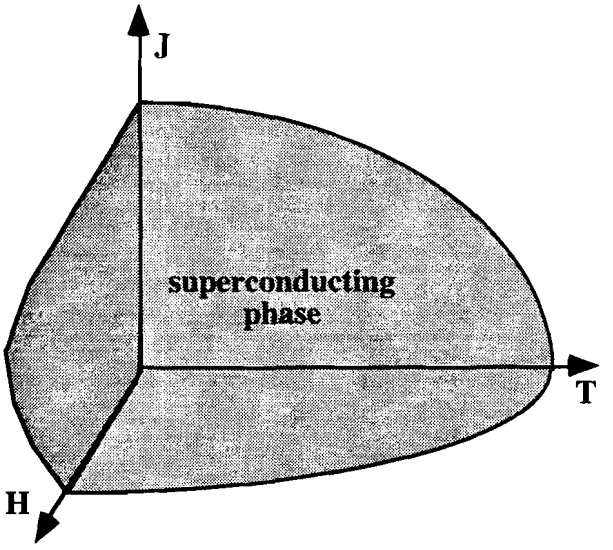

Figure 3.1.1 The J-H-T phase diagram showing the superconducting state.

It is beyond the scope of this work to discuss most of the physical properties of superconductors, for example Josephson tunneling, vortex dynamics in type II superconductors, microwave properties and thermodynamics. We shall only discuss the properties that are relevant to our superconducting switching device.

3.2 Different Classes of Superconducting Materials.

There are over 6000 known superconducting elements, compounds and alloys classified into several groups according to their properties. We shall give a brief description of each group, focusing on practical superconducting materials.

3.2.1 Metals

Superconductivity was first discovered by Kammerlingh-Onnes in thin capillary tubes of Hg. Although the majority of superconductors are not pure elements but alloys and compounds, metals were the first to be identified as superconductors. They are also the most extensively studied and the best understood materials. Table 3.2.1 shows the values of T_c and H_c of some metallic superconductors[34]. Nb has the highest T_c at 9.3K. The mechanism of superconductivity is the pairing of electrons with opposite spin and momentum through electron phonon interaction. The BCS theory is best applicable to this class of materials.

Table 3.2.1 Critical temperature and magnetic field of some metallic superconductors.

Element	T_c (K)	H_c (G)
Al	1.196	99
α-Hg	4.15	411
Nb	9.26	1980
Pb	7.19	803
Sn	3.72	305

3.2.1 Alloys

For the fabrication of high-field superconducting magnets, metals with low critical magnetic fields were found unsuitable. The discovery of type II metallic alloys, with high upper critical field (H_{c2}), was crucial to the manufacturing of superconducting magnets. Nb-Zr alloy was first used to make magnets and was subsequently replaced by Nb-Ti. Nb-Ti is a ductile alloy with T_C = 9.5 K and $BB_{c2} = \mu_0 H_{c2}$= 13.6 T. This is the material for most superconducting magnets, including the one used in our experiment. The preferred composition is 46.5-50% Ti and 53.5-50% Nb.

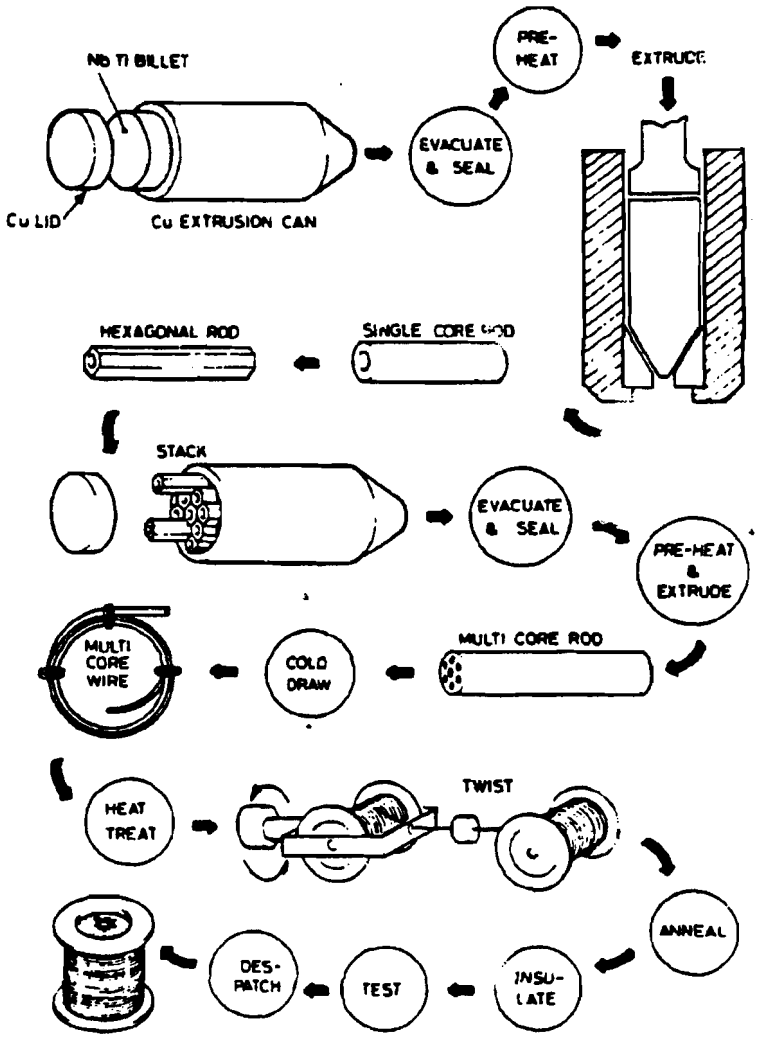

Figure 3.2.1 Manufacturing process of filamentary Nb-Ti copper composite wire [35].

Fig. 3.2.1 shows the major process steps for the wire manufacture, starting from a NbTi billet inside a copper extrusion can. The extruded bar is cut into hexagonal rods and extruded into multifilamentary wire. The reason for producing a multifilamentary wire is to maximize the surface-to-volume-ratio of the superconductor which carries the current in a surface layer. The copper matrix provides mechanical stability and shunts the higher normal resistance NbTi in the event of a quench (a catastrophic breakdown of superconductivity caused by exceeding J_c or rise in temperature due to a cryogenic fault). The copper matrix also allows rapid conduction of heat away from the superconductor when the quench occurs.

3.2.3 A15 materials

Until the discovery of High-T_c cuprates, most of the higher T_c materials belonged to this group which is named after their crystal structures. This class of materials have the stoichiometry A_3B, where A is a transition metal (Nb, V, Ta, etc.) and B is a metal or semiconductor (usually from IIIA or IVA columns of the periodic table), such as Ga, Ge, Sn or Si. Nb_3Ge has the highest T_c of 23K. These compounds exhibit high upper critical fields (36T for Nb_3Ge, 22T for Nb_3Sn) and are ideal for producing high field superconducting magnets. Although brittleness makes it difficult to produce wires, the problem is solved by drawing a multifilamentary wire of A15 compound (V_3Ga or Nb_3Sn) embedded in a bronze stabilizing matrix. It is important to mention here that T_c of A15 compounds is very sensitive to change in the stoichiometry, and the 3:1 ratio is found to yield the compound with maximum T_c.

Filamentary Nb_3Sn manufactured by the bronze process[35]. Nb rods are inserted in a bronze cylinder with drilled holes. The bronze cylinder is then extruded and drawn or drawn directly. The wire is then heat treated at 700°C for 1-10 days. During this heat treatment tin from bronze reacts with Nb to form Nb_3Sn.

3.2.5 B1 compounds

These compounds have the B1 crystal structure (like NaCl) which is face-centered cubic with alternating A and B in all directions. Compounds like $NbN_{0.92}$ (T_c =16K) and $NbC_{0.1}N_{0.9}$ (T_c =18K) have high transition temperatures and are far more resistant to radiation damage and disorder than A15 compounds. These are also brittle but are extensively used in thin film form for superconducting electronics.

3.2.4 Cuprates

The discovery of superconductivity in La-Ba-Cu-O system[36] by Bednorz and Muller (1986) resulted in an unprecedented intensity of research throughout the world, in search of high temperature superconductors. Transition temperatures higher than the liquid nitrogen temperature (77K) in Y-Ba-Cu-O system made superconductors a household name. The key component was identified to be $YBa_2Cu_3O_{7-\delta}$, known as YBCO or 1-2-3.

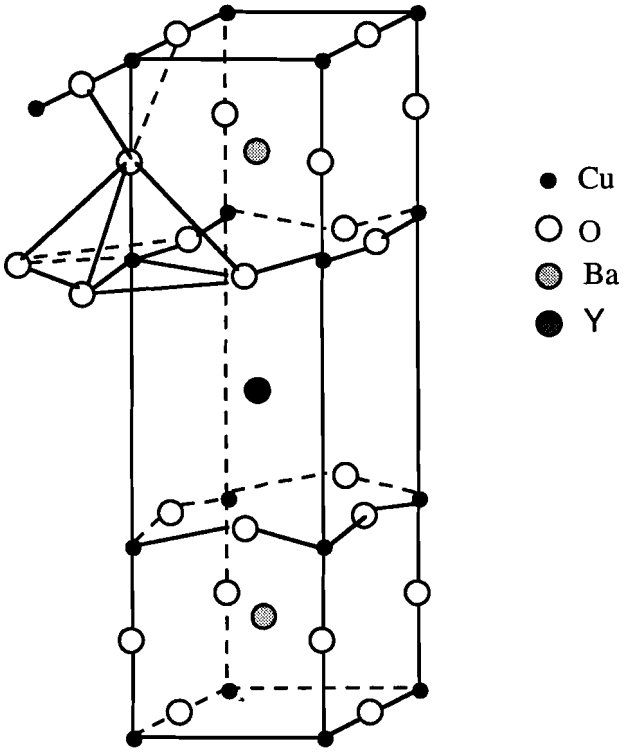

Figure 3.2.2 Crystal structure of $YBa_2Cu_3O_7$. a = 3.8198 Å, b = 3.8849 Å and c = 11.6762 Å.[37]

This breakthrough is particularly important since liquid nitrogen is comparatively much cheaper than liquid helium as a cryogen, and large scale industrial applications with high-T_C superconductors cooled by liquid nitrogen appear feasible. Subsequently, superconductors in the systems Bi-Sr-Ca-Cu-O with T_C up to 110K, Tl-Ba-Ca-Cu-O with T_C up to 125K, and Hg-Ba-Ca-Cu-O with T_C up to 130K were discovered.

The crystal structures of copper oxides are anisotropic, exhibiting two-dimensional features (Cu-O planes). In addition, the 1-2-3 material (Y-Ba-Cu-O) has a well defined one dimensional feature, namely, the chains. The anisotropy of the crystal structure manifests itself in the high conductivity along the Cu-O planes. The metallic behavior of Cu-O planes is attributed to removal of electrons or formation of holes in Y-Ba-Cu-O (1-2-3) or La-Sr-Cu-O (2-1-4) systems. Formation of chains in 1-2-3 compounds is responsible for the removal of electrons and the conductivity depends on the concentration of O in the planes. The crystal structure of $YBa_2Cu_3O_7$ is shown in Fig. 3.2.2.

3.3 Electrical and Magnetic Properties

3.3.1 Electrical resistivity

The electrical resistivity in superconductors vanishes for temperatures below a critical value, called the critical temperature (T_c). If we measure the resistivity of a superconductor as it is cooled down from room temperature, we observe that the resistivity drops abruptly to zero at the critical temperature. This transition of the material from a normal or resistive state to the superconducting state is attributed to pairing of electrons through an attractive interaction of electrons. For most conventional superconductors, this attractive electron-electron interaction is explained by the Bardeen-Cooper-Schriefer (BCS) theory[38]. Below T_c , electrons of opposite momentum and spin form pairs, called Cooper pairs. The attractive interaction results from the distortion of the ionic lattice by the motion of an electron and is mediated by lattice vibrations or phonons. For high temperature ceramic superconductors there is evidence of pair formation, although whether they are mediated by phonons or by other means (such as excitons) is a matter of controversy.

An example of the superconducting transition is shown in Fig. 3.3.1.1. The resistance of a 20-μm wide microbridge of 400 nm thick YBCO film on $LaAlO_3$ is plotted as a function of temperature. The zero-resistance transition temperature (T_{c0}) is 91.5 K and the width of the transition is 0.5 K. This is one of the samples used for the inductively-coupled switch (chapter 6).

In the superconducting state the material can carry a dc current without loss. However if the current exceeds a certain critical value, called the critical current (I_c), the material becomes resistive again. More accurately, it is the critical current density (J_c) that determines whether the material will make a transition to the normal state. If the current distribution is non-uniform, as is often the case, the transition occurs in the region where J_c is exceeded.

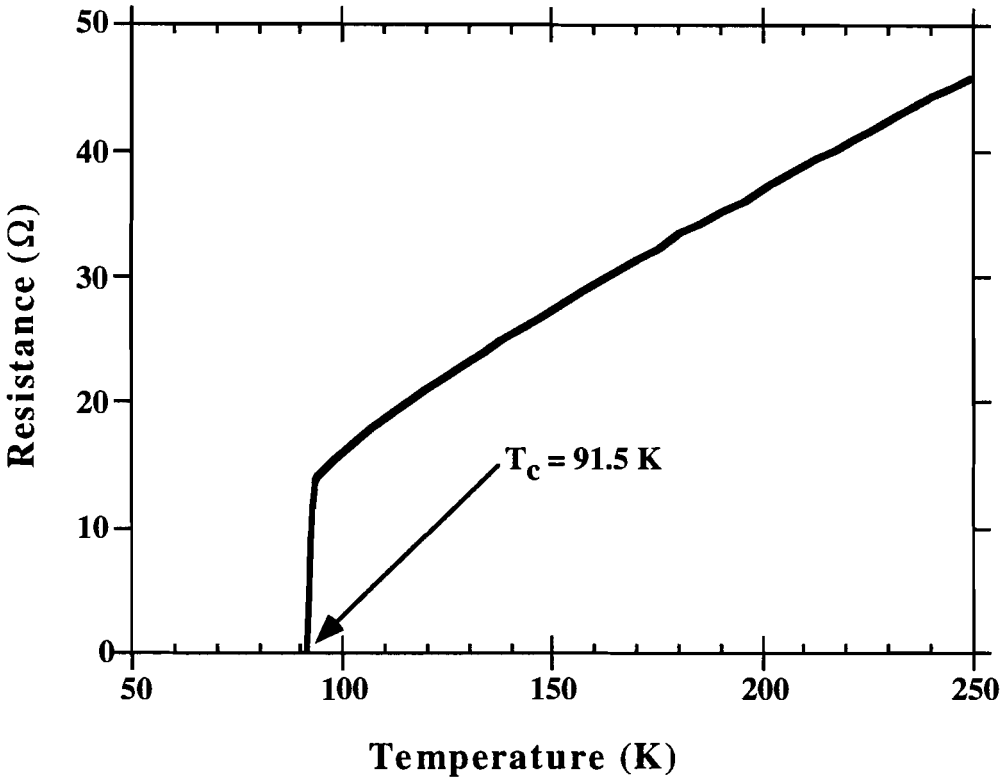

Figure 3.3.1.1 Resistance of a thin YBCO film drops to zero at a transition temperature of 91.5 K.

3.3.2 The two-fluid model

As the superconductor is cooled below its transition temperature, an increasing fraction of the electrons form Cooper pairs in such a way as to lower the total energy of the system. At T = 0, the pairs form the lowest energy state, called the ground state. There is an energy gap[1] (Δ) between this ground state and the lowest available excited state. Electrons may be excited from the ground state by increasing the temperature (phonons) or by electromagnetic radiation (photons), providing an energy greater than Δ for each electron. Since the electrons are paired two excitations must be created to break a pair, requiring a minimum energy of 2Δ. This is the binding energy of a Cooper-pair. Thus a superconductor at $T << T_c$ does not absorb a photon of energy less than 2Δ. The energy gap is a monotonically decreasing function of temperature and

[1] also called the gap parameter or the order parameter

reduces to zero at T_C. The value of the gap at T = 0 is $\Delta(0) = 1.76 k_B T_c$, according to the BCS theory. For high-T_C cuprate materials the exact nature of the gap is not well understood, although the existence of a gap of the order of $k_B T_c$ has been confirmed.

Two electrons of opposite spins ($\uparrow$ and $\downarrow$) and momenta ($\vec{k}$ and $-\vec{k}$) constitute a pair. Therefore, an excitation must create an electron ($\vec{k}\uparrow$) and annihilate its pair ($-\vec{k}\downarrow$). Since the occupation probability of an electron much below and much above the Fermi surface are 1 and 0 respectively, creation of an excitation much below the Fermi surface resembles a hole and the one much above resembles an electron. Around the Fermi surface the occupation probability is between 0 and 1. The excitations in that range are either electron-like or hole-like depending on whether they are above or below the Fermi surface[39]. These excitations are called *quasiparticles* (quasiholes and quasielectrons).

Electrical conduction of superconductors can be understood by a simple model, called the *two-fluid model*, that assumes existence of two parallel conduction channels, consisting of Cooper pairs and quasiparticles, at a temperature $0 < T < T_c$.[39] The Cooper pairs conduct current without resistance and the resistance of the normal channel is shunted by the zero-resistance superconducting channel. The supercurrent density (J_s) depends on the number density of electron pairs (n_s),

$$J_s = -n_s e^* v_s, \tag{3.3.2-1}$$

where $e^* = 2e$, and v_s is the velocity of the superconducting pairs. The normal fluid carries a current density, J_n, given by

$$J_n = -n_n e v_n, \tag{3.3.2-2}$$

where n_n and v_n are number density and velocity of the normal fluid. The admittance of the material to ac fields has both a real and an imaginary part. The real part, corresponding to losses, is due to the normal fluid, while the imaginary part is due to the inertia of the superconducting fluid[2] [Fig. 3.3.2.1]. The equivalent circuit element for the normal fluid is a resistance with resistivity $\rho = \rho_n n / n_n$, where $n = n_s + n_n$. The

[2]There is a small component due to the inertia of the normal fluid that is usually neglected.

superconducting fluid corresponds to an inductive circuit element, called the *kinetic inductance* (section 3.3.3). This inductive component shorts out any dc current. The two-fluid model is valid only for sub-gap ac fields (well below THz frequencies).

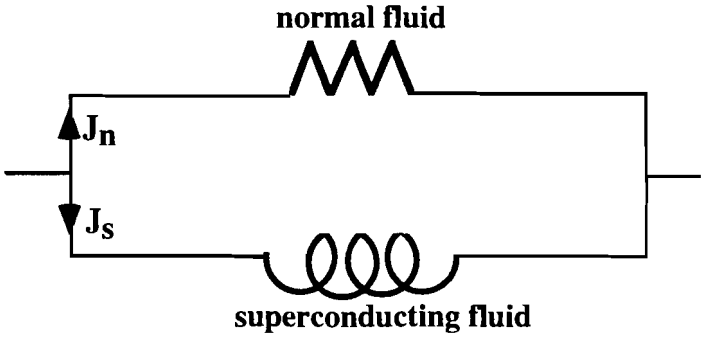

Figure 3.3.2.1 The two-fluid model.

3.3.3 Meissner Effect, London's Equations and Penetration Depth

In addition to the 'perfect' conducting property, superconductors exhibit the Meissner effect[39]. This effect, resulting in flux expulsion from the bulk of a superconducting material, can be summarized as follows. If a superconductor is placed in an external magnetic field (B_{ext}), lossless screening currents are set up in a thin surface layer of the material. The screening currents completely compensate the external field. In other words, the magnetization (M) produced by the screening currents is equal and opposite to the field H, inside the bulk of the superconductor. We know that, $B = \mu_0(H + M)$ and $M = \chi H$. Therefore, for a superconductor, χ = -1 and B = 0 and it is a perfect diamagnet.

To describe the electrodynamics of the superconducting state, F. and H. London formulated two equations which are known as the first and second London's equations[39]. Although these were formulated much before the BCS theory was proposed, they can be derived from the microscopic BCS theory. The two equations relating supercurrent, J_S, with the electric and magnetic fields are as follows[3]:

$$\partial \mathbf{J}_s / \partial t = \mathbf{E} / \mu_0 \lambda^2 , \qquad (3.3.3\text{-}1)$$

[3]More generally Eq. 3.3.3-10

$$\nabla \times \mathbf{J_s} + \mathbf{B}/\mu_0 \lambda^2 = 0. \qquad (3.3.3\text{-}2)$$

The parameter λ is known as the London *penetration depth* and is given by,

$$\lambda = \sqrt{m^*/\mu_0 n_s e^{*2}}, \qquad (3.3.3\text{-}3)$$

where m^*, n_S^* and e^* are the effective mass, density and charge of Cooper pairs. From Maxwell's equation,

$$\nabla \times \mathbf{H} = \mathbf{J_s}. \qquad (3.3.3\text{-}4)$$

Combining equations 3.3.3-2 and 3.3.3-4 we get,

$$\nabla^2 \mathbf{B} + \mathbf{B}/\lambda^2 = 0, \qquad (3.3.3\text{-}5)$$

and

$$\nabla^2 \mathbf{J_s} + \mathbf{J_s}/\lambda^2 = 0. \qquad (3.3.3\text{-}6)$$

Equations 3.3.3-5 and 3.3.3-6 explain the Meissner effect. Let us consider an interface between vacuum and semi-infinite superconductor as shown in Fig. 3.3.2.1 where a z-directed magnetic field (B_0) is applied. This gives rise to a current J_{sy} in the superconductor in the y-direction. From equations 3.3.3-5 and 3.3.3-6 we get,

$$\frac{\partial^2 B_z}{\partial x^2} = \frac{B_z}{\lambda^2} \Rightarrow B_z = B_0 e^{-x/\lambda} \qquad (3.3.3\text{-}7)$$

and

$$\frac{\partial^2 J_{sy}}{\partial x^2} = \frac{J_{sy}}{\lambda^2} \Rightarrow J_{sy} = \frac{B_0}{\lambda \mu_0} e^{-x/\lambda}. \qquad (3.3.3\text{-}8)$$

Both the magnetic field and the screening current density decay exponentially with a characteristic length λ. The penetration depth (λ) is an important parameter in superconductors and the values for some materials are listed in Table 3.3.3.1. For anisotropic high temperature superconductors (e.g. YBCO) the effective mass along c-axis (m_c^*) is much larger than the effective mass in the ab plane (m_{ab}^*). Therefore, from equation 3.3.3-3, the penetration depth along c-axis (λ_c) is smaller than that in the ab plane (λ_{ab}).

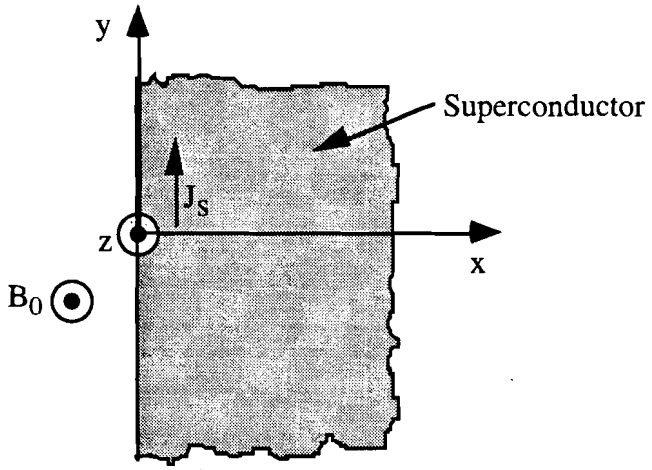

Figure 3.3.3.1 Screening currents (J_S) are set up inside the superconducting half-space to screen the applied field B_0.

Table 3.3.3.1 Penetration depth of superconductors

Material	Penetration Depth (nm)
Nb	40
NbN	250
Nb-Ti	60
Nb_3Sn	80
$YBa_2Cu_3O_7$	150 (along c-axis) 600 (in ab plane)
$Bi_2Sr_2Ca_2Cu_3O_{10}$	200 (along c-axis) 1000 (in ab plane)

Kinetic Inductance

Kinetic inductance is the inductance associated with the kinetic energy of the superconducting fluid[4]. Let us consider a superconducting bridge of length ℓ, width w, and thickness d carrying a constant current I. If the supercurrent density (J_S) is assumed to be uniform,

[4]This is in addition to the usual magnetic inductance.

$$J_s = I/wd \tag{3.3.3-9}$$

Assuming J_S to be constant, differentiating equation 3.3.2-1 we get,

$$\frac{dJ_s}{dt} = 0$$

$$\Rightarrow n_s \frac{dv_s}{dt} + v_s \frac{dn_s}{dt} = 0$$

$$\Rightarrow \frac{dv_s}{dt} = -\frac{J_s}{n_s^2 e^*} \frac{dn_s}{dt} \tag{3.3.3-10}$$

Now from London's equation[39],

$$dv_s/dt = (e^*/m^*)E. \tag{3.3.3-11}$$

Combining equations 3.3.3-9, 3.3.3-10 and 3.3.3-11 and substituting V=E.ℓ we obtain,

$$V = I\frac{\ell}{wd}\frac{m^*}{e^{*2}}\left(-\frac{1}{n_s^2}\frac{dn_s}{dt}\right) = I\frac{dL_{kin}}{dt}. \tag{3.3.3-12}$$

Therefore kinetic inductance (L_{kin}) is defined by,

$$L_{kin} = (\ell/wd)\left(m^*/n_s e^{*2}\right) = \mu_0 \lambda^2 (\ell/wd). \tag{3.3.3-13}$$

The kinetic energy of the superconducting fluid can be written in terms of the kinetic inductance as

$$E_{kin} = \left(\frac{1}{2} m^* v_s^2 n_s\right)\ell wd = \frac{1}{2} L_{kin} I^2. \tag{3.3.3-14}$$

3.3.4 Critical Magnetic Field for Type I Superconductors

We have mentioned the critical magnetic field (H_c) before. This is the magnetic field at which the superconductor makes a transition to the normal state (χ=0). Fig. 3.3.4.1 shows the magnetization as a function of externally applied magnetic field ($H_{ext} = B_{ext}/\mu_0$) for a type I superconductor. Fig. 3.3.4.2 shows the temperature

dependence of H_c. For type I superconductors, H_c is the same as the thermodynamic critical field ($H_{c,th}$) which is defined in terms of difference in free energies as follows,

$$G_n(0,T) - G_S(0,T) = -V_S \int_0^{H_{c,th}} \mathbf{M}.d\mathbf{H} = \frac{1}{2}\mu_0 H_{c,th}^2(T) V_s \qquad (3.3.4\text{-}1)$$

We can see that for zero applied field below T_C , G_n > G_S, implying that the material will be in the superconducting state, which is the lower free energy state. If we apply a field $\mathbf{H}_{ext} = \mathbf{H}$, for a superconducting slab of width $a >> \lambda$, B = 0, inside the superconductor and therefore $dG_S = 0$. For the same slab in the normal state $\mathbf{B} = \mu_0\mathbf{H}$ and $dG_n = -V\mu_0\mathbf{M}.\mathbf{dH}$.

$$d\left[G_n(\mathbf{H},T) - G_s(\mathbf{H},T)\right] = -V\mu_0\mathbf{H} \bullet d\mathbf{H} \qquad (3.3.4\text{-}2)$$

Integrating from 0 to some field H_{ext},

$$G_n(\mathbf{H},T) - G_S(\mathbf{H},T) = \frac{1}{2}\mu_0 V\left[H_{c,th}^2 - H_{ext}^2\right] \qquad (3.3.4\text{-}3)$$

For $H_{ext} < H_{c,th}$ ($G_n > G_s$), the material is in Meissner state (B=0) and for $H_{ext} > H_{c,th}$, the material is in normal state.

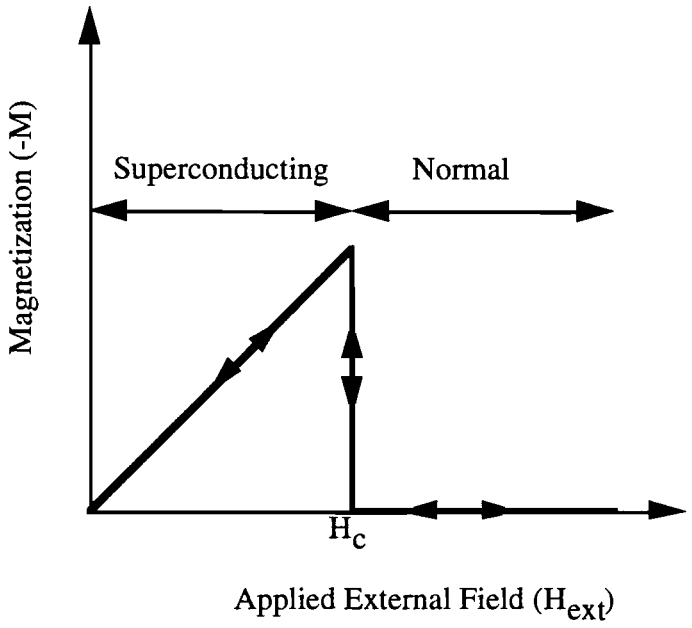

Figure 3.3.4.1 Magnetization of Type I superconductor showing superconducting and normal phases below and above the critical field (H_C) respectively.

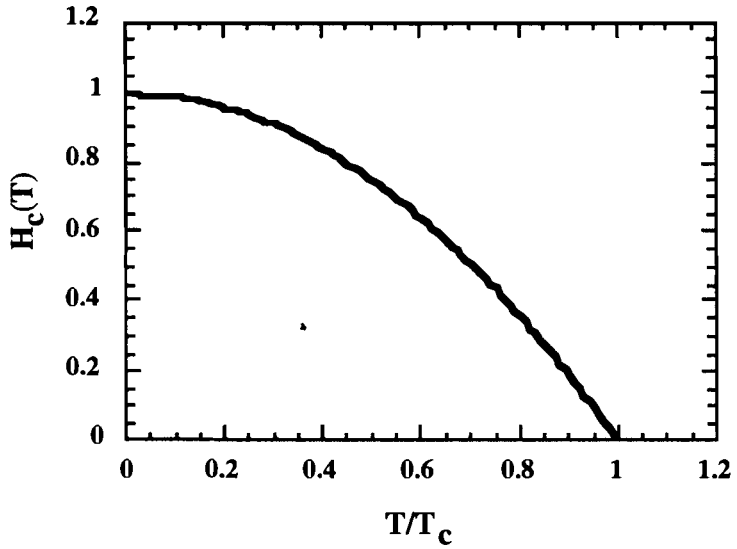

Figure 3.3.4.2 Critical field (H_C) as a function of temperature(T). The temperature dependence is approximately given by $H_c(T) = H_c(0)\left[1-\left(T/T_c\right)^2\right]$.[39]

3.3.5 Demagnetization Factor

So far, in our discussion we have ignored the effect of the shape of the superconductor. Geometrical shape results in the distortion of the internal magnetic field H of a material and is described by a demagnetization factor (D). For a very long cylindrical rod $D \approx 0$. If we take an ellipsoidal material with its major axis parallel to the external field then the magnetization changes the effective field (B_{eff}) the material experiences.

$$B_{eff} = B_{ext} - D\mu_0 M . \tag{3.3.5-1}$$

M for a superconductor in the Meissner state is determined by the screening surface currents and is therefore given by,

$$M = -B_{eff}/\mu_0 . \tag{3.3.5-2}$$

Combining equation (3.3.5-1) and equation (3.3.5-2) we get,

$$B_{eff} = \frac{B_{ext}}{1-D}. \tag{3.3.5-3}$$

For example, D=1/3 for a sphere and so for a spherical sample

$$B_{eff} = \frac{3}{2} B_{ext}. \tag{3.3.5-4}$$

Fig. 3.3.5.1 shows a sample with the shape of an ellipsoid of revolution. If a magnetic field is applied along the axis of revolution the demagnetization factor can be approximated by,

$$D = 1 - \pi a/2b \ . \tag{3.3.5-5}$$

For a thin plate with the field applied perpendicular to the plate can be approximated by an ellipsoid with $a<<b$. In this case D approaches unity as a/b approaches zero. From equation 3.3.5-3,

$$\lim_{a/b \to 0} B_{eff}/B_{ext} = 2b/\pi a = O(b/a) \tag{3.3.5-6}$$

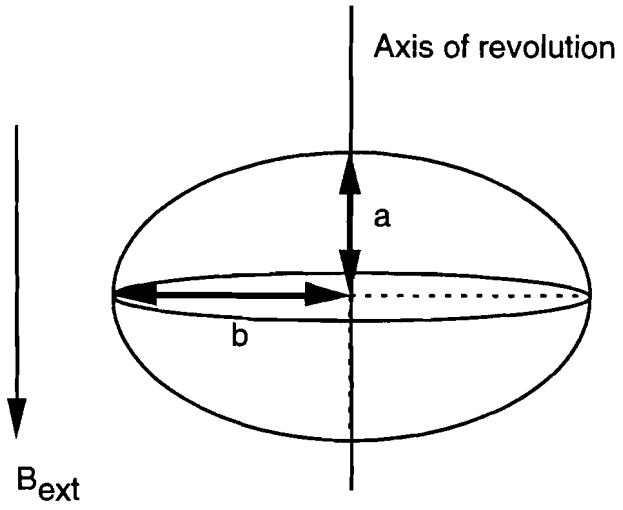

Figure 3.3.5.1 An ellipsoid of revolution with a magnetic field applied along the axis of revolution.

In our experiments we have used 1 cm^2 thin films of thickness 600-800 nm, a/b $< 10^{-4}$. If flux is completely excluded, the field just outside the superconductor will be extremely high due to this effect. As will be explained in section 3.3.9, the depression of critical current density in high local magnetic field will allow flux entry from the edges. Consequently, complete flux exclusion does not take place in this situation. As the flux is allowed to enter at the edge, the demagnetization factor also decreases.

3.3.6 Critical Magnetic Fields for Type II Superconductors

Virtually all practical superconductors, including the high-T_C compounds, are type II superconductors. Only the simple elemental ones (Pb, Hg, Sn, In, Al) are type I. Therefore, we will focus our attention on the magnetic properties of the type II supercnductors. In type II superconductors, there is a lower critical field (H_{c1}) and an upper critical field (H_{c2}). For $H_{ext} < H_{c1}$ the material is in the Meissner state. For $H_{c1} < H_{ext} < H_{c2}$ flux enters the material in the form of vortices or flux quanta and the material is in a "mixed" or vortex state. For $H_{ext} > H_{c2}$ the material becomes normal. To find H_{c1} and H_{c2} we can do a thermodynamic analysis similar to the one for type I materials. Before we do that it may be appropriate to look at the entering of magnetic flux above H_{c1}, from an intuitive point of view.

The difference between a normal and superconducting region of the same material lies in the fact that the pair density n_c is zero in the normal region but is finite (being a function of T) in the superconducting region. The condensation of electron pairs is responsible for the reduction of free enthalpy making the superconducting state thermodynamically favorable. The pair density n_c does not change to zero abruptly at a phase boundary but varies over a characteristic length, called the coherence length (ξ).

We have two energy contributions at interface between superconducting and normal regions[40]. The first one, E_M is associated with exclusion of magnetic field and the second one, E_C is the pair condensation energy. In the normal region, $E_M = 0 = E_C$. In a superconducting region of volume V, $E_C = \frac{1}{2}\mu_0 H_{c,th}^2 V$. At the interface the field penetrates to a depth λ and E_M is smaller by an amount,

$$\Delta E_M = \frac{1}{2}\mu_0 A\lambda H^2 \text{ for } H < H_{c,th}, \text{ where, } A \text{ is the interface area.}$$

The condensation energy E_C is also reduced since the pair density varies over a length ξ by the amount $\Delta E_C = \frac{1}{2}A\xi\mu_0 H_{c,th}^2$.

$$\Delta E = \Delta E_C - \Delta E_M = (\xi H_{c,th}^2 - \lambda H^2)\frac{1}{2}\mu_0 A \qquad (3.3.6\text{-}1)$$

We see that the loss of condensation energy is over-compensated by the gain in exclusion energy, if $\Delta E < 0$, so that the formation of interface can be accompanied by a gain in energy. For $\Delta E < 0$,

$$\xi H_{c,th}^2 < \lambda H^2$$

or,
$$\frac{H_{c,th}^2}{H^2} < \frac{\lambda}{\xi} \qquad (3.3.6\text{-}2)$$

So if $\lambda > \xi$, even for $H < H_{c,th}$, there will be magnetic field penetration into the superconductor. Intuitively, it is easy to see that for this type of material allowing field to penetrate we have reduced the exclusion energy E_M so that the material can still remain superconducting. Therefore, higher external fields will be required to break down the superconductivity.

This intuitive picture is justified in detail by the Ginzburg-Landau theory[41]. The ratio $\kappa = \lambda/\xi$ is called the Ginzburg-Landau Kappa. At a field $H = H_{c1}$, it becomes energetically favorable for the magnetic field to penetrate the superconductor. The field penetration occurs in quantized amounts[5], called vortices. A vortex has a normal *core*[6] of radius ξ, surrounded by superconducting region, where the screening current and magnetic field still vary on the scale of λ as given by Eqs. 3.3.3-5 and 3.3.3-6. The thermodynamic critical field H_c can be expressed from G-L theory as,

$$H_c = \frac{\phi_0}{2\sqrt{2}\pi\mu_0\lambda\xi}. \qquad (3.3.6\text{-}3)$$

H_{c1} can be expressed in terms of the thermodynamic critical field and the ratio of coherence length and penetration depth as [41]

$$H_{c1} = H_{c,th}\left\{\frac{1}{4\sqrt{2}}\frac{\xi}{\lambda} + \frac{1}{\sqrt{2}}\frac{K_0(\xi/\lambda)}{\frac{1}{2}\frac{\xi^2}{\lambda^2}K_0(\xi/\lambda) + \frac{\xi}{\lambda}K_1(\xi/\lambda)}\right\} \qquad (3.3.6\text{-}4)$$

and K_0 and K_1 are modified Bessel functions of second kind of order 0 and 1 respectively.

Figure 3.3.6.1 shows H_{c1}/H_c as a function of κ and for $\kappa > 0.2$ $H_{c_1} < H_c$. For small κ ($\lambda << \xi$) $H_c < H_{c_1}$ and the material becomes normal before vortices can enter and the material is type I. In contrast fpr large κ ($\lambda >> \xi$) $H_{c_1} < H_c$ and the material is type II. Ginzburg-Landau Theory gives the critical value of κ as $1/\sqrt{2}$. So if $\kappa < 1/\sqrt{2}$ the material is type I and $\kappa > 1/\sqrt{2}$ the material is type II.

If applied field increases, at some point the vortex cores start to overlap and the material ceases to be superconducting. This field is the upper critical field ($H_{c\,2}$). Ginzburg Landau theory gives the value for $H_{c\,2}$ as[41]

---

[5]A flux quantum is a fundamental quantity defined as $\phi_0 = h/2e = 2.07 \times 10^{-15}$ Wb, where h is the Planck's constant and e is the electronic charge.

[6]A region of depressed order parameter.

$$H_{c2} = \frac{\phi_0}{2\pi\mu_0\xi^2} \tag{3.3.6-5}$$

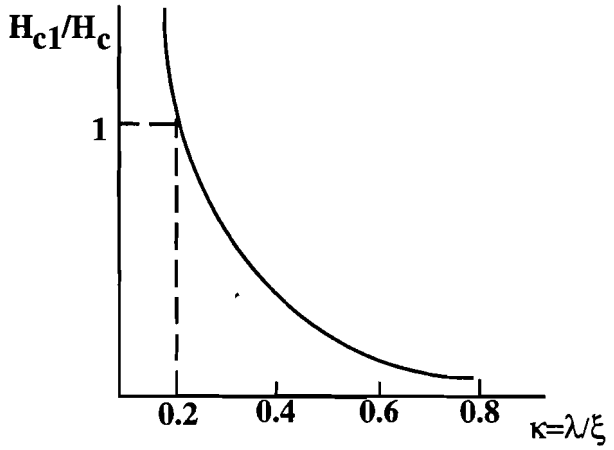

Figure 3.3.6.1 The ratio of lower critical field and the thermodynamic critical field as function of the Ginzburg-Landau κ.

It is interesting to note that in the limit when $\lambda >> \xi$ (which applies for YBCO)

$$\lim_{\lambda>>\xi} H_{c1} = \frac{\phi_0}{4\pi\mu_0\lambda^2}\ln(\lambda/\xi) \tag{3.3.6-6}$$

$$H_{c_1}H_{c_2} = H_c^2\ln(\kappa) \tag{3.3.6-7}$$

Fig. 3.3.6.2 shows the magnetization of a type II superconducting material.

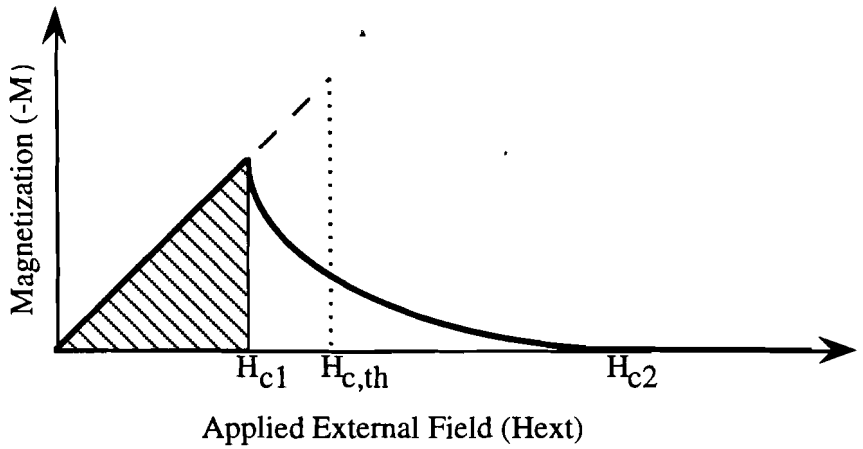

Figure 3.3.6.2 Magnetization of type II superconductor showing upper and lower critical fields along with the thermodynamic critical field.

So far in our discussions we have assumed the material to be isotropic. However, high temperature superconductors like YBCO are highly anisotropic due to their planar crystalline structure (section 3.2.4). In section 3.3.2 we have seen how this anisotropy affects the penetration depth ($\lambda_c < \lambda_{ab}$). The coherence length ξ is anisotropic too ($\xi_c > \xi_{ab}$). In other words,

$$\frac{\xi_c}{\xi_{ab}} = \frac{\lambda_{ab}}{\lambda_c}. \tag{3.3.6-8}$$

Therefore, the critical magnetic fields, H_{c1} and H_{c2} will depend on whether the applied field is parallel to the c-axis or perpendicular to it. From equation 3.3.6-6,

$$H_{c1}^{\parallel c} = \frac{\phi_o}{4\pi\mu_o\lambda_{ab}^{\,2}} \ln\left(\frac{\lambda_{ab}}{\xi_{ab}}\right)$$

and

$$H_{c1}^{\perp c} = \frac{\phi_o}{4\pi\mu_o\lambda_{ab}\lambda_c} \ln\sqrt{\frac{\lambda_{ab}\lambda_c}{\xi_{ab}\xi_c}} \tag{3.3.6-9}$$

Since $\lambda_c < \lambda_{ab}$, the lower critical field along the c-axis is higher than that along the ab plane (i.e., perpendicular to the c-axis), $H_{c1}^{\parallel c} > H_{c1}^{\perp c}$, the logarithmic factor being slowly varying compared to $1/\lambda^2$. The values for single crystal YBCO extrapolated to zero temperature are $B_{c1}^{\parallel c}$ = 0.05 T and $B_{c1}^{\perp c}$ = 0.02 T[42]. Other authors have reported values of $B_{c1}^{\parallel c}$ = 0.069 T and $B_{c1}^{\perp c}$ = 0.012 T at 11 K[43]. From equation 3.3.6-5,

$$H_{c2}^{\parallel c} = \frac{\phi_o}{2\pi\mu_o\xi_{ab}^2}$$

and

$$H_{c2}^{\perp c} = \frac{\phi_o}{2\pi\mu_o\xi_{ab}\xi_c} \tag{3.3.6-10}$$

Since $\xi_c < \xi_{ab}$, the upper critical field along the ab-plane (i.e. perpendicular to c-axis) is higher than that along c-axis. The values of coherence lengths are ξ_c = 0.4 nm and ξ_{ab} = 3 nm. From equation 3.3.6-10, $B_{c2}^{\parallel c}$ = 36 T and $B_{c2}^{\perp c}$ = 265 T. Measurement of lower critical field from magnetization is difficult due to irreversibility in magnetization produced by flux pinning. In practice the upper critical field can be measured only close to T_C. Magnetization measurements on single crystals have yielded the slopes,

$\left.\frac{dB_{c2}^{\parallel c}}{dT}\right|_{T=T_c} = -10T/K$ and $\left.\frac{dB_{c2}^{\perp c}}{dT}\right|_{T=T_c} = -1.8T/K$ [42]. The values at zero temperature can be extrapolated as $B_{c2}^{\parallel c}$= 122 T and $B_{c2}^{\perp c}$=674 T.

3.3.7 Critical Currents in Type II Superconductor

In the previous section we have seen how flux enters a type II superconductor, when the applied field is greater than the lower critical field, in the form of vortices. This is a stable state. If the vortices are free to move they will do so under an applied current, thereby causing dissipation and limiting the current carrying capacity. However as we shall see in the next section pinning of vortices by crystalline defects allows the currents to flow without resistance around the pinned vortices. The trapping of vortices in the mixed state ($H_{c1} < H_{app} < H_{c2}$) causes an irreversible magnetization or hysteresis. Fig. 3.3.8.3 shows this hysteresis.

The upper limit of critical current density is set by the depairing current density (J_{dp}). If we assume that the pinning is so strong that the vortices do not move at all, the upper limit for current density is determined from energy associated with the current density. If the kinetic energy associated with pairs, carrying the supercurrent, exceeds the energy gained by pair condensation, the material will cease to be superconducting. We have seen that the energy gain per unit volume for the formation of the superconducting state is expressed as $\frac{1}{2}\mu_0 H_c^2$, where H_c is the thermodynamic critical field. The kinetic energy per unit volume (E_{kin}) associated with the motion of pairs is given by[41],

$$E_{kin} = n_s\left(\frac{1}{2}m^* v_s^2\right) = \frac{1}{2}\mu_0\lambda^2 J_s^2 \qquad (3.3.7\text{-}1)$$

where n_S, m^* and v_S are the density , mass and velocity of pairs and J_S is the supercurrent. Equating the kinetic energy with the energy gain we get the value of depairing current density as

$$J_{dp} = \frac{H_c}{\lambda} \qquad (3.3.7\text{-}2)$$

$\mu_0 H_C$ calculated from equation 3.3.6-7, using λ_c = 150 nm, ξ_c = 0.4 nm, $\mu_0 H_{c\,1}$= 0.05 T and $\mu_0 H_{c2}$ = 36 T, is 3.36 T. J_{dp} from the above expression is 1.7 x 10^9 A/cm^2. However as we shall see in the next section the vortex depinning current is about 20 times smaller than this. In reality the critical currents are 2-3 orders of magnitude smaller than J_{dp} [41].

The vortices repel each other. The vortices therefore form a triangular lattice (the lowest energy configuration) inside the superconductor. This is called the Abrikosov lattice[44] after its discoverer. In a type II superconductor, in the mixed state, externally driven current exerts a Lorentz-like force on the vortices. This causes the vortices to move, resulting in a non-zero resistance. However, the vortices can be "pinned" by impurities, defects or normal regions in the superconductor, thereby preventing vortex motion. We have seen how the addition of a vortex (normal core ~ ξ) raises the free energy (G) by the condensation energy associated with the core volume. This suggests that if there are normal regions existing in the superconductor, it is energetically favorable for the vortex to be in the normal region. If an external current tries to move this 'pinned' vortex, a pinning force (f_p) will oppose that movement. It must be noted that vortices form a lattice. Therefore, a pinned vortex would tend to pin the neighboring vortices.

The critical current (J_c) is defined under such conditions, as the current which will produce a Lorentz-like force ($f_L = J_c \phi_0$) that will exceed the pinning force f_p. The pinning force per unit length of vortex is given by[41]

$$f_p = \frac{\phi_0^2}{32\pi\mu_0\lambda^2\xi}. \qquad (3.3.7\text{-}1)$$

Therefore,

$$J_c^{max} = \frac{f_p}{\phi_0} = \frac{\phi_0}{32\pi\mu_0\lambda^2\xi}. \qquad (3.3.7\text{-}2)$$

If we substitute $\lambda = 140$ nm, $\xi = 1$ nm in equation 3.4-20, we get $J_c^{max} = 8.10^7$ A/cm^2. Once the applied current exceeds J_c , the vortices will become unpinned and begin to move, giving rise to dissipation.

Fig. 3.3.7.1 shows a schematic representation of current-voltage characteristics of type II superconductors. The I-V characteristics are affected by three phenomena related to flux motion, flux flow, flux creep and thermally activated flux flow (TAFF).The flux flow is a dissipating (nearly ohmic) regime where flux lines move under the Lorentz-like force exerted by the current. Flux flow resistivity(ρ_{ff}) is given in terms of normal state resistivity (ρ_n) by,

$$\rho_{ff}(B) = \rho_n \frac{B}{B_{c2}}. \qquad (3.3.7\text{-}3)$$

Flux creep occurs just below the flux flow regime (when the Lorentz-like force is just smaller than the pinning force). In this case the temperature is large enough to overcome the potential barrier due to pinning. Thermally activated flux flow can be distinguished by the fact that it occurs at currents much lower than the depinning current and takes place only when the potential barrier is low.

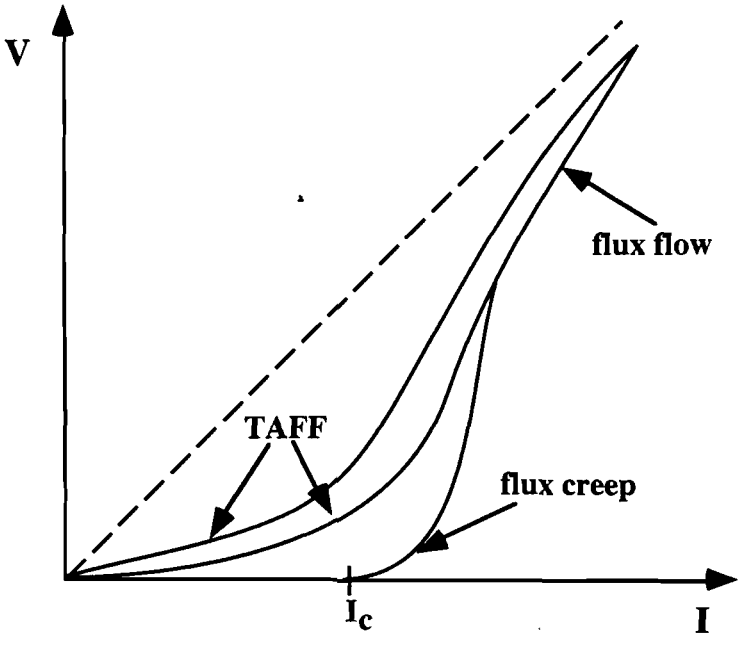

Figure 3.3.7.1 Current-voltage characteristics of type II superconductors.

3.3.8 Critical State Model for Type II Superconductor

Pinning implies that the vortex (flux) distribution is not in equilibrium. For superconductor with strong pinning, Charles Bean proposed a model that is known as the critical state model[46]. In the simplest form, the model ignores the field dependence of the critical current density (section 3.3.9) and proposes that the flux density due to pinned vortices will always produce the critical current density, J_c . The argument is as follows. For an applied field exceeding H_{c1}, vortices will enter a superconductor from the surface and get pinned. The field distribution inside the superconductor will produce screening current ($J_{scr} = \nabla \times H$). The screening current can not exceed J_c because that will drive the material normal. On the other hand, the screening current can not be smaller than J_c because that will imply weaker pinning.

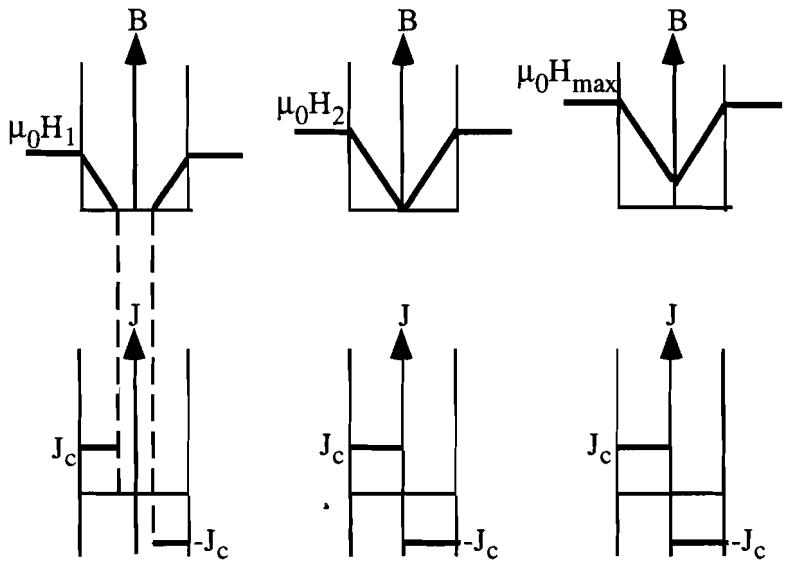

Figure 3.3.8.1 The change in average flux density and current density as the applied field H_0 is increased from H_1 to H_{max} in two steps.

For example, let us apply a field (H_{app}) parallel to the surface of a long superconducting plate of thickness ($2a$). For $H_{app} < H_{c\,1}$, the Meissner phase, screening currents in the surface layer ($\sim \lambda$) prevent flux entry. As H_{app} exceeds $H_{c\,1}$, vortices enter the superconductor from the surface and are immobilized by pinning centers near the surface. The region of superconductor penetrated by vortices now carries a constant critical current J_c . This is called the critical state. As H_{app} is increased vortices penetrate the superconductor increasingly. The critical state model

assumes that the gradient of the flux density is always constant ($\partial B/\partial x = \mu_0 J_c$) and proportional to the critical current density. The screening current is proportional to the thickness of the critical state layer and decreases the field towards the center of the plate. Fig. 3.3.8.1 shows how the field and current density vary as the applied field is increased. At $H_{app} = H^* = J_c\, a$ the vortices have penetrated fully. H^* is known as the penetration field.

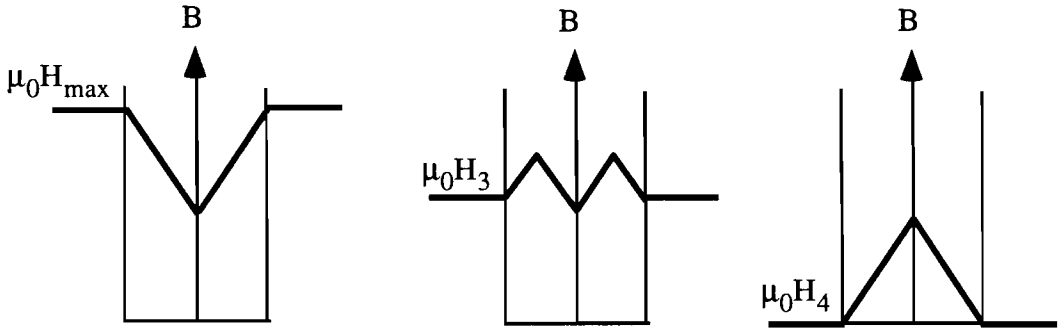

Figure 3.3.8.2 The change in average flux density as $H0$ is decreased from H_{max} of Fig. 3.3.8.1.

If the applied field is decreased gradually [Fig. 3.3.8.2], to maintain the boundary condition at the surface, the field just inside the surface has to decrease too. This means that vortices must escape the superconductor starting at the surface. The field gradient at the surface, which is now opposite in sign, is again equal to J_c ; which flows in the opposite direction. Fig. 3.3.8.3 shows the hysteresis curve.

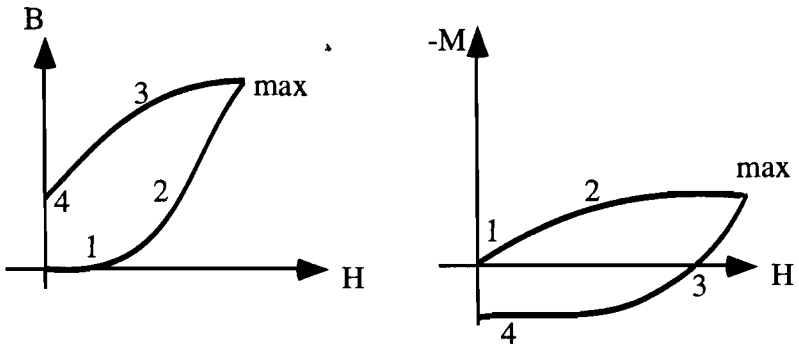

Figure 3.3.8.3 The flux density inside the superconductor and magnetization as the applied field is increased from zero to H_{max} and then decreased from H_{max} to zero.

3.3.9 Dependence of critical current density on magnetic field

Critical current density (J_c) at a given temperature is a function of the magnetic field. In the anisotropic cuprates, J_c depends on both the magnitude and the direction (relative to the crystallographic axes) of the magnetic field. The exact nature of $J_c(B)$ is not well defined, partly because the different measurement conditions regarding the applied magnetic field (dc or pulsed), type of material used (granular and epitaxial thin films, single crystals, or bulk materials), and the criteria used for determining J_c. In all cases J_c decreases as the magnetic field is increased. In granular materials (both bulk and thin films) the critical current density decreases sharply at smaller magnetic fields (< 1T). In these materials J_c is given by the intergranular weak links, and can be modeled as an array of Josephson junctions[47-49]. The depression of J_c in these weak links governs the magnetic field dependence of J_c.

In epitaxial thin films, the critical current density decreases in high magnetic field due to thermally assisted flux creep[50-53]. In different regimes it may be limited by the shearing of the flux line lattice or the individual core-pinnings[53]. The scaling of the volume pinning force ($F_p = J_c \times B$) with B is usually studied to determine the limiting mechanism for J_c.[54,55]

The planar structure of the cuprates causes anisotropy in the magnetic field dependence of J_c. The critical current density decreases more sharply in a field that is parallel to the c-axis compared to that parallel to the ab-plane. One reason for this is the greater intrinsic pinning if the flux line lies parallel to the ab-plane. The order parameter (Δ) is modulated by the planar structure being maximum at a Cu-O plane and minimum between two planes[7]. Pinning is strongest in the region of depressed order parameter. If a flux line is strictly parallel to the ab-plane it interacts with the weakly superconducting region for its entire length is pinned more effectively. If it is tilted at an angle it intersects the Cu-O planes at discrete points (where pinning is weaker). A number of studies[49,53] have explored the field-dependence of J_c by rotating the

---

[7]The coherence length (ξ) was defined in section 3.3.6 is the length scale on which the pair density (or equivalently the order parameter) changes. The coherence length in the c-direction (ξ_c) is comparable to the distance of separation between two Cu-O planes.

direction of the applied magnetic field and have confirmed that the highest J_c is observed when B is parallel to ab-plane, while it is lowest when B is parallel to the c-axis.

There are a number of semi-analytical expressions for $J_c(B)$ that are available in the literature. However, these require some empirical fitting parameters to explain experimental measurements. One such expression[50, 51], is based on the potential barrier (U),described in section 3.3.7,

$$J_c(B,T) = \frac{N_p U(B,0)}{1.07\sqrt{\Phi_0 B}}\left\{1 - \alpha\frac{T}{T_c} - \beta\left(\frac{T}{T_c}\right)^2\right\}, \qquad (3.3.9\text{-}1)$$

where Np is the density of pinning sites, and α and β are parameters close to unity. This gives a power law dependence of $J_c(B)$,

$$J_c(B) \propto B^{-\nu}, \text{ or } \log J_c(B) \propto \log B. \qquad (3.3.9\text{-}2)$$

However, the best fit in many cases is obtained by taking an exponential dependence,

$$J_c = J_{c0}\exp(-B/B_1(T)), \qquad (3.3.9\text{-}31a)$$

or equivalently, $$J_c = J_{c0}^{(1-B/B_0)}, \text{ or } \log J_c(B) \propto (1 - B/B_0), \qquad (3.3.9\text{-}3b)$$

where $B_1 = B_0/\ln(J_{c0})$. Fig. 3.3.9.1 shows the $J_c(B)$ for both c-axis and a-axis oriented films of $EuBa_2Cu_3O_7$ epitaxial thin films[52], where an exponential dependence seems reasonable. The value of B_0 is usually in the range of 10 T for $B\|c$ and decreases at higher temperatures. In spite of a decrease of about an order of magnitude, the high-T_c cuprates maintain a high enough critical current density up to several Tesla magnetic fields. $Bi_2Sr_2Ca_2Cu_3O_x$ and $Bi_2Sr_2CaCu_2Ox$ have a higher critical current density than YBCO in comparable high magnetic fields[53].

Fig. 3.3.9.2 shows the measurements of J_c of a 500 nm YBCO films on $LaAlO_3$ with $B\|c$ and $B\perp c$ up to a field of 1T at 77K. This film, purchased from NEOCERA, is similar to those used in our inductive switch experiments (chapter 5). The alignment of B with the plane of the film is not very accurate ($\pm 10°$). The value of $J_c(0)$ in this film is nearly three times higher than the ones used in our experiments.

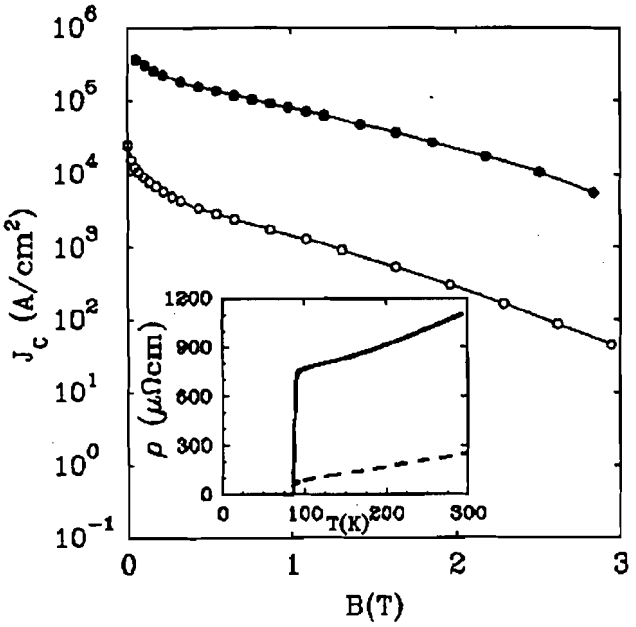

Figure 3.3.9.1 Variation of critical current density as a function of magnetic field. The closed and open symbols represent c-axis and a-axis oriented $EuBa_2Cu_3O_7$ films. Both are taken at the same reduced temperature (T/T_c=0.9). The inset shows the resistive transition.[52]

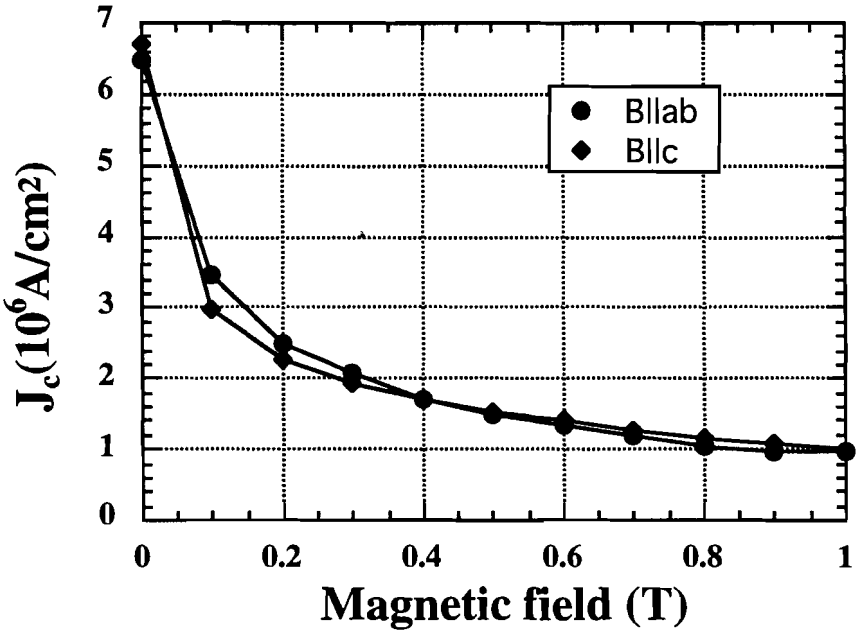

Figure 3.3.9.2 J_c(B) of $YBa_2Cu_3O_{7-x}$ films on $LaAlO_3$ substrates measured at 77K. The films are 500nm thick and a 20μm microbridge was patterned photolithographically.

3.4 Thermal Properties

For the optically triggered switches discussed in chapters 4, heat flow in the films and substrate is an important issue. In this section, we shall review specific heat and thermal conductivity of superconductors. The discussions will be confined only to properties of high temperature superconductors, mainly YBCO, in accordance with the scope of this work.

3.4.1 Specific Heat

Specific heat of high temperature superconductors can provide information regarding electronic, magnetic and vibrational excitations leading to a better understanding of the mechanism for superconductivity.

In the normal state, specific heat (at constant pressure), $C(T)$ includes several contributing excitations[34]. Among these the main contributions are due to electrons and phonons as shown in the equation below.

$$C(T) = C_{el}(T) + C_{ph}(T) \qquad (3.4.1\text{- } 1)$$

where, C_{el} is the electronic contribution and C_{ph} is the phonon term.

The electronic contribution, $C_{el}(T)$ is given by the linear term γT. The phonon term, $C_{ph}(T)$ is given by the Debye model[39] as,

$$C_{ph(T)} = \frac{12\pi^4}{5} n N_0 k_B \left(\frac{T}{\Theta_D}\right)^3 \text{ J/mole-K} \qquad (3.4.1\text{-}2)$$

where, n is the number of ions per molecular unit, N_0 is the Avogadro's number, k_B is the Boltzmann constant and Θ_D is the Debye temperature. This T^3 behavior is valid for $T << \Theta_D$.

The phase transition of the superconductor from the superconducting state to the normal state is associated with a discontinuity in specific heat due to the electronic contribution. For type I superconductors the jump in the specific heat is given by[39],

$$\Delta C = C_n - C_s = -\mu_0 V T_c \left[\left(\frac{dH_c}{dT} \right)^2 \Big|_{T=T_c} \right]. \qquad (3.4.1\text{-}3)$$

For type II superconductors, using the results from G-L theory it can established that

$$\Delta C = C_n - C_s = -\mu_0 V \frac{T_c}{\kappa^2} \frac{dH_{c2}^2}{dT^2}. \qquad (3.4.1\text{-}4)$$

BCS theory predicts a second order transition to the superconducting state with a specific heat discontinuity at $T=T_C$ given by $\frac{\Delta C}{\gamma T_c} = 1.43$, where γ is the coefficient of the electronic contribution. Values for $\Delta C/\gamma T_c$ close to 1.43 has been observed in a number of type I superconductors.

For YBCO, a similar discontinuity has been observed with $\Delta C/T_c = 55$ mJ/mole-K^2, or $\gamma_{BCS} = \Delta C / 1.43 T_c$ = 38 mJ/mole-K^2.[56] From magnetic susceptibility measurements γ has been estimated to be 35 mJ/mole-K^2. This is remarkably consistent with the γ_{BCS} obtained from the specific heat discontinuity. Fig. 3.4.1.1 shows C/T as a function of T^2 for $YBa_2Cu_3O_{7-y}$ with y = 0.0 and 1.0. The $C = AT^{-2} + \gamma T + \beta T^3$ fit is also shown. The reported measurements of $C(T)$ show considerable variation. Fig. 3.4.1.2 shows C vs. T obtained by various groups[57].

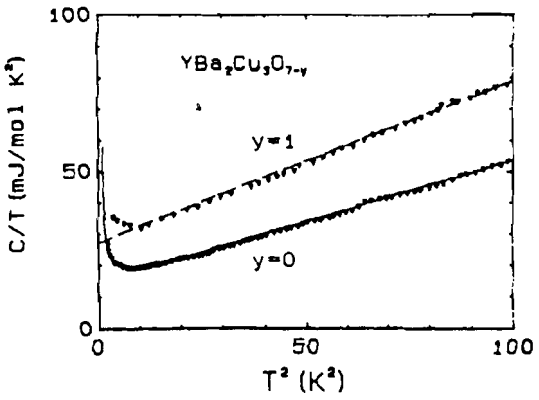

Figure 3.4.1.1 C/T vs. T^2 for $YBa_2Cu_3O_{7-y}$ with y=0.0 and 1.0 The solid curve is a $C = AT^{-2} + \gamma T + \beta T^3$ fit with A = 35 mJ-K/mole, $\gamma = 12.9 \text{mJ / mole} - \text{K}^2$, and $\beta = 0.23 \text{mJ / mole} - \text{K}^4$ [57]

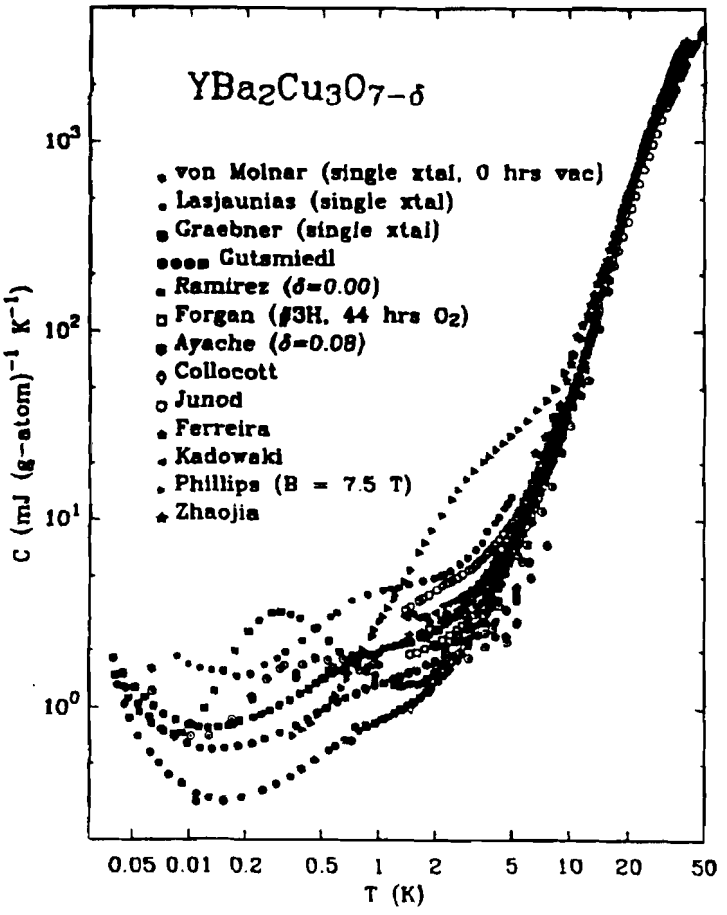

Figure 3.4.1.2 *C* vs. *T* of YBCO films obtained by various groups.[57]

3.4.2 Thermal Conductivity and Boundary Resistance

In order to understand bolometric effects arising from laser illumination of YBCO thin films it is essential to develop an understanding of heat conduction in films and out of the film. Since our experiments deal with "optically thick" films (films of thickness greater than the optical penetration depth), the incident laser energy is deposited in the top surface of the film and gradually propagates heating up the entire film. In most cases, the laser energy is in the form of short (~100 ps) pulses with low repetition rates ($\leq$ 1 kHz). The film, deposited on a suitable substrate, is mounted on a cold finger equipped with a temperature controller. We, therefore, need to study heat propagation from the top surface of the film to the cold finger through the YBCO film, the film-substrate boundary and the substrate. In the next chapter, the model of heat

propagation developed to characterize our photoresistive switch will be discussed in detail.

YBCO is a highly anisotropic material. Since all our films were c-axis oriented we shall assume, hereafter, that the perpendicular component of thermal conductivity $(K_\perp)$ represents conduction along the c-axis and the parallel (to the film surface) component $(K_\parallel)$ represents conduction in the a-b plane. Cohn et al has carried out a study of the $K_\parallel$ component on single crystal[58] and liquid phase processed (LPP) samples of $YBa_2Cu_3O_{7-\delta}$ ($\delta \leq 0.16$). For single crystals $K_\parallel$ values of 8-11 W/m-K at 300 K is typical[50]. The in-plane thermal conductivity, $K_\parallel$, can be written as a sum of lattice conductivity K_l and an electronic contribution K_e,

$$K_\parallel = K_l + K_e \ . \qquad (3.4.1\text{-}5)$$

The contribution of electrons (or carriers) to heat conduction can be calculated using Wiedemann-Franz-Lorenz (WFL) law[60],

$$K_e = L_0 \sigma T, \qquad (3.4.1\text{-}6)$$

where L_0 is the Lorenz number (2.45 x 10^{-8} WΩ/K^2), σ is the electrical conductivity, T is the temperature in Kelvin.

The lattice conductivity, K_l, is due to scattering of phonons by other phonons, carriers or defects. Both contributions are significant and comparable to each other in magnitude. A more recent study by Marshall et al.[61] on c-axis oriented film concluded an in-plane conductivity of 2.3 W/m-K at room temperature, which is lower than single crystal value. Another study by Shaw-Klein et al[62] on c-axis oriented films of thickness ranging from 0.25-1 μm derived $K_\parallel$ values in the range of 2.8-4.5 W/m-K also at room temperature.

Values of $K_\perp$, on the other hand, are considerably lower than $K_\parallel$. Using the thermal comparator method, Shaw-Klein et al, have calculated $K_\perp$ values of 0.26 W/m-K at room temperature[62]. Hagen et al, have reported values of 1-2 W/m-K for single crystals at room temperature[59].

Thermal diffusivity, D, is defined as the ratio of thermal conductivity and specific heat per unit volume (ρC).

$$D = K/\rho C. \tag{3.4.1-7}$$

Diffusion of heat through a film of thickness d can be characterized by a diffusion time $\left(\tau_{diff} = d^2/D\right)$.

If we take a nominal value of C = 0.2 J/gK and density ρ = 6.39 g/cm^3 and K= 1 W/m-K, D = 2 x 10^{-3} cm^2/s. For a film of thickness d = 0.8 μm, τ_{diff} = 818 ns.

Thermal boundary resistance (R_{bd}) is the excess thermal resistance above that of the material on either side of the interface,

$$R_{bd} = \frac{\Delta T \times A}{Q}, \tag{3.4.1-8}$$

where, ΔT is the temperature difference across the interface, A is the area of the interface, and Q is the power or rate of heat flow.

R_{bd} depends on the particular substrate and temperature. For YBCO on substrates like MgO, $LaAlO_3$ and $SrTiO_3$, it is of the order of 10^{-3} cm^{2}K/W. It must be noted that the calculation of R_{bd} depends on the width of the barrier. In Ref. 63 the barrier width was taken to be 10 Å and an R_{bd} value of 10^{-4} cm^{2}K/W is reported at 300K. An acoustic mismatch model, is often used to estimate R_{bd} and predicts a T^{-3} dependence. A study by Nahum et al[64] has shown that the actual value of R_{bd} is 10-100 times larger than that predicted by the model. This may reflect a layer of disordered material at the interface between the film and the substrate.

3.5 Optical Properties

The triggering of our superconducting opening switches is performed by optical pulses. The transition from the superconducting state to the normal state is accomplished by illuminating the switch with short infrared laser pulses. In this section we shall briefly discuss the reflectivity and absorption of superconductors.

Due to the presence of an energy gap (section 3.3.2) a superconductor does not absorb electromagnetic radiation of energy smaller than the gap. It responds to sub-gap ac fields according to the complex impedance due to normal and superconducting fluids (section 3.3.2). However, visible and near-IR radiations have photon energies (of the order of 1 eV) much larger than the gap, that is of the order of 10 meV for the material of our switch, YBCO. Therefore the optical properties (reflection and absorption) are virtually independent of temperature and the superconducting state. Room temperature measurements of the optical properties are accurate even at low temperatures.

YBCO is black. Consequently it exhibits high absorption and low reflectivity in visible to near-IR range of the optical spectrum. The high absorption is due to inter-band transitions. The optical penetration depth in YBCO is about 120–140 nm for λ=500-1000 nm[65]. This is inferred from the reflectance and transmittance measurements of YBCO on $LaAlO_3$.Usually the optical property is described in terms of a complex frequency-dependent conductivity, $\sigma(\omega)$ and dielectric function, $\varepsilon(\omega)$. These are usually computed from reflectivity measurements. In the case of high temperature superconductors, the study of optical properties reveal information regarding the band-structure of the materials. Although this is extremely important for the investigation of the nature of superconductivity of the high temperature superconductors, it is beyond the scope of our work. We are concerned only with the absorption of optical energy in the switch material.

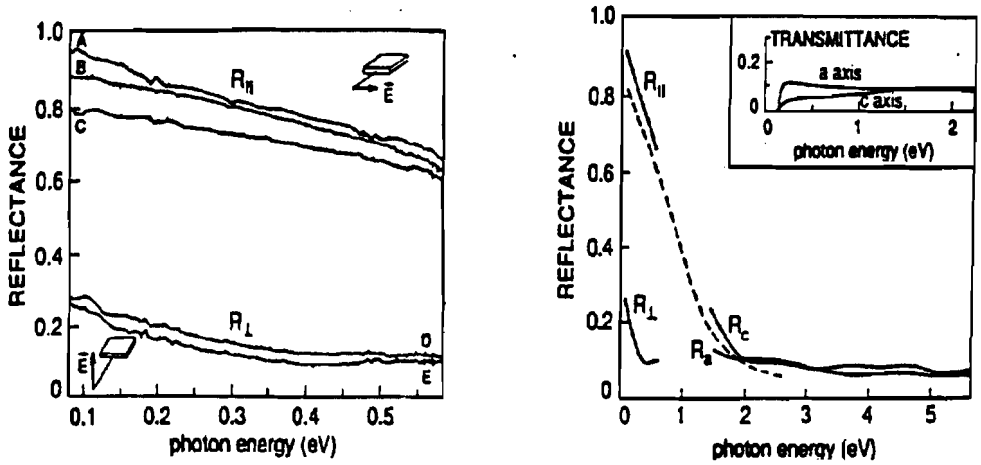

(a) (b)

Figure 3.5.1 Reflectance of YBCO. (a) Polarized IR reflectance of YBCO at normal incidence, from (A) single crystal *ab* face, (B, D, E) perpendicular to *ab* face, (C) c-axis oriented films. $R_{\perp}(\omega)$ spectra were obtained by rotating by 90° the polarizer (D) and the film (E). (b) Reflectance of YBCO single crystal, $R_{\parallel}$ and $R_{\perp}$, compared to that of thin films, R_c and R_a [broken curve : measured; solid curve : calculated from ellipsometric measurements of complex dielectric function]. Inset : transmittance of 200 nm YBCO thin films on $SrTiO_3$ oriented with c-axis and a-axis perpendicular to the substrate.[66]

Fig. 3.5.1 shows the anisotropy in reflectance and transmittance of YBCO thin films and single crystals[66]. The wavelengths[8] of light used in our experiment are 1064 nm (Nd:YAG) corresponding to photon energy of 1.17 eV. At these wavelengths reflectivity is approximately 0.2. The films used in our experiments are 600-800 nm thick, several times thicker than the optical penetration depth and are therefore called optically thick. Almost all of the incident light is absorbed. A recent study[67] on reflectance of $YBa_2Cu_3O_{6+x}$ with varying oxygen content (x=0.1-1.0) is shown in Fig. 3.5.2.

[8]YBCO is a low carrier density conductor compared to metals. The plasma frequency (ω_p) of YBCO is 1.67×10^{15} s^{-1}. This corresponds to a wavelength of 1.13 μm. For photons with shorter wavelength the reflectivity is low.

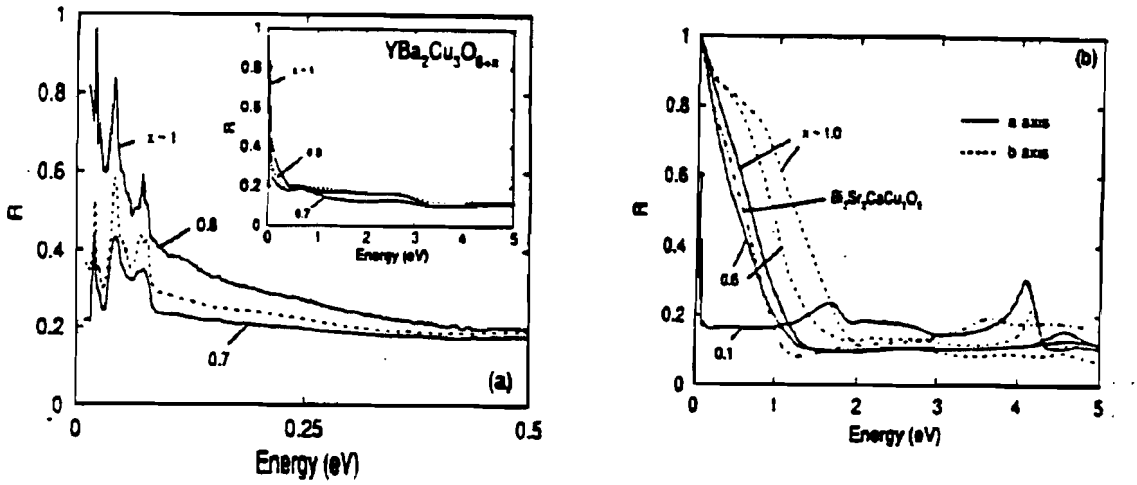

(a) (b)

Figure 3.5.2 Room temperature reflectivity of $YBa_2Cu_3O_{6+x}$ for varying x. (a) Room temperature c-axis reflectivity for x=0.7,0.8, and 1.0. The inset shows reflectivity up to an energy of 5 eV. (b) Room temperature reflectivity of at various x for polarization parallel to a-axis (solid) and b-axis (dotted).The dashed-dotted line compares reflectivity of BSCCO.[67]

We made a crude reflectivity measurement of our films at 1064 nm at near normal incidence and found the reflectivity to be approximately 0.1 which agrees well with the above-mentioned results.

3.6 Summary of material properties of YBCO

In this section we summarize the relevant material properties of YBCO. The crystalline anisotropy shows up in the physical properties. It is clearly an extreme type II superconductor ($\kappa = \lambda/\xi >> 1$).

Table 3.6.1 Properties of YBCO

Properties	Along c-axis	In a-b plane
Density	6390 kg/m^3	
Critical temperature (T_c)	85-92 K	
Normal state resistivity (ρ_n)		100 μΩ-cm
Penetration Depth (λ)	150 nm	600 nm
Coherence Length (ξ)	0.4 nm	3 nm
Lower critical field (H_{c1})	0.05 T	0.02 T
Upper critical field (H_{c2})	36 T	265 T
Specific heat (c)	200 $Jkg^{-1}K^{-1}$	
Thermal conductivity at 300 K	1–2 W/m-K	10 W/m-K
Optical absorption depth	120 nm	
Reflectivity to polarized light (Nd:YAG)	0.2	

CHAPTER 4

SUPERCONDUCTING PHOTORESISTIVE OPENING SWITCH

4.1 Principle of Operation

An ideal opening switch offers zero resistance in the "closed" state, since the switch has to conduct current in the branch of the circuit containing the switch, ideally without any voltage drop. In the "open" state the switch has to interrupt the flow of current in that branch of circuit. However, this can only be accomplished partially with real switching devices. For example, a state-of-the-art semiconductor switch used for energy extraction from a superconducting magnetic energy storage (SMES) dissipates several kilowatts of power in its closed state due to its non-zero resistance. Thus, superconductors, offering zero resistance, become a natural choice for opening switches.

A transition of the superconductor from its superconducting state to its "normal" or resistive state can be accomplished in several ways. One way of achieving this is to heat the superconductor above its transition temperature (T_c). The change can also be realized by either exceeding the current density (J_c) or the critical magnetic field (H_c). We shall discuss the merits and demerits of these methods later in the section.

Metallic or type I superconductors are good conductors in the normal state and hence do not provide a high resistance in the open state of the switch. High-T_c superconductors, on the contrary, are ceramic materials and offer much higher normal state resistance. Another advantage of using high-T_c superconductors is that they operate above liquid nitrogen temperature and require a comparatively less expensive cryogenic system. Therefore, the development of high-T_c superconductors, especially in thin film form, has made the fabrication of superconducting opening switches feasible. Critical current densities (J_c) of 1 MA/cm^2 or more can be achieved with state-of-the-art thin films of YBCO at liquid nitrogen temperature. This is the material that has been chosen for our opening switch.

Let us now turn our attention back to the three possible methods of performing the switching. Since H_{c2} for YBCO is very high (~30T), the magnetic field required to induce a transition to the resistive stage is difficult to achieve, though for granular films application of external field lowers J_c and can drive the material normal. However, granular films have low critical current densities and are not suitable for high current

applications. Exceeding the critical current density (J_c), may be a possible way to drive the material normal. Consider, for example, a superconducting shunt, across a load. It is desired that for normal operation the switch will be closed and carry the current. No current will flow through the load as long as the current through the superconducting branch is less than the critical current (I_c). If for some reason the source current increases above T_c the superconductor will be driven normal and some current will flow through the load, determined by the ratio of resistances of the load and the switch (in its resistive state). This operates as a fault current limiter[1] if we assume that the sudden increase in the source current is due to a fault. The excess current in this case gets diverted into the load resistor and dissipated. So effectively the switch opens and protects the circuit from getting destroyed due to a surge of excess current.

The third and the most efficient method is by heating the film above T_c. The main reasons why this method is more attractive than the other two are speed and convenience. As we have discussed in section 3.5, YBCO films absorb infrared and visible light very efficiently. Therefore, the switch can be heated very quickly (ns) using fast laser pulses. The convenience in design lies in the fact that it does not require an external current bias. Although current switching or switching by exceeding J_c works naturally in some cases, it may require an external bias in some others. Consider, for example energy extraction from a superconducting magnet. The superconducting switch carries the persistent current of the magnet in the closed state. Energy from the magnet is extracted by driving it normal and diverting the current to a parallel load (say, a bank of capacitors). Now if we wish to perform current switching we need to provide an external current source equipped with a suitable closing switch.

As the title of this thesis suggests, we have chosen to use the method of photoinduced heating of the film. Our choice was also influenced by an interest in studying the optical response of YBCO films. Most of the studies on optical response were made with optically thin[2] films (<200 nm). However, for a switch with high current carrying capacity thicker (~800 nm) films were used in our experiments. Consequently, a study of bolometric and nonbolometric photoresponse for optically

---

[1]see section 2.3.1 for a detailed discussion on fault current limiters.

[2]see section 3.6 for optical properties of YBCO

thick films is of considerable importance. In the last section (4.5) our results are discussed in the context of results obtained by other groups.

High current carrying capacity is one of the main advantages of superconductors. Thin film YBCO samples used in our experiments have $J_c > 1$ MA/cm^2 at 77K. For a 1-cm wide, 1 μm thick film this implies a current of 100 A. However, to test the switching we patterned our switch to a 100–250 μm wide, 2 mm long bridge from a film of thickness 800 nm. The details of the switch design are described in the next section. This switch was illuminated with a train of laser pulses. The current through the switch was applied using an external source, and voltage across a 50 Ω load connected in parallel to the switch was measured. When the switch is in the superconducting state no voltage appears across the load. When a laser pulse hits the switch a voltage is observed, indicating opening of the switch.

4.2 Switch Design

YBCO films, deposited on polished MgO substrates using rf magnetron sputtering[68, 69], were used to fabricate the photoresistive switches. The films were 800 nm thick. Each film was patterned into an H structure [Fig. 4.2.1]. The patterning was done using the laser ablation technique[70]. A Nd:YAG laser (λ=1.064 μm) was focused to a small spot (6-30 μm in diameter) on the film mounted on a computer controlled X-Y translational stage. The stage operated by stepper motors moves in 6.25 μm steps. The laser power was optimized using a $\lambda/4$ wave-plate - polarizer arrangement so that it was just enough to locally remove the superconducting material, without causing oxygen depletion from the other regions. The central bridge region which acts as the switch was typically 2 mm long and 100-250 μm wide. Silver contacts were evaporated on the four corner pads of the structure.

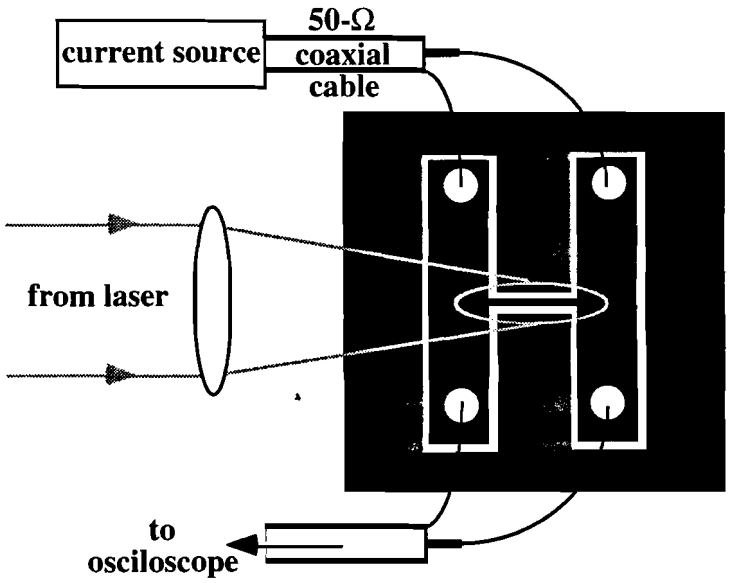

Figure 4.2.1 The photoresistive switch. The film is patterned into a H-structure and the central bridge is driven normal by laser illumination.

The film was mounted on a Copper sample holder consisting of a block on which the film was attached, and a plate screwed onto the block and also on the cold finger of a DE-204 two-stage cryocooler manufactured by APD cryogenics. The cryocooler and the sample were enclosed by an optical access cryostat. The cryostat is equipped with ports for connecting vacuum pumps, a thermocouple gauge for

measurement of the vacuum, a temperature controller and for an electrical feed-through. The electrical input and output circuits were connected inside the cryostat using stainless steel coaxial cables with SMA connectors on either end. The mating SMA connectors on the sample holder were connected to the silver contact pads on the sample by aluminum wire bonds.

The input circuit consists of a dc constant current source which drives up to 100-mA current through the switch. The output circuit consists of a 50-Ω termination across which the voltage is measured. For dc R(T) measurement a digital voltmeter was used for the measurement of voltage. The switching transients were measured by analog and digital sampling oscilloscopes interfaced with a computer. The sample was mounted inside the cryostat which was subsequently pumped down using a mechanical pump and a cryo-adsorption pump. The sample was then cooled by an APD (model HE-4) compressor driving the DE-204 cold stage. The lowest temperature achievable using this closed-cycle He refrigerator is about 16 K without a radiation shield, and about 10 K with a radiation shield. However, temperatures used for the experiment ranged from 60-85 K[3]. The temperature control was obtained using PID control with a 25Ω/25W heater resistor attached to the sample holder. After a suitable initial temperature was established the switch was illuminated by the laser. The circular laser beam from a Nd:YAG laser was made elliptical using a cylindrical lens to conform to the switch geometry. The laser had a pulse width of 170 ps[4], repetition rate of 1 kHz and a fluence varying from 0.5 - 14 mJ/cm^2 per pulse[71, 72]. The laser pulse energy absorbed by the switch is estimated by measuring the beam profile[5] and using Eq. A4.2.4-12 (Appendix 4). The experimental set-up is shown in Fig. 4.2.1.

---

[3]We were limited by laser energy when these experiments were conducted. Subsequently, a laser amplifier (Appendix 4) was installed. For the new design (section 4.6) we have obtained switching at 20K.

[4]It was recently discovered that the streak camera used to measure the laser pulse width was miscalibrated. The correct pulse width should be ~120 ps. However, this does not affect any of our calculations significantly.

[5]See Appendix 4 for details regarding the laser system and the laser beam profile.

4.3 Experimental Results

The shape of the voltage pulse depends upon three parameters: the laser fluence, the bias current and the initial sample temperature. Fig 4.3.1 shows a series of voltage pulses observed for varying fluence. The initial temperature was 70K and bias current was 30 mA. There are two distinct components of this photoresponse. A fast component, occurring at the laser trigger, had a rise time of ~4 ns and fall time of ~ 6 ns. The slower component with a rise time of ~ 50 ns was delayed with respect to the laser trigger. This delay time is hereafter referred to as the thermal (or bolometric) response time. As can be seen from Fig. 4.3.1 the two components overlap in time. The time of overlap depends mainly on the initial temperature of the film. In the next section, we shall describe a model of the switch simulating the thermal response. This analysis proves that the slower component can be described quite accurately by the one dimensional heat flow model and is, therefore, called the bolometric component. The faster component may be nonbolometric, but its origin is not clearly understood at this time, especially since the slow measuring system limits the signal bandwidth. A possible explanation is given in section 4.5. The second sharp peak occurring around 250 ns in Fig. 4.3.1 is due to the reflection of the earlier fast peak from an impedance mismatch at the current source. The reflections were delayed out of the time-window of interest (i.e. the rising edge of the response) by using a long length of transmission line. However, the falling edge does include a contribution from the reflection.

Figs. 4.3.2–4.3.9 show photoresponses for varying fluence obtained under a variety of conditions. Fig. 4.3.2 shows the response for an initial temperature of 80 K and a bias current of 30mA. Since this temperature is close to T_c (= 84 K) even a small amount of laser energy drives the switch normal. For higher values of laser fluence the bolometric response time is similar to the nonbolometric switching time(~4 ns). The two signals overlap in time. At lower values of fluence the two components can be distinguished more clearly from the difference in slope at the rising edge.

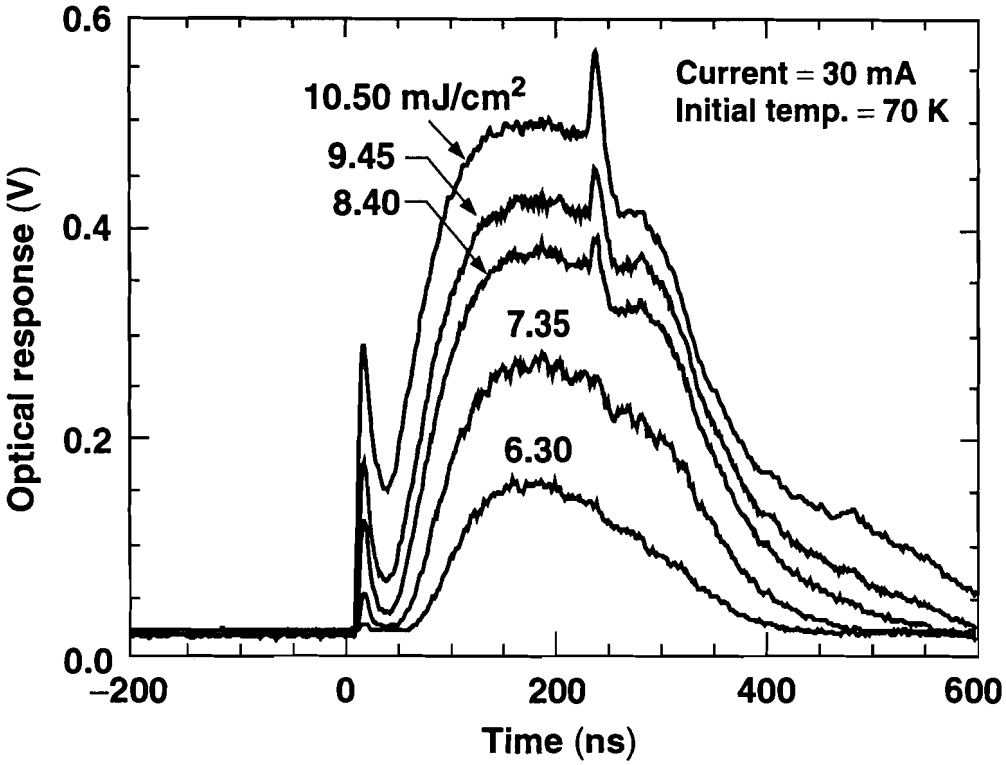

Figure 4.3.1 Photoresponse for varying fluence at 70K with a 30 mA current bias shows two switching components. The slower component is bolometric in origin. Reflection from the current source appears ~250 ns.

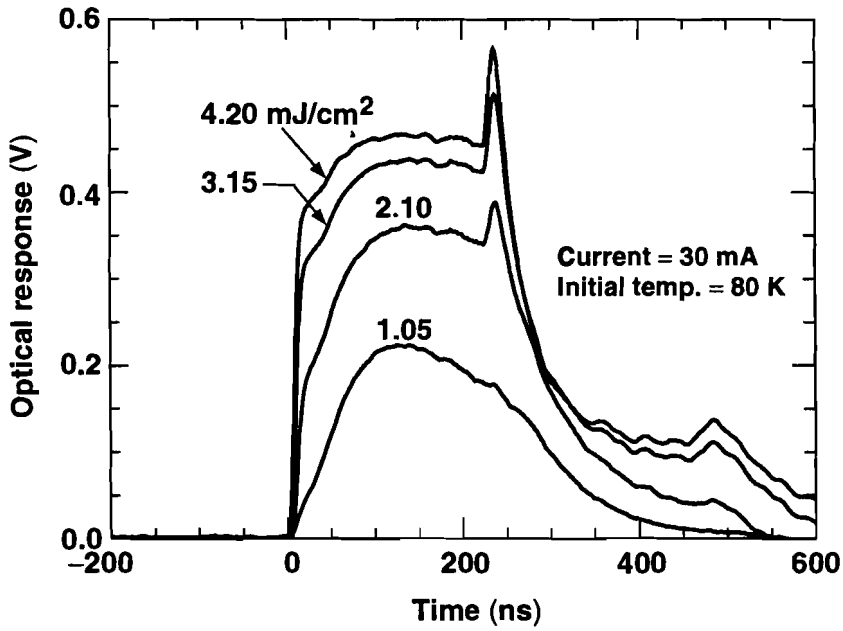

Figure 4.3.2 Photoresponse for varying fluence at 80K with a 30 mA current bias.

At 70K two sets of data at 100mA and 10mA shown in Figs. 4.3.3 and 4.3.4 respectively. The nonbolometric component is fixed in time (with respect to the laser trigger) but the bolometric component gets increasingly delayed as laser fluence is decreased. This is natural since the temperature of the entire superconductor needs to be above T_c for a voltage to appear across it if only the bolometric component is considered. The effect is more pronounced at lower levels of current. For example, Fig. 4.3.4, shows the two components entirely separated in time. For lower values of laser fluence, however, there is no nonbolometric component (Fig. 4.3.3).

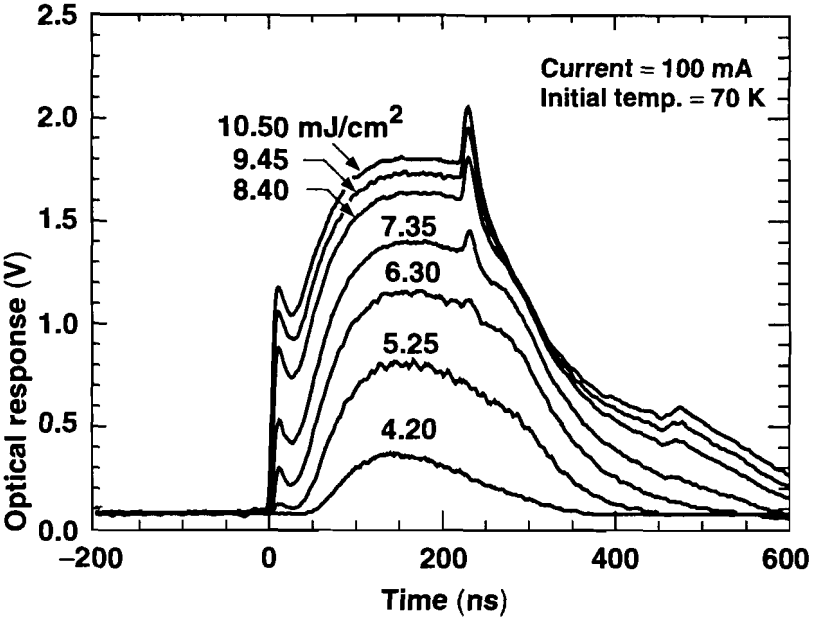

Figure 4.3.3 Photoresponse for varying fluence at 70K with a 100 mA current bias.

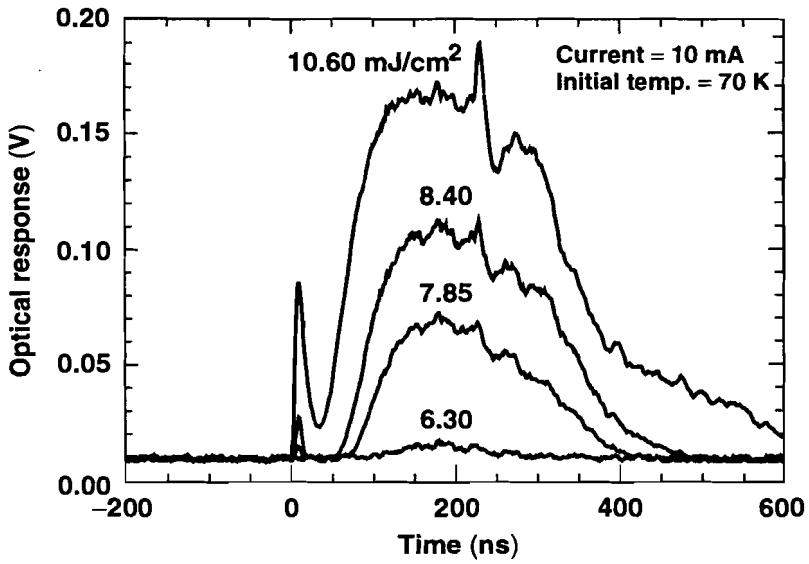

Figure 4.3.4 Photoresponse for varying fluence at 70K with a 10 mA current bias.

If we cool the sample to a lower temperature, 65K (Fig. 4.3.5, Fig. 4.3.6) the two components can be identified more clearly. We did not observe a signal at this temperature (65K) for bias currents of 10mA or lower. We were also limited by laser fluence at low temperatures.

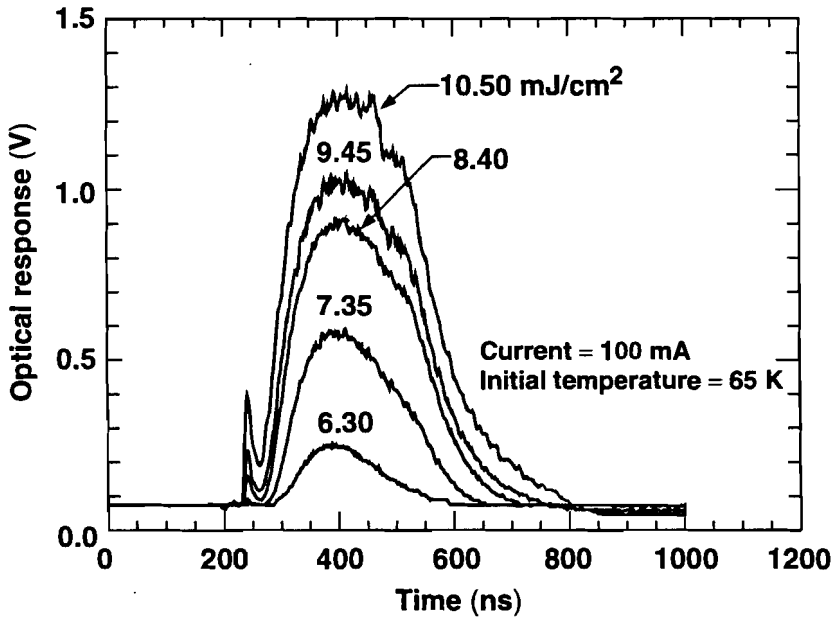

Figure 4.3.5 Photoresponse for varying fluence at 65K with a 100 mA current bias.

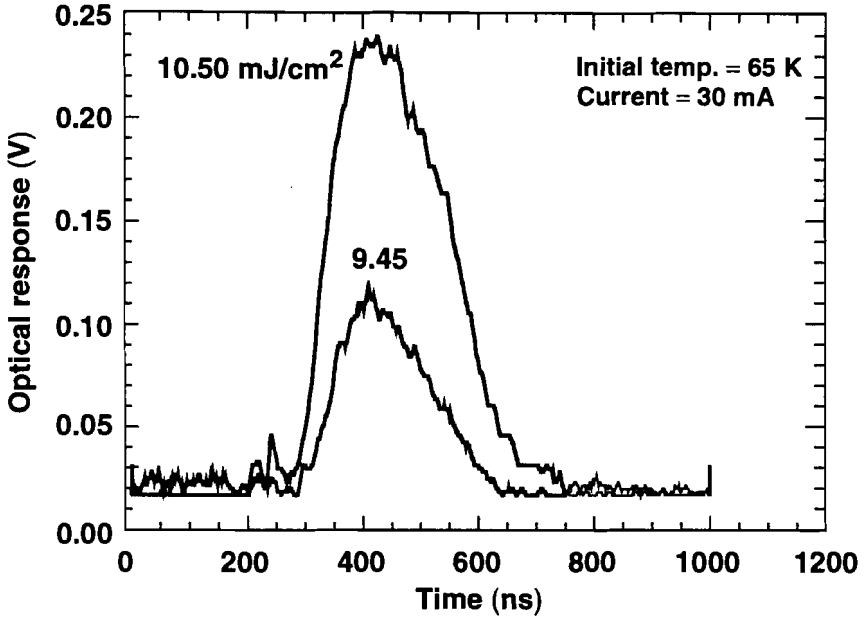

Figure 4.3.6 Photoresponse for varying fluence at 65K with a 30 mA current bias.

Fig 4.3.7 shows the dependence of the photoresponse on the bias current. Fig. 4.3.7 shows the responses at 70K for a laser fluence of 10.5 mJ/cm^2 at three different values of bias current. Since the voltage levels depend on the bias currents it is difficult to compare the three responses, though it is obvious that the temporal overlap of the two components is less at lower currents. The magnitudes of both the bolometric and the nonbolometric components scale with the current. Also, the response time is longer for lower values of current.

The dependence on initial temperature can be seen in Figs. 4.3.8 and 4.3.9. In Fig. 4.3.8 the curves correspond to 10.5 mJ/cm^2 and 100 mA current bias. For an initial temperature of 60K the response is purely bolometric and delayed by about 50 ns with respect to the laser trigger. At 65K a small nonbolometric component can be observed. The falling edge of the fast component overlaps with the rising edge of the slower component. At 70K the overlap of the two components increase. Fig 4.3.9 is similar showing three responses at 70K, 75K, and 80K at a lower fluence (7.35 mJ/cm^2) and a smaller bias current (10mA).

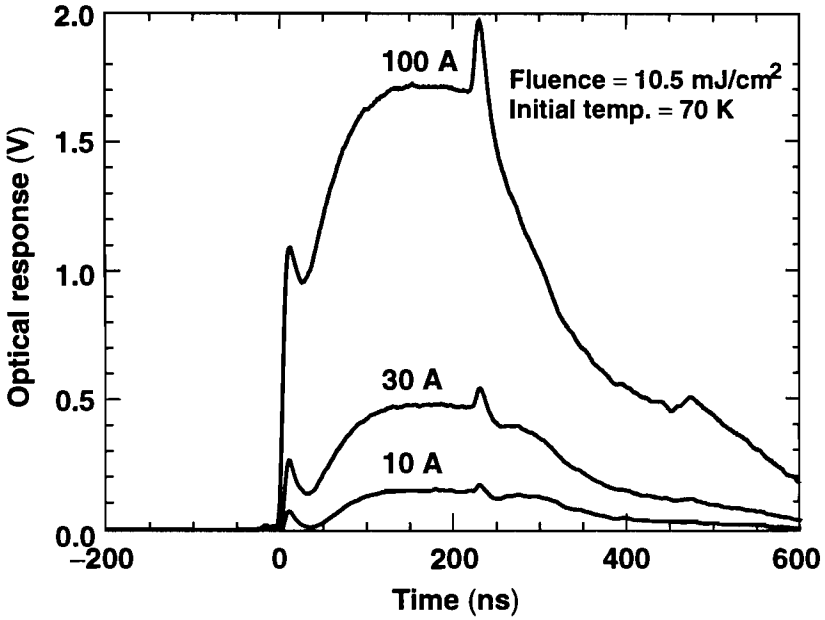

Figure 4.3.7 Photoresponse depends on the bias current. (a) responses at 10 mA, 30 mA and 100 mA at a fluence of 10.5 mJ/cm^2 at 70K.

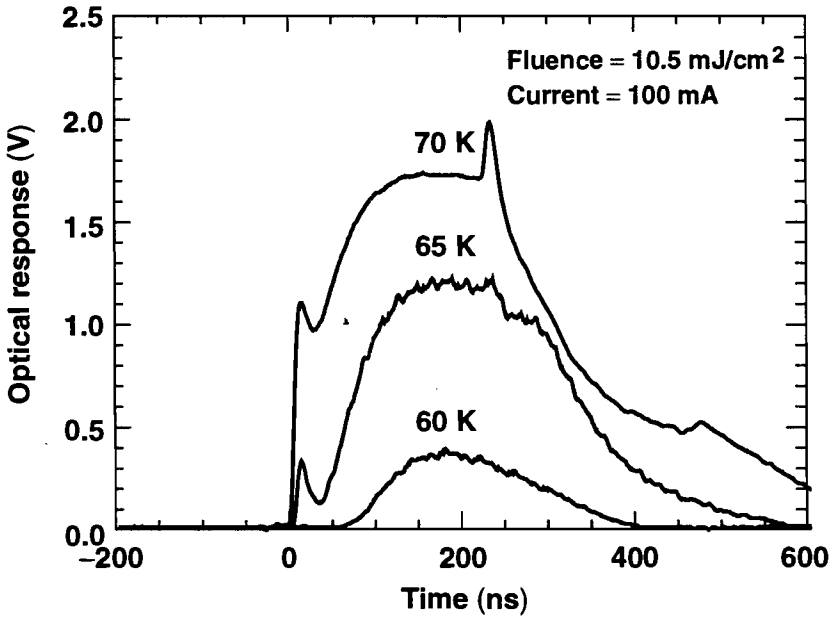

Figure 4.3.8 Photoresponse at different initial temperatures (70K, 65K, and 60K) at a fixed current bias (100 mA) and laser fluence (10.5 mJ/cm^2).

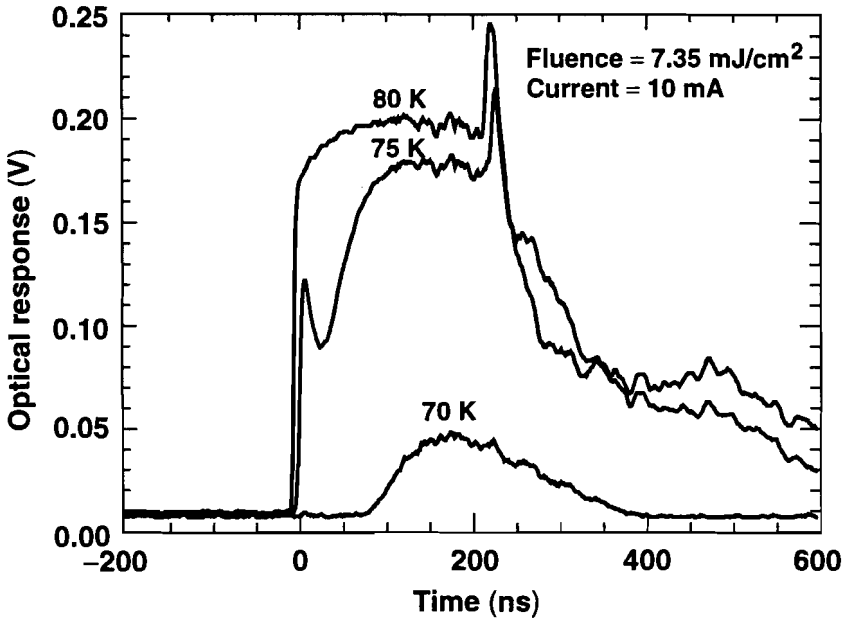

Figure 4.3.9 Photoresponse at different initial temperatures (70K, 75K, and 80K) at a fixed current bias (10 mA) and laser fluence (7.35 mJ/cm^2).

4.4 Modeling and simulation of the bolometric component

We have simulated the thermal response of the laser-irradiated HTS thin-film bridge. Although the thermal conductivity is higher in the lateral direction, along the a-b planes (section 3.4), the smallest lateral dimension (100 μm) is more than 100 times the thickness (800 nm) of the film. Since diffusion time scales with the square of distance, heat diffusion takes place mainly along the thickness (x-direction). The heat diffusion is calculated by numerically solving the heat-equation in one dimension,

$$\partial/\partial x\{K(T)\partial T/\partial x\} = \rho\,\partial/\partial t\{c(T)T\} \qquad (4.4\text{-}1)$$

where K is the thermal conductivity, ρ is the density and $c(T)$ is the temperature dependent specific heat.

The film and the substrate are divided into discrete layers. The film is divided into n slices[6]. The substrate is divided into $n/8$ slices. The temperature of each layer is calculated as a function of time and is used to compute the bolometric photoresponse.

Thermal conductivity (K) of YBCO film is taken to be $1.1 \mathrm{Wm^{-1}K^{-1}}$, to provide the best fit between theoretical and experimental response times. This value of thermal conductivity lies within the range of reported measured values of thermal conductivity of YBCO films [Section 3.3.2]. The thermal conductivity of crystalline MgO is given by the approximate formula

$$K_M = k_1 + k_2 T \ \mathrm{Wcm^{-1}K^{-1}}, \qquad (60\ \mathrm{K} < \mathrm{T} < 100\ \mathrm{K})$$

where $k_1 = 21.25$, and $k_2 = -0.1875$.

in the temperature range of interest. Specific heat of MgO is calculated under the T^3 approximation, with Debye temperature (θ_D) of 946 K.

$$c_M = 12\pi^4 R(T/\theta_D)^3/5 = aT^3 \ \mathrm{JK^{-1}mol^{-1}} \qquad (4.4\text{-}2)$$

---

[6] typically n = 64, so that for 8000 Å thick film, slices are 125 Å thick.

The specific heat ($c(T)$) of YBCO was measured[73] and fit with a linear function

$$c(T) = mT + b \text{ JK}^{-1}\text{kg}^{-1}, \qquad (4.4\text{-}3)$$

where, $m = 2.83$ and $b = -39.7$.

Since the laser pulse is much shorter (150 ps) than the photoresponse, we assume instantaneous absorption of energy. We also assume uniform illumination of the entire switch area. Light absorption falls off exponentially as a function of film thickness. The fluence ($F(x)$) at a distance x below the surface of the fim, can be expressed in terms of the optical pentration depth ($1/\alpha$) as,

$$\mathrm{F(x)} = \mathrm{F_0}\exp(-\alpha x), \qquad (4.4\text{-}4)$$

where $\alpha = 8.33 \times 10^6$ m^{-1} is used.

The energy density ($E(x)$) in the switch as a function of the film thickness is,

$$E(x) = -d\mathrm{F}/dx = \alpha \mathrm{F_0}\exp(-\alpha x) \qquad (4.4\text{-}5)$$

The temperature distribution along the thickness of the film is found by calculating the temperature rise from the initial temperature (T_0), given by

$$E(x) = \int_{T_0}^{T(x)} \rho c(T)dT, \qquad (4.4.5)$$

as
$$T(x) = -\frac{b}{m}\left[1 - \frac{b}{m}\left\{1 + \frac{m}{b^2}\left(mT_0^2 + 2bT_0 + 2E(x)/\rho\right)\right\}\right]; \qquad (4.4\text{-}6)$$

where ρ is the density of YBCO.

The first and second partial derivatives of T(x,t) with respect to x are calculated by finite differences. The time-evolution of the temperature profile is then calculated using Eq. (4.4-1),

film :
$$T(t + \Delta t) = T + \frac{\Delta t K T''}{\rho(2mT + b)} \qquad (4.4\text{-}7)$$

substrate : $$T(t+\Delta t) = T + \left[\left\{(k_1 + k_2 T)T'' + k_2 T'^2\right\} / 4a\rho_M T^3\right]\Delta t, \qquad (4.4\text{-}8)$$

where ρ_M is the density of MgO, $T = T(t)$, $T' = \partial T(x,t)/\partial t$, and $T'' = \partial^2 T(x,t)/\partial t^2$.

A time-dependent temperature profile is shown in Fig. 4.4.1 assuming a uniform illumination of the crossbar with the mean intensity of the Gaussian distribution (13.86 mJ/cm^2) and an initial temperature of 70 K.

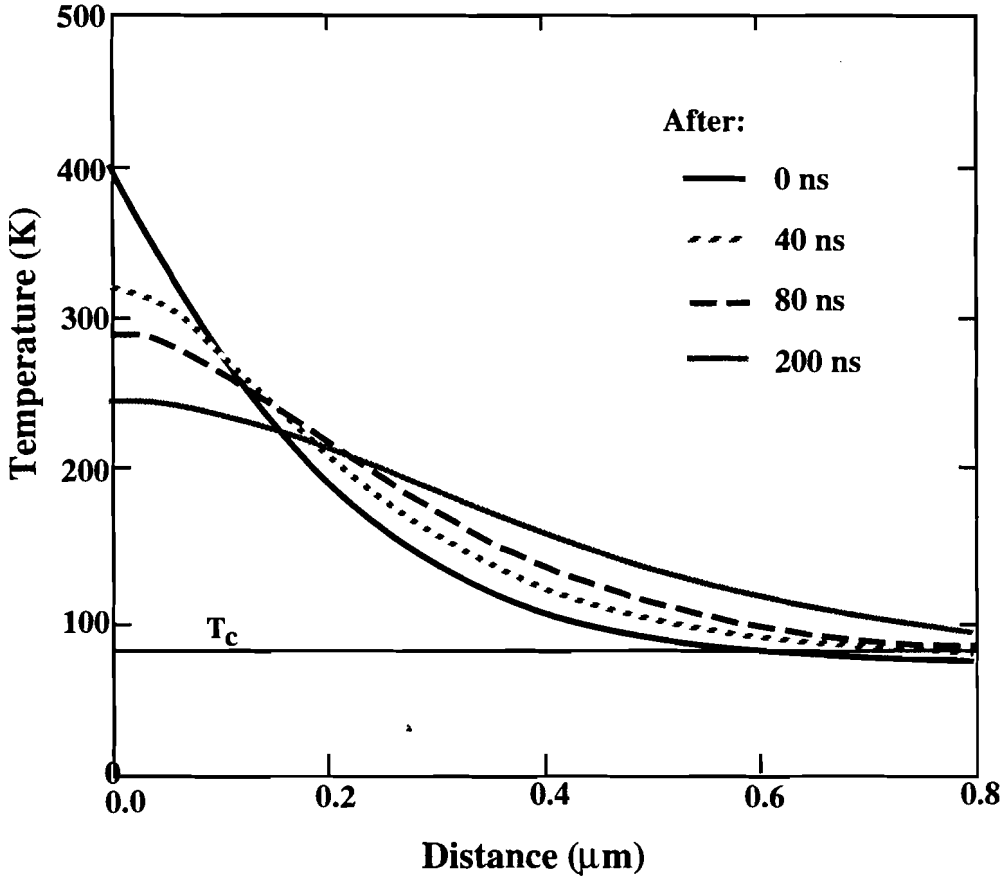

Figure 4.4.1 Time variation of the temperature distribution across the thickness of the film.

This temperature distribution is used to compute the critical current in each slice based on the measured dc characteristics of the film. It is assumed that if at a given instant of time there are slices with temperature below T_c they will carry supercurrent unless the current density in the slice exceeds the estimated critical current density. The electrical model is a parallel combination of temperature-dependent resistors, one for

each slice. If the sum of the critical currents in the slices with $T < T_c(I_{sc})$ exceeds the applied current (I_0) there is no voltage signal at the output. A slice with temperature above T_c has a normal resistance that varies with temperature.

After a period of time, called the response time of the switch, I_{sc} becomes less than I_0 and there is a non-zero equivalent resistance in the switch, resulting in a voltage signal at the output. This happens because all the slices except for a few are above the critical temperature. In this case the output signal is computed by an iterative redistribution of the current between the superconducting and the normal slices. The redistribution is done so that the voltage across all the slices is the same. However, due to the high critical currents of our samples and the small currents we used (<100 mA) this condition ($I_0 > I_{sc}$) was satisfied over a very short period of time. When all slices have $T>T_c$ we have a set of normal resistors in parallel, with resistance varying according to their respective temperatures. In this case, the output voltage can be determined analytically.

Experimentally obtained resistance versus temperature data at different bias currents have been used in this simulation to determine the normal resistance. A set of simulated signals with varying fluence are shown in Fig. 4.4.2 (a). These correspond to a initial temperature of 70K and a bias current of 30 mA. The response time of the signal increased as the fluence decreased. The dependence of response time on temperature and the bias current is shown in Fig. 4.4.2 (b). The response time increases at lower temperatures and lower bias currents.

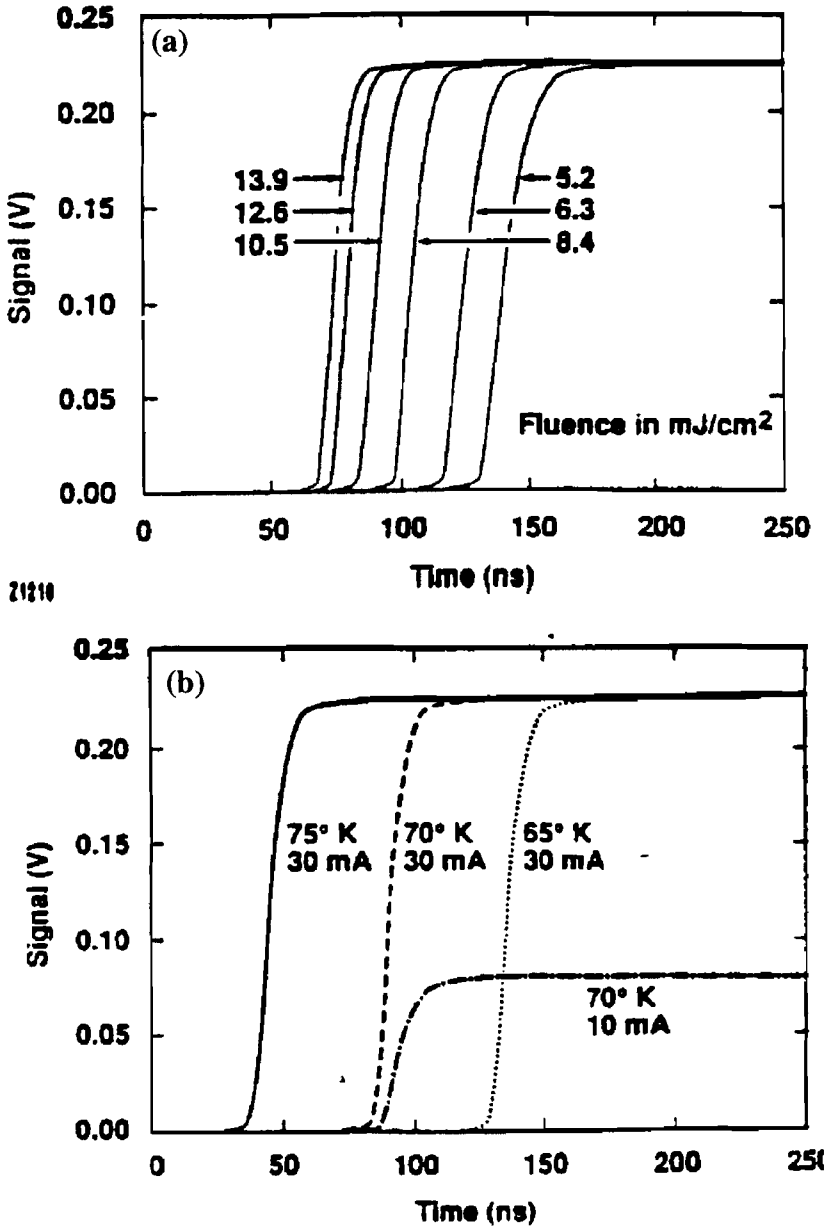

Figure 4.4.2 Simulated signals showing the variation of the response time. (a) response time increases with decreasing laser fluence, (b) response time increases for lower initial temperature and lower bias current.

In the simulation, uniform illumination across the switch at the mean intensity was assumed. Without this approximation, the simulation would have been extremely complicated involving solution of 3-D flow in anisotropic YBCO and a spatially varying resistance function. In the experiment, the central portion of the switch receives

more energy than the peripheral part and is expected to go normal while the edges of the switch are still superconducting. The time required for the temperature to exceed the critical temperature will be less than that calculated with the uniform illumination approximation at the center, and more at the edges. This can be conceived as a network of normal and superconducting resistors. Resistors in each layer form a mesh. The resistors representing the hot central part of the switch will offer normal resistance while the peripheral ones will be superconducting. Each node in a layer is connected to the corresponding nodes in the neighboring layers. This three dimensional network contains time-varying, nonlinear resistors and the analysis becomes complicated. However, a qualitative assessment of the effect of nonuniform illumination on the signal can be made. The response time of the switch will be reduced (by about 10%), since the central part goes normal before the "uniformly illuminated" film. It will also increase the thermal rise time (by about 25%, including the reduction of the response time) because the edge of the illuminated region goes normal after the central region of the film.

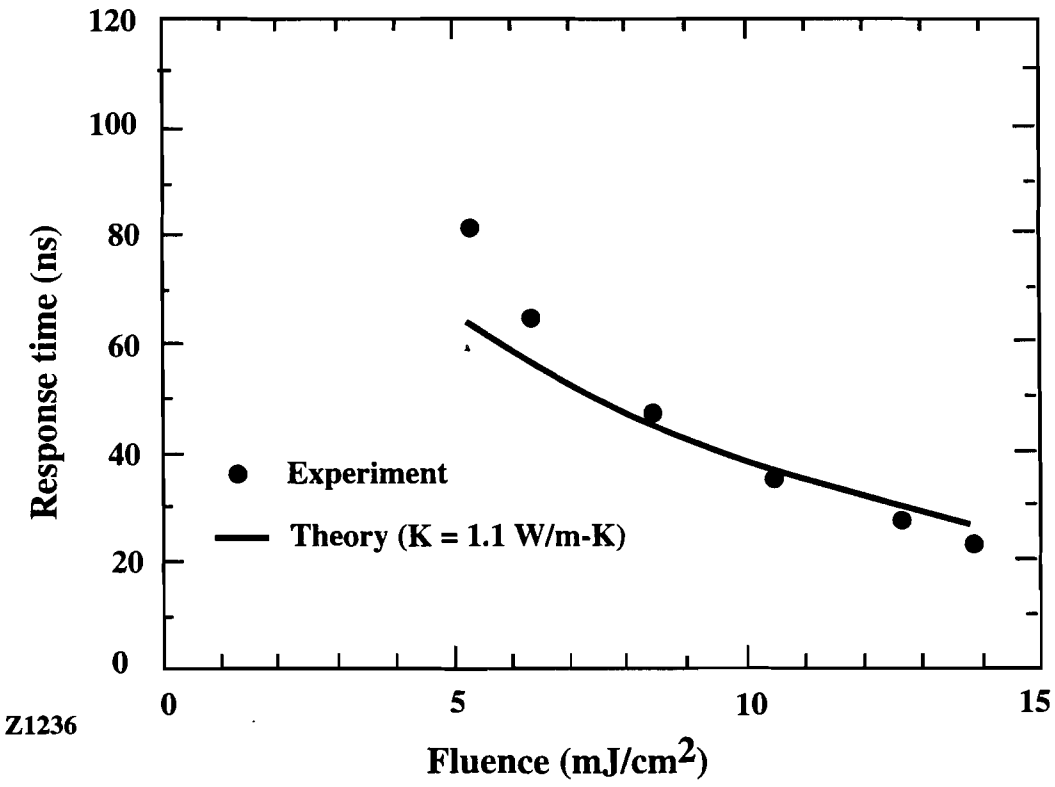

Figure 4.4.3 Thermal response time of the switch increases with decreasing fluence.

The experimentally obtained response times are plotted against the laser fluence, along with the response times calculated by our thermal simulation [Fig. 4.4.3]. The theoretical curve in Fig. 4.4.3 is calculated using the peak rather than the mean intensity of the Gaussian distribution. As mentioned above, the peak intensity at the center of the film determines the time at which the sample starts to go normal and, therefore, the response time. The calculated response time is a function of the thermal conductivity of the sample.

4.5 Discussion

The photoresponse of superconductors has been an active area in he recent years. The research in many cases have been motivated by the prospect of developing highly sensitive photodetectors over a very broad range of wavelengths. Both granular and epitaxial films of low and high-T_c materials have been studied. A sensitive optical detector using superconducting $BaPb_{0.7}Bi_{0.3}O_3$ thin films reported by Enomoto and Murakami[74] operating in the wavelength range of 1-8 μm exhibited a sensitivity of 10^4 V/W. This encouraged a number of groups to study the photoresponse of high-T_c thin films, since it also provides information regarding the underlying physical processes governing the superconducting state of these new-found materials. The research in this field encompasses a wide variety of superconducting materials and device structures, operating regimes and photon energies. While most of the work in the field of superconducting optoelectronics is focused towards photodetector[75-82] and fast mixer[83-86] applications, an optically activated photoresistive opening switch is another interesting application. Although the switch and the detector applications require different regimes of operation in terms of temperature, current density, and applied magnetic fields, the mechanisms involved are essentially the same.

The term bolometric photoresponse is reserved for a mechanism that involves a change of resistance of the material through heating. This is also called the equilibrium response because the superconducting material is assumed to remain in thermodynamic equilibrium. The bolometric response, for low fluence, is proportional to the slope of the resistance (R) vs. temperature (T) curve (dR/dT). When biased with a transport current, the bolometer would develop a voltage that can be measured to detect the incident radiation. A number of groups[87-89] have observed only this type of response.

All other mechanisms are usually referred to as nonbolometric or nonequilibrium effects. Nonbolometric responses have been observed by a number of groups and have been attributed to different phenomena. There is a lot of controversy regarding these nonequilibrium effects, especially because they often overlap and are difficult to resolve given the experimental constraints.

One such nonbolometric effect is the *hot-electron effect*[90-100]. As the name suggests, this indeed involves heating and is not fundamentally different from the bolometric mechanism. The incident photons break Cooper-pairs and impart their energy to the quasiparticles[7]. The energetic (or "hot") quasiparticles interact with other quasiparticles and lattice phonons. The quasiparticle interaction time (τ_{e-e}) is of the order of 100 fs, much shorter than the the electron-phonon relaxation time (τ_{e-ph}). The quasiparticles, therefore, reach an equilibrium distribution before they can react with the lattice. This allows decoupling of the electron subsystem from the lattice. The system can be thermally modeled as two subsystems, the quasiparticles and the lattice, with the electronic (C_{el}) and lattice (C_{ph}) specific heats (section 3.4) respectively, connected by a channel for heat conduction. The effective thermal conductance of the channel ($K_{e\text{-}ph}$) is related to the electron-phonon relaxation time (τ_{e-ph}) as

$$K_{e-ph} = d^2 C_{el} / \tau_{e-ph}, \tag{4.5-1}$$

where d is the thickness of the film. Like the resistive bolometric response described earlier, the resistance goes up due to electronic conduction and a voltage is observed across the device carrying a transport current. However, τ_{e-ph} is very short (~ps) and the two systems equilibriate unless the hot electrons can be extracted from the film before they can heat up the lattice. The dependence of the hot-electron response on temperature is different from that of the bolometric response.

Following electron-phonon interactions the excited quasiparticles lose their energy and recombine to form pairs through phonon emission. The system recovers as the phonons escape (~100 ps) from the film through the substrate. This process of recovery is often limited by the reflection of phonons back into the film due to an acoustic mismatch at the film-substrate interface.

The other prevalent effect is due to the change of kinetic inductance of the superconducting material[101-103]. The kinetic inductance is inversely proportional to the pair density, n_s (Eq. 3.3.3-13). Incident photons break pairs directly and indirectly through either equilibrium or nonequilibrium heating of excited quasipaticles and/or

---

[7]The terms electrons and quasiparticles have been interchangeably used to imply excitations.

phonons. This causes a rapid decrease in the pair density causing the kinetic inductance to rise sharply in time. The temporal change of kinetic inductance produces a voltage response,

$$V_{KI} = I_{bias}\, \partial L_{kin} / \partial t. \qquad (4.5\text{-}2)$$

There is a negative response during quasiparticle recombination as kinetic inductance decreases. Since the recombination process is slower, the magnitude of this negative response is much smaller.

All the above mechanisms, in spite of the nomenclature, are different manifestations of time-varying heating effects integrated over the entire volume of the superconductor. There is another mechanism, the photofluxonic effect[105-107], that takes into account absorption of individual photons. A photon impinging on the superconductor creates a local hot-spot and nucleates a fluxon-antifluxon pair. Under a current bias, the fluxon and the antifluxon accelerate in opposite directions due to the Lorentz force and produces a transverse voltage. This is a quantum detector analogous to semiconductors where an electron-hole pair, created by an incident photon, produce a photo-current under a voltage bias.

A number of groups studying granular films attribute the photoresponse to photon-assisted phase-slips at inter-granular (Josephson) junctions[74,108]. The granular films are viewed as an array of weak-links at grain boundaries. The junction responds to photons of energy comparable to the energy gap (see discussion in section 3.5) but for visible or near-IR photons the granular structure is irrelevant.

The results of nonbolometric photoresponses of YBCO thin films observed by a number of groups are summarized in Table 4.5.1. All these experiments were on high quality c-axis oriented epitaxial YBCO thin films.

The nonequilibrium dynamics in the superconductor following a pulsed optical excitation is complex due to the interaction between photons, pairs, quasiparticles, phonons and vortices. The interactions and associated times are listed below.

1) Pair breaking by photons : Photons break pairs generating high and low energy quasiparticles.

2) Excitation of low energy quasiparticles by photons.

3) Pair breaking by quasiparticles :The high energy quasiparticles break pairs generating more quasiparticles by resulting in an avalanche production (cascading) of quasiparticles. This is referred to as electron-electron (e-e) scattering. The time scale ($\tau_{e\text{-}e}$) is of the order of 100 fs.

4) Pair breaking by e-ph scattering : After the initial phase of cascading, it becomes energetically favourable for energetic quasiparticles (with energy greater than 2Δ) to thermalize through emission of optical phonons breaking additional pairs. This is referred to as electron-phonon scattering and the associated time constant ($\tau_{e\text{-}ph}$) is also of the order 1-10 ps.

5) Pair breaking by phonons : The energetic phonons also contribute by dissociating more pairs.

6) Phonon escape : Since the film is connected to a temperature bath through the substrate, phonons escape the superconductor through the substrate. The acoustic mismatch at the film-substrate interface causes reflection of phonons.

8) Quasiparticle recombination : As the incident optical energy is shared by quasiparticles, phonons and vortices and finally lost by phonon escape, the energy spectrum of the quasiparticles approach the equilibrium spectrum. The equilibrium is restored as quasiparticles recombine to form pairs. This process is also mediated by emission of phonons. The quasiparticle dynamics is governed by the Rothwarf-Taylor equations[109].

Table 4.5.1 Nature of nonbolometric photoresponse observed by different groups

Film thickness	Type of laser used	Speed	Origin	Reference
70 nm	0.63μm, 10 ps pulse	90 ps	hot-electron	Semenov[90]
150 nm	1.06μm, 150 ps pulse	1-10 ns	hot-electron	Frenkel[93]
20-200 nm	665 nm, 300-fs pulse	100 ps	hot-electron	Johnson[95]
70 nm	0.7-7 THz FIR pulses	120 ps	hot-electron	Nebosis[99]
30 nm	1.06μm, 1.5 ps pulse	30 ps	quasiparticle	Ghis[100]
30 nm	620 nm, 300 pulse	1-10 ns	kinetic inductance	Bluzer[101]
30-260 nm	532 nm, 100 ps pulse	500 ps	kinetic inductance	Hegmann[103]
100 nm	790 nm, 150 fs pulse	1.5 ps	kinetic inductance	Hegmann[104]
40 nm	pulsed YAG(1.06μm)	1 ns	photofluxonic effect	Culbertson[107]
90-200 nm	laser diode (827 nm)		vortex depinning	Yotsuya[110]
250-600 nm	chopped He-Ne (633nm)		photoinduced flux creep	Zeldov[111]
800 nm	1.06μm, 170 ps pulse	10 ns	?	this work

As we have seen in the previous section there were two distinct switching components in our experiment. While the slower response can be adequately explained using a thermal model, the origin of the faster component can not be understood clearly. The fast recovery (5-6 ns) of the faster component, followed by the secondary thermal rise, suggests that it is not associated with the energy redistribution in the film. Although a nonbolometric signal has been observed by many groups, to our knowledge, we are the only one to observe it in optically thick films. Johnson has even claimed that nonbolometric photoresponse can not be observed in optically thick films[95], which we believe is wrong.

The quasiparticle recombination time observed experimentally (τ_{exp}) is greater than the intrinsic recombination time (τ_r) due to phonon trapping. The smallest value of τ_r will occur if the phonon escapes without getting reflected from the film-substrate interface, and corresponds to the ratio of thickness to the velocity of sound. In our case this is approximately 100 ps. This is still rather small compared to the 10 ns time scale observed by us. However the quasiparticle relaxation is expected to be slower due to phonon trapping as we have mentioned earlier.

We derived an expression for kinetic inductance of a bridge in section 3.3. We rewrite Eq. 3.3.3-13 in terms of the plasma frequency,

$$L_{kin} = (\ell/wd)\mu_0\lambda^2 = (\ell/wd)\left(1/\varepsilon_0\omega_p^{*2}\right). \tag{4.5-3}$$

The electronic plasma frequency (ω_p) is related to the superelectron plasma frequency (ω_p^*) as

$$\omega_p^2 = \omega_p^{*2}\frac{n}{2n_s} = \omega_p^{*2}\frac{1}{f_s}. \tag{4.5-4}$$

The factor of 2 in the expression of fractional pair density ($f_s = 2n_s/n$) takes into account the fact that electrons are paired in the superconducting state. Substituting equation 4.5-4 in equation 4.5-3 gives us the following expression for the kinetic inductance:

$$L_{kin} = \frac{\ell}{wd}\frac{1}{\varepsilon_0\omega_p^2}\frac{1}{f_s} \tag{4.5-5}$$

For a given bias current (I), the voltage (V) due to a change in kinetic inductance can be calculated using equation 4.5-5 as

$$V = I\frac{\Delta L_{kin}}{\Delta t} = \frac{I}{\Delta t}\frac{\ell}{wd}\frac{1}{\varepsilon_0\omega_p^2}\left(\frac{1}{f_s^{final}} - \frac{1}{f_s^{initial}}\right) \tag{4.5-6}$$

In our case, ℓ = 2 mm, w =100 μm, d = 800 nm, I=100 mA and Δt = 170 ps (the laser pulse width). ω_p has been measured to be 1.67 x 10^{15} s^{-1}[103]. If we assume that the fractional pair density is 1 initially and decreases to 0.5 during this time, from equation 4.5-6, V= 596 μV. If we assume that f_s^{final} is 0.9 instead, V = 66μV. Alternatively, we can use equation 3.3.3-13 and use change in penetration depth to calculate this voltage. The functional temperature dependence of penetration depth λ is given by,

$$\lambda(T) = \lambda_0/\sqrt{1-(T/T_c)^4} \tag{4.5-7}$$

where λ_0 is the zero temperature penetration depth. Taking T = 70 K, T_c = 84 K and λ_0= 200 nm, we get λ(T=70) = 278 nm. The voltage can be expressed as,

$$V_{kin} = I\frac{\Delta L_{kin}}{\Delta t} \approx \frac{I}{\Delta t}\frac{\ell}{wd}\mu_0\lambda_0^2 \qquad (4.5\text{-}8)$$

Using the same values of ℓ, w, d, I, and Δt we obtain V_{kin} = 739 μV. These value are three orders of magnitude smaller than the fast component we have observed. As we have discussed earlier in this section heat propagation in the films take several tens of nanoseconds before the whole film is normal. Therefore, the assumption made in the calculation of the kinetic inductance effect for heating of the film in the time interval of 170 ps is not correct. The above calculation implies that the bolometric kinetic inductance effect would not account for the fast component observed by us.

However, the observed voltage might arise from an inductive change due to current redistribution in the H-structure of the switch. The current in the switch structure flows through the bridge and also at the top electrodes [Fig. 4.5.1(a)]. The current can be equivalently expressed as the sum of current loops S at the electrodes and a component directly through the bridge [Fig. 4.5.1(b)]. When the laser irradiates the bridge and the surrounding parts [Fig. 4.2.1 and Fig. 4.5.1(c)], the current redistributes itself taking the path of least resistance, as shown in Fig. 4.5.1(c). This redistribution allows flux to move in, causing the inductance to change, and gives rise to a voltage between the top electrodes. The magnitude of the fast response is about 1 V for a current of 100 mA [Fig. 4.3.3] and the rise time is approximately 4 ns. The equivalent change in inductance (ΔL) is given by,

$$V = I\frac{\Delta L}{\Delta t}, \qquad (4.5\text{-}9)$$

which gives a value of 2.5 nH. From Fig. 5.1.1(c), the effective change of the inductance is of the order of the inductance of the loop (S) at the top electrodes. The loop S is approximately a square with sides, a = 2mm. The inductance therefore is of the order of μ_0a, or 2.4 nH. This seems to agree well with the inductance required for the observed response. As for the response time, it would be of the order of L/R, that corresponds to a resistance, $R \sim 0.6\Omega$, for the flux to cross. This also seems quite reasonable. It would be possible to test this hypothesis by screening the contact region from the laser light, but this was not pursued. The apparent absence of a delay time in the data seems somewhat perplexing, but it is possible that the initial heating reduces the critical current enough for flux flow to occur.

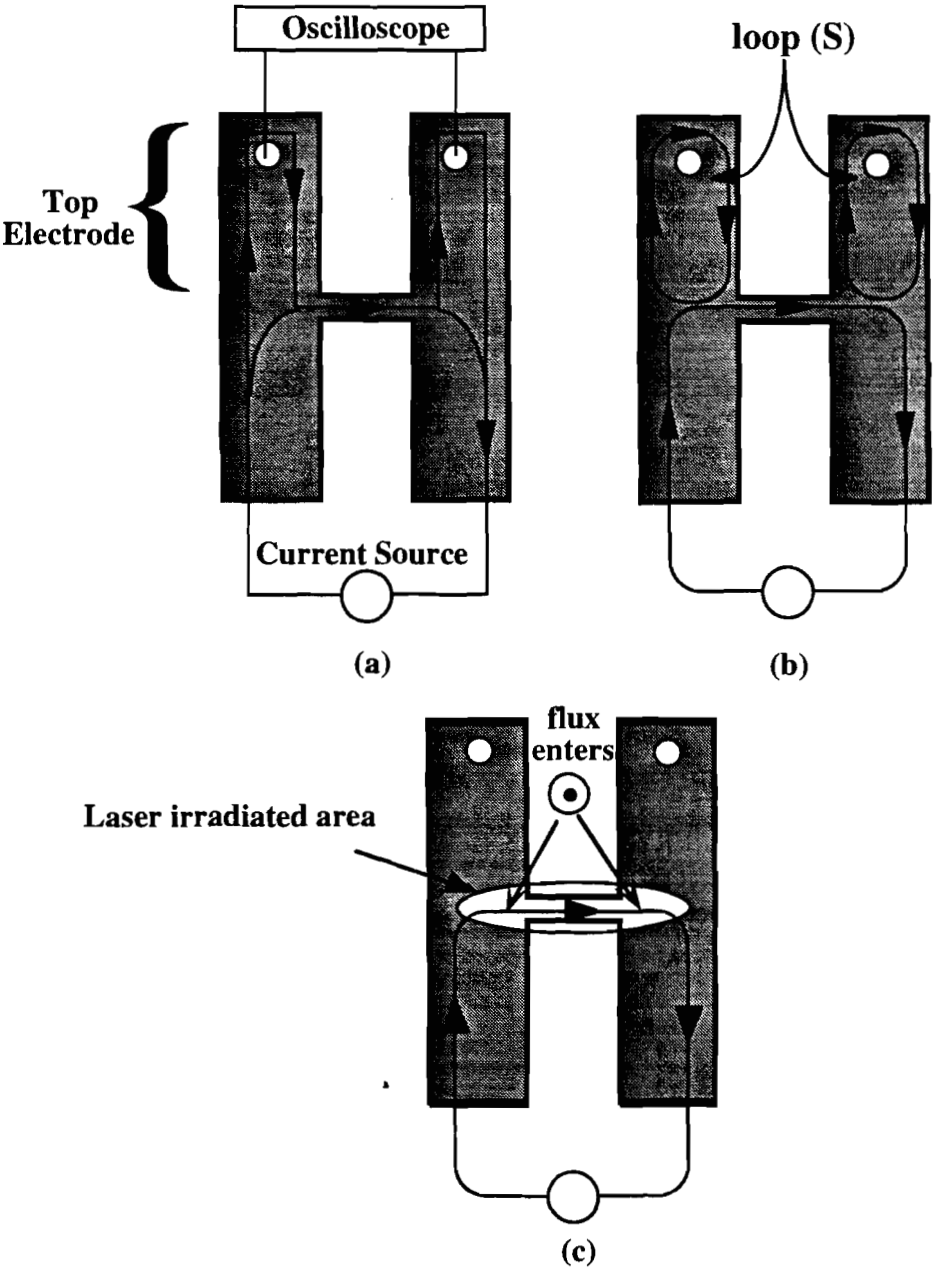

Figure 4.5.1 Current redistribution in electrodes. (a) Before optical illumination some current flows through the top electrodes. (b) The current distribution in (a) can be decomposed into loops (S) at the top electrodes and a branch through the bridge. (c) When the bridge and the adjacent parts of the H-structure become resistive, the current in the structure will redistribute. The current in the loops decay allowing flux entry.

4.6 Scaling the photoresistive switch up to higher current

In the experiments described in section 4.2, we illuminated a small bridge to verify the photoresistive effect. To scale up to higher currents we need a switch of larger area. The installation of a flashlamp pumped Nd:YAG amplifier (Appendix 4, section A4.2.3) enabled us to irradiate a larger region with better uniformity. A new design was developed as a part of a summer high school research project[112].

The new design is shown in Fig. 4.6.1. The switch is made with a 500-nm thick 1 cm^2 YBCO film on $LaAlO_3$. Two silver contact pads (3 mm X 1 cm) were evaporated and annealed, leaving a 4 mm long, 1 cm wide exposed region at the center to act as the switch. Two 1-in diameter cylindrical copper pieces served as the sample holder. The top surfaces of these two pieces are machined flat. The film is placed between the sample holders with the contact pads resting on the flattened surface. A copper clamp is used to make pressed contact between the pads and the copper sample holder. Thin indium foils are inserted between the copper surface and the silver pad for better contact.

The sample holders have a central hole. Two 0.25-in hollow copper tubes are welded to each sample holder. These serve as current leads as well as liquid cryogen feedthroughs. A plastic spacer between the copper plates provide a continous cryogen flow-path while electrically isolating the two plates. Three nichrome rods are inserted symmetrically and serve as low resistance shunts across the switch.

The sample is placed in a vacuum chamber with optical access. A 100 A current source is connected to the copper current leads. The voltage is also measured across the lead with a digitizing oscilloscope. Either liquid helium or nitrogen is used to cool the switch. For this arrangement, the laser shines through the substrate.

When the switch is in its superconducting state, the current flows through it from one copper plate to the other. When the laser pulse triggers a transition to the normal state the current is diverted to the shunt resistors, and a voltage is observed. Since we wanted to maximize the current capacity for the given film size we were forced to choose a low resistance geometry. We needed low resistance shunts to protect the switch. These films had a sheet resistance of 6 Ω/sq at room temperature, and

therefore a normal state resistance of about 2.4 Ω at room temperature, and about 1 Ω just above the transition. Each nichrome rod (0.4 cm long) has a resistance of 1.8 mΩ (at 77K) giving a combined resistance of 0.4 mΩ. The total contact resistance was measured to be 0.8 mΩ, giving 0.4 mΩ for each Ag contact pad.

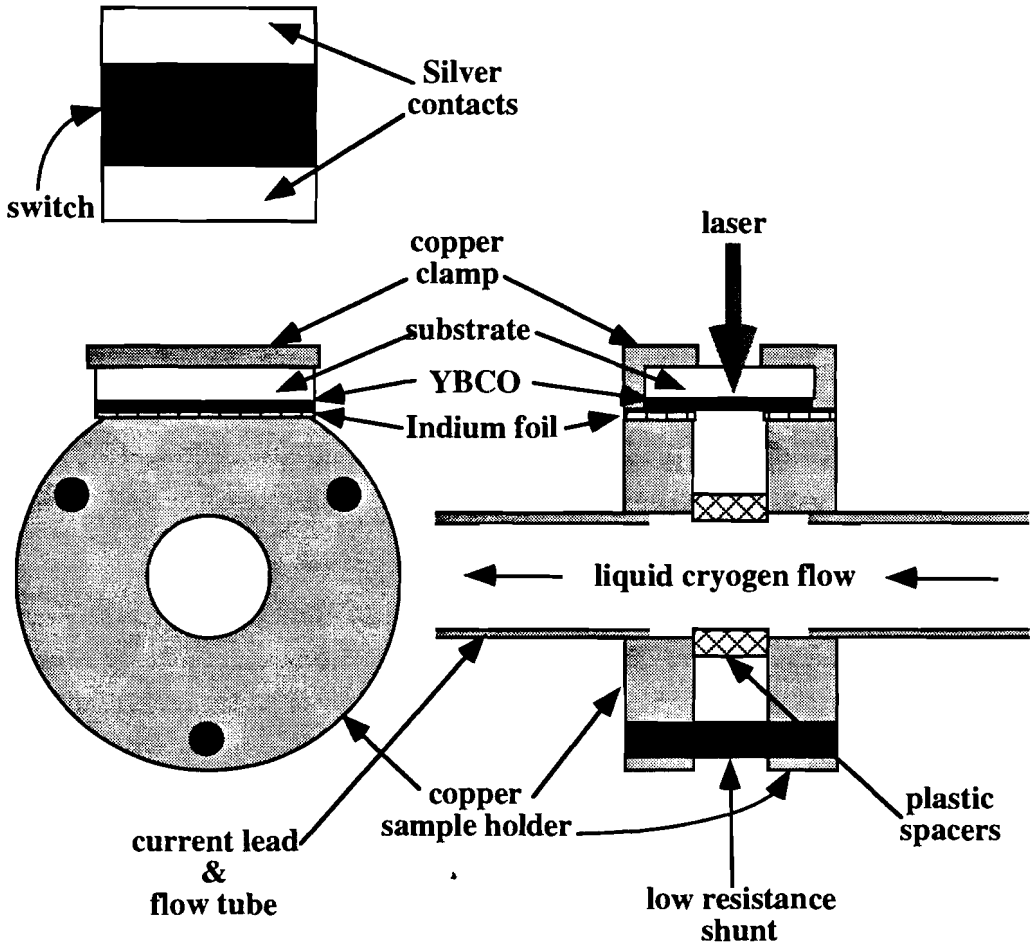

Figure 4.6.1 New design of high current switch.

We tested the switch to currents up to 40 A at 80 K and 80 A at 20 K. These correspond to a current density of 0.8 MA/cm^2 and 1.6 MA/cm^2 respectively. The resistive response has a slow exponential tail with a time constant of 200-300 ns and has an overlapping inductive response (10-20 ns) from current redistribution to the Nichrome rods. The preliminary results are encouraging, but several issues involving optimizing the shunt resistance and electromagnetic screening will have to be resolved.

4.7 Disadvantages of the photoresistive switch design : Motivation for a contactless switch

The main problem with the photoresistive switch is the electrical contact between the superconductor and the rest of the circuit. The main advantage of a superconducting opening switch (chapter 2) is the zero closed state resistance. However, the contact resistance between the film and the contact pads is in series with the switch. If the contact resistance is large, not only does it produce a non-zero resistance, but also generates a lot of heat because of the large currents that the switch is required to carry. This is a serious drawback since obtaining large area, low resistance metallic contacts to YBCO is difficult. Even with a contact resistance of 1 mΩ, for a 100 A switch the joule heating is 10 W.

The contact problem poses a fundamental limitation on high current switching, and prevents us from exploiting the large critical current of the superconductor. Anticipating such problems, we decided to explore the possibility of a contactless switch. The inductive switch, described in chapter 5, solves this problem.

Although for our low current (< 100 mA) experiments the contact resistance was not large enough to cause the switch to fail, the aluminum wire bonds used to connect the pads failed frequently. The wire bonds are also mechanically unstable and made sample mounting a tedious process. These problems could also be eliminated by designing a contactless switch. However, with the new high current design (section 4.6) the problem with wire bonds does not arise. Finally, the contactless switch does not require patterning of the film.

CHAPTER 5

SUPERCONDUCTING INDUCTIVELY COUPLED SWITCH

5.1 Principle of Operation

While both the photoresistive switch and the inductively coupled switch perform the action of an opening switch, the principles of their operation are entirely different. The photoresistive switch is a *current diverter*. It diverts previously shunted current into the load during its resistive ("open") state. On the other hand, the contactless inductively coupled switch acts a *flux diverter*. It diverts previously screened magnetic flux in the load circuit.

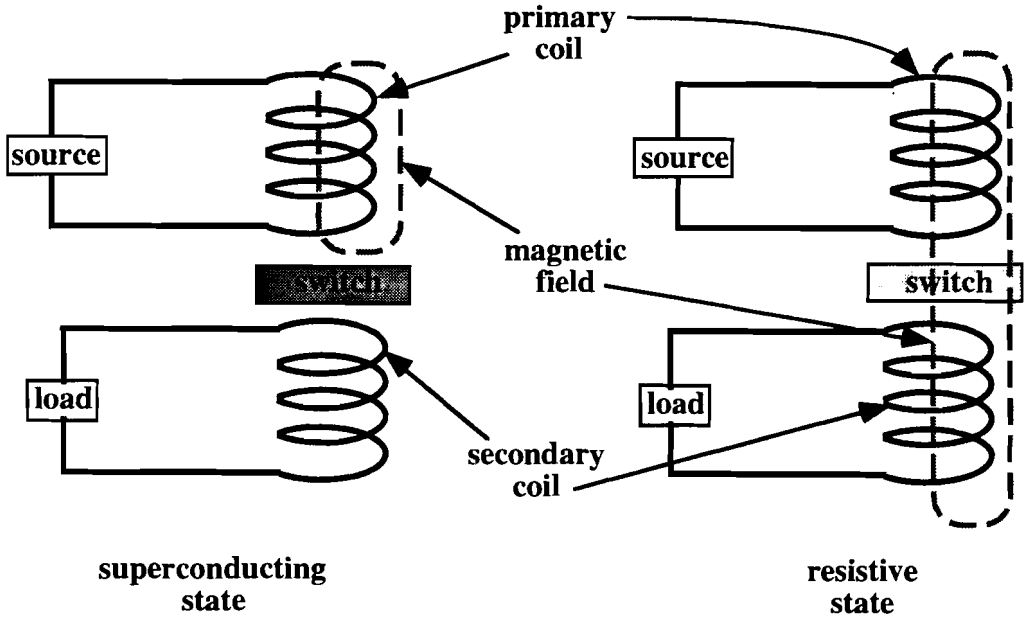

Figure 5.1.1 Operation of the inductively-coupled switch. In the superconducting state the switch screens the primary and the secondary coil. The magnetic field produced in the primary coil by the source current gets coupled into the secondary when the switch goes to a resistive state.

In its simplest form, the switch consists of a superconducting material placed between the primary and the secondary coils of a transformer (Fig. 5.1.1). A current source drives current in the primary coil, producing a magnetic field. While the switch is superconducting, it screens the magnetic flux and there is no flux-coupling between the two coils. If a load is connected across the secondary coil, the voltage across the load would be zero. Under illumination by a laser pulse, the film makes a transition to the resistive state and the screening currents decay, allowing magnetic flux produced by the primary current to couple into the secondary. The temporal change of flux coupling

(Φ) through the secondary coil results in an induced voltage ($V = -\partial\Phi/\partial t$) pulse across the load. Since the superconducting material acts as a flux screen, a high temperature cuprate material (like YBCO) with a high upper critical field (H_{c2}) is ideally suited for the inductive switch.

There are three components of the switching system : (i) the source (the primary coil in our discussion), (ii) the switch (the superconducting film) and (iii) the load circuit (the secondary coil and load). In an application such as energy extraction from a superconducting magnetic energy storage system (SMES), the source will be a superconducting magnet. The switch will be a superconducting flux screen of appropriate size, and the load circuit will consist of a coil connected to a load (typically resistive or capacitive).

The different components are not in physical contact and can be at different temperatures. For the example above, the source or the magnet may be operated at liquid helium temperature (4K) while the superconducting film may be at liquid nitrogen temperature (77K) and the load circuit at room temperature.

A major advantage of this configuration is the absence of any electrical contacts to the film. In contrast to the photoresistive switch (chapter 4), the inductive switch does not require any electrical contacts to the film. A major limitation regarding high current operation of such a photoresistive switch is imposed by the metallic contacts to the superconducting bridge. This limitation prevents us from utilizing the full current carrying capacity of the superconductor.

Fast heating of the film is necessary to perform the switching, and this is accomplished by irradiating the film with laser pulses. The scheme used for this design is essentially the same as the photoresistive switch. Optical triggering also provides accurate timing.[1]

We have seen in section 3.3 how superconductors expel and exclude magnetic flux. In type II superconductors such as YBCO, there exists a lower critical field (H_{c1})

---

[1]The accurate timing control using the laser triggering can be used for synchronization of multiple switches. Please see discussion in section 5.5.

and an upper critical field (H_{c2}). When the applied field, H_{app}, is smaller than the lower critical field, H_{c1}, the superconductor is in the Meissner state and the flux is initially excluded completely[2]. The flux penetrates the film following laser irradiation and is expelled again as the film regains its superconducting state. The operation in this situation is reversible and the switching can be repetitive.

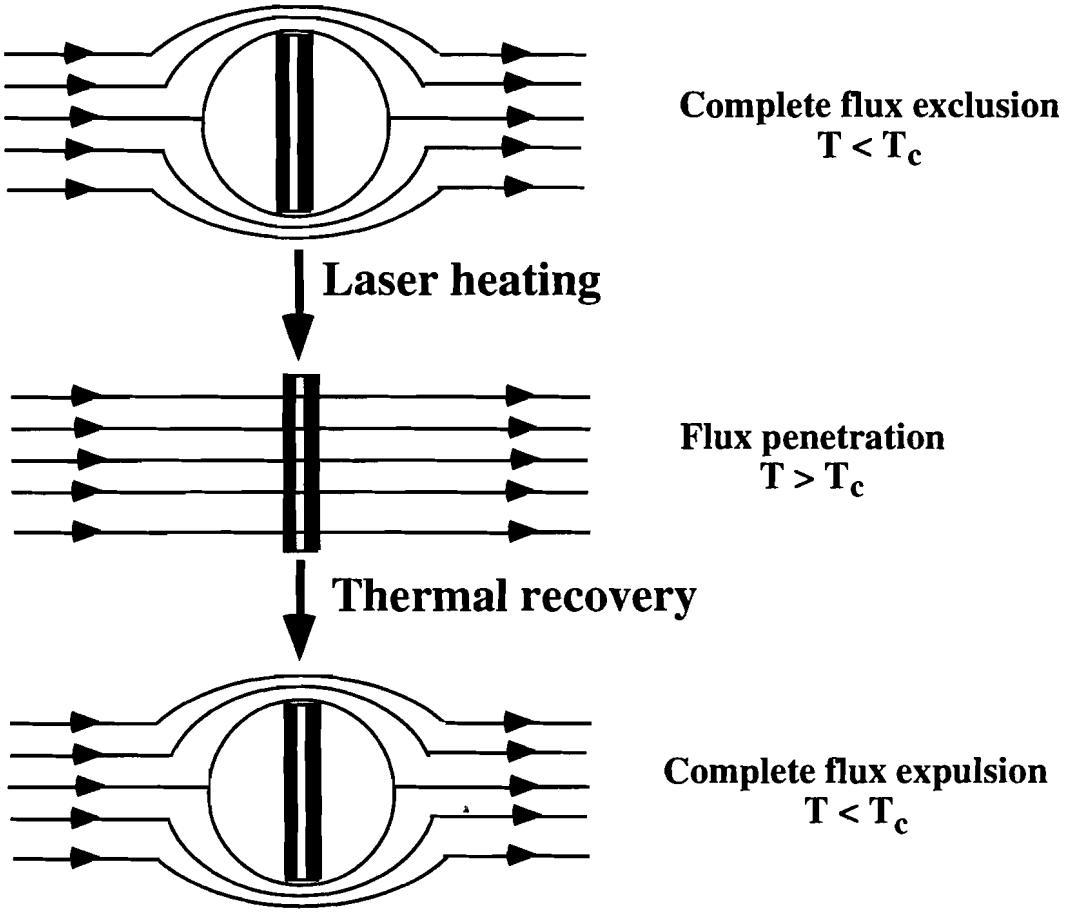

Figure 5.1.2 Flux exclusion and expulsion in the reversible (Meissner) regime for $H_{app} < H_{c1}$

[2]However see the discussion on demagnetization effects in section 3.3.5.

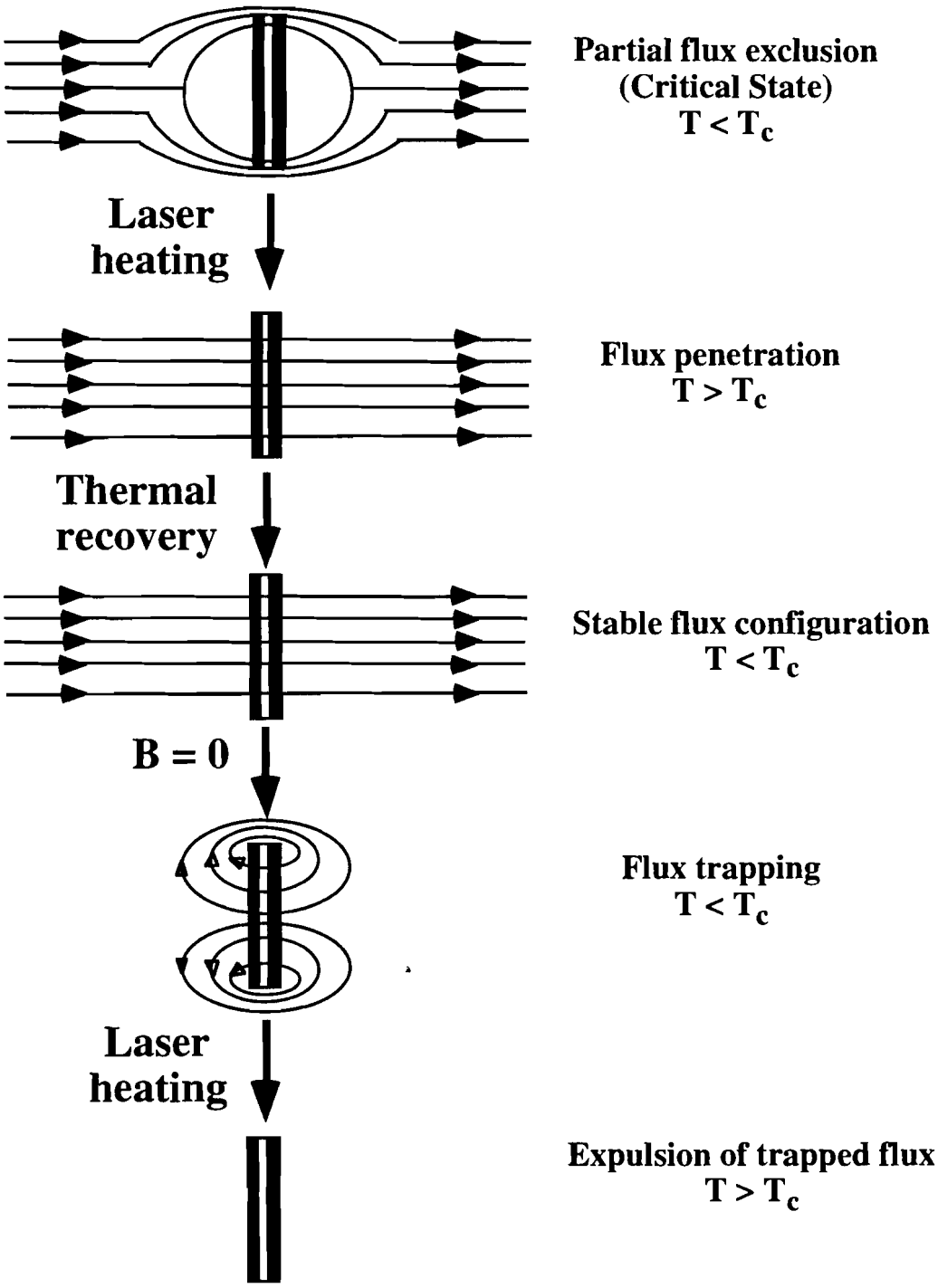

Figure 5.1.3 In the irreversible regime, $H_{c1} \leq H_{app} \leq H_{c2}$, the initially excluded flux is trapped once it penetrates the film.

However, for $H_{c1} \leq H_{app} \leq H_{c2}$, there is partial flux exclusion due to pinning (section 3.3.7). This is the critical state. When the flux penetrates the superconductor following a laser trigger, it reaches a stable configuration and subsequent cooling of the film in a magnetic field will not expel the flux. This will prevent the switch from operating repetitively. However, for certain applications a single-shot operation may be sufficient, and in that case an HTS switch can be operated in fields close to the effective screening field determined by the critical current density of the film. To reset the switch the trapped flux is expelled by turning off the external field and heating the film above T_c (e.g., by another laser pulse). Figures 5.1.2 and 5.1.3 show the operations in the Meissner state and the critical state respectively.

In the preliminary experiments done at low fields ($<H_{c1}$) the switch operation was indeed repetitive. Using a superconducting magnet to generate fields higher than H_{c1} we have found that the switch only operates in the single shot mode as expected.

We have found no evidence that the superconducting film degrades with repeated operation. The switches in our experiments have been triggered by 150-ps pulses from a Nd:YAG laser at repetition rates up to 1 kHz. In principle, high repetition rates are limited by the thermal recovery time of the switch[3]. However the time for the heat to escape (through the substrate) is of the order of 1μs. In our experiments the repetition rate was limited by that of the laser amplifier[4].

---

[3]Since the load voltage of the inductively coupled switch is the derivative of flux coupling, the width of the voltage pulse is much shorter than the thermal recovery time.

[4]In cases where a flash-lamp pumped laser amplifier is used to further amplify the output of the regenerative amplifier, the maximum repetition rate is only 4Hz. The regenerative amplifier itself can be operated up to a few kHz repetition rates.

5.2 Experimental Results in low magnetic field

In the preliminary experiments described in this section we have confirmed the inductively coupled switching. Thin YBCO films (thicknesses varying from 500 to 800 nm) were deposited on heated MgO substrates (1 cm x 1 cm) by rf magnetron sputtering. The films have $T_c > 85$ K and $J_c > 1MA/cm^2$ at 77K. We have used identical copper coils as the primary and secondary coils of the configuration described in the previous section [Fig. 5.2.1]. To enhance mutual inductance the flat, washer-shaped coil geometry was used. Typically a 100-turns coil had an inside diameter of 3 mm, an outside diameter of 6 mm and an inductance of 50 μH.

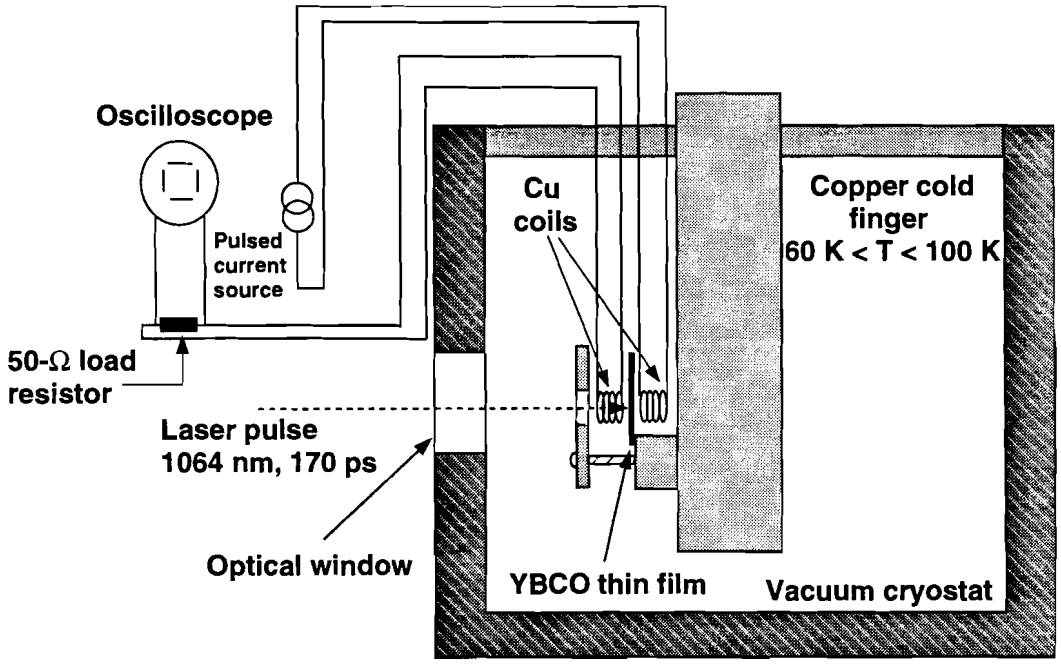

Figure 5.2.1 Experimental set-up for the inductive switch.

The switch was placed inside an optical access cryostat (the same as the one used for photoresistive switch, section 4.1.2). It was irradiated with light from a mode-locked Nd:YAG laser (1.064 μm). The sample holder consists of a copper block with a circular hole of 8mm, a thinner, matching copper plate [Fig. 5.2.2] with a similar hole, a copper plate connecting the assembly to the cold finger and another copper plate connected to the block hosting the heater resistor. The thermometer (Si diode) is

mounted on the block. Holes on either side of the sample (consisting of the film and the coils) provided optical access from either side.

We experimented with various coil geometries. First, a solenoid wound around thin glass tubes was tried. The mutual inductance between the two coils falls off rapidly with increasing distance. The mutual inductance coefficient ($\kappa = M^2/L_1 L_2$) in this configuration was low ($\kappa \approx 0.01 - 0.02$). Moreover, it was difficult to maintain the alignment of the two coils strictly vertical to the plane of the film, which is necessary for laser illumination.

To improve the mutual inductance we decided to use flat washer shaped coils (pancake coils[113]) [Fig. 5.2.2] made from 40G and 46G insulated copper wire coated with rubber cement. To prevent the films from getting scratched by the coil a thin (12μm) sheet of Teflon™ was used between the film and the coil and the whole assembly was clamped tightly together. The mutual inductance coefficient in some cases were as high as 0.4, though typically it was around 0.2. The mutual inductance was first measured using an LCR meter at room temperature. The coils were then placed inside the cryostat separated by a substrate (without a superconducting film) and cooled down. The mutual inductance was then measured by applying a sinusoidal voltage of frequency up to 1 MHz across one of the coils while measuring the voltage across the other one.

Flux screening was tested using a sinusoidal current in the primary. As the film was cooled through the superconducting transition temperature (T_c) the flux coupling between the coils reduced by more than 95 % of the coupling above T_c within 1-2K below the onset of transition.

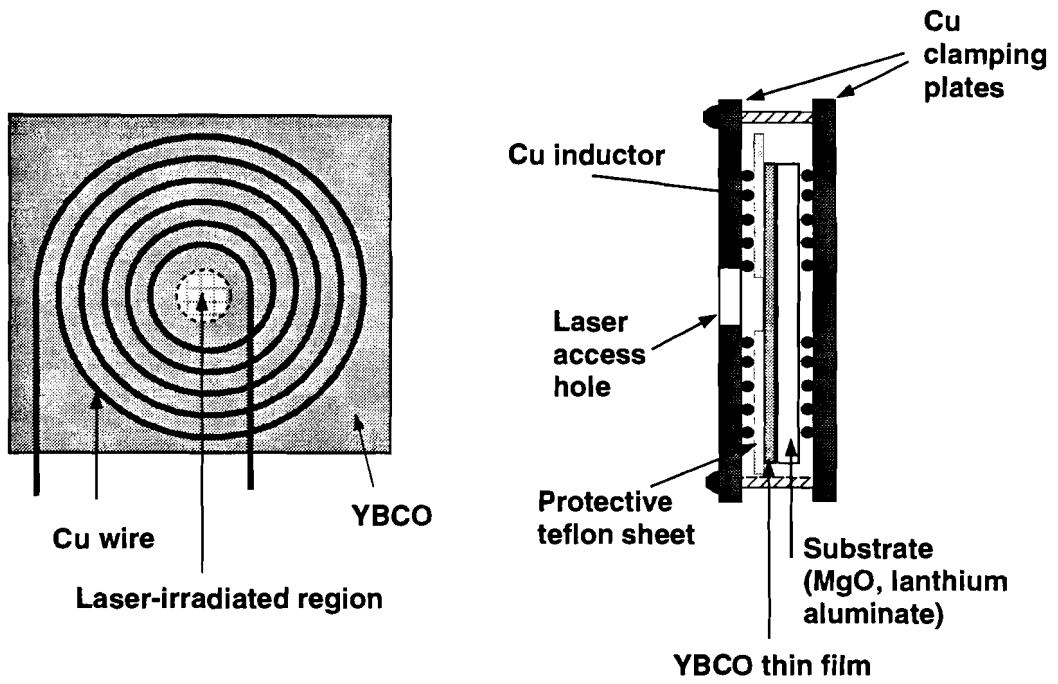

Figure 5.2.2 The inductive switch configuration showing the use of pancake coils as the primary and secondary coils and the sample holder.

The switching was tested using 5-μs current pulses at low duty cycle, instead of dc, to avoid joule heating in the primary coil. The current pulse was synchronized with the laser pulse such that each laser pulse arrives at the center of a current pulse. The primary current pulse is long enough so that the optical effects take place during a time when the primary coil produces a constant (dc) flux. The current pulse also produces a positive and a negative voltage pulse across the secondary load corresponding to its leading and trailing edges. Above T_c, these voltage pulses indicate the amount of flux coupling to the secondary coil and can be used to compare with the optical response. As the film was cooled below T_c and irradiated with laser pulses a voltage pulse was observed at the load. The amplitude of this voltage pulse varied with laser fluence (Fig. 5.2.3). The voltage pulse occurring at the laser trigger shows a transition of the film from the superconducting to the normal state by optical heating, allowing the flux produced by the primary coil to couple to the secondary coil.

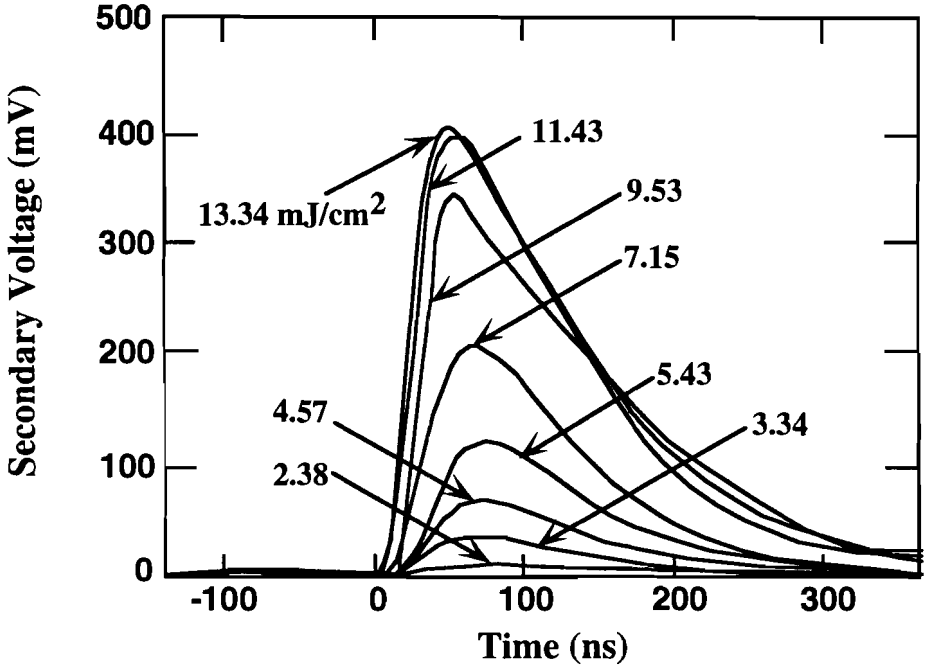

Figure 5.2.3 Photoinduced switching observed in the inductively coupled switch of Fig.5.2.1 showing induced voltage in the secondary coil for varying fluence at 76 K. The laser trigger occurs at t =0.

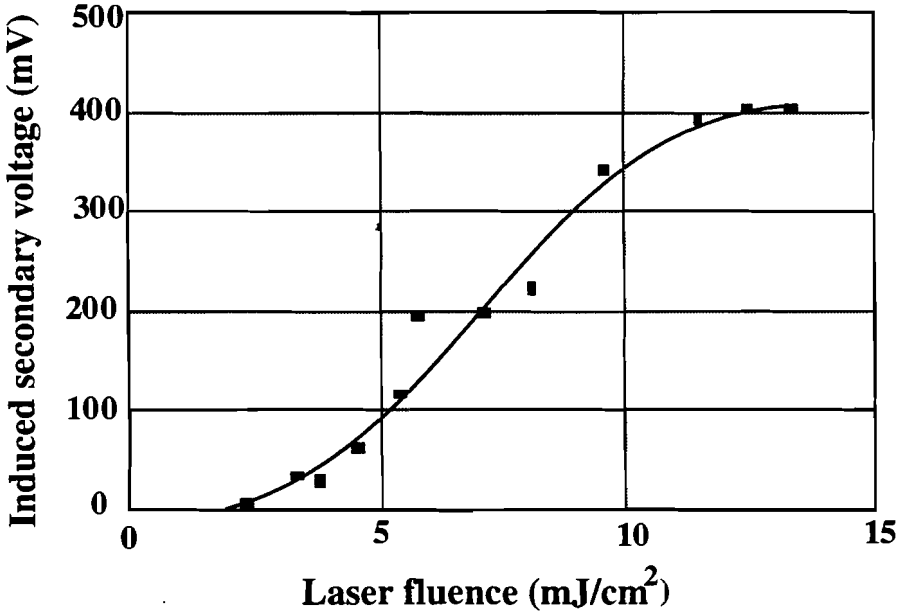

Figure 5.2.4 Peak of the photoinduced secondary voltage as a function of laser fluence. Saturation above 12 mJ/cm^2 indicates complete transition of the film to the normal state under optical illumination. The line is a guide to the eye.

5.3 Experimental Results in high magnetic field with a multi-turn secondary coil

For the high field experiments the primary coil was a superconducting magnet [Fig. 5.3.2.1]. The magnet used in our experiment is a Nb-Ti solenoid cooled by liquid helium. The magnet is rated at 100A and a maximum field of 4T.

5.3.1 The magnet system

The magnet (American Magnetics Inc., 1976) is housed in a liquid helium dewar (Janis Research Systems). The magnet dewar consists of a liquid helium chamber surrounded by two shields enclosed in vacuum. The space between the two shields is filled by super-insulation. The inner and outer shields are connected to the second and first stages of a two stage expander (APD Cryogenics: Model DE202) respectively. The expander is driven by the Model HE-4 compressor. The typical temperatures attained using the compressor alone are 100 K on the outer shield and 50 K on the inner shield. The magnet has a horizontal warm bore of length 22 inches and diameter 4.75 inches. We designed (Appendix 5) a liquid nitrogen/helium flow optical access cryostat to fit inside the warm bore of the magnet.

The magnet is charged using 100 A He-vapor cooled current leads. The charging and discharging of the magnet is controlled by a current source programmer (American Magnetics, Model 411). The current source used to charge the magnet is rated at 100 A and 10 V(Sorensen: Model SRL10-100). The magnet inductance is of the order of 10 H. The current ramp rate while charging ($\frac{dI}{dt} = \frac{V}{L}$) is therefore limited[5] to 1 A/s. The minimum ramp rate available with the programmer is 0.01 A/s. An energy absorber (American Magnetics Inc. : Model 600) is placed in series with the charging circuit so that in the unlikely event of a quench the energy will be dumped into this series resistor.

---

[5]The 0.1A/s setting should be chosen on the current source programmer. The ramp rate can be varied by adjusting the multiplier dial.

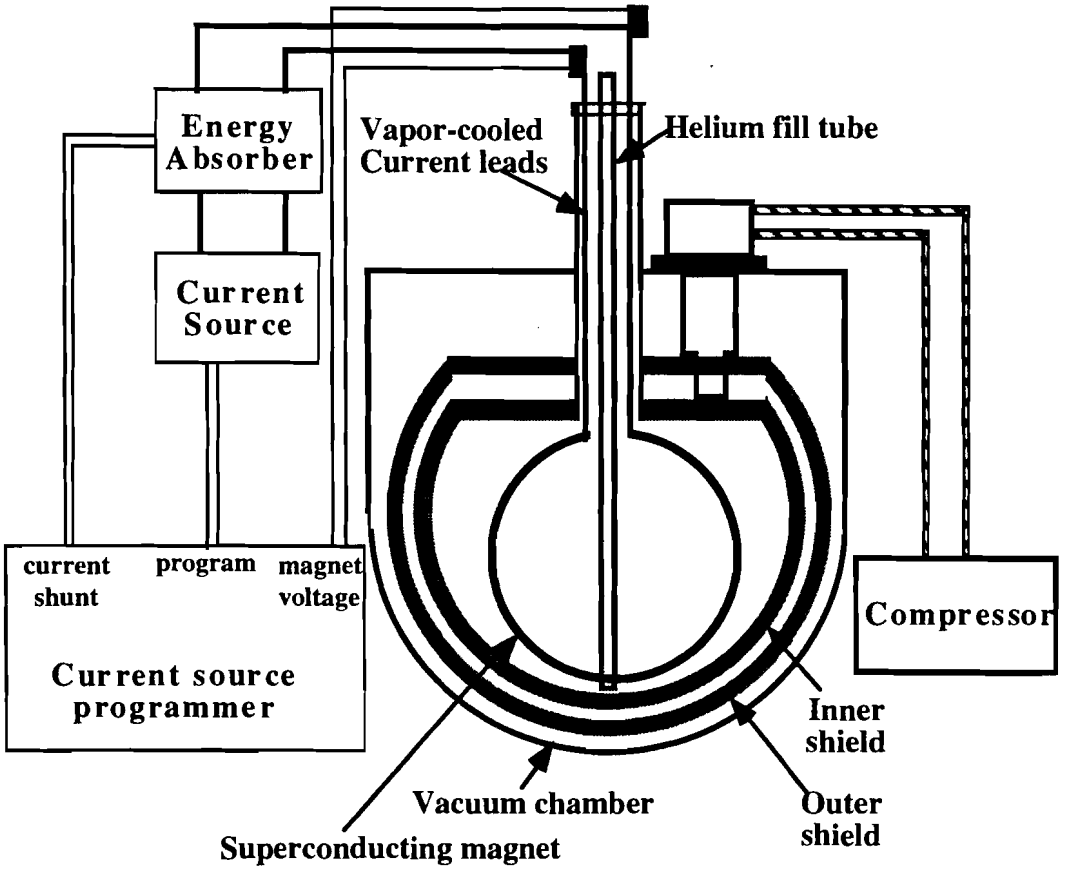

Figure 5.3.1.1 The superconducting magnet system. The inner and outer shields are cooled by the two cooling stages of a closed cycle helium refrigerator.

5.3.2 The flow cryostat and the sample holder

The flow cryostat can be used with both liquid nitrogen and helium. There are optical windows (with anti-reflection coating) on either side. A double-walled liquid feedthrough is designed to maintain vacuum in the cryostat. The liquid enters through the inner tube and cools a copper end plate, that is also used as a sample holder. It returns through the outer tube and vents outside.

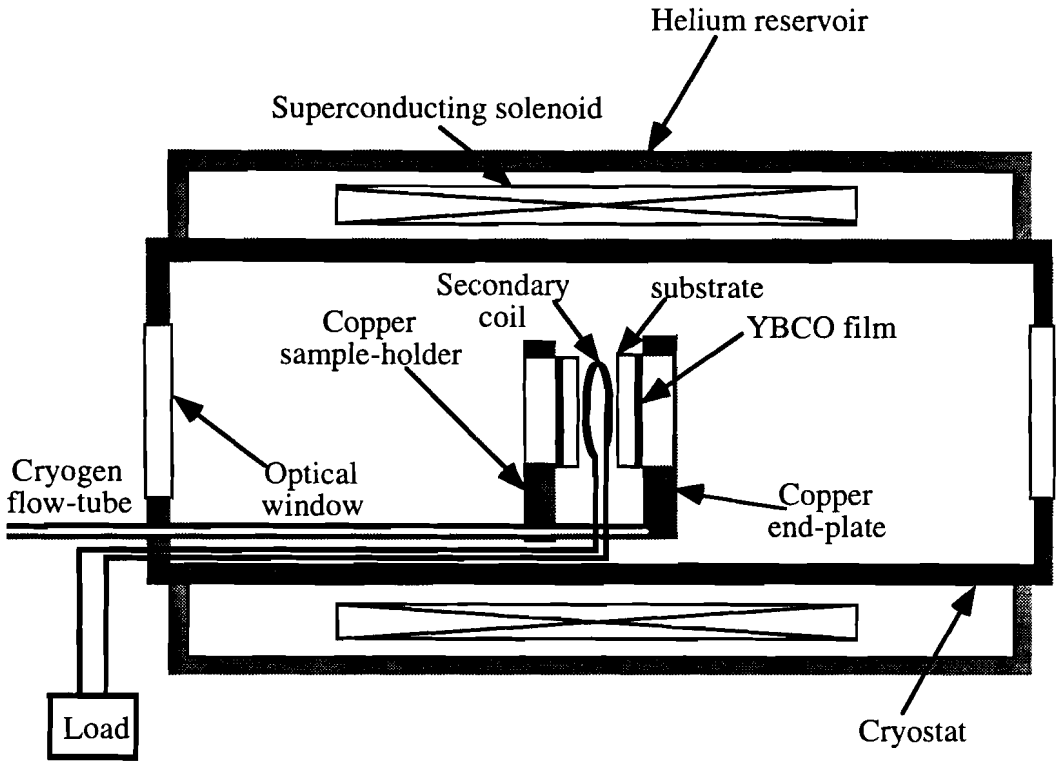

Figure 5.3.2.1 The high field experiments are performed with a superconducting magnet acting as the primary coil. The switch is placed inside a cryostat cooled by liquid nitrogen/helium.

The sample holder consists of two circular copper disks (dia. 2 inches) with square windows (1cm X 1cm).The films, placed on either side of the secondary coil, are supported by the copper disks. The YBCO films used in this experiment were[6] 500-600 nm thick on $LaAlO_3$ substrates. Platinum resistance thermometers were mounted on one of the copper sample holders next to the film. These thermometers have less than 0.01% error in fields up to 5 T and are preferred over silicon diodes used in the earlier experiments. Fig. 5.3.2.1 shows a schematic drawing of the cryostat and the magnet.

The copper secondary coil was wound around a circular alumina disk (thickness 2mm, diameter 5mm) and impregnated with insulating dope to protect it from electrical breakdown. The coil was then placed inside a custom-made circular hole in a 2mm

---

[6]Some these samples were laser-deposited YBCO/$LaAlO_3$ films purchased from NEOCERA, a commercial manufacturer of thin films.

thick piece of Teflon™ and fixed in place using epoxy resin. The Teflon piece was used to ensure a flat surface for the film to be supported against. This precaution is necessary because of the magnetic force on the film when the magnet is charged. In our sample configuration the magnetic field is axial and perpendicular to the surface of the film. For this configuration the film is in unstable equilibrium and will not experience a torque. If, however, the film alignment deviates from the vertical it will experience a torque which will tend to rotate the film by 90 degrees [Fig. 5.3.2], a position of stable equilibrium, and crack it. The torque can be estimated as follows,

$$\text{Torque}(\mathbf{T}) = \text{magnetic moment } (\mathbf{m}) \times \mathbf{B}$$

For B = 4T and a sample volume of 1 cm^3, the torque can be estimated as 12.7 N-m.

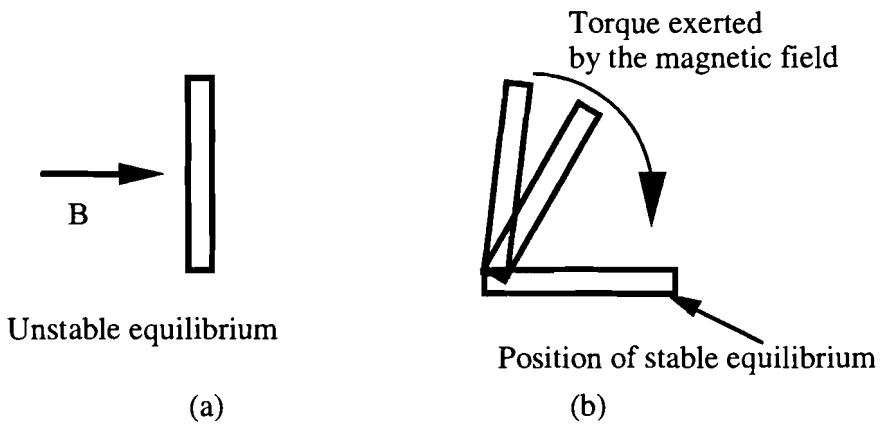

Figure 5.3.2.2 Torque on the film due to perpendicular magnetic field. (a) When the film surface is perpendicular to the B-field the film is in unstable equilibrium and does not experience a torque. (b) If the initial position of the film deviates from the vertical the film will have a tendency to rotate.

5.3.3 The laser system and data acquisition

A Nd:YAG laser beam (λ = 1064 nm) was used to illuminate the films from either side through a splitter arrangement [Fig. 5.3.3.2]. The YAG oscillator produces a train of 150-ps mode-locked pulses separated by 12-ns. This pulse train is injected into the regenerative amplifier through an optical fiber. A single pulse is chosen for

amplification by applying a suitable high-voltage on a Pockels cell[7]. The energy of the pulse is amplified to 250μJ. Illumination of both films required an energy level ranging from 5-20 mJ. Therefore a double-pass flashlamp-pumped YAG amplifier was used to boost the energy of the pulse. This allowed us to produce laser pulses of energy up to 30 mJ. A schematic diagram of the laser system is shown in Fig. 5.3.3.1. Further information on the laser system is included in Appendix 4.

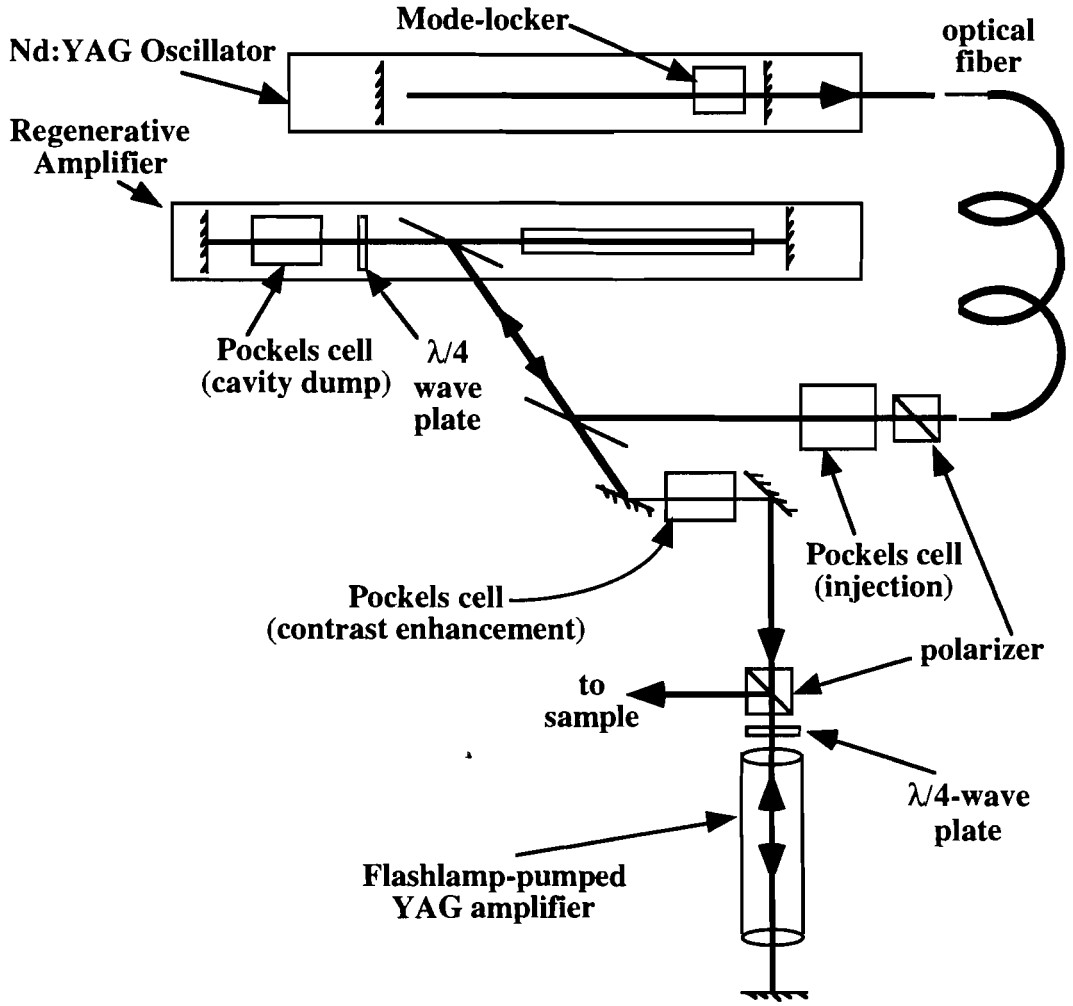

Figure 5.3.3.1 YAG laser system used to produce 150-ps laser pulses of energy up to 30 mJ. For a more detailed drawing of the amplifier systems see Fig. A4.1.1 in Appendix 4.

---

[7]The electro-optic crystal rotates the polarization of the incoming light only during the time when the high-voltage is on.

The laser pulse width was measured by scanning a razor blade across the beam and measuring its energy. The razor blade was mounted on a stepper motor controlled stage that was synchronized with the data acquisition from the energy meter. The automated measurement of the laser beam profile ensured that the entire film was heated above T_c. The spatial profile of the laser beam is Gaussian for the fundamental mode used in our experiments.

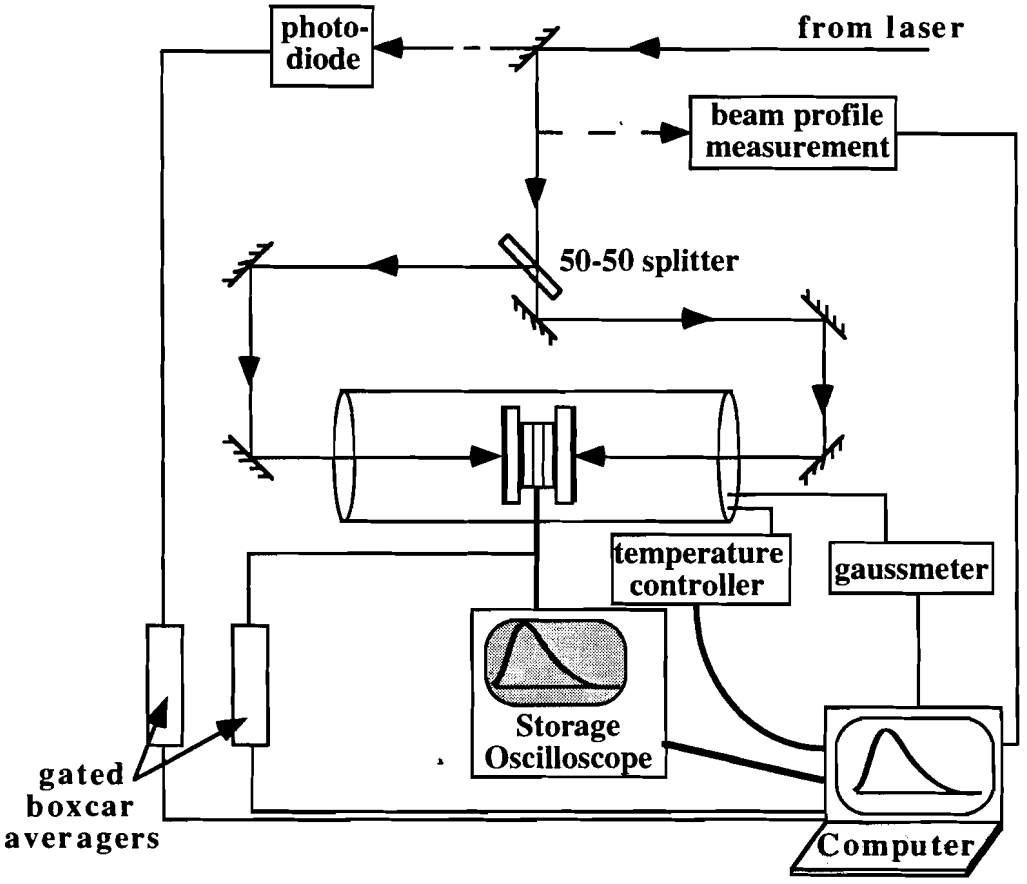

Figure 5.3.3.2 The experimental set-up for the high field experiments showing the laser illumination scheme and the data acquisition system.

A stainless steel semi-rigid coaxial cable is used to conduct the secondary voltage signal. The signal is acquired by a Tektronix SCD-5000 storage oscilloscope and averaged using a gated box-car averager, both interfaced with a computer [Fig. 5.3.3.2]. The oscilloscope records 16 waveforms corresponding to 16 consecutive laser shots. The computer data acquisition program also acquired the laser intensity of each pulse from a photodiode. This is important since the laser intensity fluctuates and a

measurement of average laser intensity does not provide information regarding the particular laser pulse that initiates flux motion. This allowed us to correlate the detected secondary voltage and laser intensity precisely.

The experiment was conducted as follows. The sample was first cooled by liquid nitrogen or helium to the desired temperature. The magnet was then charged using the current programmer at a ramp rate of 0.1 A/s. The persistent switch heater current was 60 mA supplied by a constant current source. After the desired level of current is established in the magnet the persistent switch heater is turned off allowing persistent current to flow through the magnet. The magnetic field was measured using a hall probe and a gaussmeter.

With the magnet charged the switch was illuminated by the laser. The YBCO films screening the secondary coils were driven normal by this laser irradiation allowing flux to penetrate. A secondary voltage (of negative sign, called the *charge signal*) appeared across the load. The voltage was found to decrease exponentially with subsequent shots [Fig 5.3.3.3]. The magnet was then discharged by heating up the persistent switch. Since the field in these experiments were above H_{c1} some flux was trapped in the YBCO films following the flux penetration. Driving the films normal again expels this flux and we observed the corresponding secondary voltage signal (of positive sign, called the *discharge signal*). As before this voltage decreased exponentially with subsequent shots [Fig. 5.3.3.3]. In both cases the voltage as a function of shot number (n) was found to closely fit the relationship, $\frac{V(n+1)}{V(n)} = e^{-0.6}$. Charge and discharge signals were observed up to a magnet field of 3T at a temperature of 27K. At liquid nitrogen temperature, however, voltage signals were observed only up to 0.4 T.

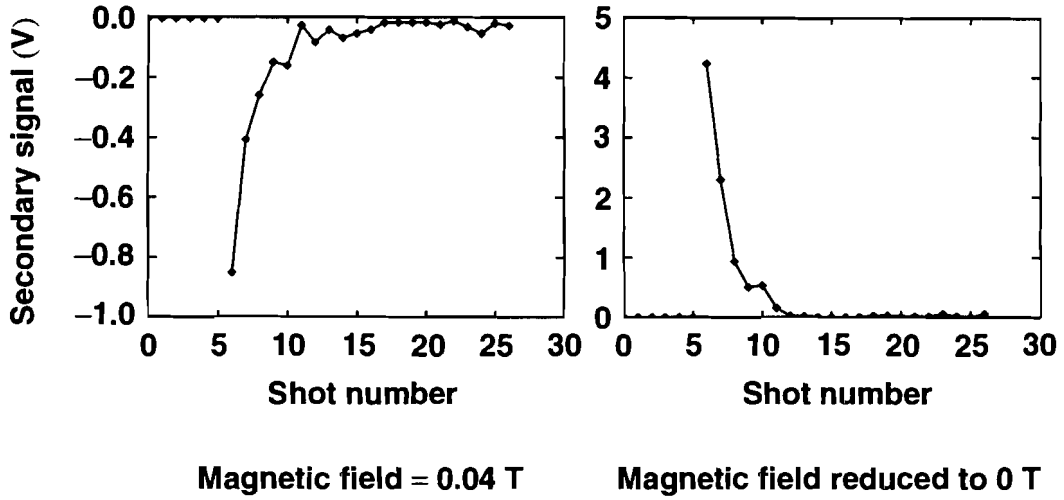

Figure 5.3.3.3 The secondary voltage signal decreases exponentially with laser shots. The shutter opens at shot number 6. So that should be taken as n=1.

A strange, anomalous signal has been observed when the switch operates while the magnet is charged at a particular value of the field. We made as set of observations of both the charge and the discharge signals for varying magnetic field. The charge signal was always negative and the discharge signal positive with a singular exception when both were of positive signs. An example of this is shown in Fig. 5.3.3.4. The peak secondary voltages for consecutive laser shots are shown for three values of the applied magnetic field. The charge signal at 0.06 T field had the reverse polarity and is called the anomalous signal. We made a careful study of this phenomenon by changing the sample, and with different sample configurations (described in section 5.3.4). Although the value of the field at which the anomaly occurred varied slightly it was reproducibly observed.

Since the flux dynamics in the irreversible vortex state depends on the previous value of the field in the film, the signal may have arisen from unexpelled trapped flux in the film. This may be related to the presence of inverse domains [114] seen with magneto-optical imaging. Pinned flux at the center produces flux of opposite polarity at sample edges, which are strong enough to nucleate reverse votices and has been shown to be energetically stable. When the next charge signal is measured these negative flux may move out resulting in a voltage of opposite sign as has been observed. Interestingly, this was never observed with a single-turn secondary coil (described in section 5.4). Also, occurance of this phenomenon at only one value of applied field

seems intriguing. Further investigation with muliple coils at different locations rather that a single secondary coil is required to resolve this phenomenon.

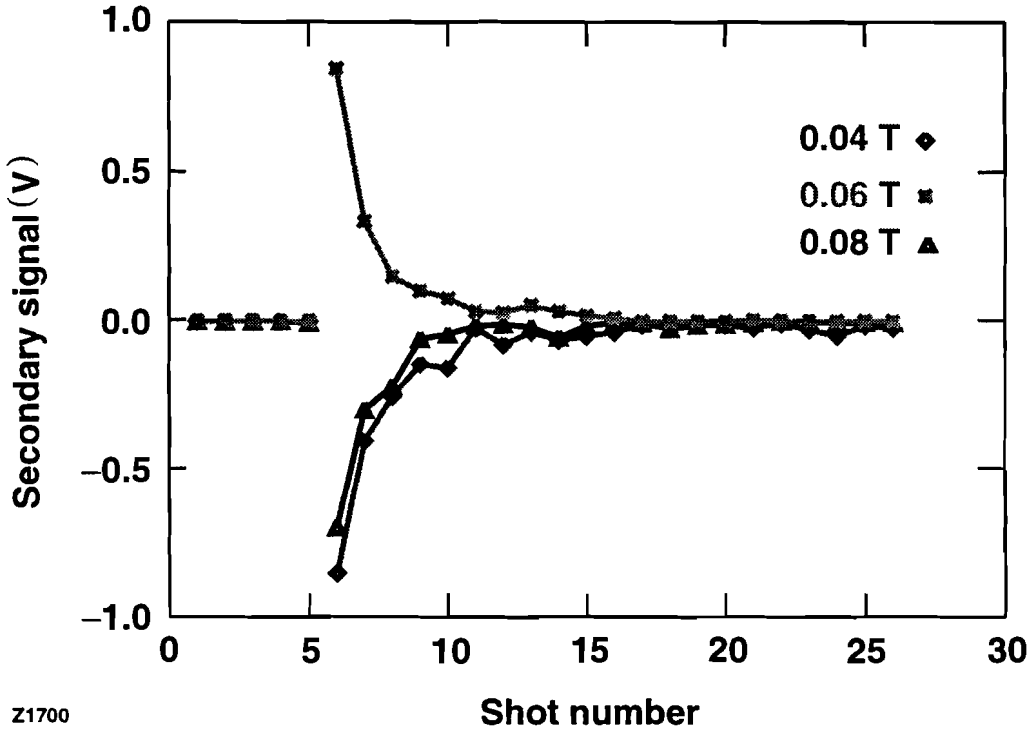

Figure. 5.3.3.4 Anomalous charge signal in the inductive switch. The switch temperature is 80 K.

5.3.4 Discussion of results

These preliminary results show that the observed signal was much less than the expected response. The secondary voltage can be fitted to an exponential,

$$v(t) = -V_0 e^{-\frac{t}{\tau}}, \qquad (5.3.4.1)$$

where V_0 is the peak amplitude and τ the decay time constant. The mean and the mean square signals can be expressed as follows,

$$\langle v(t)\rangle = -\frac{V_0\tau}{T}(1-e^{-\frac{T}{\tau}}) \text{ and } \langle v^2(t)\rangle = -\langle v(t)\rangle V_0 - \frac{T}{2\tau}\langle v(t)\rangle^2 \qquad (5.3.4.2)$$

Using typical numbers like $\langle v(t)\rangle$ =-1 V, τ =50 ns and T = 450 ns for a field(B) of 0.02 T, energy (E) dissipated in a 50-Ω resistor (R) is given by

$$E = \frac{T}{R}\langle v^2(t)\rangle = 40.5 \text{ nJ}. \qquad (5.3.4.3)$$

The corresponding stored energy, assuming an excluded volume[8] [Fig. 5.3.4.1] of 1 cm^3 is given by

$$E_{stored} = \frac{B^2}{2\mu_0}(\text{vol.}) = 15.9\mu\text{J}. \qquad (5.3.4.4)$$

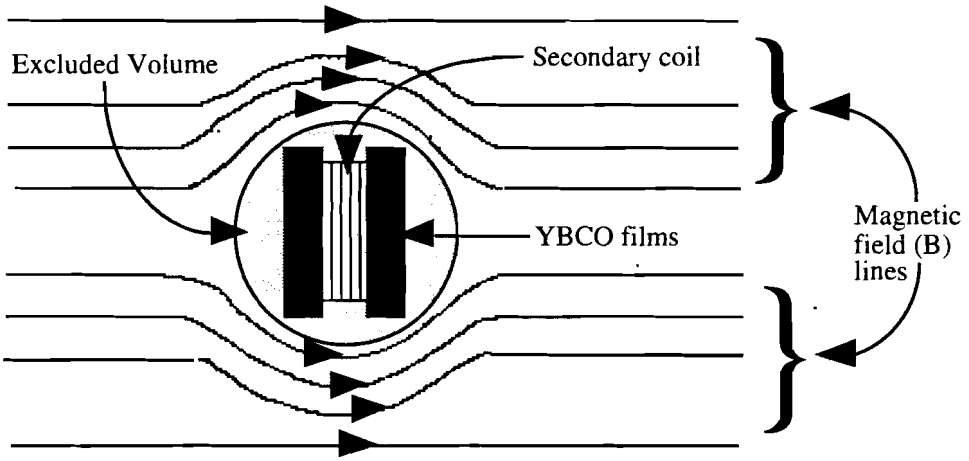

Figure 5.3.4.1 Magnetic field lines bend around the superconducting films due to flux screening. When the films are heated above their critical temperature field lines will move in. The extracted energy corresponds to the "excluded volume" in the figure.

It is clear from the above calculations that the extracted energy is much smaller than the stored energy. It was initially believed to have been caused by screening due to a residual dark superconducting ring at the edge of the film. The edge of the film was supported against the sample holder and was not illuminated as shown in Fig. 5.3.4.2. Our initial belief was a result of a simple calculation based on the critical state model (section 3.3.5). To estimate the width of a superconducting ring (Δx), required to screen out a field of 1T, we take H=10^4 A/cm and J_c =10^6 A/cm^2. Δx is given by

[8]A more detailed calculation of the excluded volume will be presented in chapter 6.

$\Delta x = H/J_c = 100\mu m$. This implied that even after allowing for field intensification at the edges (demagnetization due to the thin film geometry) the 1mm wide dark ring would be wide enough to keep most of the field screened even when the rest of the film was normal. As we shall see in the next chapter, this calculation was incorrect.

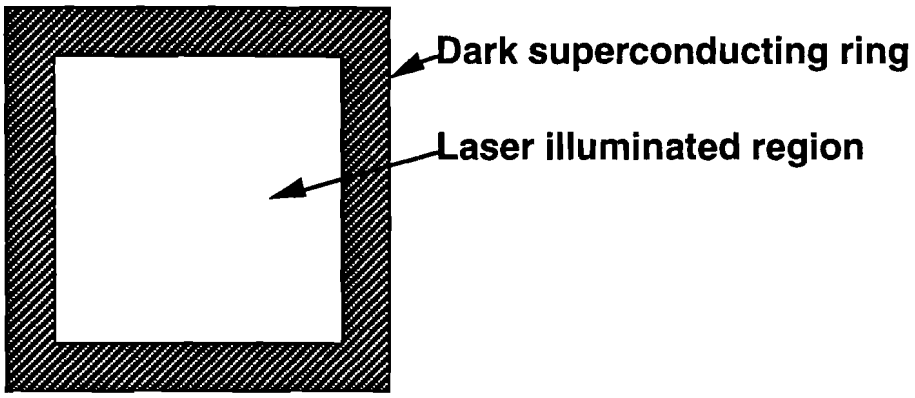

Figure 5.3.4.2 The dark region is not illuminated by laser and remains superconducting while the central illuminated region goes normal.

Three experiments outlined below confirmed that the dark region was not responsible for flux screening.

1) The film was supported along its edge in the previous design which prevented a 1mm wide region around the edge from receiving laser illumination. This can be avoided by changing the support structure so that the film is only supported at the four corners [Fig. 5.3.4.3]. The result was essentially the same as before. The flux motion took place over several laser shots and the secondary voltage had the same magnitude.

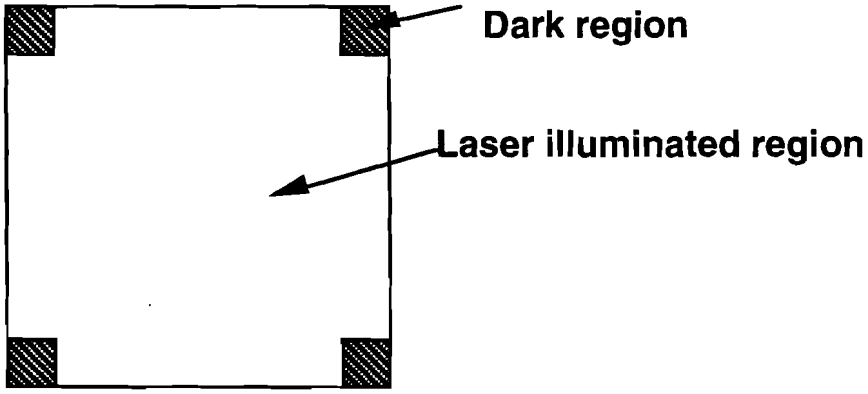

Figure 5.3.4.3 The film is supported only at the four corners. This modification will avoid any screening currents after the laser illumination.

2) The film was patterned so as to etch away the film from the region of support. The result was again the same as before.

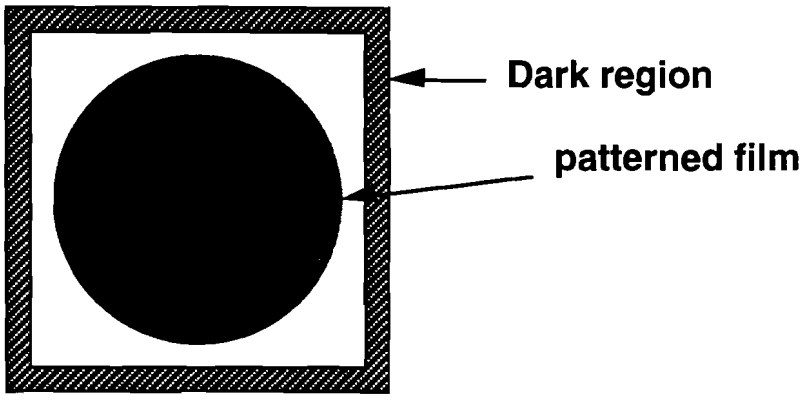

Figure 5.3.4.4 The film is patterned into a circle in the region of illumination. The entire film is illuminated under this scheme.

3) In order to screen the applied magnetic field, we need a superconducting ring wide enough to provide screening currents. If the assumption that a 1mm wide dark ring was responsible for flux exclusion was correct, we could use 1 mm wide ring instead of the whole film to perform the switching. Moreover, under this configuration, switching can be accomplished by heating only a small portion of the ring as shown in Fig. 5.3.4.5. for this scheme the required laser energy will be about 100 times smaller than before. The resultant secondary voltage pulse was smaller compared to the earlier one by an order of magnitude and did occur over several shots as before.

These results provided important insights to the problem of flux exclusion leading to a complete analysis for the thin film geometry described in chapter 6. The slow flux entry, as evidenced by secondary voltage pulses of diminishing amplitude for several laser shots, was also present in the ring sample (Fig.5.3.4.5). This implies that in this case the time of flux entry is dominated by the large L/R time-constant of the secondary coil rather than the flux diffusion time through the film.

The other conclusion from these experiments is that the even when the whole film was used as a flux screen only a small fraction of the flux was excluded, while field partially penetrated the film. In the next chapter we shall show that for complete flux exclusion the required critical current density is at least an order of magnitude higher for a film of comparable thickness. Also it is the critical current rather than

current density that determines the flux exclusion. The simple one-dimensional analysis used earlier to estimate the width of the superconducting ring required for flux exclusion is only valid if the superconductor is a long cylinder (or a thick slab). On the contrary, a two-dimensional analysis of the critical state is required to understand the case of a thin film.

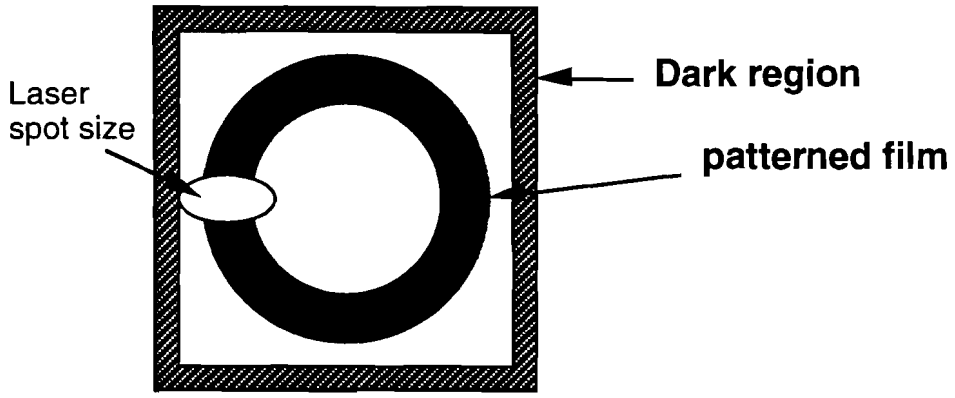

Figure 5.3.4.5 The film is patterned as a ring so that only a portion of the ring needs to be illuminated to allow flux entry.

The flux entry into the film took place over a few laser shots. Evidently, the process of flux entry requires more time than the thermal recovery time of the film following optical heating. The speed of flux motion in the irradiated film depends on the self and mutual inductances, and resistances of the magnetically coupled system consisting of the film and the secondary coil. Since the secondary voltage is the time derivative of flux, faster flux motion would give a larger voltage pulse. The flux entry would be faster if the self inductance of the secondary coil was smaller. Therefore the multi-turn secondary coil was substituted with a single turn coil for our next experiment.

5.4 Experimental results in high magnetic field with single turn secondary coil

The experiments with a single turn secondary coil were performed using the same samples in the same experimental set up described in the earlier section. The secondary coil was patterned on a copper coated printed circuit board (PCB). The 200-μm wide coil had a radius of 3.5 or 4 mm. A coplanar strip line, also patterned on the PCB, connected the coil to an SMA connector. The signal was conducted out of the cryostat using a stainless steel coaxial cable. For this experiment, we used the same superconducting magnet as the primary coil. The laser system and data acquisition were the same as described in section 5.3.3.

As expected, reduction of the secondary inductance enabled fast flux motion. Consequently, the secondary voltage pulse was much larger and narrower. A series of experiments were done by varying magnetic field, sample temperature and laser fluence.

In contrast to the previous measurements with multi-turn secondary, only one voltage pulse was observed in most of the experiments. This indicates that excluded flux moved in and reached a stable configuration during the first laser shot. This is also a direct consequence of the enhanced speed of flux motion. In a few cases a second pulse was observed, and these cases correlated well with the occasional low intensity laser shot. Due to inherent instabilities in the system, occasionally the laser energy falls drastically for one particular shot. When such "misses" occur the laser energy may be enough to depress the screening currents and initiate flux entry, but does not heat the film for a sufficiently long time to allow complete flux motion. In those cases two or more pulses were observed.

In Figure 5.4.1 we show the best result achieved so far. The largest secondary voltage was observed at the lowest temperature (12 K) attained in our cryostat. The external field was 0.2 T. The rise time of the pulse was 2.5 ns.

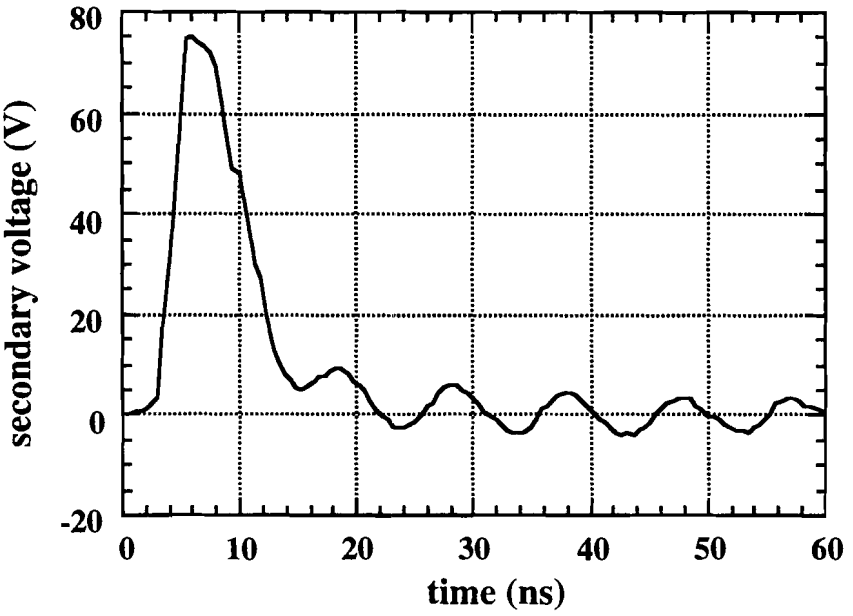

Figure 5.4.1 Secondary voltage pulse taken at T=12K, and an applied magnetic field of 0.2 T. The rise time of the pulse is 2.5 ns. We believe that this includes a thermal delay for the optically thick film.

Variation of laser energy can lead to two different results depending on the magnitude. If the laser energy is too small, there is no signal. If the laser energy is large enough to initiate flux motion (missed shot), multiple voltage pulses are observed. However in most cases (as seen in Fig. 5.4.2) reduction of laser energy only results in an increased delay in flux motion. This shows up as progressively broader and shorter voltage pulses for decreasing laser energy.

Interestingly, the flux ($\Phi = \int V(t)dt$) associated with these secondary voltage pulses is the same in all cases[9]. This implies that all the excluded flux is moving in even for the smaller laser energies, that are sufficient for heating the film long enough. The smaller the laser energy the slower is the heating of the entire film. Thus for smaller laser energies, initially only the top section of the optically thick film is heated above T_c while a superconducting section at the bottom of the film still maintains some screening

[9]Except for the one for 1.27 mJ energy. Due to a limited time window for data acquisition this pulse was not entirely captured. Therefore the time integration was incomplete. Extrapolation gives the value of the flux very close to the others.

currents. This retards the flux motion. The heat eventually propagates down and the entire volume of the film becomes normal.

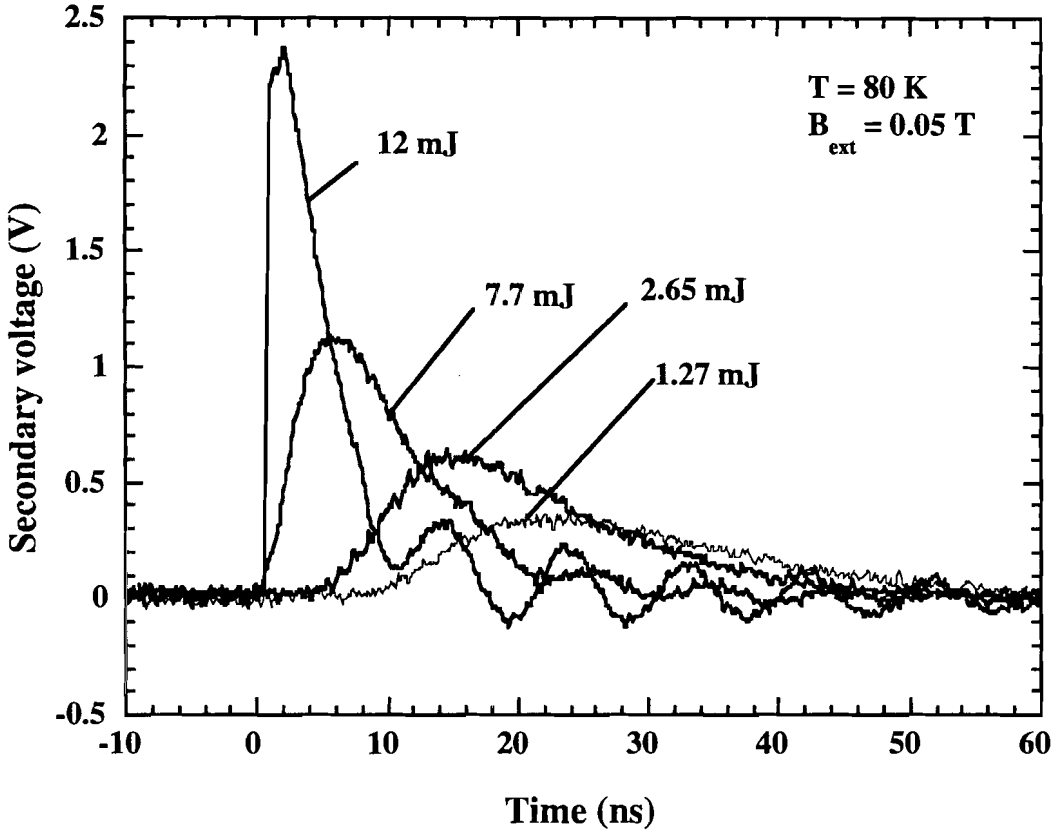

Figure 5.4.2 Flux motion is faster for higher laser energies. The flux associated with each pulse is the same.

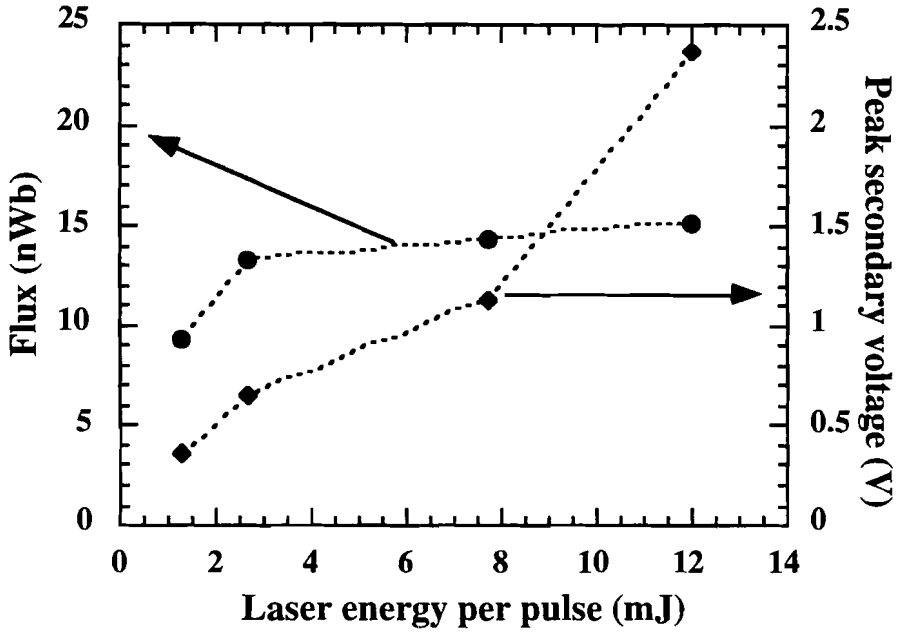

Figure 5.4.3 As laser energy is increased for the same flux, peak voltage rises sharply, indicating faster flux motion.

If the temperature of the films is lowered the critical current density increases. The higher critical current gives rise to larger flux screening. Therefore lowering the temperature gives a larger voltage pulse, and also larger flux (Fig. 5.4.4).

In the case when the screening currents are weak enough that the applied field penetrates the entire film, the secondary voltage or flux is independent of the field. In this case the whole film is in the critical state. The excluded flux is directly proportional to the critical current density. Figure 5.4.5 shows that a variation of applied magnetic field from 0.1 to 1 T does not affect the flux or the secondary voltage.

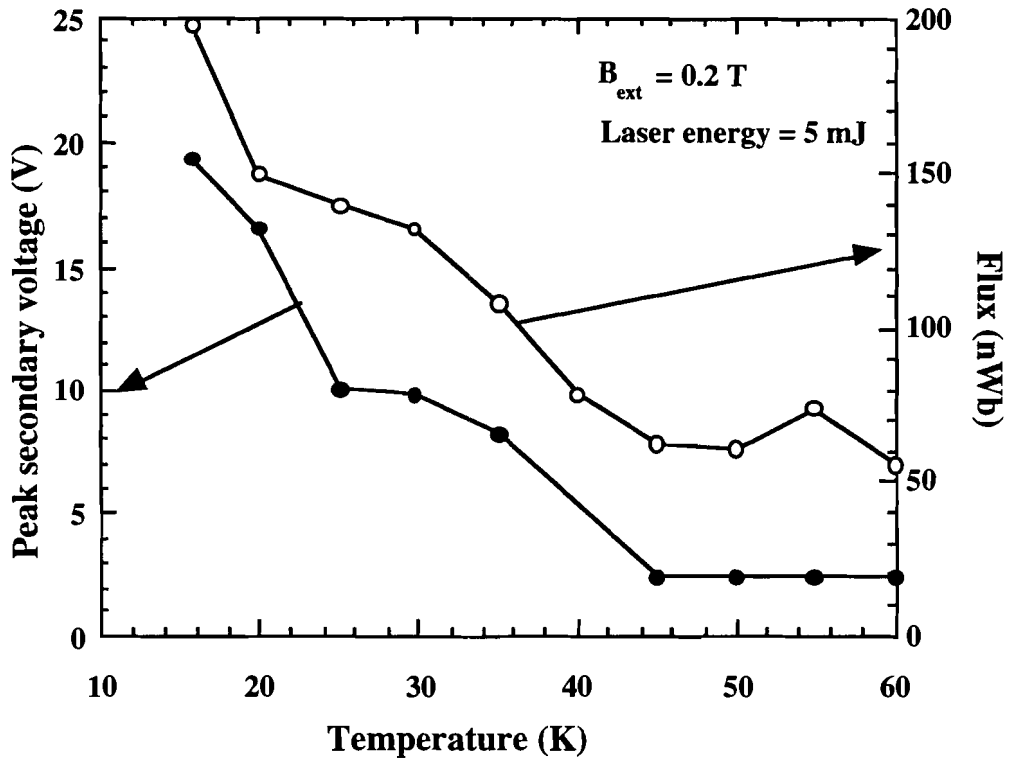

Figure 5.4.4 Larger critical current at lower temperature corresponds to a larger amount of excluded flux. The voltage pulse at low temperatures are consequently larger.

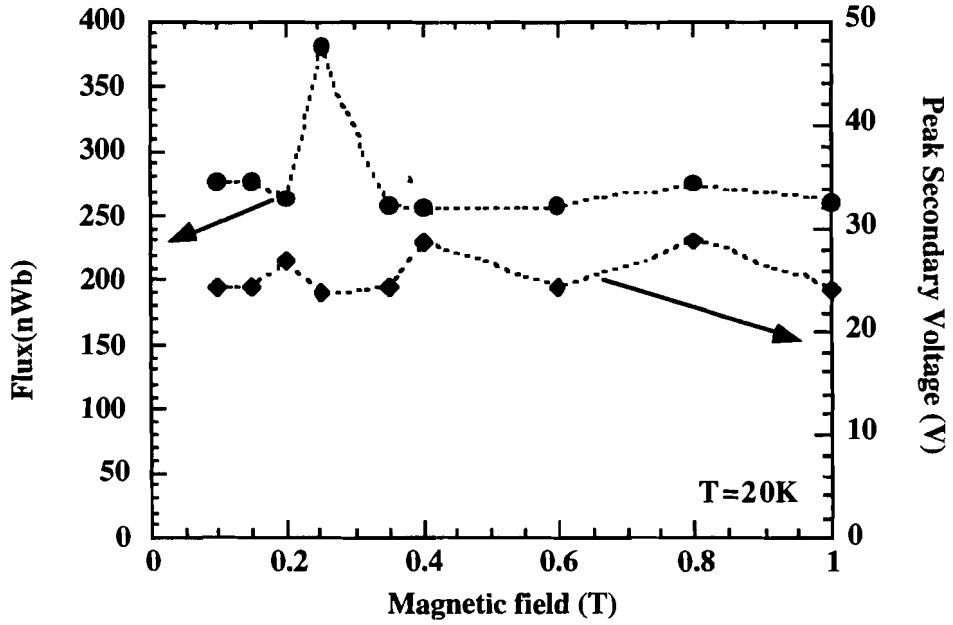

Figure 5.4.5 Peak secondary voltage and magnetic flux are essentially independent of magnetic field.

5.5 Discussion

Although our experimental results are encouraging for the inductively-coupled switch, it is far from attaining maturity. The energy extracted was of the order of 100 nJ which is several orders of magnitude less than what is required for its intended applications. However, this is not unexpected given the constraints of the experiment and the material properties of our switch.

Let us examine the principle of energy extraction from a magnetic energy storage. Initially a flux screen is present inside the magnet. The magnetic field lines will bend around it, creating a volume of exclusion around the flux screen (Fig. 5.3.4.1), and will lower the effective inductance of the magnet. When the screen is removed, the flux lines will redistribute changing the inductance of the magnet. Since flux inside the superconducting magnet loop ($\Phi = LI$) remains constant, this implies a reduction of current. Using subscripts 1 and 2 to denote the former and the latter states, we can calculate the extracted energy as,

$$\Delta E = E_1 - E_2 = \frac{1}{2}\left(L_1 I_1^2 - L_2 I_2^2\right). \tag{5.5-1}$$

Now the energy extraction efficiency (γ) can be defined as

$$\gamma = \frac{\Delta E}{E_1} = 1 - \frac{L_2 I_2^2}{L_1 I_1^2} = 1 - \frac{L_1}{L_2} = 1 - \frac{I_2}{I_1}, \tag{5.5-2}$$

where $L_1 < L_2$ and $\Phi = L_1 I_1 = L_2 I_2$. Therefore, we can achieve a high efficiency by distorting the field as much as possible inside the magnet to obtain a lower value of L_1. In other words, if we can exclude most of the volume inside the magnet initially, we can extract a significant fraction of energy.

With a small 1 cm switch our excluded volume was a small fraction of the magnet volume. With a larger diameter switch (for example a film on a 2 in substrate), it would be possible to exclude a larger volume. The other alternative is to fill up the volume inside the magnet with a large number of these switches. There is a current multiplication scheme, called the Programmed Inductive Element (PIE) approach[115] which allows sequential discharge of several switches, rated at a fraction of the required

output rating, to produce the desired output waveform. This is a general scheme that can be applied to any type of switch. Here the opening switches are connected to the load through a corresponding closing switch (Fig. 5.5.1). An opening switch and its corresponding closing switch[10] are triggered in rapid succession, followed by the triggering of other pairs. The limitation of this scheme is the requirement of precise triggering control. If the switches are not triggered within a short temporal window the discharged energy from one switch will destroy other switches. Although the PIE scheme has not been implemented in practice, especially because the above mentioned timing requirement, we might be able to take advantage of our precisely controllable and fast optical triggering to use it to connect a set of switches. There is a fundamental limitation which prevents us from achieving high extraction efficiency. As we increase the excluded volume inside the magnet, the flux lines are squeezed into narrow spaces greatly increasing the local field intensity. Consequently, the flux screening will be less efficient and the volume of exclusion will shrink. There will be a maximum volume of extraction and extraction efficiency. We haven't analyzed these issues of energy extraction. If this approach is undertaken in future a quantitative analysis will be necessary.

There is a more serious materials issue which needs to be addressed. As we have mentioned in section 5.3, a naïve estimate with a one-dimensional critical state model gives a misleading picture regarding screening of a large magnetic field with a thin film. It was estimated that a narrow ring of width 100μm would screen a field of 1 T. This argument is incorrect for thin films, but will be valid for a long hollow cylinder. We need to perform a complete two dimensional analysis of the critical state to analyze the flux dynamics of the thin film geometry (chapter 6).

---

[10]Or a set of closing switches depending on the number of opening switches.

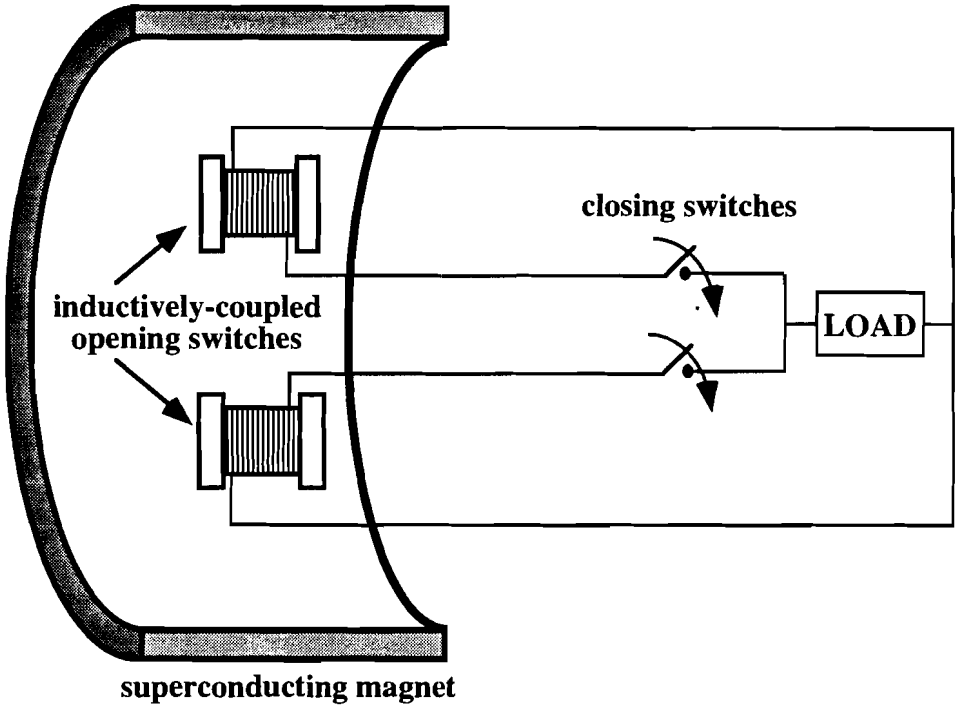

Figure 5.5.1 The Programmed inductive element (PIE) scheme. A large load current is obtained by sequentially triggering a set of opening switches, rated at a fraction of the load current, through a set of closing switches.

As we shall see in chapter 6, the amount of excluded flux depends on the total screening *current* (not the current density) supported by the superconducting film. We shall also see that the critical current densities of our film are not large enough for complete exclusion of magnetic fields of the order of 0.1 T. A reasonably accurate estimate can be found by comparing the surface current density (I_S) and field ($H = B/\mu_0$). The critical current density required to exclude a given field is[11]

$$J_c = \frac{I_s}{d} \approx \frac{H}{d} = \frac{B}{\mu_0 d}. \tag{5.4.1}$$

For a film of thickness 500 nm, and B = 0.1 T, the required critical current density is $2 \times 10^7 \, \mathrm{A / cm^2}$. This value, while not unreasonable for the best reported films, is at

[11]This is an order of magnitude estimate and is strictly valid when the film is fully penetrated by external field.

least an order of magnitude higher than our films. Therefore, in our experiments most of the field would have penetrated the film in its superconducting state, and a small fraction was excluded by the screening currents. This small fraction of applied field moves in upon laser illumination and therefore the amount of energy extracted from the field is much smaller than the ideal case of complete flux exclusion. Although the bulk material has a critical current density 100 times smaller than that of a thin film, the total screening current will be greater due to the added gain in thickness. For example, a 1–2 mm thick cylinder, like the ones in an inductive fault current limiter (section 2.3.1), can be used instead. For applications not requiring very fast switching, a switch based on bulk material would be more suitable.

CHAPTER 6

ANALYSIS OF TRANSIENT FLUX DYNAMICS IN SUPERCONDUCTING INDUCTIVELY COUPLED SWITCH

6.1 Modeling the screening currents in a superconducting disk

A superconductor placed in an external magnetic field produces screening currents. These screening currents generate a magnetic field that opposes the external field (B_{ext}). In the Meissner regime, $B_{ext} < B_{c1}$, the screening currents exclude the external field completely. In the vortex state, $B_{ext} > B_{c1}$, partial flux penetration takes place. The screening currents, constrained by the local critical current density, configure to minimize the region of flux penetration. A simple one-dimensional model of the critical state has been discussed earlier in section 3.2.7.

The simple one-dimensional analysis of the critical state is applicable for bulk superconductors, where the longitudinal dimension (parallel to the direction of external field) is not small compared to the lateral dimension (perpendicular to the direction of the external field). If the longitudinal dimension is small compared to the lateral one, however, the large demagnetization factor causes enhancement of the field strength at the outer edge of the superconductor. The demagnetization effect (section 3.2.4) in thin films, placed in an external magnetic field perpendicular to the film surface, is strong. Therefore, magnetic flux can penetrate from the edge of the thin film even when $B_{ext} < B_{c1}$.

In the recent years, there has been a lot of work on the critical state in superconducting thin films. However, most of this work concentrates on the magnetostatic currents and fields. While, there is some work on response to sinusoidal ac magnetic field, the issues regarding transient changes of the critical state (e.g., when the film makes a rapid transition to a resistive state from a superconducting one) has not been investigated. Analytical solutions for the current and field distributions in thin disks have been obtained by Mikheenko and Kuzovlev[116], assuming field-independent critical current densities. This result is of singular importance, since it solves a problem to which an analytical solution was not perceived to be possible. Brandt[117-119] has studied and compared different geometries including strip lines. Frankel[120] and Daümling and Larbalestier[121] have calculated fields and currents numerically, for constant and field-dependent critical current densities. Zeldov *et al.*[122] have extensively studied the effect of transport current on magnetization in

superconducting strips. Semi-empirical calculations by Theuss *et al.*[123] determine current and radial component of the magnetic field (B_r) from magneto-optical measurements of $B_z(r)$ in *c*-axis-oriented YBCO thin films.

The calculation of current and field distribution is an essential part of understanding the critical state dynamics in our thin film inductively coupled switches. We have developed a self-consistent model that allows us to formulate the magnetic fields and screening currents, under static and dynamic conditions. The model, based on the evaluation of magnetic vector potential due to current loops, leads to a numerical methodology that lends itself to efficient computation.

Let us consider a film of thickness d, shaped like a circular disk of radius R. Initially we assume that the critical current density (J_c) is constant (independent of magnetic field). The externally applied field ($\hat{z}B_{ext}$) is parallel to the axis of the circular disk. We divide the disk into n concentric strips of equal width ($w = R/n$). Each of these strips is considered to be a loop carrying a surface current (I_s), neglecting any variation of the current density (J) across the thickness. The circular strip with radius r_j carries a surface current I_{sj} (Fig. 6.1.1).

6.1.1 Vector potential due to a current loop

Let us consider a single current loop of radius ρ, carrying a current I, in the plane of the disk (z=0), centered at r=0 (Fig. 6.1.1.1). By definition[1][124,125],

$$\bar{A} = \frac{\mu_0}{4\pi}\oint \frac{Id\bar{l}}{r} \qquad (6.1.1\text{-}1)$$

Due to the cylindrical symmetry, $\bar{A}$ is independent of the azimuth, ϕ, in cylindrical coordinates. We choose our point of observation, P(r,0,z) at $\phi = 0$ plane, without any

[1]This and other formulas involving vector potential, field and current can be found in most texts on electromagnetism. However, details of the calculations are often left out and the use of unit systems other than SI add to confusion. The use of References 123 and 124 are highly recommended for similar magnetostatic analyses.

loss of generality. Let us take two current elements of length *dl at* ϕ' and $-\phi'$. The current elements are equidistant from P, the distance being

$$|\overline{R}| = R = \sqrt{r^2 + \rho^2 - 2r\rho\cos\phi' + z^2}\,. \qquad (6.1.1\text{-}2)$$

The resultant contribution from the two current elements at ϕ' and $-\phi'$ is in the $\hat{y}$ direction, given by

$$d\overline{A} = \frac{\mu_0 I\rho}{4\pi R} d\bar{l} = \hat{y}\frac{\mu_0 I\rho}{2\pi R}\cos\phi' d\phi'. \qquad (6.1.1\text{-}3)$$

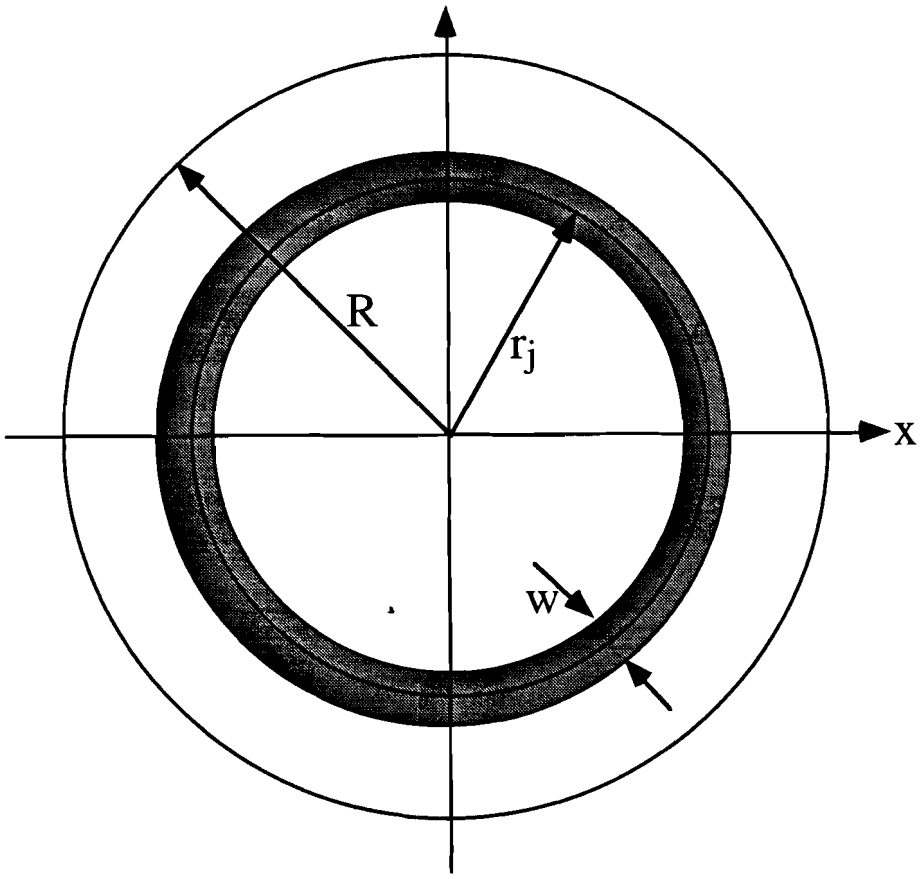

Figure 6.1.1 A thin circular disk of radius *R* is divided into concentric strips of width *w*.

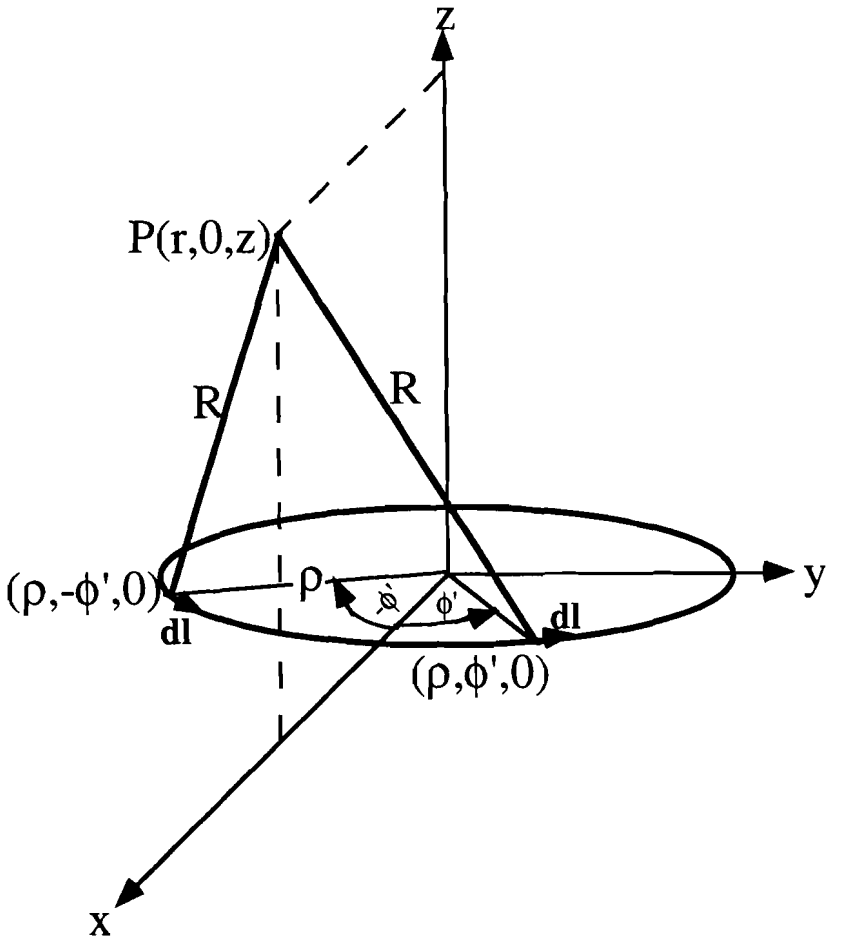

Figure 6.1.1.1 Vector potential due to a current loop of radius r in the z=0 plane. The point of observation, P, is in the ϕ=0 plane. Two current elements, equidistant from P are shown.

We note that $\overline{A}$ is perpendicular to the plane of observation ($\phi = 0$ plane). Therefore $\overline{A}$ has only a $\hat{\phi}$-component, given by

$$A_\phi = \frac{\mu_0 I \rho}{2\pi} \int_0^\pi \frac{\cos\phi' d\phi'}{\sqrt{r^2 + \rho^2 - 2r\rho\cos\phi' + z^2}}. \qquad (6.1.1\text{-}4)$$

Equation (6.1-4) is solved by substituting $\theta = \frac{\pi - \phi'}{2}$ and $k = \frac{4r\rho}{(r+\rho)^2 + z^2}$[2].

The vector potential can then be expressed as,

---

[2] Some authors denote k by κ^2 and write $K(\kappa)$ and $E(\kappa)$ instead of $K(k)$ and $E(k)$.

$$A_\phi(r,\phi,z)=\frac{\mu_0 I}{\pi}\sqrt{\frac{\rho}{rk}}\left\{(1-k/2)K(k)-E(k)\right\}, \qquad (6.1.1\text{-}5)$$

where $K(k)=\int_0^{\pi/2}\left(1-k\sin^2\theta\right)^{-1/2}d\theta$, and $E(k)=\int_0^{\pi/2}\left(1-k\sin^2\theta\right)^{1/2}d\theta$ are the complete elliptic integrals of the first and second kind respectively. In the special case when the point of observation is in the plane of the loop (z=0), equation (6.1.1-5) simplifies to

$$A_\phi(r,\phi,0)=\frac{\mu_0 I}{2\pi}(1+\rho/r)\left\{(1-k/2)K(k)-E(k)\right\}, \qquad (6.1.1\text{-}6)$$

where $k=\frac{4r\rho}{(r+\rho)^2}$. These can be evaluated using standard techniques, that are built into mathematical software packages, like MATLAB™[126].

6.1.2 Magnetic field due to a current loop

Magnetic field due to this current loop can be obtained by taking the curl of $\overline{A}$.

$$\overline{B}=\nabla\times\overline{A}=-\hat{r}\frac{\partial A_\phi}{\partial z}+\hat{z}\frac{1}{r}\frac{\partial}{\partial r}\left(rA_\phi\right). \qquad (6.1.2\text{-}1)$$

The radial and axial components of $\overline{B}$ are[3] given by,

$$B_r(r,\phi,z)=\frac{\mu_0 Iz}{2\pi r\sqrt{(r+\rho)^2+z^2}}\left\{-K(k)+\frac{\rho^2+r^2+z^2}{(\rho-r)^2+z^2}E(k)\right\}, \qquad (6.1.2\text{-}2a)$$

and

$$B_z(r,\phi,z)=\frac{\mu_0 I}{2\pi\sqrt{(r+\rho)^2+z^2}}\left\{K(k)+\frac{\rho^2-r^2-z^2}{(\rho-r)^2+z^2}E(k)\right\}. \qquad (6.1.2\text{-}2b)$$

The radial field changes sign above ($z>0$) and below($z<0$) the plane of the loop but the axial component does not. In the special case of z=0, we have

---

[3] Please refer to Eqs. (AI-14) and (AI-16) in Appendix I for the derivatives of K and E.

$$B_r = 0, \text{ and } B_z = \frac{\mu_0 I}{2\pi}\left\{\frac{K(k)}{(\rho+r)} + \frac{E(k)}{(\rho-r)}\right\}, \qquad (6.1.2\text{-}3)$$

where $k = \dfrac{4r\rho}{(r+\rho)^2}$.

6.2 Magnetostatic currents and fields of a single superconducting disk

In our model, described in the preceding section, we have represented the screening currents in the superconducting disk to consist of n circular loops, at radial locations r_j. The current in the j^{th} loop is $I_{sj} \times w$. The radial component of the magnetic field is zero at the plane of the film. We evaluate axial component of the field (B_z) at m points on the z=0 plane, at radial locations r_i. We choose the values of r_i such that $r_{i+1} - r_i = w$ (Fig. 6.2.1).

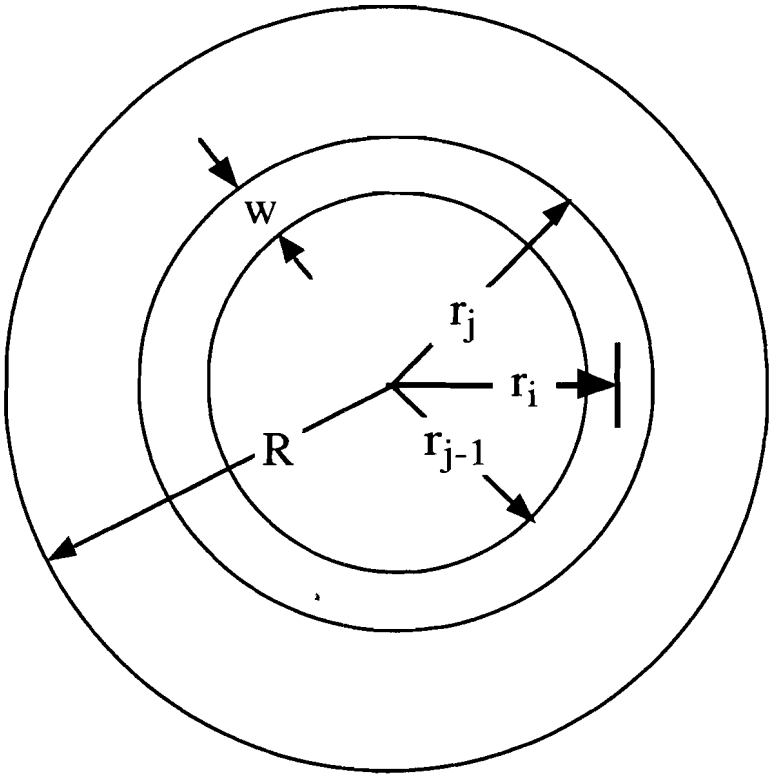

Figure 6.2.1 The field is calculated at radial locations r_i, halfway between two consecutive current loops.

B_z at any point is calculated by adding the contributions of each current loop at that point as,

$$B_z(r_i, \phi, 0) = \sum_{j=1}^{n} b_{ij} I_{sj}, \qquad (6.2\text{-}1)$$

or in matrix notation as,

$$\mathbf{B_z} = \mathbf{bI_s}, \tag{6.2-2}$$

where $\mathbf{B_z}$ is an $m \times 1$ vector, $\mathbf{b}$ is an $m \times n$ matrix, and $\mathbf{I_s}$ is an $n \times 1$ vector. The elements of $\mathbf{b}$ are given by,

$$b_{ij} = \frac{\mu_0 w}{2\pi}\left[\frac{K(k_{ij})}{(r_j + r_i)} + \frac{E(k_{ij})}{(r_j - r_i)}\right], \tag{6.2-3}$$

where, $k_{ij} = \frac{4 r_i r_i}{(r_j + r_i)^2}$. The matrix form is particularly appropriate for matrix-based packages like MATLAB™[126], which are used for most of our calculations here (Appendix 3).

6.2.1 Zero-flux current distribution

For complete flux exclusion, B_z is zero for $r_i \leq R$. Considering n field locations (i = 1,2,...,n) and n current loops (j= 1,2,...,n), the zero-flux surface current distribution ($\mathbf{I_s^0}$) can be calculated, for a given external field (B_{ext}), by imposing a set of n boundary conditions,

$$B_z(r_i) = \sum_{j=1}^{n} b_{ij} I_{sj} = -B_{ext} \quad \text{for } i = 1,2,...,\text{n.} \tag{6.2.1-1}$$

In matrix form,

$$\mathbf{I_s^0} = -B_{ext}\mathbf{b}^{-1}\mathbf{U} \tag{6.2.1-2}$$

where $\mathbf{U}$ is the $n \times 1$ unity vector. Fig. 6.2.1.1 shows the zero-flux surface current distribution as a function of the radial distance from the center of the disk (r). The 500-nm thick disk has a diameter of 1 cm. The external magnetic field of 0.2 T is along the $-\hat{z}$-direction. These values have been chosen for all our calculations to facilitate comparison with experimental results. The number (n) of current loops is 25, so that width of each strip is 200 μm. The results are also compared to an analytical expression described in section 6.2.3.

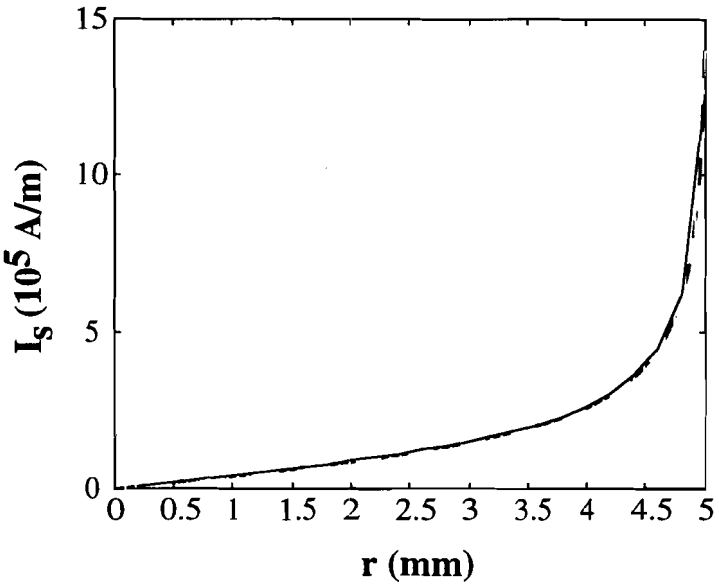

Figure 6.2.1.1 Zero flux surface current distribution calculated by our model (solid line) with n = 25, and by the analytical expression (dotted line) of Eq. 6.2.3-1. The results are virtually identical.

6.2.2 J_c-limited current distribution

If the external field is large enough, the required zero-flux surface current distribution exceeds the critical surface current I_{sc} ($J_c \times d$). In that case, we have a J_c-limited current distribution. The flux penetrates into the disk from the outside edge. The current redistributes itself to keep the central region flux free. The J_c-limited surface current distribution ($\mathbf{I_s}$) is calculated from $\mathbf{I_s^0}$ by the following iterative procedure.

The first step compares the surface current in the outermost ring (I_{sn}) to I_{sc} . If $I_{sn} < I_{sc}$, the current distribution is not J_c-limited, and $\mathbf{I_s} = \mathbf{I_s^0}$. If $I_{sn} > I_{sc}$, then I_{sn} is set equal to I_{sc} and the procedure outlined in section (6.2.1) is used to compute the surface currents for the remaining n-1 rings. We solve n-1 simultaneous equations,

$$\sum_{j=1}^{n-1} b_{ij} I_{sj} + b_{in} I_{sc} = - B_{ext}, \qquad (6.2.2\text{-}1)$$

for i=1,2,....,n. In other words, we calculate a current distribution so that the field is zero everywhere in the film except for the outermost ring.

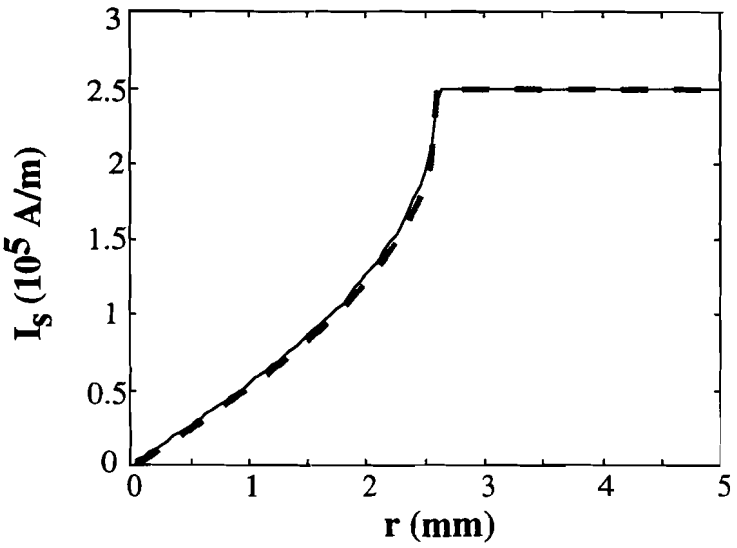

Figure 6.2.2.1 Surface current distribution as a function of radial distance (r) for our model (solid line) with n = 25, and the analytical expression (dotted line) given by Eq. (6.2.3-2).

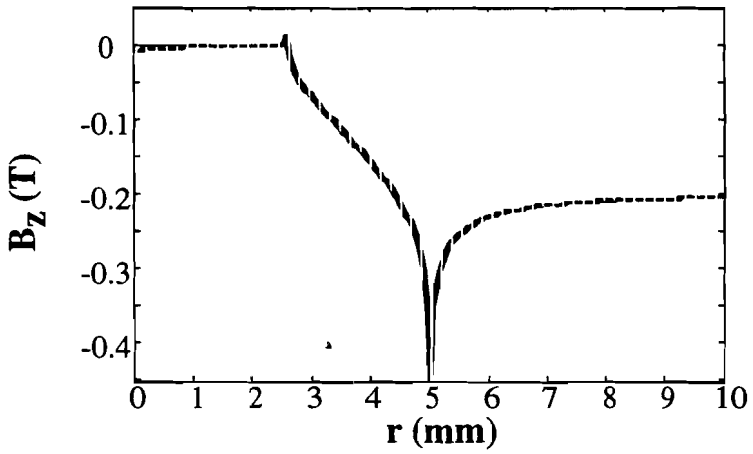

Figure 6.2.2.2 Magnetic field distribution as a function of radial distance (r) for our model (solid line) with n = 25, and that calculated using the analytical expression for the J_c-limited surface current given by Eq. (6.2.3-2).

At each subsequent step (p) of our iteration, we compare $I_{s(n-p+1)}$ to I_{sc}. If $I_{s(n-p+1)} > I_{sc}$, it is set equal to I_{sc}.. We then solve n-p simultaneous equations of the form,

$$\sum_{j=1}^{n-p} b_{ij} I_{sj} + I_{sc} \sum_{j=n-p+1}^{n} b_{ij} = -B_{ext}, \qquad (6.2.2\text{-}2)$$

for i=1,2,.....,n-p. We stop at the p^{th} step of iteration if $I_{s(n-p+1)} < I_{sc}$, or after n steps. The latter corresponds to the critical state, where there is flux penetration throughout the disk and the surface current distribution is uniform and equal to I_{sc}. The J_c-limited surface current distribution and the corresponding magnetic field distribution is shown in Figs. 6.2.2.1 and 6.2.2.2.

6.2.3 Analytical expressions for current distributions

We have so far neglected the field dependence of J_c. Under this assumption analytical expressions for the magnetostatic current and field distributions can be found. The agreement between the analytical expressions for this special case and numerical results obtained by our model is excellent (Fig. 6.2.1.1) and validates our numerical method. The elegant analytical expressions for the zero-flux and J_c-limited current distribution were obtained by Mikheenko and Kuzovlev[115]. The zero-flux surface current distribution is

$$I_s^0(r) = -\frac{4B_{ext}}{\pi\mu_0}\sqrt{\frac{r}{R^2 - r^2}}, \qquad (6.2.3\text{-}1)$$

and the J_c-limited surface current distribution is

$$I_s(r) = -\frac{2I_{sc}}{\pi}\tan^{-1}\left[\frac{r}{R}\sqrt{\frac{R^2 - a^2}{a^2 - r^2}}\right], \qquad (6.2.3\text{-}2)$$

where the radius (a) of the central flux-free region is $a = R/\cosh(2B_{ext}/\mu_0 I_{sc})$.

6.2.4 Incorporation of the field-dependent critical current density

For any given $J_c(B)$, the current and field distributions can be obtained by the algorithm outlined in sections (6.2.1) and (6.2.2). The key difference is that the critical surface current is non-uniform and has a distribution, $I_{sc}(r)$, expressed as $I_{sc}(r_j) = J_c(B(r_j)) \times d$. At the p^{th} step of iteration (Eq. 6.2-7) for calculation of J_c-limited current distribution, $I_{s(n-p+1)}$ is compared to $I_{sc}(r_{n-p+1})$. $I_{sc}(r_j)$ is calculated at

each step by calculating the field distribution ($\mathbf{B_z} = \mathbf{bI_s}$) first and then modifying $I_{sc}(r_j)$ according to $J_c(B)$. We calculate a modified $\mathbf{I_s}$ using Eq. 6.2.2-2 and repeat the process of modifying $\mathbf{B_z}$, $\mathbf{I_{sc}}$, and $\mathbf{I_s}$ iteratively until the difference between two successive field distributions are very small (typically one millionth of B_{ext}).

For example, if we assume $J_c(B) = J_c(0)^{(1-|B|/B_0)}$, which represents a linear decay of log J_c with respect to the magnitude of B (Eq. 3.3.9-3b), we obtain a modified surface current distribution as shown in Fig. 6.2.4.1(a). Fig. 6.2.4.1(b) shows the corresponding field distribution compared to the constant-J_c case. The assumed field dependence of J_c can also be written as $J_c(B) = J_c(0)e^{-|B|/B_1}$, where $B_1 = B_0/\ln J_c(0)$.

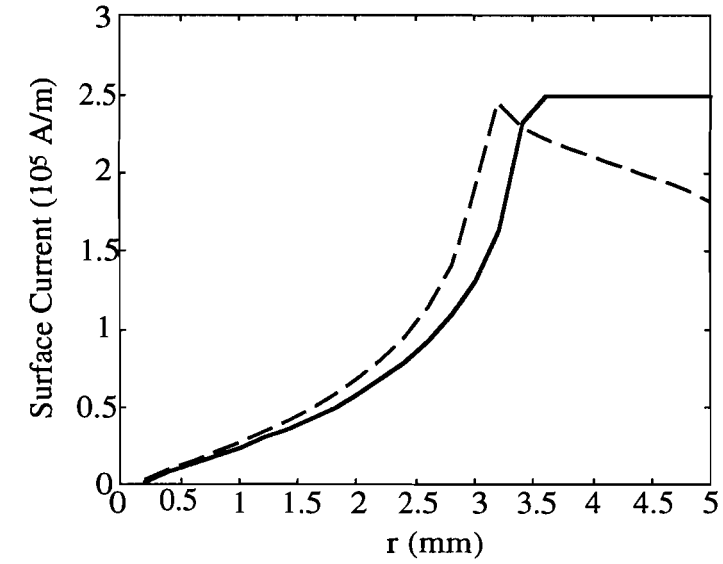

(a)

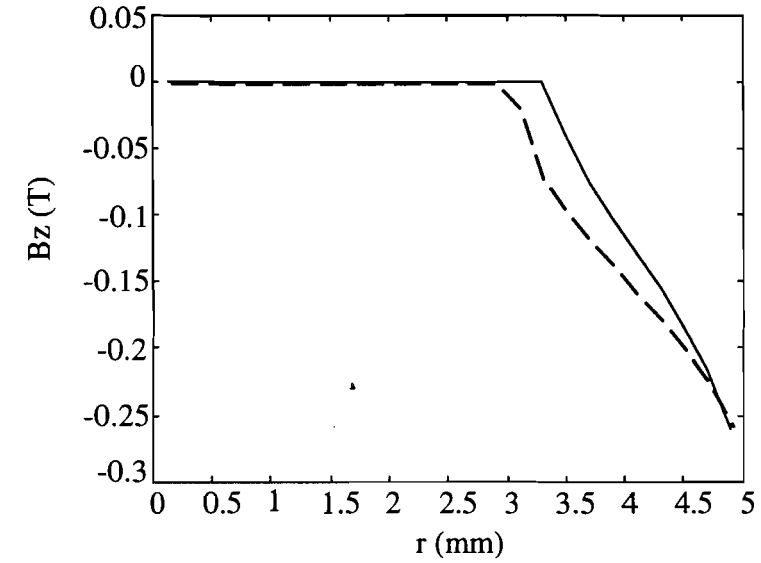

(b)

Figure 6.2.4.1 (a) Surface current and (b) field distribution for constant $J_c(B)$ (solid line) and $J_c(B) = J_c(0)^{(1-|B|/B_0)}$ (dashed line), where B_0 is 10 T, and $J_c(0)$ is 5×10^7 A/cm^2 in an external field of –0.2 T. In this case two identical 1-cm-diam, 500-nm-thick films are separated by 2 mm, and the external field is –0.2 *T*.

6.3 The case of two superconducting disks (experimental configuration)

To simulate the experimental configuration (section 5.3), we need to extend our calculations to include two identical films separated by a distance c (Fig. 6.3.1). Since the current distributions in the two films are identical, we can rewrite Eqs. (6.2-1) and (6.2-2), using the superscripts *I* and *II* for the two films, as follows:

$$B_z(r=r_i,z=0)=\sum_{j=1}^{n} b_{ij}I_{sj}=\sum_{j=1}^{n}\left(b_{ij}^{I}+b_{ij}^{II}\right)I_{sj}=-B_{\text{ext}} \qquad (6.3\text{-}1)$$

where $z = 0$ is the plane of the first film, indicated by the superscript *I*, and $z = c$ is the plane of the second film, indicated by the superscript *II*. The elements of matrices $\mathbf{b^I}$ and $\mathbf{b^{II}}$ are given by Eqs. (6.1.2-3) and (6.1.2-2b) respectively as

$$b_{ij}^{I}=\frac{\mu_0 w}{2\pi}\left[\frac{K(k_{ij}^{I})}{(r_j+r_i)}+\frac{E(k_{ij}^{I})}{(r_j-r_i)}\right], \qquad (6.3\text{-}2)$$

where $k_{ij}^{I}=\dfrac{4r_i r_i}{(r_j+r_i)^2}$,

and $$b_{ij}^{II}=\frac{\mu_0 w}{2\pi\sqrt{(r_j+r_i)^2+c^2}}\left\{K(k_{ij}^{II})+\frac{r_j^{\,2}-r_i^{\,2}-c^2}{(r_j-r_i)^2+c^2}E(k_{ij}^{II})\right\} \qquad (6.3\text{-}3)$$

where $k_{ij}^{II}=\dfrac{4r_j r_i}{(r_j+r_i)^2+c^2}$.

Solution of Eq. (6.3-1) yields the zero-flux current distribution from which we then calculate the J_c-limited current distribution following the same algorithm as in the case of a single film.

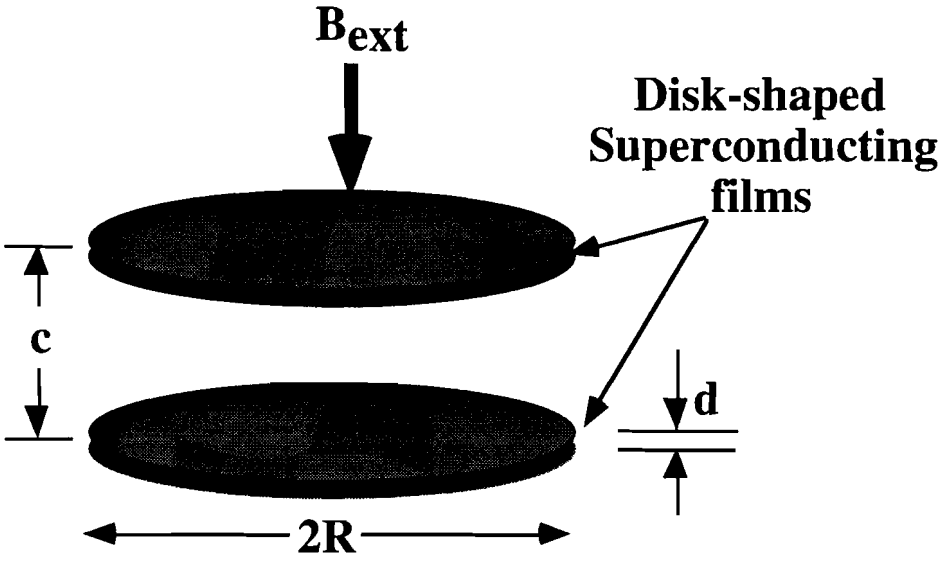

Figure 6.3.1 Two identical coaxial disks of thickness d and radius R separated by a distance c. The external field is parallel to the axis of the disks.

6.3.1 Effect of radial magnetic field

In contrast to the case of a single thin film disk, where the radial component of the field is zero at the plane of the film, there will be a small radial component of the field produced by screening currents in one film at the plane of the other film. The presence of this radial field (B_r) does not change the current distribution appreciably and therefore has been ignored. The radial field produced by the film *II* (at z=c) at the plane of the film *I* (at z=0) is given by,

$$B_r(r_i,\phi,0) = \sum_{j=1}^{n} b_{ij}^{r\,II} I_{sj}, \qquad (6.3.1\text{-}1)$$

where the elements of matrix $\mathbf{b}^{\mathbf{r}\,\mathbf{II}}$ are given by Eq. (6.1.2-2a) as,

$$b_{ij}^{r\,II} = -\frac{\mu_0 wc}{2\pi r_i\sqrt{(r_j+r_i)^2+c^2}}\left[-K(k_{ij}^{II})+\frac{r_j^2+r_i^2+c^2}{(r_j-r_i)^2+c^2}E(k_{ij}^{II})\right]. \qquad (6.3.1\text{-}2)$$

This radial field is compensated inside film *I* by an anti-symmetric component of the azimuthal screening currents at the top and the bottom surface of the film. This can be understood by assuming that the top half of the film carries a surface current

distribution of $(\mathbf{I_s} + \Delta\mathbf{I_s})/2$ and the bottom half carries a surface current distribution of $(\mathbf{I_s} - \Delta\mathbf{I_s})/2$. While the axial field (B_Z) remains unchanged, this current distribution produces a self-induced radial field inside the film. This self-induced radial field cancels the radial field produced by screening currents in the other film. The self-induced radial field due to two half-disks at $z = \pm d/2$, at the central plane of the film (z=0) is given by,

$$B_r(r_i,\phi,0) = \sum_{j=1}^{n} b_{ij}^{r'} \frac{I_{sj} + \Delta I_{sj}}{2} + \sum_{j=1}^{n} \left(-b_{ij}^{r'}\right) \frac{I_{sj} - \Delta I_{sj}}{2} = \sum_{j=1}^{n} b_{ij}^{r'} (\Delta I_{sj}), \quad (6.3.1\text{-}3)$$

The elements of matrix $\mathbf{b^{r'}}$ in Eq. (6.3.1-3) are given by[4],

$$b_{ij}^{r'} = \frac{\mu_0 w(d/2)}{2\pi r_i \sqrt{(r_j + r_i)^2 + (d/2)^2}} \left[-K(k^{r'}) + \frac{r_j^2 + r_i^2 + (d/2)^2}{(r_j - r_i)^2 + (d/2)^2} E(k^{r'}) \right], (6.3.1\text{-}4)$$

where $k^{r'} = \dfrac{4 r_i r_j}{(r_j + r_i)^2 + (d/2)^2}$.

To calculate the anti-symmetric component of the surface current ($\Delta\mathbf{I_s}$), we solve the matrix equation

$$\mathbf{b^{r'}} \mathbf{I}_s + \mathbf{b^{r''}} \Delta\mathbf{I}_s = 0, \text{ or } \Delta\mathbf{I}_s = -\left(\mathbf{b^{r''}}\right)^{-1} \mathbf{b^{r'}} \mathbf{I}_s. \quad (6.3.1\text{-}5)$$

For films of thickness d = 500 nm, separated by c = 2 mm, $\Delta\mathbf{I_s}$ is an order of magnitude smaller than $\mathbf{I}_s$. We can therefore, get a good estimate of flux penetration and pinning from considering the axial component of magnetic field only. Subdivision of the disk along the thickness and analysis of radial field provides interesting insights to the problem. For example $B_r \propto 1/z$ for small z.[5] The component of the Lorentz force ($\overline{F} = \hat{\phi} J_\phi \times \hat{r} B_r$) on the vortices due to the radial field (B_r) is vertical ($\hat{z}$). The vertical

---

[4] An important difference between the self-radial field matrix $\mathbf{b^{r'}}$ and the axial field matrix $\mathbf{b^{I}}$ is that the former calculates the field at the center of the film due to a current differential on either side, while the latter ignores the variation of current distribution along the film thickness.

[5] See Appendix 2 for a detailed analysis.

dimension of the disk (500 nm) is very small compared to the radius (5 mm). Therefore, even if the vortices entering the disk are not exactly vertical their motion is primarily limited by the vertical ($\hat{z}$) component of the field. Our analysis suggests that the field lines inside the disk are indeed nearly vertical, since the radial component is small. We can incorporate a complete self-consistent analysis taking into account the radial fields as well as the axial fields in our model. This, however, requires decreasing the width of each current ring to a size comparable to the thickness of the film[6] and subdivision of the disk along its thickness, corresponding to a thousand times more current elements. The increase in the complexity of computation and the computational time does not seem justifiable for the accuracy required for our analysis.

---

[6] As explained in Appendix 2, the radial field contribution at a point is due to an azimuthal current loop directly above (or below) the point and falls off as 1/z in the near field. We approximate the surface current distribution by dividing it into discrete loops of thickness w=R/n. Therefore, the width of the discrete loops (w) has to be of the order of the distance (z) between the point of observation and the location of the current ring. This distance is a fraction of the film thickness. In other words, w<d for accurate evaluation and would require n>10,000.

6.4 Transient analysis of current and magnetic field

6.4.1 Case I (single disk)

In this section we calculate the changes in the current and field distributions following a transition of the superconducting disk into its normal state ($T > T_c$). Initially we shall assume that this transition is instantaneous. When the film becomes resistive, the screening currents decay, allowing flux to move in. The process of flux entry associated with the decay of current is calculated by the time evolution of the magnetic vector potential.

The flux-diffusion equation can be derived in terms of the vector potential (A_ϕ) from the following well known relation :

$$E_\phi = -\nabla V - \frac{\partial A_\phi}{\partial t}. \qquad (6.4.1\text{-}1)$$

For the circular current distribution described in Section 6.1, the voltage (V) in a loop can not have a spatial variation, implying $\nabla V = 0$. Using the sheet resistance (R_σ) of the disk in the normal state, Eq. (6.4.1-1) can be written, in terms of surface current (I_s) as

$$\frac{\partial A_\phi}{\partial t} = -R_\sigma I_s. \qquad (6.4.1\text{-}2)$$

For a given surface current distribution, $\mathbf{I_s}$, we can get the vector potential at the plane of the film as

$$A_\phi(r_i) = \sum_{j=1}^{n} a_{ij} I_{sj}$$

or in matrix notation, $\mathbf{A} = \mathbf{a}\mathbf{I_s}$.[7] (6.4.1-3)

---

[7] The subscript ϕ in the expression of vector potential is dropped for simplicity. Unless otherwise specified it will be assumed that A has only $\hat{\phi}$-component.

The elements of **a** are given by Eq. (6.1.1-6) as

$$a_{ij} = \frac{\mu_0 w(r_j + r_i)}{2\pi r_i}\left[\left(1 - \frac{k_{ij}}{2}\right)K(k_{ij}) - E(k_{ij})\right], \qquad (6.4.1\text{-}4)$$

where $k_{ij} = \dfrac{4r_i r_j}{(r_i + r_j)^2}$. Equation (6.4.1-2) can now be written in matrix notation as

$$\frac{\partial \mathbf{A}}{\partial t} = -R_\sigma \mathbf{I_s}. \qquad (6.4.1\text{-}5)$$

Starting with the initial current and potential distributions, $\mathbf{I}_s(t = 0)$ and $\mathbf{A}(t = 0)$, we calculate the time evolution of potential, current, and field using discrete time increments (Δt). From Eq. (6.4.1-5), we get at time $t + \Delta t$,

$$\mathbf{A}(t + \Delta t) = \mathbf{A}(t) - R_\sigma \Delta t \mathbf{I_s}, \qquad (6.4.1\text{-}6)$$

$$\mathbf{I_s}(t + \Delta t) = \mathbf{a}^{-1}\mathbf{A}(t + \Delta t)\ , \qquad (6.4.1\text{-}7)$$

and

$$\mathbf{B_z}(t + \Delta t) = \mathbf{b}\mathbf{I_s}(t + \Delta t)\ . \qquad (6.4.1\text{-}8)$$

6.4.2 Case II : Two identical disks

In the case of two identical films placed parallel to each other, separated by a distance c, we proceed by evaluating the total vector potential at the surface of one of the films produced by currents in both the films. Using superscripts *I* and *II* to denote the two films as in Eq. (6.3-1), we express the elements of matrix **a** at the plane of film *I* as,

$$a_{ij} = a_{ij}^{I} + a_{ij}^{II}\ , \qquad (6.4.2\text{-}1)$$

where

$$a_{ij}^{I} = \frac{\mu_0 w}{2\pi}\left(1 + \frac{r_j}{r_i}\right)\left\{\left(1 - \frac{k_{ij}^{I}}{2}\right)K\left(k_{ij}^{I}\right) - E\left(k_{ij}^{I}\right)\right\}\ ,$$

and

$$a_{ij}^{II} = \frac{\mu_0 w}{\pi}\sqrt{\frac{r_j}{r_i k_{ij}^{II}}}\left\{\left(1 - \frac{k_{ij}^{II}}{2}\right)K\left(k_{ij}^{II}\right) - E\left(k_{ij}^{II}\right)\right\}\ ,$$

k_{ij}^{I} and k_{ij}^{II} being the same quantities defined in Eqs. (6.3-2) and (6.3-3). Equations (6.4.1-6)–(6.4.1-8) can then be used to calculate the current and field distributions as they evolve in time. Fig. 6.4.2.1 shows the surface current and field distribution at different instants of time, for a 0.5-μm-thick film with $J_c = 5 \times 10^7$ A/cm^2 and sheet-resistance (R_σ) of 1 Ω, in an externally applied field (B_{ext}) of –0.2 T. The time scales with $\mu_0 R/R_\sigma$.

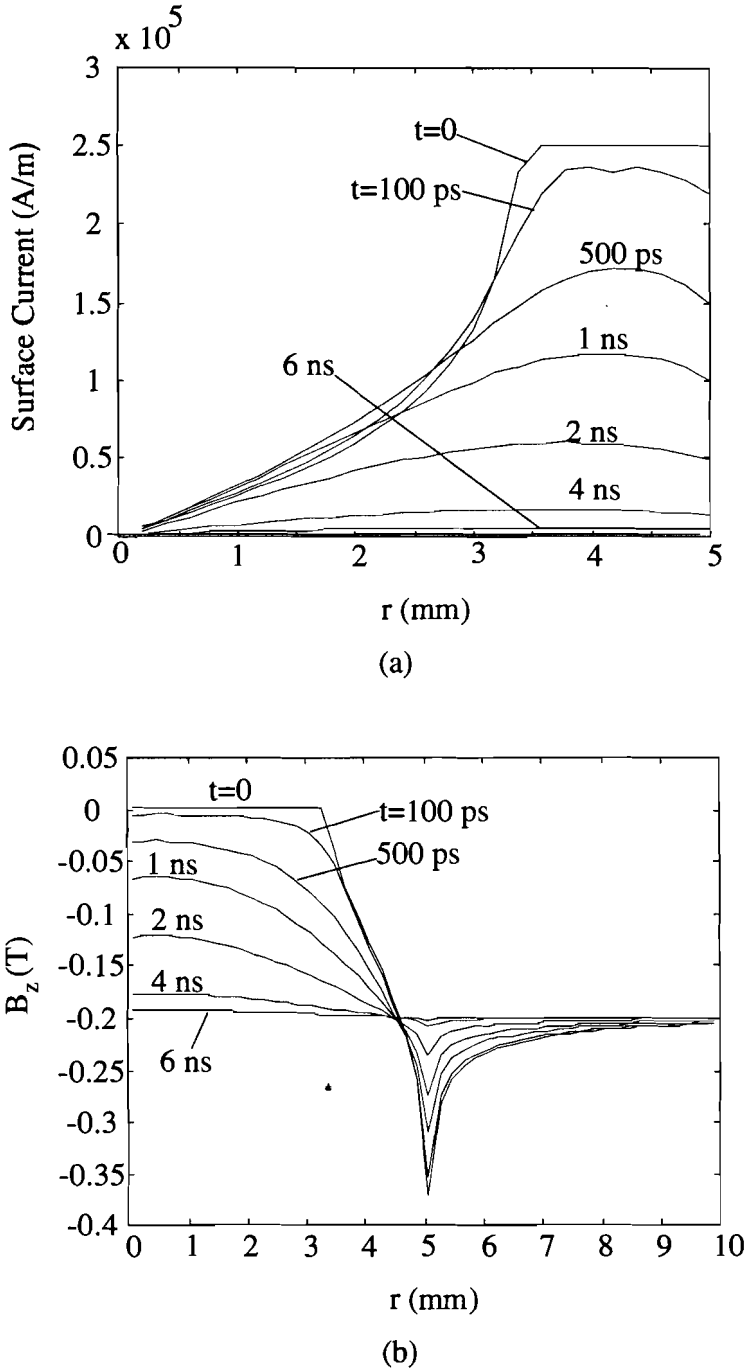

Figure 6.4.2.1 (a) Surface current ($I_S(r,t)$), and (b) magnetic field ($B_Z(r,z=0,t)$) distributions at different instants of time. This is for the two identical 1 cm diameter, 500 nm thick films centered at $r = 0$ and separated by 2 mm, with J_c=5.10^7 A/cm^2. The external field is 0.2 T. The films become resistive ($R_\sigma = 1\Omega$) at t=0.

6.5 Coupling of transient flux in an output (secondary) coil

In order to make a switch, the additional flux that moves into the excluded volume between the two films must couple to a secondary coil. Fig. 6.5.1 shows the two films with the secondary coil placed between them.

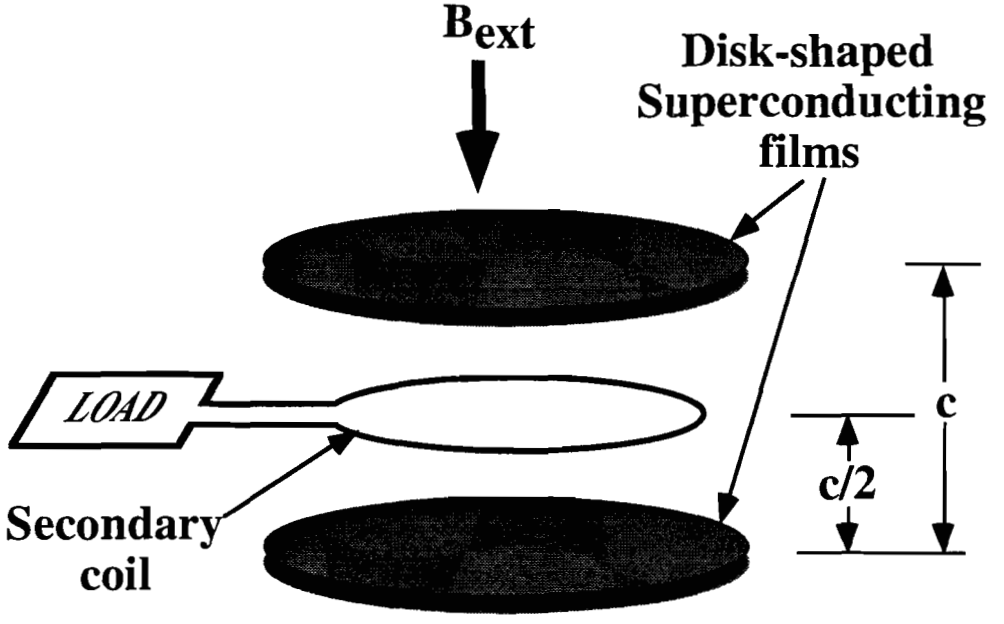

Figure 6.5.1 A secondary coil, connected with the load circuit placed halfway between two superconducting disks.

Therefore, the flux motion will be governed by the circuit comprising the films and the secondary coil. This circuit analysis is carried out by modeling the film rings with lumped self and mutual inductances and resistances. We shall discuss the technique of calculation of mutual inductance between two coaxial current loops and then proceed with the circuit analysis.

6.5.1 Mutual inductance between two coaxial circular loops

Fig. 6.5.1.1 shows two coaxial circular loops of radii a and b, carrying currents I_a and I_b are separated along the axis ($\hat{z}$) by a distance c. Mutual inductance (M_{ab}) between the two loops is defined as the flux produced at the loop b by unit current in loop a.

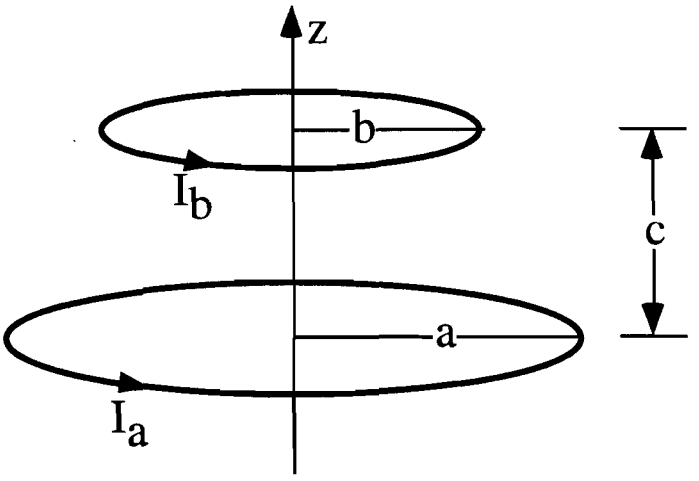

Figure 6.5.1.1 Two coaxial circular loops of radii a and b, carrying currents I_a and I_b are separated along the axis ($\hat{z}$) by a distance c.

Since the loops are coaxial the vector potential due to one loop is the same at all points of the other loop. Therefore,

$$M_{ab} = \frac{\Phi_{ab}}{I_a} = \frac{\oint \bar{A}_a \bullet d\bar{l}_b}{I_a} = \frac{2\pi b A_a}{I_a}. \qquad (6.5.1\text{-}1)$$

Mutual inductance is reciprocal, $M_{ab} = M_{ba}$. Combining Eq. (6.5.1-1) with Eq. (6.1.1-5),

$$M_{ab} = 2\mu_0 \sqrt{\frac{ab}{k}}\left[(1-k/2)K(k) - E(k)\right] \qquad (6.5.1\text{-}2)$$

where $k = \dfrac{4ab}{(a+b)^2 + c^2}$. The expression for coplanar loops can be simplified by changing the modulus, k, and using the properties of the elliptic integrals.[8] Defining $k' = (b/a)^2$, for $b < a$, we can write

$$K(k) = (1+b/a)K(k'), \text{ and } \quad E(k) = \frac{2a}{a+b}E(k') - (1-b/a)K(k'). \qquad (6.5.1\text{-}3)$$

Mutual inductance can then be written as

---

[8] See Appendix I for details.

$$M_{ab} = 2m_0 a[K(k') - E(k')]. \qquad (6.5.1\text{-}4)$$

If $a < b$, we must interchange a and b in the above analysis. The modulus of elliptic integrals must be less than 1.

6.5.2 Circuit analysis of the coupled system

Let us first consider a single film placed near a single turn secondary coil of radius r_s. The film become resistive at $t = 0$. The inductance and resistance of the i^{th} ring (radius = r_i) is denoted by L_i and R_i respectively. The mutual inductance between two rings of radii r_i and r_j is denoted by M_{ij}. The secondary coil has an inductance of L_s and a resistance of R_s. The mutual inductance between the secondary coil and the i^{th} ring of the film is M_{si}. We now have $n + 1$ inductively coupled circuits. Using Kirchhoff's law in each circuit, we can write the following system of differential equations for currents I_i in each loop:

$$\mathcal{L}\frac{d\mathbf{I}}{dt} + \mathcal{R}\mathbf{I} = 0 \qquad (6.5.2\text{-}5)$$

where $\mathcal{L}$ and $\mathcal{R}$ are $(n + 1) \times (n + 1)$ matrices and $\mathbf{I}$ is a $(n + 1) \times 1$ vector. The matrix $\mathcal{L}$ is partitioned as shown in Fig. 6.5.2.1 below.

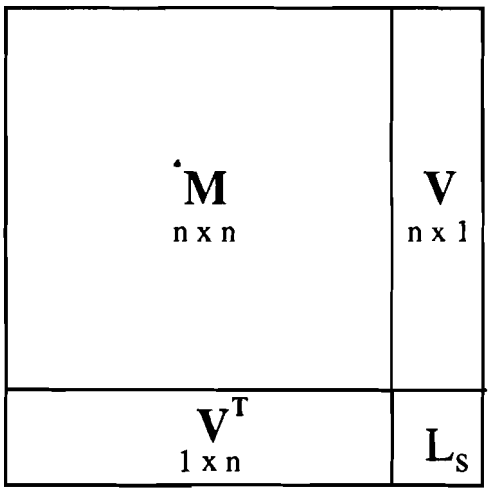

Figure 6.5.2.1 The inductance matrix $\mathcal{L}$, for a film coupled to the secondary coil, is partitioned into four submatrices: **M** represents the self and mutual inductances of n rings of the film, **V** and its transpose $\mathbf{V}^T$ represent mutual inductance between the secondary coil and the n rings of the film, and L_s is the self-inductance of the secondary coil.

M is a symmetric $n \times n$ matrix, whose main diagonal is given by,

$$\mathrm{M}_{ii} = L_i = \mu_0(r_i + q_i)\left[\left(1-\frac{k_i^f}{2}\right)K\left(k_i^f\right) - E\left(k_i^f\right)\right], \quad (6.5.2\text{-}2)$$

[9]

where $q_i = r_i - \frac{w}{2}$ and $k_i^f = \frac{4r_i q_i}{(r_i + q_i)^2}$.

The off-diagonal elements, M_{ij}, represent the mutual inductance between the i^{th} and j^{th} current loops. Since **M** is symmetric we need to calculate only the upper triangular elements. Using Eq. (6.5.1-4), we get the j^{th} superdiagonal (and the j^{th} sub-diagonal) of **M** as

$$M_{i(i+j)} = M_{(i+j)i} = 2\mu_0 r_{i+j}\left[K(k_{ij}^m) - E(k_{ij}^m)\right] \quad (6.5.2\text{-}3)$$

where, $k_{ij}^m = \left(r_i / r_{i+j}\right)^2$. **V** is a $n \times 1$ vector and $\mathbf{V}^{\mathbf{T}}$ is its transpose. The elements of **V**, representing the mutual inductance between the i^{th} current loop and the secondary coil can be calculated using Eq. (6.5.1-2) as

$$V_i = 2\mu_0\sqrt{\frac{r_i r_s}{k_i^s}}\left[\left(1-\frac{k_i^s}{2}\right)K\left(k_i^s\right) - E\left(k_i^s\right)\right] \quad (6.5.2\text{-}4)$$

where $k_i^s = \frac{4r_i r_s}{(r_i + r_s)^2 + (c/2)^2}$. The secondary coil inductance (L_S) can be approximated in the limit of $w_s << r_s$ as[10],

$$L_s = \mu_0(r_s - w_s/4)\left[\ln(16r_s/w_s) - 2\right] \quad (6.5.2\text{-}5)$$

where w_s is the width, and r_s is the radius of the coil. w_s = 200 μm is used for our calculations.

The matrix $\mathcal{R}$ is diagonal, with elements

---

[9] See Appendix 2

[10] See Appendix 2 for the formula of self-inductance of a current loop.

$$\mathcal{R}_{ii} = \frac{2\pi r_i}{w} R_\sigma, \tag{6.5.2-6}$$

and

$$\mathcal{R}_{(n+1)(n+1)} = \mathrm{R}_s \ . \tag{6.5.2-7}$$

We obtain the initial current distribution ($t = 0$) for $i = 1,..,n$ by multiplying the J_c-limited surface current (I_{si}) by the width w. At $t = 0$, current in the secondary coil, I_{n+1}, is zero. Solving Eq. (6.5.2-1) we get,

$$\mathbf{I}(t) = \exp\left(-\mathcal{L}^{-1}\mathcal{R}\, t\right)\mathbf{I}(0) \ . \tag{6.5.2-8}$$

$I_{n+1}(t)$ is the current in the secondary coil. We calculate the current vector $I(t)$ at each time interval Δt. The typical value for Δt was 100 ps; this is small compared to $\mu_0 R/R_\sigma = 6.3$ ns. The output voltage is given by

$$V_{\text{out}}(t) = I_{n+1} R_s \ . \tag{6.5.2-9}$$

For two films (at $z = 0$ and $z = c$) and a coil between them (at $0 < z < c$), the matrix $\mathcal{L}$ will be $(2n + 1) \times (2n + 1)$ and can be partitioned into smaller matrices as shown in Fig. 6.5.2.2.

M n x n	**G** n x n	$\mathbf{V}^{\mathrm{I}}$ n x 1
$\mathbf{G}^{\mathrm{T}}$ n x n	**M** n x n	$\mathbf{V}^{\mathrm{II}}$ n x 1
$\mathbf{V}^{\mathrm{I}\,\mathrm{T}}$ 1 x n	$\mathbf{V}^{\mathrm{II}\,\mathrm{T}}$ 1 x n	L_s

Figure 6.5.2.2 The inductance matrix $\mathcal{L}$, for two films, is partitioned into nine submatrices. **G** is the mutual inductance matrix between the two films, $\mathbf{V}^{I}$ and $\mathbf{V}^{II}$ represent mutual inductance between the secondary coil and the n rings of film I and film II. **M** and L_s are the same as in Fig. 6.5.2.1.

The matrix **M** represents the self and mutual inductances of the rings belonging to either film and is the same as defined in Eqs. (6.5.2-2) and (6.5.2-3). $\mathbf{V}^I$ and $\mathbf{V}^{II}$ are vectors representing the mutual inductance between the secondary coil and the rings of film I and II respectively. When the coil is placed at $z = c/2$, halfway between the two films, $\mathbf{V}^I = \mathbf{V}^{II} = \mathbf{V}$. The elements of matrix **G**, G_{ij} repre157sents the mutual inductance between the i^{th} ring of one film and the j^{th} ring of the other.

$$G_{ij} = 2\mu_0\sqrt{\frac{r_i r_j}{k_{ij}^c}}\left[\left(1-\frac{k_{ij}^c}{2}\right)K\left(k_{ij}^c\right)-E\left(k_{ij}^c\right)\right], \qquad (6.5.2\text{-}10)$$

where $k_{ij}^c = \dfrac{4r_i r_j}{\left(r_i + r_j\right)^2 + c^2}$.

The matrix $\mathcal{R}$ is diagonal, with elements

$$\mathcal{R}_{ii} = \mathcal{R}_{(n+i)(n+i)} = \frac{2\pi r_i}{w}R_\sigma \quad (\text{for } i = 1,2,\ldots,n) \qquad (6.5.2\text{-}11)$$

and

$$\mathcal{R}_{(2n+1)(2n+1)} = R_S \ . \qquad (6.5.2\text{-}12)$$

The initial condition ($t = 0$) for current vector **I** is

$$I_i(0) = I_{n+i}(0) = I_{si} \times w \quad (\text{for i=1,2,...,n}) \qquad (6.5.2\text{-}13)$$

and

$$I_{2n+1}(0) = 0 \ , \qquad (6.5.2\text{-}14)$$

where I_{si} is the J_c-limited surface current of the i^{th} ring of either film. The voltage across the secondary coil (V_{out}) is given by

$$V_{out}(t) = I_{2n+1}(t) \times R_S. \qquad (6.5.2\text{-}15)$$

Figure 6.5.2.3 compares the $V_{out}(t)$ for four different values of R_S. The secondary voltage is in the shape of a pulse, representing the varying speed of flux entry. The speed of flux entry, and therefore the rise and fall time of the pulse, is limited by the output circuit inductance and resistance. For higher resistance the flux entry is faster.

In Fig. 6.5.2.4 we compare the secondary current in the case of a single film with that in the case of two films. The distance between the coil and the film is the same in both cases. Better flux screening and, therefore, a larger output current is achieved with two films instead of one.

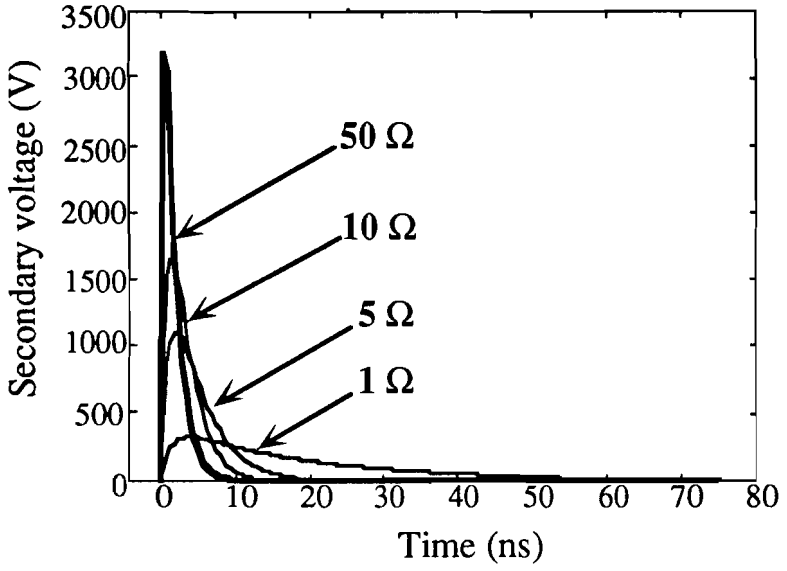

Figure 6.5.2.3 The voltage pulse produced at a single-turn secondary coil for different values of output resistance (R_s). Two identical 1-cm-diam, 500-nm-thick, disk-shaped superconducting films with $J_C = 5 \times 10^7$ A/cm^2 are placed on either side of a 4-mm-radius secondary coil at a distance of 1 mm. The externally applied field (B_{ext}) is –0.2 T. The films become resistive ($R_\sigma = 1\Omega/\text{sq}$) at t = 0.

Energy in the secondary circuit is given by,

$$E_{out}(t) = \int_0^t I_{2n+1}^2(t) R_s dt = \int_0^t \left(V_{out}^2 / R_s\right) dt. \qquad (6.5.2\text{-}16)$$

Part of the energy is dissipated in the films. The energy dissipated in each ring is given by,

$$E_i(t) = E_{n+i}(t) = \int_0^t I_i^2 \mathcal{R}_{ii} dt. \qquad (6.5.2\text{-}17)$$

So the fraction of energy (f) extracted by the secondary coil is given by,

$$f = \frac{E_{out}}{E_{total}} = \frac{\mathcal{R}_{(2n+1)(2n+1)} I_{2n+1}^2}{\sum_{i=1}^{2n+1} \mathcal{R}_{ii} I_i^2}. \qquad (6.5.2\text{-}18)$$

With an optimized output circuit this fraction is about 0.5.

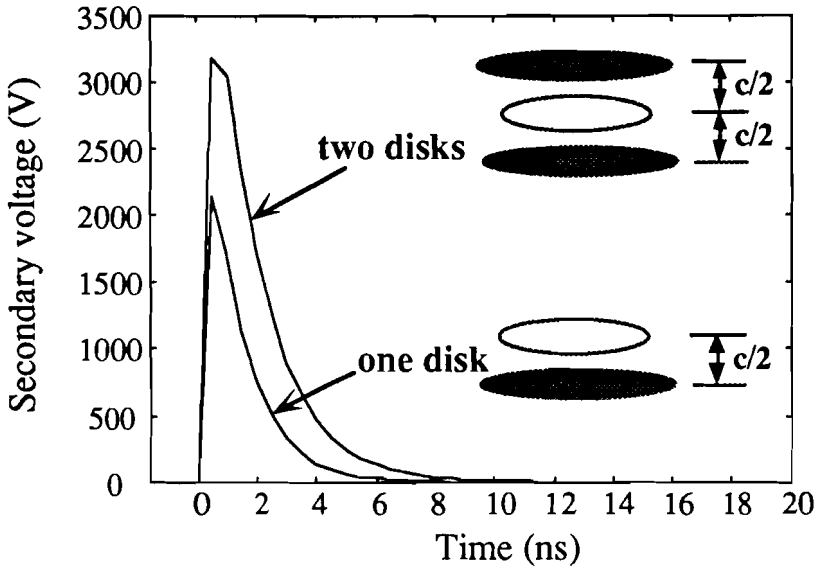

Figure 6.5.2.4 A comparison of secondary voltage pulses in the one-film and two-film configurations. In both cases output resistance is 50 Ω. The films are 1 cm in diameter, 500 nm thick with $J_c = 5 \times 10^7$ A/cm^2. External field is –0.2 T. The film(s) become resistive ($R_\sigma = 1\Omega/\text{sq}$) at t = 0.

We can also calculate the amount of flux coupled out in the secondary coil and an effective volume of exclusion (V_{excl}). The amount of flux coupled out is

$$\Phi_{out}(t) = \int_0^t V_{out}^2(t)dt, \qquad (6.5.2\text{-}19)$$

and can be normalized with respect to the flux in the secondary after complete penetration as

$$\phi_{out} = \frac{\Phi_{out}}{\pi r_s^2 B_{ext}}. \qquad (6.5.2\text{-}20)$$

For the values used in Fig. 6.5.5, $\phi_{out} = 0.73$. This can also be checked by calculating the amount of flux initially present in the coil before driving it normal. We can calculate the field distribution at the plane of the secondary coil as

$$\mathbf{B}_z(r, z = c/2) = \mathbf{b}^s \mathbf{I}_s(0), \tag{6.5.2-21}$$

where the matrix elements of $\mathbf{b}^s$ are given by,

$$b_{ij}^s = \frac{\mu_0 w}{2\pi\sqrt{(r_j + r_i)^2 + c^2/4}} \left\{ K(k_{ij}^s) + \frac{r_j^2 - r_i^2 - c^2/4}{\left(r_j - r_i\right)^2 + c^2/4} E(k_{ij}^s) \right\} \tag{6.5.2-22}$$

and $\mathbf{I}_s(0)$ is the surface current distribution at t=0. We integrate this field over the area of the secondary coil to obtain the amount of flux initially present in the coil,

$$\Phi_{init} = 2\pi \int_0^{r_s} B_z^s r dr = 2\pi w \sum_{i=1}^{r_s/w} r_i B_i^s. \tag{6.5.2-23}$$

The extracted flux, Φ_{out} is related to Φ_{init} as,

$$\Phi_{init} = \pi r_s^2 B_{ext} - \Phi_{out}. \tag{6.5.2-24}$$

The volume of exclusion can be estimated by dividing the total energy (E_{total}) by the energy density of the applied field as

$$\dot{V}_{excl} = \frac{E_{total}}{B_{ext}^2/2\mu_0}. \tag{6.5.2-25}$$

This can be expressed as a fraction (called the *volume coefficient*) of the spherical volume of radius R, the radius of the film. The volume coefficient (v) for the parameter values of Fig. 6.5.2.3 is $v = V_{excl} / \left(4\pi R^3/3\right) = 0.41$.

6.6 Heating below T_c : Flux-flow regime

So far we have assumed that the films are heated to their normal state ($T > T_c$); hence, the flux diffusion is governed by the normal state resistance (R_{ns}). If the films are heated to a temperature below the critical temperature (T_c), the critical depinning current is reduced, and flux diffusion takes place in the superconducting state. The vortices move radially inward because the current flows in the $\hat{\phi}$ direction. The resistance associated with the flux motion is the flux flow resistance ($R_{ff} = R_{ns}|B|/B_{c2}$), neglecting flux pinning. We can incorporate this in our model by changing the matrix $\mathcal{R}$ appropriately. For each time interval Δt, we calculate the field distribution from the current distribution using Eq. (6.4.1-8) and scale the value of sheet resistance to $R_\sigma = |B|/B_{c2}$. Fig. 6.6.1 shows the resultant secondary voltage, which is much slower than the case of heating to the normal state. The value for upper critical field along the c axis was taken to be 50 T.[127]

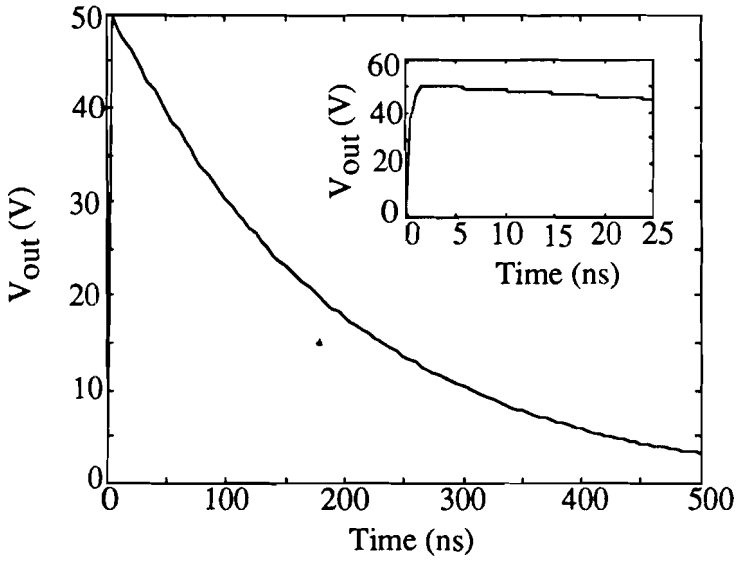

Figure 6.6.1 Voltage pulse for superconducting films heated to flux-flow regime. The films are 1 cm in diameter, 500 nm thick with $J_C = 5 \times 10^7$ A/cm^2 prior to heating and greatly reduced afterwards. External field is –0.2 T. A 50-Ω output resistance is assumed. B_{c2} is 50 T. The inset shows the rising edge of the voltage pulse with an expanded time scale.

6.7 Comparison with experimental results

We have seen in chapter 5 that the inductively coupled switch is based on the transient flux motion in superconducting films. The superconducting electromagnet (source) produces the external magnetic field and a single-turn copper secondary coil is used to couple out the excluded flux that moves in[128]. The films were irradiated by 150-ps Nd:YAG laser pulses. We observed output voltage pulses up to 80 V with a rise time of about 2 ns. In Fig. 6.7.1 we show one such pulse with a peak voltage of 45 V. It is compared to a voltage pulse calculated by our numerical technique. The critical current density (J_c) of the film was chosen to match the flux coupled out $\left[\Phi = \int V(t)dt\right]$. The value of J_c was found to be 1.33×10^6 A/cm^2, which is of the right order of magnitude. We measured the critical current density of the film to be 2.5×10^6 A/cm^2 at 77K and zero magnetic field. The slight discrepancy may be due to some reduction of J_c with magnetic field (section 3.3.9).

For our theoretical calculation instantaneous transition to the normal state was assumed. The thickness of the films used was 500 nm, which is much greater than the optical penetration depth (120 nm). Therefore, only the top part of the film absorbs the light initially and is heated above T_c. (section 4.5). The bottom part of the film remains superconducting, though carrying smaller screening currents due to a temperature rise. We have calculated the temperature profile along the thickness of the film as a function of time using a 1-D heat diffusion model. For the fluence levels used in our experiments (5–12 mJ/cm^2), the top 40% to 60% of the film is heated instantaneously above T_c. It takes 15–20 ns before the entire bulk of the film is normal. The magnetic flux starts moving in as soon as the laser illuminates the film, but the screening currents in the superconducting section of the film retard flux motion. The output voltage, the time derivative of flux coupled to the secondary coil, appears as a shorter and broader pulse compared to the case of instantaneous transition of the whole film to its resistive state. The effect of diffusive heating of the film on the speed of flux entry has been observed by varying the laser fluence.[11] There is good agreement between our theoretical simulation and experimental observation (Fig. 6.7.1). The apparent discrepancies between the peak voltages in the two cases can be explained by the thermal delay in optically thick films. Analyses combining the magnetic and the thermal

diffusion will be required in future for a complete quantitative characterization of the high-current switch.

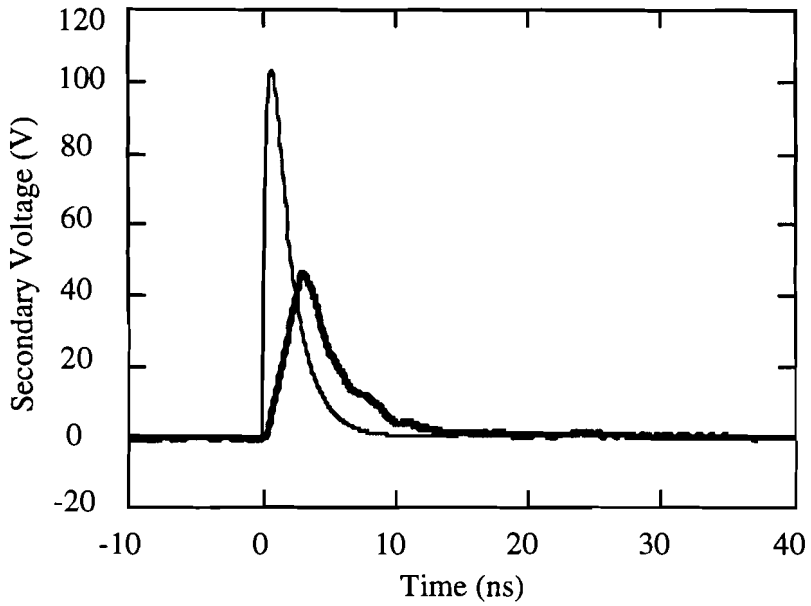

Figure 6.7.1 A comparison between the experimentally obtained voltage waveform (thick line) to one simulated by our model (thin line) , preserving the time integral of the output voltage. External field of 0.2 *T* was applied by a superconducting magnet to two 1-cm-diam films separated by 2 mm. The slower pulse onset in the experiment is due to inhomogeneous heating of the film, which was not accounted for in the model.

We have not noticed any difference between the square and the circular geometries experimentally. This is because the large field strength at the corners[11] of the square geometry will cause penetration and reduce the excluded region to a circle. Therefore the modeling with cylindrical geometry is appropriate even for square samples, especially since the analysis is simplified in the cylindrical geometry.

[11] due to demagnetization effect (section 3.3.5).

CHAPTER 7

CONCLUSION

High temperature superconducting devices will have a significant impact in the field of electrical engineering in the coming years. The research in this field can be categorized into three main categories : Materials, Large scale devices, and Electronics. In this thesis, we have tried to capture the flavors of each of these rapidly diverging categories. The thin film switching devices that we have studied probably belong to the third category since they are primarily electronic devices. However, the applications that we have focused on are large scale high power applications. Although thin films are almost never used in high power applications, we have attempted to demonstrate performance approaching moderately high current levels. The materials issues such as critical current density and flux dynamics in superconductors are of extreme importance. A detailed study of rapid flux motion, and thermal modeling of optically irradiated thin films for characterization of the switches was done. Although fabrication and processing of the thin film devices were not the main focus of this work, some work on sputter deposition of thin YBCO films and patterning them using wet etching and laser ablation methods was performed.

This research also addresses both the scientific and the engineering aspects. While studying interesting physical properties like the optical response and the critical state of the high temperature superconducting thin films, we have always been motivated by the engineering applications and carefully investigated the design issues.

Two different switching devices, the photoresistive switch and the inductively-coupled switch have been studied. The photoresistive switch precedes the inductively coupled switch, which was conceived to circumvent some contact problems with the former design. Since this idea was original and involved many challenging experimental and theoretical problems, most of the work has concentrated on this type of opening switch. Both designs take advantage of high absorption of near-infrared radiation of YBCO to achieve fast, efficient, and accurately controllable triggering with short (150-200 ps), Nd:YAG (λ = 1064 nm) laser pulses.

The photoresistive opening switch is a current diverter. The device switches to the resistive (or *open*) state from a zero-resistance superconducting (or *closed*) state upon optical triggering. High normal state resistance of the ceramic YBCO allows the current to transfer to a parallel load, when the switch opens. The switch is an 800 nm

thick, 100–250 μm wide microbridge, patterned by laser ablation. We have studied the response of the switch by varying three parameters : the laser fluence, initial temperature, and the current bias. Unlike most other groups studying photoresponse of superconducting films, we used optically thick films (thickness greater than the optical penetration depth 120–140 nm) for enhanced current capacity. For the first time, we observed a fast response in addition to a bolometric one, in thick films. Actually the delayed bolometric response, at lower temperatures, allowed us to clearly separate the fast (10 ns) response from the slower bolometric response. The experimentally observed thermal delay between the laser trigger (called the response time) and the onset of the bolometric response closely matches the result from a one-dimensional heat propagation model of the switch. The response time increases for lower values of laser fluence, initial temperature and the bias current. The fast switching component does not have any delay with respect to the laser trigger irrespective of laser fluence. We have not found a convincing argument regarding the origin of this fast component, which we believe was limited by the slow measuring system. Several nonbolometric mechanisms proposed in the literature have been considered and found either unsatisfactory or incompatible. A semi-quantitative agreement with the experimental results is found by an explanation based on an inductive response involving current redistribution, but hasn't been fully investigated. Preliminary experiments on a new design with a 1 cm wide, 500 nm thick switch geometry exhibits switching currents up to 80 A. A wider switch on a 2 in substrate will be tested in near future.

The inductively-coupled switch is a flux diverter. The switch is a thin superconducting film isolating two inductively coupled circuits, the source (primary) and the load (secondary). Irradiation with a laser pulse drives the switch to its resistive state causing the screening currents to decay. The excluded primary flux penetrates the film and couples to the secondary. The time derivative of the flux coupling at the secondary coil appears as a voltage pulse across the load. This switch has a contactless design and can be maintained at a different temperature from the primary or the secondary coil. Since the switch voltage is the time derivative of flux moving in or out of the film, the faster the flux motion, the higher the energy delivered at the load. Also, the fall time of the derivative response does not depend on the thermal recovery like the photoresistive switch.

We tested this idea at low magnetic fields, where the switch operated repetitively. Encouraged by the success of the low field experiment, we undertook a project to use this switch in conjunction with a large superconducting magnet, serving as the primary. This design is ideally suited for application in energy extraction from superconducting energy storage system[1][130], an emerging technology for power-quality improvement. In the high field regime, the vortex state, the flux motion is irreversible and the switching is single-shot. We did a series of experiments, changing the secondary coil design and the film configuration. The speed of flux entry depends on the inductive (L/R) response of the film and the secondary circuit. Best results (voltage pulse with rise times as short as 2.5 ns, a width of 10 ns and 75 V peak) were obtained with a single-turn secondary coil. Two films on either side of the secondary coil were used to obtain better flux screening.

The transient flux motion in high-T_c films in the vortex state is a complex and challenging problem. A thorough analysis of the screening current and magnetic field distributions in thin superconducting disks was performed. A novel technique, involving calculation of the magnetic vector potential in the cylindrical geometry, produced an efficient numerical algorithm for magnetostatic and transient analysis of the critical state. Our results exactly match the elegant analytical expression available under the simplifying assumption of field-independent critical current density, for the static case. Our analysis and the associated numerical algorithms are flexible and adaptable to a variety of problems concerning macroscopic flux dynamics in superconductors. The experimental results are in good agreement with the predictions of the theoretical model.

These thin film switching devices are very fast and optically controlled. We were limited by the critical current density of the YBCO films, which though comparable to the state-of the-art thin films fall short of the requirements of a practical device by at least an order of magnitude. Larger devices, multiple devices operating in sequence, and devices based on bulk materials need to be studied in future.

---

[1]Although we have not established the practicality of this new design for energy extraction, we have obtained a patent on the optically triggered inductively-coupled opening switch [130].

BIBLIOGRAPHY

1. W. M. Parsons, "Mechanical Switches", *Opening Switches, Advances in Pulsed Power Technology*, Vol. 1, ed. A. Guenther, M. Kristiansen, and T. Martin, Plenum Press, New York 1987.

2. J. D. van Wyk, and J. A. Ferreira, "Some present and future trends in power electronic converters," *Proceedings of the 1992 International Conference on Industrial Electronics, Control, Instrumentation, and Automation*, vol. 1, San Diego, USA, Nov. 1992.

3. L. Nashelsky and R. Boylestad, *Devices : Discrete and Integrated*, ch. 7, Prentice-Hall Inc., New Jersey, 1981.

4. M. Kahn, "Solid State Opening Switches", *Opening Switches, Advances in Pulsed Power Technology*, Vol. 1, ed. A. Guenther, M. Kristiansen, and T. Martin, Plenum Press, New York 1987.

5. *Proceedings of 8th and 9th IEEE International Pulsed Power Conference* (IEEE, New York, 1991 and 1993).

6. K. H. Schoenbach and G. Schaefer, "Diffused Discharge Opening Switches", *Opening Switches*, Advances in Pulsed Power Technology, Vol. 1, ed. A. Guenther, M. Kristiansen, and T. Martin, Plenum Press, New York 1987.

7. R. W. Schumacher and R. J. Harvey, "Low Pressure Plasma Opening Switches", *Opening Switches*, Advances in Pulsed Power Technology, Vol. 1, ed. A. Guenther, M. Kristiansen, and T. Martin, Plenum Press, New York 1987.

8. R. J. Comisso et al, "The Plasma Erosion Opening Switch", *Opening Switches*, Advances in Pulsed Power Technology, Vol. 1, ed. A. Guenther, M. Kristiansen, and T. Martin, Plenum Press, New York 1987.

9. R. E. Reinovski, "Fuse Opening Switches for Pulse Power Applications", *Opening Switches*, Advances in Pulsed Power Technology, Vol. 1, ed. A. Guenther, M. Kristiansen, and T. Martin, Plenum Press, New York 1987.

10. B. N. Turman and T. J. Tucker, "Explosively-Driven Opening Switches", *Opening Switches*, Advances in Pulsed Power Technology, Vol. 1, ed. A. Guenther, M. Kristiansen, and T. Martin, Plenum Press, New York 1987.

11. N. C. Anderson, E. Thornton, O'Grady and Rellon, "An Explosive High Voltage Closing and Opening Switch", Proceedings of *8th IEEE International Pulsed Power Conference*, San Diego, California ,1991, ed. R. White and K. Prestwich.

12. T. L. Francavilla, R. D. Ford, W. H. Lupton, N. M. Alford, And C. S. Saunders, "An Explosive Opening Superconducting Switch", *IEEE Trans. on Magnetics,* vol. 27, no. 2, pp. 1870-1873, March 1991.

13. E. M. Honig, "Inductive Energy Storage Circuits and Switches", *Opening Switches*, Advances in Pulsed Power Technology, Vol. 1, ed. A. Guenther, M. Kristiansen, and T. Martin, Plenum Press, New York 1987.

14. P. Tixador, "Superconducting Current Limiters–Some Comparisons and Influential Parameters," *IEEE Trans. Appl. Supercond.*, vol. 4, no. 4, pp. 190-198, December 1994.

15. K. E. Gray and D. E. Fowler, "A superconducting fault-current limiter," *J. Appl. Phys.* vol. 49, no. 4, pp. 2546-2550, April 1978.

16. L. S. Fleishman, Yu. A. Bashkirov, V. A. Arestenu, Y. Brissette, and J. R. Cave, "Design Considerations for an Inductive High-Tc Superconducting Fault Current Limiter," *IEEE Trans. Appl. Supercond.*, vol. 3, no. 1, pp. 570-573, March 1993.

17. L. Salasoo, "Comparison of superconducting fault limiter concepts in electric utility applications," *IEEE Trans. Appl. Supercond.*, vol. 5, no. 2, pp. 1079-1082, June 1995.

18. V. Meerovich, V. Sokolovsky, G. Jung, S. Goren, "High-Tc Superconducting Inductive Current Limiter for 1kV/25A performance," *IEEE Trans. Appl. Supercond.*, vol. 5, no. 2, pp. 1044-1046, June 1995.

19. D. W. A. Willén and J. R. Cave, "Short Circuit Test Performance Of Inductive High Tc Superconducting Fault Current Limiters," *IEEE Trans. Appl. Supercond.*, vol. 5, no. 2, pp. 1047-1050, June 1995.

20. P. Tixador, "Experimental results on an hybrid superconducting current limiters," *IEEE Trans. Appl. Supercond.*, vol. 5, no. 2, pp. 1055-1058, June 1995.

21. W. Paul, T. H. Baumann, J. Rhyner, and F. Platter, "Tests of 100kW High-Tc Superconducting Fault Current Limiter," *IEEE Trans. Appl. Supercond.*, vol. 5, no. 2, pp. 1059-1062, June 1995.

22. M. Ichikawa and M. Okazaki, "A Magnetic Shielding Type Superconducting Fault Current Limiter Using a Bi2212 Thick Film Cylinder," *IEEE Trans. Appl. Supercond.*, vol. 5, no. 2, pp. 1067-1070, June 1995.

23. Yu. A. Bashkirov, I. V. Yakimets, L. S. Fleishman, and V. G. Narovlyanskii, "Application of Superconducting Shields in Current-Limiting and Special-Purpose Transformers," *IEEE Trans. Appl. Supercond.*, vol. 5, no. 2, pp. 1075-1078, June 1995.

24. M. Ferrier, "Stockage d'energie dans un enroulement supraconducteur," in *Low Temperature and Electric Power*, London England:1970,Pergamon, pp. 425-432.

25. R. W. Boom and H. A. Peterson, "Superconductive Energy Storage for Power Systems," *IEEE Trans. on Magnetics*, vol. MAG-8, no. 3, pp. 701-703, September 1972.

26. C. DeWinkel and J. D. Lamoree, "Storing Power for Critical Loads", IEEE Spectrum, pp. 38-42, June 1993.

27. X. Huang, S. F. Kral, G. A. Lehmann, Y. M. Lvovsky, and M. Xu, "30 MW Babcock and Wilcox SMES Program for Utility Applications," *IEEE Trans. Appl. Supercond.*, vol. 5, no. 2, pp. 428-432, June 1995.

28. C. A. Luongo, "Review of the Bechtel Team's SMES Design and Future Plans for a Technology Demonstartion Unit," *IEEE Trans. Appl. Supercond.*, vol. 5, no. 2, pp. 422-427, June 1995.

29. G. W. Ullrich, "Summary of the DNA SMES Development Program," *IEEE Trans. Appl. Supercond.*, vol. 5, no. 2, pp. 416-421, June 1995.

30. K. E. Gray, T. Lenihan, and J. Tarczon, "Thin Film Superconducting Switches," *IEEE Trans. on Magnetics*, vol. MAG-15, no. 1, pp. 175-177, January 1979.

31. T. L. Francavilla, D. L. Peebles, H. H. Nelson, J. H. Claassen, S. A. Wolf, and D. U. Gubser, "A Laser Quenched Superconducting Switch for Pulsed Power Applications," *IEEE Trans. on Magnetics*, vol. MAG-23, no. 2, pp. 1397-1400, March 1987.

32. Y. Tzeng, C. Cutshaw, T. Roppel, C. Wu, C. W. Tanger, M. Belser, R. Williams, and L. Czekala, "High-temperature superconductor opening switch," *Appl. Phys. Lett*, vol. 54, no. 10, pp. 949-950, March 1989.

33. A. V. Zharkov, E. V. Kalinin, V. A. Kashurnikov, and V. Yu. Kosyakov, "Operating regimes of an optically controlled superconducting switch in a system with an inductive store," *Sov. Phys. Tech. Phys.*, vol. 34, no. 10, pp. 1162-1164, October 1989.

34. V. Z. Kresin and S. A. Wolf, *Fundamentals of Superconductivity*, Plenum Press, New York 1990.

35. M. N. Wilson, *Superconducting Magnets*, Oxford University Press, Oxford 1983.

36. J. G. Bednorz and K. A. Muller, "Possible high-Tc superconductivity in Ba-La-Cu-O," *Z. Phys. B.*, vol. 64, pp. 189, 1986.

37. A. Santoro, "Crystallography" in *High Temperature Superconductivity*, ed. J. W. Lynn, Springer-Verlag, New York 1990.

38. J.Bardeen, L.N.Cooper, and J.R.Schrieffer, "Theory of superconductivity," Phys.Rev., Vol.108, pp.1175-1204, 1 December 1972.

39. T. Van Duzer and C. W. Turner, *Principles of Superconductive Devices and Circuits*, Elsevier North Holland Inc., New York, 1981

40. W. Buckel, *Superconductivity - Fundamentals and Application*, VCH Verlagsgesellschaft mbH, Weinheim, 1991

41. T. P. Orlando and K. A. Delin, *Foundations of Applied Superconductivity*, Addison-Wesley Publishing Company Inc., Reading, MA, 1991

42. M. Cyrot and D. Pavuna, *Introduction to Superconductivity and High-T_C Materials*, World scientific Publishing Co., Singapore 1992.

43. A. Umezawa, G. W. Crabtree, and J. Z. Liu, Physica C153-155, 1461 (1988).44.

44. A.A.Abrikosov, "On the magnetic properties of superconductors of the second group," *Sov.Phys., JETP*, Vol.5, pp.1174-1182, 15 December 1957.

45. C.P.Bean, "Magnetization of hard superconductors," *Phys. Rev. Lett.*, Vol. 8, pp.250-253, 15 March 1962.

46. Y.B.Kim, C.F.Hempstead, and A.R.Strnad, "Magnetization and critical supercurrents," *Phys. Rev.*, Vol. 129, pp. 528-535, 15, January 1963.

47. G. Costabile, R. De Luca, S. Pace, A. Saggese, and A. M. Testa, "Temperature and magnetic field dependence of critical currents in granular superconductors," *IEEE Trans. Appl. Supercond.*, vol. 5, no. 2, pp. 1395-1398, June 1995.

48. M. N. Cuthbert, et al., "Trânsport and Magnetisation Measurements of Bi2223/Ag Tapes and the Role of Granularity on Critical Current Limitation," *IEEE Trans. Appl. Supercond.*, vol. 5, no. 2, pp. 1391-1394, June 1995.

49. M. Dhallé, M. N. Cuthbert, J. Thomas, G. K. Perkins, A. D. Kaplin, M. Yang, and M. Gorringe, "Dissipation in BSCCO/Ag 2212 ribbons," *IEEE Trans. Appl. Supercond.*, vol. 5, no. 2, pp. 1317-1320, June 1995.

50. G. E. Alvarez, M. Koyanagi, H. Yamasaki, and M. Matsuda, "Effects of the Flux Creep and Pinning energies on the Critical Current Density of High Quality $Y_1Ba_2Cu_3O_X$ Epitaxial Films," *IEEE Trans. Appl. Supercond.*, vol. 5, no. 2, pp. 1533-1536, June 1995.

51. B. Zhao, S. Kuroumaru, Y. Horie, E. Yanada, T. Aomine, H. Okhubo, and S. Mase, "Flux creep in c-axis oriented $Y_1Ba_2Cu_3O_x$ epitaxial thin films," *Physica C*, vol. 179, pp. 138, 1991.

52. M. Velez, J. I. Martin, and J. L. Vicent, "Critical Current and Thermal Activation in a-axis oriented $EuBa_2Cu_3O_7$ thin films," *IEEE Trans. Appl. Supercond.*, vol. 5, no. 2, pp. 1537-1540, June 1995.

53. L. Schultz, B. Roas, P. Schmitt, P. Kummeth, and G. Saeman-Ischenko, "Comparison of the critical current anisotropy in YBaCuO and BiSrCaCuO films," *IEEE Trans. on Magnetics*, vol. 27, no. 2, pp. 990-996, March 1991.

54. D. P. Hampshire, K. E. Gray, and R. T. Kampwirth, "Scaling laws for the critical current density of NbN films in high magnetic fields," *IEEE Trans. Appl. Supercond.*, vol. 3, no. 1, pp. 1246-1252, March 1993.

55. V. M. Pan, V. F. Solovjov, V. L. Svetchnikov, and H. Freyhart, "Anisotropic flux pinning in $YBa_2Cu_3O_{7-\delta}$ single crystals," *IEEE Trans. Appl. Supercond.*, vol. 5, no. 2, pp. 1892-1895, June 1995.

56. J. E. Crow and N. Ong, "Thermal and Transport Properties", *High Temperature Superconductivity*, ed. J. W. Lynn, Springer-Verlag, New York 1990.

57. H. E. Fischer, S. K. Watson and D. G. Cahill, "Specific Heat, Thermal Conductivity and electrical Resistivity of High Temperature Superconductors," *Comments Cond. Mat. Phys.*, vol. 14, no. 2, pp. 65-127, 1988.

58. J. L. Cohn, S. A. Wolf, T. A. Vanderah, V. Selvamanickam and K. Salama, "Lattice Thermal conductivity of $YBa_2Cu_3O_{7-\delta}$," *Physica C*, 192(1992), pp. 435-442.

59. S. J. Hagen, Z. Z. Wang and N. P. Ong, "Anisiotropy of the thermal Conductivity of $YBa_2Cu_3O_{7-y}$," *Physical Review B*, vol. 40, no. 13, pp 1989-1992, 1989

60. C. Kittel, *Introduction to Solid State Physics*, 6th Edition, John wiley &Sons Inc., New York 1986.

61. C. D. Marshall et al, *Phys. Rev. B.*, vol. 43, pp. 2696, 1991.

62. L. J. Shaw-Klein, S. J. Burns, A. M. Kadin, S. D. Jacobs and D. S. Mallory, "Anisotropic Thermal Conductivity Of $YBa_2Cu_3O_{7-\delta}$ Thin Films", *Superconductor Science and Technology*, vol. 5, iss. 6, pp. 368-372, June 1992.

63. C. D. Marshall, A. Tokmakoff, I. M. Fishman, C. B. Eom, J. M. Phillips and M. D. Fayer, "$YBa_2Cu_3O_{7-x}$ films with MgO and $SrTiO_3$ substrates using the Transient Grating Method", *J. Appl. Phys.*, vol. 73, no. 2, pp. 850-857, 1993.

64. M. Nahum, S. Verghese, P. L. Richards and K. Char, "Thermal Boundary resistance for $YBa_2Cu_3O_{7-\delta}$ Films", *Appl. Phys. Lett.*, vol. 59, no. 16, pp. 2034-2036, October 1991.

65. Z. M. Zhang, B. I. Choi, T. A. Le, M. I. Flik, M. P. Siegel, and J. M. Phillips, "Infrared Refractive Index of Thin $YBa_2Cu_3O_7$ Superconducting Films," *Journal of Heat Transfer*, vol. 114, pp.644-652, August 1992.

66. I. Bozovic, K. Char, S. J. B. Yoo, A. Kapitulnik, M. R. Beasley, and T. H. Geballe, Z. Z. Wang, S. Hagen, N. P. Ong, D. E. Aspens, and M. K. Kelly, "Optical anisotropy of $YBa_2Cu_3O_{7-x}$", *Physical Review B*, Vol. 38, No. 7, pp. 5077-5080, September 1988.

67. S. L. Cooper, D. Reznik, A. Kotz, M. A. Karlow, R. Liu, M. V. Klein, W. C. Lee, J. Giapintzakis, D. M. Ginsberg, B. W. Veal, and A. P. Paulikas, "Optical studies of the a-, b-, and c-axis charge dynamics in $YBa_2Cu_3O_{6+x}$", *Physical Review B*, Vol. 47, No. 13, pp. 8233-8248, April 1993.

68. A. M. Kadin, P. H. Ballentine, J. Argana, and R. C. Rath, "High Temperature Superconducting Films by RF Magnetron Sputtering," *IEEE Transactions on Magnetics*, MAG-25, pp. 2437-2440 (1989).

69. P. H. Ballentine, "High Temperature Superconducting Thin Films : Sputter Deposition and Fast Optical Switching," *Ph.D. Thesis*, University of Rochester, 1993.

70. P. H. Ballentine, A. M. Kadin, M. A. Fisher, D. S. Mallory, and W. R. Donaldson, "Microlithography of High-Temperature Superconducting Films: Laser ablation vs. Wet Etching," *IEEE Transactions on Magnetics*, MAG-25, pp. 950-953 (1989).

71. D. Gupta, W. R. Donaldson, K. Kortkamp and A. M. Kadin, "Optically Activated opening Switches", SPIE. vol. 1632, *Optically Acivated Switching II*, ed. Lubriel, pp. 190-195, 1992.

72. D. Gupta, W. R. Donaldson, K. Kortkamp and A. M. Kadin,, "Optically Triggered Switching of Optically Thick YBCO Films", *IEEE Trans. Appl. Supercond.*, vol. 3, no. 1, pp. 2895-2898, March 1993.

73. Z. Chen, Y. Zhao, H. Yang, Z. Chen, D. Zheng, Y. Qian, B. Wu, and Q. Zhang, "Specific Heat Anomaly of Single Phase $YBa_2Cu_3O_{7-\delta}$ at Superconducting Transition Temperature," *Solid State Communications*, vol. 64, no. 5, pp. 685-687, 1987.

74. Y. Enomoto and T. Murakami, "Optical Detector Using Superconducting $BaPb_{0.7}Bi_{0.3}O_3$ Thin Films", *J. Appl. Phys.* 59(11), pp. 3807-3814, June 1986.

75. A. Frenkel, "High Temperature Superconducting Thin Films as Broadband Optical Detectors," *Physica C*, vol. 180, pp. 251-258, 1991.

76. P. L. Richards, J. Clarke, R. Leoni, Ph. Lerch, S. Verghese, M. R. Beasley, T. H. Geballe, R. H. Hammond, P. Rosenthal, and S. R. Spielman, "Feasibility of the high T_c superconducting bolometer," *Appl. Phys. Lett.* vol. 54, no. 3, pp. 283-285, 16 January 1991.

77. S. Verghese, P. L. Richards, K. Char, D. K. Fork, T. H. Geballe, "Feasibility of infrared imaging arrays using high T_c superconducting bolometer," *J. Appl. Phys.* vol. 71, no. 6, pp. 2491-2498, 15 march 1992.

78. M. Leung, P. R. Broussard, J.H. Claassen, M. Osofsky, S. A. Wolf, And U. Strom, "Optical detection in thin granular films of Y-Ba-Cu-O at temperatures

between 4.2 and 100 K," *Appl. Phys. Lett.* vol. 51, no. 24, pp. 2046-2047, 14 December 1987.

79. R. S. Nebosis, R. Steinke, P. T. Lang, W. Schatz, M. A. Heusinger, K. F.Renk, G. N. Gol'tsman, B. S. Karasik, A. D. Semenov, and E. M. Gershenzon, "Picosecond $YBa_2Cu_3O_{7-\delta}$ detector for far-infrared radiation," *J. Appl. Phys.* vol. 72, no. 11, pp. 5499-5499, 1 December 1992.

80. B. Dwir and D. Pavuna," A sensitive YBaCuO thin film bolometer with ultrawide wavelength response," *J. Appl. Phys.* vol. 72, no. 9, pp. 3855-3861, 1 November 1992.

81. X.He, J.Musolf, E.Waffenschmidt, K.Heime, H. Wolf, and K. Pierz, "Silicon Ion Implantation Of YBaCuO Films For Bolometer Applications," *IEEE Trans. Appl. Supercond.*, vol. 5, no. 2, pp. 2439-2442, June 1995.

82. E. Steinbeiß, W. Michalke, H. Neff, and B. Schwierzi, "Combined Photodiode And High-Tc Transition Edge Bolometer Function On Zirconia Buffered Silicon Membranes," *IEEE Trans. Appl. Supercond.*, vol. 5, no. 2, pp. 2416-2418, June 1995.

83. M. Zorin, G. N. Gol'tsman, B. S. Karasik, A. I. Elantev, E. M. Gershenzon, M. Lingren, M. Danerud, and D. Winkler, "Optical Mixing in $YBa_2Cu_3O_{7-x}$ Films," *IEEE Trans. Appl. Supercond.*, vol. 5, no. 2, pp. 2431-2434, June 1995.

84. D. E. Prober, "Superconducting terahertz mixer using a transition-edge bolometer," *Appl. Phys. Lett.* vol. 62, pp. 2119-2121, April 1993.

85. B. S. Karasik, G. N. Gol'tsman, B. M. Voronov, S. I. Svechnikov, E. M. Gershenzon, H. Ekström, S. Jacobsson, E. Kollberg, And K. S. Yngvesson, "Hot Electron Quasioptical Nbn Superconducting Mixer," *IEEE Trans. Appl. Supercond.*, vol. 5, no. 2, pp. 2232-2235, June 1995.

86. A. Skalare, W. R. McGrath, B. Bumble, H. G. Leduc, P. J. Burke, A. A. Verhijen, D. E. Prober, "A Heterodyne Receiver At 533 Ghz Using A Diffusion-

Cooled Superconducting Hot Electron Bolometer Mixer," *IEEE Trans. Appl. Supercond.*, vol. 5, no. 2, pp. 2236-2239, June 1995.

87 M. G. Forrester, M. Gottlieb, J. R. Gavaler, and A. I. Braginski, "Optical response of epitaxial films of $YBa_2Cu_3O_{7-\delta}$," *Appl. Phys. Lett.* vol. 53, no. 14, pp. 1332-1334, 3 October 1988.

88. M. G. Forrester, M. Gottlieb, J. R. Gavaler, and A. I. Braginski, "Optical response of epitaxial and granular films of $YBa_2Cu_3O_{7-\delta}$ at temperatures from 25 K to 100 K," *IEEE Trans. on Magnetics*, vol. 25, no. 2, pp. 1327-1330, March 1989.

89. P. Langlois, D. Robbes, M. L. C. Singh, C. Gunther, D. Bloyet, J. F. Hamet, R. Desfeaux, and H. Murray, "Superconducting fast microbolometers operating below their critical temperature," *J. Appl. Phys.* vol. 76, no. 6, pp. 3858-3868, 15 September 1994.

90. A. D. Semenov, G. N. Gol'tsman, I. G. Gogidze, A. V. Sergeev, E. M. Gershenzon, P. T. Lang and K. F. Renk, "Subnanosecond Photoresponse of a YBaCuO Thin Film to Infrared and Visible Radiation by Quasiparticle Induced Suppression of Superconductivity", *Appl. Phys. Lett.* **60**(7), pp.903- 905, February 1992.

91. E. M. Gershenzon, G. N. Gol'tsman, A. D. Semenov and A. V. Sergeev, "Mechanism of Picosecond Response of granular YBaCuO Films to Electromagnetic Radiation", *IEEE Transactions on Magnetics*, vol. 27, no. 2, pp. 1321-1324, March 1991.

92. M. Nahum, "Design Analysis of a novel hot-electron bolometer," *IEEE Trans. Appl. Supercond.*, vol. 3, no. 1, pp. 2124-2127, March 1993.

93. A. Frenkel, M. A. Saifi, T. Venkatesan, C. Lin, X. D. Wu and A. Inam, "Observation of Fast Nonbolometric Optical Response of Nongranular High Tc $YBa_2Cu_3O_{7-x}$ Superconducting Thin Films", *Appl. Phys. Lett.*, **54**(16), pp. 1594-1596, April 1989.

94. A. Frenkel, M. A. Saifi, T. Venkatesan, P. England, X. D. Wu and A. Inam , "Optical Response of Nongranular High-Tc $YBa_2Cu_3O_{7-x}$ Superconducting Thin Films", *J. Appl. Phys.*, 67(6), pp. 3054-3068, March 1990.

95. M. Johnson, "Nonbolometric Photoresponse of $YBa_2Cu_3O_{7-\delta}$ Films", *Appl. Phys. Lett.*, vol. 59, no. 11, pp. 1371-1373, September 1991.

96. W. R. Donaldson, A. M. Kadin, P. H. Ballentine and R. Sobolewski, "Interaction of Picosecond Optical Pulses with High T_c Superconducting Films", *Appl. Phys. Lett.*, vol. 54, no. 24, pp. 2470-2472, June 1989.

97. H. S. Kwok, J. P. Zheng, Q. Y. Ying and R. Rao, "Nonthermal Optical Response of Y-Ba-Cu-O Thin Films", *Appl. Phys. Lett.*, vol. 54, no. 24, pp. 2473-2475, June 1989.

98. L. Shi, G. L. Huang, C. Lehane, D. H. Kim, and H. S. Kwok, "Study of photoresponse of high-Tc Y-Ba-Cu-O superconducting ultrathin films using a picosecond laser pulse train," *Appl. Phys. Lett.*, vol. 63, no. 20, pp. 2830-2832, 15 November 1993.

99. R. S. Nebosis, M. A. Heusinger, W. Schatz, K. F. Renk, G. N. Gol'tsman, B. S. Karasik, A. D. Semenov and G. M. Gershenzon, "Ultrafast Photoresponse of a Stuctured $YBa_2Cu_3O_{7-\delta}$ Thin Film to Ultrashort FIR Laser Pulses", *IEEE Trans. Appl. Supercond.*, vol. 3, no. 1, pp. 2160-2162, March 1993.

100. A. Ghis, S. Pfister, J. C. Villegier, M. Nail and J. P. Maneval, "Ultrafast nonbolometric Photoresponse of $YBa_2Cu_3O_{7-x}$ Thin Films", *IEEE Trans. Appl. Supercond.*, vol. 3, no. 1, pp. 2136-2139, March 1993.

101. N. Bluzer, "Temporal relaxation measurements of photoinduced nonequilibrium in superconductors," *J. Appl. Phys.*, vol. 71, no. 3, pp. 1336-1348, 1 February 1992. N. Bluzer, "Temporal relaxation of nonequilibrium in Y-Ba-Cu-O measured from transient photoimpedance response," *Phys. Rev. B*, vol. 44, no. 18, pp. 10222-10233, 1 February 1992.

102. N. Bluzer, "Biexponential Decay And Delay Artifact In The Photoresponse Of Superconductors", IEEE Transactions on Applied Superconductivity, vol. 3, no. 1, pp. 2869-2872, March 1993.

103. F. A. Hegmann, and J. S. Preston, "Origin of The Fast Photoresponse of $YBa_2Cu_3O_{7-\delta}$ Epitaxial Thin Films," *Phys. Rev. B*, vol. 48, pp. 16023, 1993.

104. F. A. Hegmann, D. Jacobs-Perkins, C.-C. Wang, S. H. Moffat, R. A. Hughes, J. S. Preston, M. Currie, P. M. Fauchet, T. Y. Hsiang, and R. Sobolowski, " Electro-optic sampling of 1.5-ps photoresponse signal from $YBa_2Cu_3O_{7-\delta}$ thin films," *Appl. Phys. Lett.*, vol. 67, no. 2, pp. 285-287, 10 July 1995.

105. A. M. Kadin, M. Leung, and A. D. Smith, "Photon-assisted vortex depairing in two-dimensional superconductors," *Phys. Rev. Lett.* vol. 65, pp. 3193-3196, 1990.

106. A. M. Kadin, M. Leung, A. D. Smith and J. Murdock, "Photofluxonic Detection : A New Mechanism for Infrared Detection in Superconducting Thin films", *Appl. Phys. Lett.*, vol. 57, pp. 2847-2849, December 1990.

107. J. C. Culbertson, U. Strom, S. A. Wolf, and W. W. Fuller, "Response of granular superconducting $YBa_{2.1}Cu_{3.4}O_{7-x}$ to light," *Phys. Rev. B*, vol. 44, no. 17, pp. 9609-9618, 1 November 1991.

108. S. Bhattacharya, M. Rajeswari, I. Takeuchi, X. X. Xi, S. N. Mao, C. Kwon, Q. Li, and T. Venkatesan, "Mechanisms of optical response in $YBa_2Cu_3O_{7-\delta}$ superconducting thin films and grain-boundary weak links," *J. Appl. Phys.*, vol. 76, pp. 2830, 1994.

109. A. Rothwarf and B. N. Taylor, "Measurement of Recombination Lifetimes in Superconductors", Phys. Rev. Lett, Vol. 19, No. 1, pp. 27-30, July 1967.

110. T. Yotsuya, H. Imokawa and Q. S. Yang, "Infrared Radiation Detection with $YBa_2Cu_3O_{7-d}$ microbridge", *Japanese Journal of Applied Physics*, vol. 30, no. 12B, pp. 2091-2094, December 1991.

111. E. Zeldov, N. M. Amer, G. Koren and A. Gupta, "Nonbolometric Optical Response Of $YBa_2Cu_3O_{7-\delta}$ Epitaxial Films", *Phys. Rev. B.*, vol. 39, no. 13, pp. 9712-9714, May 1989.

112. Chen-Lin Lee, "High Current Switching Using Thin Film Superconductors," *Summer Research Reports*, 1994 Summer Research Program for High School Juniors at the University of Rochester's Laboratory for Laser Energetics.

113. J. H. Claassen, M. E. Reeves, and R. J. Soulen, Jr., "A contactless metohd for measurement of the critical current density and critical temperature of superconducting films," *Rev. Sci. Instrum.*, vol. 62, pp. 996-1004, April 1991.

114. Th. Schuster, M. R. Kolischka, B. Ludescher, and H. Kronmüller, "Observation of inverse domains in high T_c superconductors," *J. Appl. Phys.* vol. 72, no. 4, pp. 1478-1485, August 1992.

115. T. Burke, J. Carter, M. Weiner, and N. Winsor, "Analysis of Current Multiplication Circuit utilizing Programmed Inductive Elements (PIE)," private communication; also presented at the IEEE's High Voltage Workshop, Monterey, CA, March 1988.

116. P. N. Mikheenko and Yu. E. Kuzovlev, *Physica C*, vol. 204, pp. 229, 1993.

117. E. H. Brandt, *Phys. Rev. B*, vol. 49, pp. 9024 (1994).

118. E. H. Brandt and M. Indenbom, *Phys. Rev. B* , vol. 48, pp. 12,893, 1993.

119. E. H. Brandt, "Square and Rectangular Thin Superconductors in a Transverse Magnetic Field," *Phys. Rev. Lett.*, vol. 74, no. 15, pp. 3025-3028, April 1995.

120. D. J. Frankel, *J. Appl. Phys.*, vol. 50, pp. 5402, 1979.

121. M. Däumling and D. C. Larbalestier, *Phys. Rev. B*, vol. 40, pp. 9350 (1989).

122. E. Zeldov, J. R. Clem, M. McElfresh, and M. Darwin, "Magnetization and transport currents in thin superconducting films,"*Phys. Rev. B*, vol. 49, pp. 9802, 1994.

123. H. Theuss, A. Forkl, and H. Kronmüller, *Physica C*, vol. 190, pp. 345, 1992.

124. W. R. Smythe, *Static and Dynamic Electricity* , McGraw-Hill, New York, 1950.

125. E. Durand, *Electrostatique et Magnétostatique* , Masson, Paris, 1953.

126. MATLAB, version 4.2, The Mathworks, Inc.

127. A. Bourdillon and N. X. Tan Bourdillon, *High Temperature Superconductors: Processing and Science* (Academic Press, Boston, 1994).

128. D. Gupta, W. R. Donaldson, and A. M. Kadin, "Transient Flux Dynamics in Optically Irradiated YBCO Thin-Film Switches," *IEEE Trans. Appl. Supercond.*, vol. 5, no. 2, pp. 1371-1374, June 1995.

129. M. Abramowitz and I. A. Stegun, *Handbook of Mathematical Functions*, Dover Publications, Inc., New York, 1965.

130. W. R. Donaldson, D. Gupta, and A. M. Kadin, "High Power Energy Transfer System Utilizing High Temperature Superconductors," U.S. Patent Number 5,339,062, Aug. 16, 1994.

APPENDICES

Appendix 1 : Elliptic Integrals and their properties

In our calculation of magnetic vector potential (A) and field (B), we have used *K(k)* and *E(k)* , the complete elliptic integrals of the first and second kinds, extensively. An elliptic integral of the first kind, $F(\varphi|k)$, is defined in terms of the parameter k as

$$F(\varphi|k)=\int_0^{\varphi}\left(1-k\sin^2\theta\right)^{-1/2}d\theta=\int_0^{\sin\varphi}\left[\left(1-t^2\right)\left(1-kt^2\right)\right]^{-1/2}dt, \qquad \text{(A1-1)}$$

and the elliptic integral of the second kind, $E(\varphi|k)$, is defined as

$$E(\varphi|k)=\int_0^{\varphi}\left(1-k\sin^2\theta\right)^{1/2}d\theta=\int_0^{\sin\varphi}\left(1-t^2\right)^{-1/2}\left(1-kt^2\right)^{1/2}dt. \qquad \text{(A1-2)}$$

When $\varphi=\pi/2$, the integrals are called complete. So *K(k)* and *E(k)* are defined as

$$K=K(k)=F(\pi/2|k)=\int_0^{\pi/2}\left(1-k\sin^2\theta\right)^{-1/2}d\theta, \qquad \text{(A1-3a)}$$

and

$$E=E(k)=E(\pi/2|k)=\int_0^{\pi/2}\left(1-k\sin^2\theta\right)^{1/2}d\theta \qquad \text{(A1-3b)}$$

The infinite series representations of *K* and *E* are as follows :

$$K(k)=\frac{\pi}{2}\left[1+\left(\frac{1}{2}\right)^2k+\left(\frac{1\cdot3}{2\cdot4}\right)^2k^2+\left(\frac{1\cdot3\cdot5}{2\cdot4\cdot6}\right)^2k^3+\cdots\right] \qquad \text{(A1-4a)}$$

$$E(k)=\frac{\pi}{2}\left[1-\left(\frac{1}{2}\right)^2\frac{k}{1}-\left(\frac{1\cdot3}{2\cdot4}\right)^2\frac{k^2}{3}-\left(\frac{1\cdot3\cdot5}{2\cdot4\cdot6}\right)^2\frac{k^3}{5}-\cdots\right] \qquad \text{(A1-4b)}$$

where $|k|<1$. The limiting values of K and E are

$$\lim_{k\to0}K(k)=\lim_{k\to0}E(k)=\pi/2, \qquad \text{(A1-5)}$$

$$\lim_{k\to1}K(k)=\infty, \qquad \text{(A1-6)}$$

and $$\lim_{k\to 1} E(k) = 1. \qquad \text{(A1-7)}$$

The divergence in Eq. (A1-6) is logarithmic. The cases of parameter k approaching unity are encountered in evaluation of self-inductance of a circular loop and calculation of radial field (B_r) just above a current loop. These are discussed in Appendix II.

An alternative evaluation of K and E, simplifies the expression of mutual inductance between two coplanar coaxial circular loops. This is done by changing the parameter k. Defining $k' = 1 - k$, we can write

$$K(k) = \frac{2}{1+\sqrt{k'}} K\left(\left[\frac{1-\sqrt{k'}}{1+\sqrt{k'}}\right]^2\right), \qquad \text{(A1-8a)}$$

and $$E(k) = \left(1+\sqrt{k'}\right) E\left(\left[\frac{1-\sqrt{k'}}{1+\sqrt{k'}}\right]^2\right) - \frac{2\sqrt{k'}}{1+\sqrt{k'}} K\left(\left[\frac{1-\sqrt{k'}}{1+\sqrt{k'}}\right]^2\right). \qquad \text{(A1-8b)}$$

Substituting c=0 in Eq. (6.5-2) gives the expression for mutual inductance between two coplanar coaxial circular loops as

$$M_{ab} = 2\mu_0 \sqrt{\frac{ab}{k}} \left[(1-k/2)K - E\right] = \mu_0 (a+b)\left[(1-k/2)K - E\right] \qquad \text{(A1-9)}$$

where $k = \dfrac{4ab}{(a+b)^2}$. Since

$$\sqrt{k'} = \sqrt{1 - \frac{4ab}{(a+b)^2}} = \frac{a-b}{a+b}, \qquad \text{(A1-10)}$$

and therefore, $$\left[\frac{1-\sqrt{k'}}{1+\sqrt{k'}}\right] = \frac{b}{a}, \qquad \text{(A1-11)}$$

Eqs. (A1-5a) and (A1-5b) simplify to

$$K(k) = \frac{a+b}{a} K\left(b^2/a^2\right), \qquad \text{(A1-12a)}$$

and $$E(k) = \frac{2a}{a+b} E\left(b^2/a^2\right) - \frac{a-b}{a} K\left(b^2/a^2\right). \qquad \text{(A1-12b)}$$

Substituting Eqs. (A1-12a) and (A1-12b) in (A1-9) we get

$$M_{ab} = 2\mu_0 a\left[K\left(b^2/a^2\right) - E\left(b^2/a^2\right)\right]. \tag{A1-13}$$

The derivatives of K and E with respect to $\kappa (= \sqrt{k})$, r and z are used to evaluate the magnetic field from the vector potential due to a circular current loop. By differentiating the series expansions in Eqs. (A1-4a) and (A1-4b), we obtain,

$$\frac{\partial K}{\partial \kappa} = \frac{E}{\kappa\left(1-\kappa^2\right)} - \frac{K}{\kappa}, \tag{A1-14a}$$

and

$$\frac{\partial E}{\partial \kappa} = \frac{E-K}{\kappa}. \tag{A1-14b}$$

For the vector potential due to a circular current loop of radius ρ,

$$k = \kappa^2 = \frac{4r\rho}{(r+\rho)^2 + z^2}. \tag{A1-15}$$

From Eq.(A1-15) we get

$$\frac{\partial \kappa}{\partial r} = \frac{\kappa}{2r} - \frac{\kappa^3}{4r} - \frac{\kappa^3}{4\rho} \tag{A1-16a}$$

$$\frac{\partial \kappa}{\partial z} = -\frac{z\kappa^3}{4r\rho} \tag{A1-16b}$$

Eqs. (A1-14a), (A1-14b), (A1-16a), (A1-16b) are used to derive Eqs. (6.1-8a) and (6.1-8b) from Eq. (6.1-7).

Appendix 2 : Two problems involving the logarithmic divergence

Here we shall discuss two different problems, (i) calculation of self-inductance of a thin circular loop, and (ii) evaluation of radial magnetic field just above or below a circular current loop. The reason for dealing with these two problems together is that the same mathematical manipulation required for the logarithmically diverging complete elliptic integral of the first kind, *K(k)*, occurs in both these problems.

As described in Eq. (A1-6) and Ref, K(k) diverges logarithmically as k approaches unity. We rewrite (A1-3a) as

$$\begin{aligned} K &= \int_0^{\pi/2} \left(1 - k\sin^2\theta\right)^{-1/2} d\theta \\ &= \int_0^{\pi/2-\phi_0} \left(1 - k\sin^2\theta\right)^{-1/2} d\theta + \int_{\pi/2-\phi_0}^{\pi/2} \left(1 - k\sin^2\theta\right)^{-1/2} d\theta \\ &= I_1 + I_2 \end{aligned} \tag{A2-1}$$

where $1-k << \phi_0 << 1$. We have decomposed the integral into two parts so that the diverging part (I_2), that occurs near π/2, has been separated from the nondiverging part (I_1) in the limit $k \to 1$. In both cases we make the following change of variables,

$$\phi = \pi/2 - \theta. \tag{A2-2}$$

The first part is given by,

$$\begin{aligned} \lim_{k\to 1} I_1 &= \lim_{k\to 1} \int_{\phi_0}^{\pi/2} \frac{d\phi}{\sqrt{1-k\cos^2\phi}} \\ &= \int_{\phi_0}^{\pi/2} \csc\phi d\phi \\ &= \ln\left(\tan\frac{\pi}{4}\right) - \ln\left(\tan\frac{\phi_0}{2}\right) \\ &\approx -\ln\frac{\phi_0}{2} \end{aligned} \tag{A2-3}$$

The second part is given by

$$\lim_{k\to 1} I_2 = \lim_{k\to 1} \int_0^{\phi_0} \frac{d\phi}{\sqrt{1-k\cos^2\phi}}$$

$$= \lim_{k\to 1} \int_0^{\phi_0} \frac{d\phi}{\sqrt{1-k\left(1-\phi^2\right)}}$$

$$= \lim_{k\to 1} \frac{1}{\sqrt{k}} \ln\left(2\phi_0\sqrt{\frac{k}{1-k}}\right)$$

$$= \ln\frac{2\phi_0}{\sqrt{1-k}} \qquad \text{(A2-4)}$$

Combining Eqs (A2-3) and (A2-4), we get

$$\lim_{k\to 1} K(k) = \ln\frac{2\phi_0}{\sqrt{1-k}} - \ln\frac{\phi_0}{2} = \ln\frac{4}{\sqrt{1-k}} \qquad \text{(A2-5)}$$

Problem 1 : Self-inductance of a thin loop

We shall now find an expression for the self-inductance of a thin loop of width w, and radius a , shown in Fig. (A2-1). The self-inductance (L) is given by the mutual inducatance of two rings with radii a and $b = a - w/2$. From (A1-13) we get,

$$L = M_{ab} = 2\mu_0 a\left[K\left(b^2/a^2\right) - E\left(b^2/a^2\right)\right]. \qquad \text{(A2-6)}$$

Since $w << b,a$,

$$k = (b/a)^2 = (1-w/2a)^2 \to 1. \qquad \text{(A2-7)}$$

Combining Eqs. (A2-5), (A1-7), and (A2-6), we get[1]

[1]This expression is similar to the one given in [39], but contains the next higher order term.

$$L = 2\mu_0 a\left[\ln\left(\frac{4}{\sqrt{1-(1-w/2a)^2}}\right)-1\right]$$
$$= \mu_0 a\left[\ln(16a/w)-2\right] \quad . \qquad \text{(A2-8)}$$

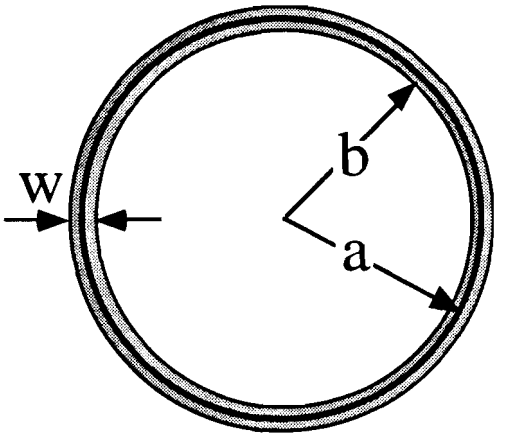

Figure A2.1 A thin loop of width w and radius a. The self-inductance of the loop is calculated in the limit $w << a$.

A better approximation can be obtained by using Eq. (A1-9) instead of Eq. (A1-13) for the expression of mutual inductance, since the value of k in that equation will be closer to unity.

$$L = M_{ab} = \mu_0(a+b)\left[(1-k/2)K - E\right], \qquad \text{(A2-9)}$$

where
$$k = \frac{4ab}{(a+b)^2} = \frac{1-w/2a}{(1-w/4a)^2}, \qquad \text{(A2-10)}$$

and therefore,
$$1-k = \left(\frac{w/4a}{1-w/4a}\right)^2 \approx (w/4a)^2 \qquad \text{(A2-11)}$$

Combining Eqs. (A2-5), (A1-7), (A2-9), (A2-10), and (A2-11), we get

$$L = \mu_0(2a-w/2)\left[\ln\left(\frac{4}{(w/4a)}\right)-1\right]$$
$$= \mu_0(a-w/4)\left[\ln(16a/w)-2\right] \qquad \text{(A2-12)}$$

Problem 2 : Radial field near a thin current loop

For a circular current loop of radius ρ carrying a current I (Fig. 6.1.2), the radial field is given by Eq. (6.1-7a) as

$$B_r(r,\phi,z)=\frac{\mu_0 Iz}{2\pi r\sqrt{(r+\rho)^2+z^2}}\left\{-K(k)+\frac{\rho^2+r^2+z^2}{(\rho-r)^2+z^2}E(k)\right\}, \quad \text{(A2-13)}$$

where $k=\dfrac{4r\rho}{(r+\rho)^2+z^2}$.

B_r changes sign at the plane of the loop (z = 0) and is positive above the loop (z > 0). The radial field is strong only when we are very close to the loop ($r \approx \rho$, and $z << \rho$).

The parameter k in Eq. (A2-13) for $r=\rho$ is

$$k=\frac{4\rho^2}{4\rho^2+z^2}\rightarrow 1. \quad \text{(A2-14)}$$

Combining Eqs. (A2-13), (A1-7), (A2-5) and (A2-14), we get

$$\begin{aligned} B_r &= \frac{\mu_0 Iz}{2\pi\rho\sqrt{4\rho^2+z^2}}\left\{-\ln\left(4\Big/\sqrt{1-\frac{4\rho^2}{4\rho^2+z^2}}\right)+\frac{2\rho^2+z^2}{z^2}\right\} \\ &\approx \frac{\mu_0 Iz}{4\pi\rho^2}\left\{\ln(z/16\rho)+\frac{2\rho^2}{z^2}\right\} \\ &\approx \frac{\mu_0 I}{\pi z} \end{aligned} \quad \text{(A2-15)}$$

B_r falls off as 1/z in the near-field close to the loop, since the logarithmic term diverges much more slowly than the $1/z^2$ term. For a superconducting disk modeled with azimuthal screening-current loops the effect will be somewhat smeared. At a point (r, ϕ, $z << \rho$) the primary contribution to B_r will be from the current loop directly below it. Since our model takes loops of width w and treats them as thin, the discretization needs to be fine ($w = R/n$ of the same order as thickness d) for an accurate evaluation of the self radial field discussed in section 6.3.1.

Appendix 3 : MATLAB Programs

We start with the calculation of the static current and field distributions assuming J_C is independent of B (*comparison_Mik.m*). The fluxmotion in one and two-film configurations are calculated with *fluxmotion.m* and *fluxmotion_2.m* respectively; only the latter in included. This is followed by one of the many similar programs for calculation of the simulated voltage pulse (*circuit_mod1.m*). Other variations (*circuit_mod2.m – circuit_mod5.m*) of this program calculate different voltage pulses for a set of critical current densities or field dependent current distribution (this uses the function *Jc_B2.m* or one similar to that), response in the flux flow regime and so on. Other variations compute the volume coefficient (*circuit_vol.m*) and extracted energy (*circuit_fracE.m*). Those are not included in this appendix. The self radial field (section 6.3.1) is calculated (*radial.m*) using a differential component of the surface current distribution. There are a number of functions that are used in these programs and are also included.

A3.1 comparison_Mik.m

```
%       Comparison of current distribution limited by the critical
%       current density in a superconducting film by our method
%       with that of Mikheenko and Kuzovlev
%
jc=5e11;                        % critical current density
t=0.5e-6;                       % thickness
isc=jc*t;                       % surface critical current
radius=5e-3;                    % radius of disk
n=100;                          % # of rings
mu=4*pi*1e-7;
drj=radius/n;                   % discrete intervals in radial direction
rj=drj:drj:radius;              % locations of I loops
rrj=drj:drj:(2*radius);
ri=rrj-drj/2;                   % locations of field/potential evaluation
x=(rj-drj)/radius;              % Mikheenko

% calculate the bz(i,j)s such that B(i)=b(i,j)I(j)

for j=1:n
```

```
        for i=1:2*n
                ki=(rj(j)*ri(i)*4)/(rj(j)+ri(i))^2; % ki=k^2=m (elliptic)
                        coeff=(drj*mu/2/pi)*(rj(j)/ri(i)+1);
                        [ellk,elle]=ellipke(ki);
                        a_sup(i,j)=coeff*((1-ki/2)*ellk-elle);
                        coeff1=(drj*mu/2/pi)/(rj(j)+ri(i));
                        coeff2=(rj(j)+ri(i))/(rj(j)-ri(i));
                        bz(i,j)=coeff1*(ellk+elle*coeff2);
        end
end
bz_sub=bz(1:n,:);
a=a_sup(1:n,:);

% solve the matrix equation bz.I=Q, where bz is the coefficient
% matrix and I and Q are I and bound. cond column vector
% and Bz=0 inside the disk Bz(i)=bz(i,j)I(j)=0

Bext=-0.2;
Q=linspace(-Bext,-Bext,n);
Is_deep=inv(bz_sub)*Q';                    % surface current
plot(rj*1000,Is_deep','y')
hold on

%       Mikheenko and Kuzovlev's flux free surface current density

Is_mik=(-Bext*4/pi/mu)*x./sqrt(1-x.^2);
plot(rj*1000,Is_mik','y--')
hold off

% Compute modified Is distribution so that Is in any ring
% is limited to Isc, the critical surface current.

m=n;
% critical_sum is the field due to the outer rings at Ic, for modification
% of Q. Q will be called q as its size diminishes with each iteration
% bzsmall is the corresponding submatrix of bz.

critical_sum=linspace(0,0,n);
while Is_deep(m) > isc
  Is_deep(m) = isc;                                    % limit Is to isc
  m=m-1;
  if m==0, break, end
        bzsmall=bz(1:m,1:m);
```

```
   p=isc.*bz(1:m,m+1);
   critical_sum=critical_sum(1:m)+p';
   q=Q(1:m)-critical_sum;
   cur=inv(bzsmall)*q';
   clear bzsmall;
   clear q;
   Is_deep(1:m)=cur;
end

%       Mikheenko's jc-limited current distribution

Hc=isc/2;                                       % screened field
a=1/cosh(Bext/Hc/mu);                           % a*radius=radius of flux-free region
for j=1:n
        if rj(j) > a*radius
                Is_mik(j)=isc;
        else
                Is_mik(j)=(isc*2/pi)*atan(x(j)*sqrt((1-a^2)/(a^2-x(j)^2)));
        end
end
plot(rj*1000,Is_deep','w')
hold on
plot(rj*1000,Is_mik','r')
hold off
title('Comparison of Mikheenko result with ours (Jc=5e7 A/cm^2, t=1e-6 m')
xlabel('radial distance from center (mm)')
ylabel('surface current density I (A/m)')

%       calculation of field by our method (Bz_deep)
Bz_deep=bz*Is_deep+Bext;

%       calculation of field by Mik's method (Bz_mik)
Bz_mik=bz*Is_mik'+Bext;

plot(ri*1000,Bz_deep,'w')
hold on
plot(ri*1000,Bz_mik,'r')
hold off
xlabel('radial distance from center (mm)')
ylabel('magnetic field B (T)')
title('Comparison of Mikheenko result with ours')
```

A3.2 fluxmotion_2.m

```
%       M-file to compute the time evolution of magnetic field
%       and current distribution, for two identical films.
%       It first calculates the surface current distribution
%       for a given  critical current density and then evolves
%       the current distribution using the relation dA/dt=-rho*J.

jc=5e11;                                % critical current density
t=0.5e-6;                               % thickness
isc=jc*t;                               % surface critical current
radius=5e-3;                    % radius of disk
n=25;                                   % # of rings
mu=4*pi*1e-7;
drj=radius/n;                   % discrete intervals in radial direction
rj=drj:drj:radius;              % locations of I loops
rrj=drj:drj:(2*radius);
ri=rrj-drj/2;                   % locations of field/potential evaluation
z=0:0.5e-3:2e-3;
nz=5;

% calculate a_sup and bz matrices
% such that A(i)=a(ij)Is(j) and Bz(i)=bz(ij)Is(j)

for i=1:2*n
 for j=1:n
  ki_1=(rj(j)*ri(i)*4)/(rj(j)+ri(i))^2;
  ki_2=(rj(j)*ri(i)*4)/((rj(j)+ri(i))^2+z(nz)^2);
        coeffa1=(drj*mu/2/pi)*(rj(j)/ri(i)+1);
        coeffa2=(drj*mu/pi)*sqrt(rj(j)/ri(i)/ki_2);
        coeff1=(drj*mu/2/pi)/(rj(j)+ri(i));
   coeff2=(rj(j)+ri(i))/(rj(j)-ri(i));
        coeff3=(drj*mu/2/pi)/sqrt((rj(j)+ri(i))^2+z(nz)^2);
  coeff4=(rj(j)^2-ri(i)^2-z(nz)^2)/((rj(j)-ri(i))^2+z(nz)^2);
        [ellk1,elle1]=ellipke(ki_1);
        [ellk2,elle2]=ellipke(ki_2);
        a1(i,j)=coeffa1*((1-ki_1/2)*ellk1-elle1);
        a2(i,j)=coeffa2*((1-ki_2/2)*ellk2-elle2);
        a_sup(i,j)=a1(i,j)+a2(i,j);
        bz1(i,j)=coeff1*(ellk1+elle1*coeff2);
        bz2(i,j)=coeff3*(ellk2+elle2*coeff4);
        bz(i,j)=bz1(i,j)+bz2(i,j);
 end
end
```

```
bz_sub=bz(1:n,:);
a=a_sup(1:n,:);

% solve the matrix equation bz.I=Q, where bz is the coefficient
% matrix and I and Q are I and bound. cond column vector
% and Bz=0 inside the disk Bz(i)=bz(i,j)I(j)=0

Bext=-0.2;
Q=linspace(-Bext,-Bext,n);
Is=inv(bz_sub)*Q';                          % surface current

% Calculate the field, B(i,j) at i and due to the
% computed Is distribution at j

Bz=bz*Is+Bext;

% For plotting play with the following commented lines
%plot(ri(1:n)*1000,B')
%print
%plot(rj*1000,I')
%hold on
%print

% Compute modified Is distribution so that Is in any ring
% is limited to Isc, the critical surface current.

m=n;

% critical_sum is the field due to the outer rings at Ic, for modification
% of Q. Q will be called q as its size diminishes with each iteration
% bzsmall is the corresponding submatrix of bz.

critical_sum=linspace(0,0,n);
while Is(m) > isc
  Is(m) = isc;                                    % limit Is to isc
  m=m-1;
  if m==0, break, end
        bzsmall=bz(1:m,1:m);
   p=isc.*bz(1:m,m+1);
   critical_sum=critical_sum(1:m)+p';
   q=Q(1:m)-critical_sum;
   cur=inv(bzsmall)*q';
   clear bzsmall;
```

```
   clear q;
   Is(1:m)=cur;
   %plot(rj*1000,I')
         Bz=bz*Is+Bext;
end
%print
%hold off
A=a*Is;
plot(rj*1000,Is','w')
%plot(ri*1000,Bz','w')
title('Time evolution of magnetic field as flux diffuses (Jc=5e7 A/cm^2')
xlabel('radial distance(mm)')
ylabel('Bz(r,t) in T')
hold on
% print

%%      For 3_D plots un-comment %% lines
%%columns=linspace(0,0,25);
%%rows=linspace(0,0,50);
%%B_rt=rows'*columns;
%%B_rt(:,1)=B;

%
         for i=1:n
                  for j=1:n
                           ki_mid=(rj(j)*ri(i)*4)/((rj(j)+ri(i))^2+z((nz+1)/2)^2);
                           coeff5=(drj*mu/2/pi)/sqrt((rj(j)+ri(i))^2+z((nz+1)/2)^2);
                  coeff6=(rj(j)^2-ri(i)^2-z((nz+1)/2)^2)/((rj(j)-ri(i))^2+z((nz+1)/2)^2);
                           [ellk,elle]=ellipke(ki_mid);
                           bz_center(i,j)=2*coeff5*(ellk+elle*coeff6);
                  end
         end

%        Time evolution of current, vector potential and field after it goes normal

% For total current un-comment %* lines
%* I_total=linspace(0,0,500);
dt=1e-11;                                  %       Time interval
sheetres=1;                                %       sheet resistance is 1 ohm
flux=linspace(0,0,600);
Energy=linspace(0,0,600);
Reff=linspace(0,0,600);
for i=1:600
```

```
A=A-(dt*sheetres).*Is;
Is=inv(a)*A;
Bz=bz*Is+Bext;
Bz_center=bz_center*Is+Bext;
flux(i)=-(2*pi*drj)*(ri(1:n)*(bz_sub*Is+Bext));

%% if floor(i/20)*20==i
%%  B_rt(:,(i/20))=B;
%% end

if i<=10
        if floor(i/10)*10==i
                plot(rj*1000,Is','w')
                %plot(ri*1000,Bz','w')
        end
elseif i<=100
        if floor(i/50)*50==i
                plot(rj*1000,Is','w')
                %plot(ri*1000,Bz','w')
        end
else
        if floor(i/200)*200==i
                plot(rj*1000,Is','w')
                %plot(ri*1000,Bz','w')
        end
end
end
hold off
time=dt*(1:1:600);
%plot(time*1e9,flux)
%title('Flux diffusion in the film (Jc=5e7 A/cm^2) ')
%xlabel('time(ns)')
%ylabel('Flux (Wb)')
%*plot(time*1e9,I_total)
%%time=dt*(20:20:500)
%%mesh(time*1e9,ri*1000,B_rt)
%
%       normalized flux=flux/(pi.r^2.B)
%
norm_flux_2=flux/(pi*radius^2*abs(Bext));
%subplot(2,1,1)
%plot(time*1e9,norm_flux_2,'w')
%title('Normalized Flux in the film (Jc=5e7 A/cm^2) ')
```

```
%xlabel('time(ns)')
%ylabel('normalized flux')
V=diff(flux)/dt;
%E=dt*sum(V.^2)
%subplot(2,1,2)
%plot(time(2:500)*1e9,V)
%title('Transient voltage due to flux diffusion (Jc=5e7 A/cm^2)')
%xlabel('time(ns)')
%ylabel('Voltage (V)')
```

A3.3 circuit_mod1.m

```
% M-File to calculate the output current for the inductive switch
% Version2
%       Note for Deep :  This is the basic program
%                        If you need to make changes use this as a reference but
%                        leave this one unchanged

%       Calculate Jc-limited current distribution (See Jc_B.m)

Jc_B

sheetres=1;
b=4e-3;                                  % radius of output coil
Rout=50;

% Initial current distribution (Static)

Iout(1)=0;
is(n+1:2*n)=is(1:n);
is(2*n+1)=Iout(1);
is0=is;

% In the plane of the film the argument of the elliptic
% functions is called kf, the one between the film1 and
% output coil is called kz1, the one between film2 and output
% coil is called kz2. If output coil is centrally placed
% kz1=kz2=kz. The argument for cross coupling between the films
% is called kc. The distance between the films is 2z.

z=c/2;
kz=((4*b).*r)./((r+b).^2+z^2);
kcmain=(r.^2)./(r.^2+z^2);
kf=(4.*q.*r)./(r+q).^2;
```

```
[ellkz,ellez]=ellipke(kz);
[ellkcm,ellecm]=ellipke(kcmain);
[ellkf,ellef]=ellipke(kf);

%       Construct the LM matrix for each film plane

L=mu.*(r+q).*((1-kf/2).*ellkf-ellef);          % Inductance of film_rings
% plot(r,L)
A1=diag(L);
for j=1:n-1
        for i=1:n-j
                ki=(r(i)/r(i+j))^2;
                [ellki,ellei]=ellipke(ki);
                M(i)=2*mu*r(i+j)*(ellki-ellei);
        end
        A1=A1+diag(M,j)+diag(M,-j);
        clear M;
end

% Calculate the coupling between two films

main_diag=(2*mu).*sqrt(r.^2+z^2).*((1-kcmain/2).*ellkcm-ellecm);
A3=diag(main_diag);
for j=1:n-1
        for i=1:n-j
                kc=4*r(i)*r(i+j)/((r(i)+r(i+j))^2+4*z^2);
                [ellkc,ellec]=ellipke(kc);
                M3(i)=mu*(r(i)+r(i+j))*((1-kc/2)*ellkc-ellec);
        end
        A3=A3+diag(M3,j)+diag(M3,-j);
        clear M3;
end
A(1:n,1:n)=A1;
A(n+1:2*n,1:n)=A3;
A(1:n,n+1:2*n)=A3;
A(n+1:2*n,n+1:2*n)=A1;
A(2*n+1,1:n)=(2*mu).*sqrt(r.*b./kz).*((1-kz./2).*ellkz-ellez);
A(1:n,2*n+1)=A(n+1,1:n)';
A(2*n+1,n+1:2*n)=A(2*n+1,1:n);
A(n+1:2*n,2*n+1)=A(1:n,2*n+1);
A(2*n+1,2*n+1)=mu*(b-dr/4)*(log(16*b/dr)-2);
V=eig(inv(A));
```

```
R(1:n)=(2*pi*sheetres/dr).*r;
R(n+1:2*n)=R(1:n);
R(2*n+1)=Rout;
B=diag(R,0);

Iout(1)=is0(2*n+1)*dr;
In(1)=is0(n)*dr;
I1(1)=is0(1)*dr;
dt=0.5e-9;
m=40;
time=0:dt:dt*m;
energy=0;
I=is0*dr;                          % current I is surface current X width

for i=1:m
        I=expm(-inv(A)*B*dt)*I;
        power=R.*I'.^2;
        energy=energy+power.*dt;
        %plot(r*1000,I(1:n)')
        Iout(i+1)=I(2*n+1);
        In(i+1)=I(n);
        I1(i+1)=I(1);
end

energy_film=sum(energy)-energy(2*n+1);
energy_out=energy(2*n+1);
fraction=energy_out/sum(energy);
total_energy=sum(energy);
Vout=Iout*Rout;
%plot(Rout,fraction)
%title('Fractional output energy as a function of output resistance')
%xlabel('Output resistance (ohms)')
%ylabel('fraction of energy in the output coil')
plot(time*1e9,Vout,'w')
hold on
        %plot(time*1e9,In,'r')
        %plot(time*1e9,I1,'g')
        %title('Time evolution of currents in the film and secondary coil')
        xlabel('time (ns)')
        ylabel('Secondary Voltage (V)')
        %text(20,800,'# of rings=25')
        %text(20,700,'Rout=1 ohm')
        %text(20,600,'Jc=7e8 A/cm^2')
```

```
%end
hold off
flux=sum(Vout)*dt
```

A3.4 radial.m

```
%       Calculates the self radial field due to a differential surface current component (section 6.3.1)

mu=4*pi*1e-7;
jco=5e11;
Bzext=-0.5;
thick=0.5e-6;
n=25;
radius=5e-3;
dr=radius/n;
r=dr:dr:radius;
q=r-dr/2;
%q(1)=r(1)-dr/4;
c=2e-3;
isco=jco*thick;
isc=isco*ones(n,1);

Q=-Bzext*ones(n,1);

%       get the bz coefficients for calculation of surface current Is

bz=bzcoeff2(Bzext,n,r,q,dr,c);
Is=inv(bz)*Q;

%       Plot zero-flux current distribution

plot(r*1000,Is','r')

%       Find jc-limited current distribution

Is=jclim(n,radius,Bzext,isc,bz);
%Is=isc
plot(r*1000,Is')
%axis([0 5 0 3e5])
%xlabel('r (mm)')
%ylabel('Is(A/m)')
hold on
br=brcoeff1(n,r,dr,c);
Br=br*Is;
```

```
%plot(q*1000,Br','y')

%       Self radial field of a thick disk (section 6.3.1)
%       Differential current distribution is Isd

%ccexp=1:1:7;
%cc=10.^(-ccexp);
%for i=1:7
%       brcc=brcoeff1(n,r,dr,cc(i));
%       Brcc=brcc*Is;
%       s(i)=sum(Brcc);
%end
%semilogx(cc,s,'r')

brd=brcoeff1(n,r,dr,2*dr);
Isd=0.5*inv(brd)*br*Is;
plot(r*1000,Isd','w')
```

A3.5 bzcoeff2.m

```
function [bz] = bzcoeff2(Bzext,n,r,q,dr,c)

%       Calculates bz coefficients for two superconducting disks
%       Bzext= Ext. Field in T (Negative) (e.g -0.5)
%       n = # of rings (e.g. 25)
%       radius = radius of film in m (0.5e-3)
%       c = Distance between films in m (2e-3)

mu=4*pi*1e-7;
%       Calculate the current distribution required for complete flux
%       exclusion for an applied external field Bext

for i=1:n
 for j=1:n
  ki_1=(r(j)*q(i)*4)/(r(j)+q(i))^2;
  ki_2=(r(j)*q(i)*4)/((r(j)+q(i))^2+c^2);
        coeff1=(dr*mu/2/pi)/(r(j)+q(i));
        coeff2=(r(j)+q(i))/(r(j)-q(i));
        coeff3=(dr*mu/2/pi)/sqrt((r(j)+q(i))^2+c^2);
        coeff4=(r(j)^2-q(i)^2-c^2)/((r(j)-q(i))^2+c^2);
        [ellk1,elle1]=ellipke(ki_1);
        [ellk2,elle2]=ellipke(ki_2);
        bz(i,j)=coeff1*(ellk1+elle1*coeff2)+coeff3*(ellk2+elle2*coeff4);
 end
```

```
end
```

A3.6 brcoeff1.m

```
function [br] = brcoeff1(n,r,dr,c)

%       Calculates br coeffs for one superconducting disk at z=c
%       n = # of rings (e.g. 25)
%       radius = radius of film in m (0.5e-3)
%       c = Vertical distance at which Br is calculated m (2e-3)

mu=4*pi*1e-7;
%
for i=1:n
 for j=1:n
        k=(r(j)*r(i)*4)/((r(j)+r(i))^2+c^2);
                coeffr1=(c*dr*mu/2/pi)/r(i)/sqrt((r(j)+r(i))^2+c^2);
                coeffr2=(r(j)^2+r(i)^2+c^2)/((r(j)-r(i))^2+c^2);
                [ellk,elle]=ellipke(k);
        br(i,j)=coeffr1*(-ellk+elle*coeffr2);
 end
end
```

A3.7 Jc_B2.m

```
%       Calculation of critical current limited current and
%       field distributions when Jc is a function of B
%       Jc(B)=Jc(0)^(1-B/Bc)

mu=4*pi*1e-7;
jco=5e11;
Bzext=-0.2;
thick=0.5e-6;
n=25;
radius=5e-3;
dr=radius/n;
r=dr:dr:radius;
q=r-dr/2;
q(1)=r(1)-dr/4;
c=2e-3;
isco=jco*thick;
isc=isco*ones(n,1);
%
Q=-Bzext*ones(n,1);
```

```
%       get the bz coefficients for calculation of surface current is

bz=bzcoeff2(Bzext,n,r,q,dr,c);
is=inv(bz)*Q;

%       Plot zerflux current distribution

%plot(r,is','r')
%hold on

%       Find jc-limited current distribution

is=jclim(n,radius,Bzext,isc,bz);
%plot(r*1000,is','w')
%axis([0 5 0 3e5])
xlabel('r (mm)')
%ylabel('Surface Current (A/m)')
Bz=bz*is(1:n)+Bzext;
%plot(q*1000,Bz','w')
xlabel('r (mm)')
hold on

Ba=0.1;
Bc=10;
diff=1;
index=0;
while diff > 1e-6
        m=n;
        while abs(Bz(m)) > Ba
                isc(m)=isco^((Bc-abs(Bz(m)))/(Bc-Ba));
                if m==0, break, end
                m=m-1;
        end
        is_new=jclim(n,radius,Bzext,isc,bz);
        Bz_new=bz*is_new+Bzext;
        diff=sum((Bz_new-Bz).^2);
        index=index+1;
        Bz=Bz_new;
end
%plot(r*1000,is_new','w')
%plot(q*1000,Bz','w')
hold off
```

Appendix 4 : The laser system

In this appendix the laser system used in our experiments will be briefly described. The laser system consists of a Quantronix Nd:YAG oscillator, a Spectra Physics regenerative amplifier, a flashlamp pumped Nd:YAG amplifier, three Pockels cells, and several optical components like polarizers, waveplates, lenses and mirrors. With two stages of amplification, 100-200 ps laser pulses of wavelength 1064 nm and energy up to 30 mJ are produced. There is a streak camera set-up for the measurement of pulse width of the laser. The spatial profile of the laser beam is measured by scanning a razor blade across the beam and measuring its energy with an energy meter. We briefly describe the various components of the system below. The final section of this appendix is reserved for calculation of laser beam profile and the fraction of laser energy absorbed by rectangular and circular illuminated regions.

A4.1 Oscillator

The oscillator has a cw-pumped Nd:YAG laser head (Quantronix 114) and an acousto-optic mode locker (Quantronix 302). The mode-locker supplies 10 W of rf power at 50 MHz. The oscillator output is a train of 20 nJ pulses of width 100-200 ps, separated by 10 ns. The pulse train is monitored by displaying the signal from a photodiode on an oscilloscope. The oscillator output is launched into a single-mode optical fiber using a microscope objective. The objective and the fiber-holder are mounted on an alignment stage. On the other end of the fiber, two crossed polarizers on either side of a Pockels cell[2] (PC 1) are used to select one pulse out of the oscillator pulse train (Fig. A4.1-1). The optical fiber does not preserve polarization. The first polarizer linearly polarizes the pulse train. The Pockels Cell rotates the polarization by 90° for a time window, short enough to allow only one pulse. That pulse now goes through the cross polarizer while all others are rejected. This arrangement also protects optical feedback through the fiber which would otherwise adversely affect the oscillator stability.

---

[2] A Pockels cell is an electro-optic crystal that changes the polarization as a function of applied electric field. Therefore by applying a suitable voltage pulse it can be used to change the polarization of light.

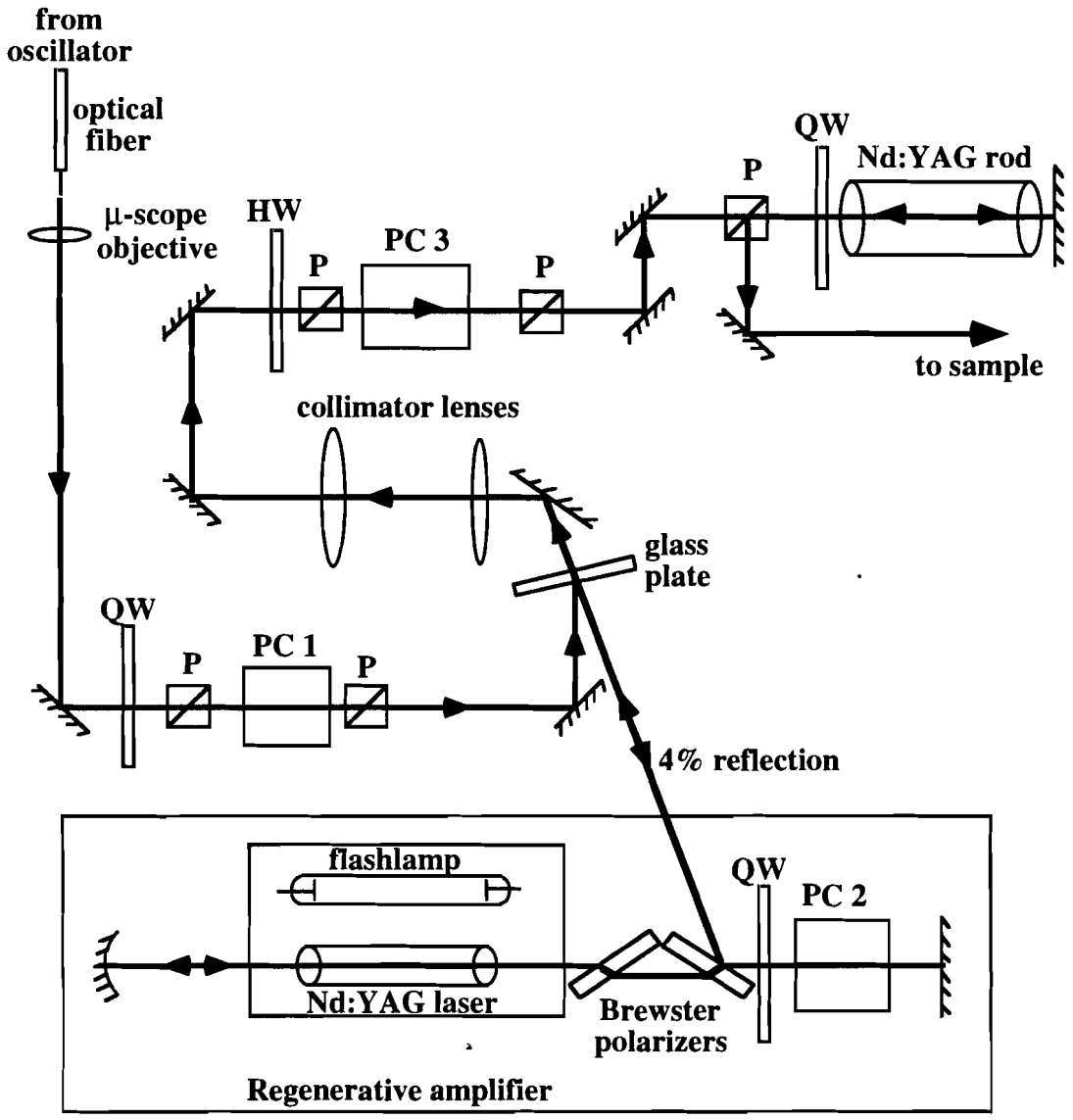

P : Polarizer
QW : Quarter-Wave plate
HW : Half-Wave plate
PC : Pockels Cell

Figure A4.1.1 The laser system. One pulse from the oscillator pulse train is injected into the regenerative amplifier and is amplified again by a passive amplifier.

A4.2 Regenerative Amplifier

The regenerative amplifier is used to increase the energy of the laser pulse by trapping it in a cavity and forcing it to pass through a flashlamp pumped YAG rod several times before dumping it out. This is achieved by injecting the pulse into the laser cavity through a Brewster plate polarizer and changing the voltage across the Pockels cell (PC 2).

The quarter-wave plate turns the polarization by 45°. If no voltage is applied across PC 2 (Fig. A4.2.1(a)) the linearly polarized light pulse is rotated twice by the quarter-wave plate before and after reflection at the end mirror. Since the polarization is rotated by 90° it now passes through the two Brewster polarizers[3] and is reflected by the curved end mirror on the other end. It is again rotated by the quarter wave plate twice and is reflected out of the cavity. If a quarter-wave voltage is applied across PC 2, it will rotate the polarization by 45°. In that situation an incoming pulse will rotate by 90° each by the wave plate and the Pockels cell (Fig. A4.2.1(b)) and will be reflected out before it can pass through the amplifier. However, if there is a pulse already present in the cavity it will undergo a rotation by 180° in each round trip and will continue to be trapped in the cavity (Fig. A4.2.1(c)). If a half-wave voltage is applied across PC 2, it will rotate the polarization by 90°. The pulse trapped in the cavity will now undergo a rotation by 270° (45° by the wave plate and 90° by the Pockels cell in either direction). It will therefore be reflected out by the Brewster plate (Fig. A4.2.1(d)). Therefore a sudden increase of voltage across the Pockels cell from the quarter-wave value to the half-wave value can be used to dump a trapped pulse out of the laser cavity. This is called *cavity dumping*.

The regenerative amplifier is a Q-switched laser. The injected pulse is amplified according to the Q-switch gain profile. Usually the pulse is dumped out at the maximum gain. However sometimes for better stability a gain slightly less than the maximum is chosen. Due to the birefringence of the YAG rod, the regenerative amplifier produces a series of pre-pulses before the main pulse. These pre-pulses are separated by the cavity transit time of 12 ns. Another Pockels cell (PC 3) with crossed

---

[3] Two polarizers are used to compensate for the path shift due to refraction (Fig. A4-1).

polarizers on either side is used to reject these pre-pulses. Usually a ratio of 10000 :1 between the main pulse and the largest pre-pulse is considered acceptable. The regenerative amplifier produces 250 μJ pulses with a repetitition rate up to a few kHz. For the photoresistive switch experiment (chapter 3) this was used without any further amplification. However, for the inductive switch since the whole switch needs to be illuminated (area = $1cm^2$) we require more laser energy. This was done using another amplifier.

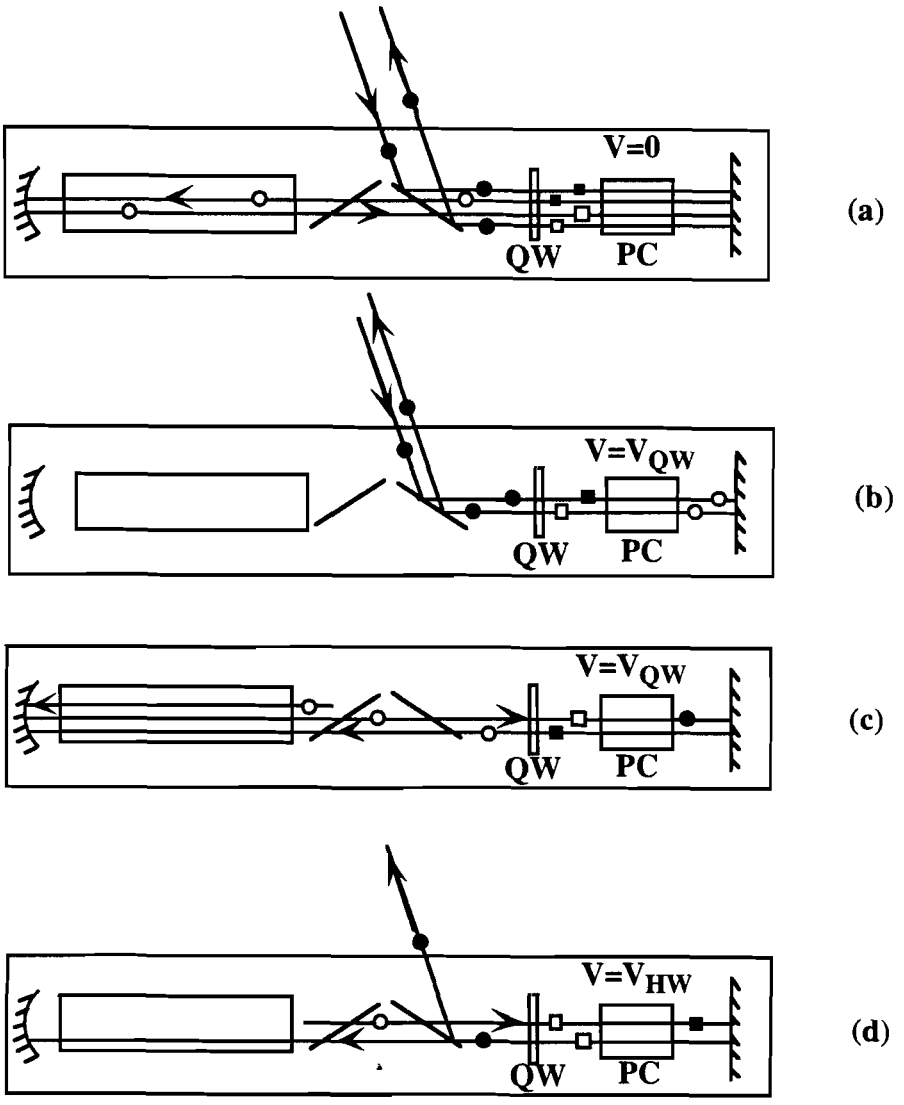

Figure A4.2.1 Regenerative amplification and cavity dumping. (a) No voltage across Pockels cell (PC). (b) Quarter-wave voltage across PC, rejects incoming pulse. (c) Quarter-wave voltage across PC, traps a pulse already present in the cavity. (d) Half-wave voltage across PC dumps the amplified pulse out. QW is a quarter-wave plate.

A4.3 High Power Amplifier

A Nd:YAG rod pumped by a high power flashlamp was used as an amplifier. The output of the regenerative amplifier is passed through this rod twice. The double pass amplification can be more than 100. Up to 30 mJ pulses have been measured. However, the repetition rate is limited to less than 4 Hz. A careful alignment is necessary to reduce the ellipticity of the amplified beam.

A4.4 Laser beam profile

It is important to know the spatial profile of the laser beam. The fundamental mode has a Gaussian profile. The energy per pulse is measured with a Molectron energy meter. To check the laser profile we scan a razor blade across the beam while measuring the laser energy. If the beam is circular the enegy density or fluence as a function of radius can be expressed as,

$$d\mathcal{F} = \frac{\mathcal{F}_0}{2\pi\sigma^2}\exp(-r^2/2\sigma^2)dr; \quad r^2 = x^2 + y^2. \tag{A4-1}$$

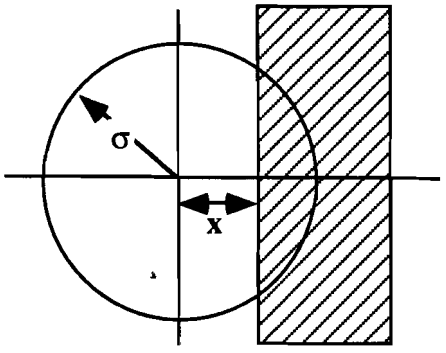

Figure A4.4.1 Laser beam profile is measured by scanning with a razor blade.

So the measured energy for a position of the razor blade is

$$\mathcal{E} = \frac{\mathcal{E}_0}{\sigma\sqrt{2\pi}}\int_{-\infty}^{x}\exp(-x^2/2\sigma^2)dr. \tag{A4.4-2}$$

Therefore the Gaussian profile and parameters like full-width-at-half-maximum (FWHM) can be extracted from E(x) measurement. It is then used to determine the right beam profile for illuminating the sample. For example, we want the laser energy to be

enough to elevate the temperature of a 1 cm diameter, 500 nm thick YBCO film for the inductive switch experiment above T_c. We also want the illumination to be as uniform as possible. Therefore, for given values of initial temperature of the sample we can compute the range of acceptable laser profiles. Typically the FWHM of the beam should be around 8 mm for best uniformity. Although flux motion will take place even if the temperature of the inductive switch is not elevated above T_c[4], it will be faster if the heating is rapid. Typically 10 mJ of energy for each film is the maximum that we have used. Only a fraction of this is actually absorbed by the film.

Let us consider the case when the laser shines on a circular disk of radius R. Let the fluence be,

$$\mathcal{F} = \frac{\mathcal{E}_0}{2\pi\sigma^2}\exp(-r^2/2\sigma^2). \tag{A4.4-3}$$

The energy contained in a circular area of radius R is given by,

$$\mathcal{E}(R) = \frac{\mathcal{E}_0}{2\pi\sigma^2}\int_0^{2\pi}\int_0^{R}\exp(-r^2/2\sigma^2)rdrd\theta. \tag{A4.4-4}$$

This integration can be done by substituting $t = r^2/2\sigma^2$,

$$\mathcal{E}(R) = \mathcal{E}_0\left[1-\exp(-R^2/2\sigma^2)\right]. \tag{A4.4-5}$$

It should be noted that the standard deviation (σ) is related to FWHM (D) as,

$$D = 2\sqrt{2\ln 2}\sigma = 2.3548\sigma. \tag{A4.4-6}$$

From Eq. (A4.4-5) when $R \to \infty$, $\mathcal{E} = \mathcal{E}_0$. At the other limit, small R

$$\mathcal{E} = \mathcal{E}_0\frac{R^2}{2\sigma^2} = \frac{\mathcal{E}_0}{2\pi\sigma^2}\left(\pi R^2\right). \tag{A4.4-7}$$

When the laser illuminates a rectangular switch the solution can not be found analytically. For the photoresistive switch the geometry is rectangular with high aspect

---

[4]see section 6.6

ratio. Therefore, a cylindrical lens was used to make the beam highly elliptical. The beam parameter (FWHM or equivalently σ) was again found by scanning razor blades along the directions of major (x) and minor (y) axes of the ellipse. The energy in the illuminated region can be calculated from this parameter.

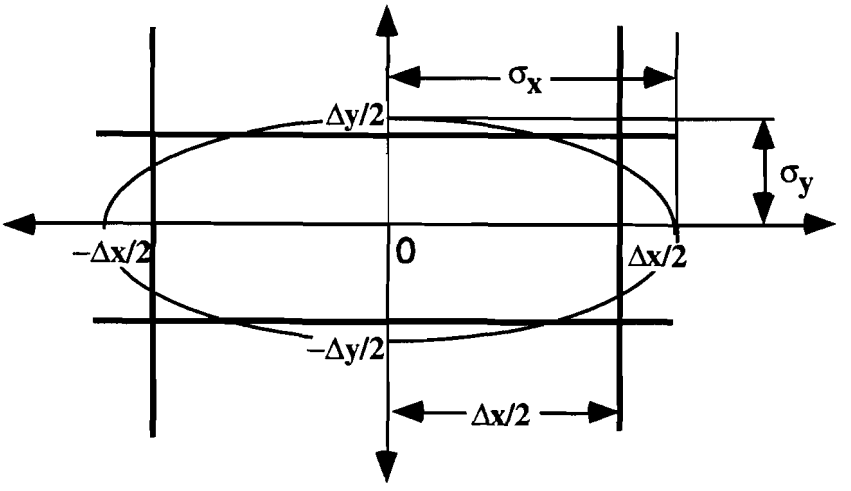

Figure A4.4.2 Measurement of laser beam profile for an elliptical beam.

The measurement of the beam profile found the 10% and 90% points on either axis. Let us say that when scanned parallel to the y-axis, the 10% and 90% points on the x-axis were $-\Delta x/2$ and $\Delta x/2$ respectively (Fig. A4.4.2). Therefore,

$$\frac{1}{2\pi\sigma_y\sigma_x}\int_{-\infty}^{\infty}\exp(-y^2/2\sigma_y^2)dy\int_{-\infty}^{-\Delta x/2}\exp(-x^2/2\sigma_x^2)dx$$

$$= \frac{1}{\sqrt{2\pi}\sigma_x}\int_{-\infty}^{-\Delta x/2}\exp(-x^2/2\sigma_x^2)dx$$

$$= 0.1 \quad , \qquad \text{(A4.4-8)}$$

$$\frac{1}{2\pi\sigma_y\sigma_x}\int_{-\infty}^{\infty}\exp(-y^2/2\sigma_y^2)dy\int_{-\infty}^{\Delta x/2}\exp(-x^2/2\sigma_x^2)dx$$

$$= \frac{1}{\sqrt{2\pi}\sigma_x}\int_{-\infty}^{\Delta x/2}\exp(-x^2/2\sigma_x^2)dx$$

and $$= 0.9 \quad . \qquad \text{(A4.4-9)}$$

Using Table 26.1 of *Handbook of Mathematical Functions* by Abramowitz and Stegun[129],

$$\Delta x/2\,\sigma_x = 0.84, \text{ or} \qquad \Delta x/1.68 = \sigma_x. \tag{A4.4-10}$$

If $-\Delta y/2$ and $\Delta y/2$ are the 10% and 90% points on the y-axis when the razor is scanned parallel to the x-axis, we obtain

$$\Delta y/1.68 = \sigma_y. \tag{A4.4-11}$$

Now the beam of energy $\mathcal{E}_0$ illuminates a rectangular switch. The energy contained in a rectangular region of length l and width w is

$$\mathcal{E}(l,w) = \mathcal{E}_0\left(\frac{1}{\sqrt{2\pi}\sigma_x}\int_{-l/2}^{l/2}\exp(-x^2/2\sigma_x^2)\,dx\right)\left(\frac{1}{\sqrt{2\pi}\sigma_y}\int_{-w/2}^{w/2}\exp(-y^2/2\sigma_y^2)\,dy\right). \tag{A4.4-12}$$

The values of these integrals are found in standard tables.

Appendix 5 : Operation of the superconducting magnet and the magnet cryostat

A5.1 The magnet

A large American Magnetics superconducting magnet was used in our high-field inductive switch experiments (sections 5.3 and 5.4).[5] The magnet consists of a Nb-Ti solenoid surrounded by two temperature shields cooled by a closed-cycle helium refrigerator (Fig. 5.3.2.1). The magnet has an 18 in. long horizontal warm bore of 5 in. diameter. The solenoid is 12 in. long. The magnetic field is measured to be constant in a 1 cubic inch volume at the center of the magnet. It varies up to 10% within 3-4 inches, along the axis of the magnet, from the center in either direction. It falls off rapidly to 1% of the central field just outside the warm bore. The central field was measured while ramping up the magnet current. It was initially increasing linearly at the rate 0.04 T/A but changed slope above 1T field. This is due to the saturation of the longitudinal Hall probe. However, the field at a point just outside the warm bore was used to calibrate the central field and was found to rise linearly with increasing current up to 100 A. The magnet is rated at a maximum field of 4 T at 100 A.

The magnet has a persistent switch. This consists of a superconducting (the same material as the magnet) shunt and a heater. The switch is opened by sending a constant current (60 mA) through the heater, driving the persistent swith normal. This allows the magnet to be connected to an external source and be charged or discharged.

Most of the peripheral components were initially missing and had to be reinstalled as we describe below.

1) Expander assembly: The refrigerator consists of a compressor that is connected to a two-stage expander assembly. The expander housing has two cold stages that cool the two shields. The expander housing is permanently installed with the magnet dewar and cannot be replaced. We purchased a DE-

---

[5] This is one of the two identical magnets built in 1976 and left unused for 15 years since 1978. The second magnet has a bent expander housing and cannot be used.

202 cold stage from APD Cryogenics, that was compatible with the original design and removed the expander from its housing and mounted it inside the previously installed housing. This is extremely tricky and requires a special tool kit . Care must be taken to avoid leakage of the pressurized helium gas (ultra pure carrier grade). If a leak occurs, the standard cleaning procedure should be followed. This involves purging the system repetitively (about 10 times) at 100 psi followed by another decontamination run by pressurizing to 240-245 psi (the operating pressure) and running the motor (about 5 times for 2 minutes each). The pressure should go up to 300-320 psi while the compressor is running.

2) Current leads: Two 100 A vapor cooled current leads were purchased from American Magnetics. These leads consist of a thick copper lead encased in a fluted stainless steel cylinder. The current leads fit into cups that are connected to the solenoid.

3) Liquid helium fill line: This is a hollow stainless steel cylinder, also purchased from American Magnetics, with an inside diameter of 0.25 in. The standard helium transfer line fits into this fill line. The fill line has a screw thread at the bottom and connects to an internal fill line, that leads the cryogen to the bottom of the helium chamber.

4) Current Source: A 100 A, 10 V variable dc current source was used to charge the magnet. The source can be programmed by applying a voltage to the control board. Two 100A copper cables are connected with copper screws and washers to the current source at one end and the magnet leads on the other.

5) Energy Absorber: The energy absorber is a resistive current limiter (section 2.3.1). It is placed in series between the current source and the magnet leads. In case the magnet quenches, the stored energy is dumped into this absorber. The energy absorber allows current flow in only one direction. The easiest way to reverse magnetic field is by interchanging the cables, connecting the absorber and the vapor-cooled leads, at the leads.

6) Current source programmer: An American magnetics programmer (Model 411) controls the current ramp rate during the charge-discharge cycles and

monitors the voltage across the magnet. While charging or discharging the $V = LdI/dt$ voltage should not exceed 5V. If the voltage limit is exceeded the indicator light goes on and the magnet might quench. The ramp rate and the maximum current can be set to ensure safe operation. The ramp rate should not exceed 0.1 A/s. The programmer sends a voltage signal to the current source and senses the current at the energy absorber.

7) Helium fill meter: Helium fill sensor consisting of a tantalum wire is installed inside the magnet. This wire goes superconducting near the boiling point of helium (4.2 K) and the fill level in the magnet chamber is measured by measuring the resistance of this wire. The fill meter ideally makes a four-point resistance measurement. However, one of the contacts is broken inside and cannot be repaired, thus allowing a three point measurement only.

8) Temperature sensors: There are two temperature sensors, one on each shield, and each is read on an analog meter. The meter requires a 9-V battery.

9) Top flange: A specially made flange is equipped with a couple of Teflon feedthoughs for the current leads and an o-ring seal for the liquid fill line. Two radiation baffles (copper coated G-10™) are attached to the flange to minimize heat loss.

The magnet operating procedure is described below.

Pre-cooling the magnet

1) Check the vacuum level of the magnet. It should be ~30 microns (of Hg) or less. If it is higher pump on the vacuum chamber using a mechanical or a cryo-adsorption pump.

2) Flush and fill the magnet with helium gas. Backpressure is maintained using is a 1psi valve. Turn on the compressor and the temperature sensors. The inner and outer shield temperatures can be monitored using the data acquisition program "temp-mon.cmd" or "mag-mon.cmd". The latter also monitors the helium level. Precooling usually takes one week and final temperatures achieved are 70 K and 85 K on the inner and outer shields respectively.

3) If faster cooling is desired, liquid nitrogen can be poured into the magnet chamber periodically. Using liquid nitrogen and the compressor together, the cooling should take about 4-5 days. After cooling down to the desired temperature the liquid nitrogen must be siphoned out and the chamber should be flushed with helium gas.

Cooling the magnet

1) Insert one end of the transfer tube in the helium tank. As soon as the liquid starts coming out of the other end, remove the 1 psi valve and insert it inside the fill line and seal it with a ferrule fitting. This is a crucial step since any air leak might cause freezing of air in the fill line.

2) Connect an ohmmeter across the magnet leads to monitor the resistance of the persistent switch. It should drop from 12.8Ω to zero as the magnet cools down to the superconducting state in about 30 minutes. After the magnet is cooled, helium starts accumulating in the chamber and fills it in about 10 minutes. The total helium consumption should be about 40-60 liters depending on speed of transfer. The magnet capacity is estimated to be around 30 liters.

3) Two tubes are placed over the top of the vapor-cooled leads and connected to a flowmeter through a Y-junction. The helium vapor vents through these tubes. A steady flow of dry nitrogen gas keeps the ice formation on the top flange to a minimum.

Charging the magnet

1) Check the wiring (Fig. 5.3.2.1). The energy absorber has two pairs of 100 A copper cable. One pair goes to the current source while the other to the magnet leads. Polarity is important. A twisted pair from the "program" output of the programmer is connected to the current source. Another twisted pair from the absorber is connected to the "current shunt input" of the programmer. Unfortunately the polarity is reversed as marked on the meter and must be corrected externally. A third twisted pair connects the current leads to the "magnet voltage" input of the programmer.

2) Turn on the programmer first and then the current source. Turn on the current source to supply 60 mA to the persistent current heater. The persistent switch (another superconducting element) opens in about 10 seconds.

3) Ramp up the magnet current while measuring the field just outside the magnet with a Gaussmeter.

4) Once the desired field is achieved close the persistent switch (turn off the heater current).

Discharging the magnet

1) Open the persistent switch and ramp down the magnet current. The magnet voltage sign should be opposite to that during charging and the measured field should reduce to zero.

2) Close the persistent switch.

Refilling the magnet

1) Most of the time the helium tank is left connected to the magnet while doing a continuous experiment. If there is helium left in the magnet after the experiment, the current leads and the fill line should be pulled up to cut down helium loss.

2) Same procedure as initial cooling is followed.

Minimizing heat leaks in the magnet

1) The main sources of heat leaks during operation is through the copper current leads, especially when a large current is flowing. Inspite of the cold helium vapor rising through the leads they conduct a large amount of heat to the helim bath. The fill line is another path for heat conduction from room temperature to the helium bath. The current leads and the fill tube should be lifted up if the magnet is operating in the persistent mode and the top flange should be replaced by another one with only a long radiation baffle attached to it. This minimizes the loss.

Precautions and troubleshooting

1) The vacuum must be checked periodically. A thermocouple gauge has been installed on the magnet.

2) Check the battery for the thermometers. The temperature reading could be lower than the real value if the battery charge is low.

3) Before cooling the helium chamber, housing the magnet, must be under helium backpressure.

4) If the resistance of the magnet does not start dropping, the helium transfer is getting blocked somewhere. The most likely place is the fill line itself. Take out the helium transfer line and check the fill line and the current leads. In the past we have removed ice blockages by inserting a copper rod.

5) Transfer should be stopped before it overfills the magnet.

6) There is always some ice formation on the top flange. This can be melted with a heat-gun if there is a need to handle the leads or the fill line (e.g., when pulling them out at the end of an experiment run).

7) A blinking voltage limit light portends a quench. Decrease ramp rate immediately.

8) The persistent switch must be closed after charging. Otherwise the magnet will lose charge since the programmer slowly ramps down the current source after charging.

A5.2 The cryostat

A liquid nitrogen/helium flow cryostat was designed to fit the 5-in. diameter horizontal warm-bore of the magnet. The cryostat was built by Janis Research Co. There are two 2 in diameter optical windows at the center of both the planar surfaces of the cryostat. The windows have an anti-reflection coating for 1064 nm light. One end of the cryostat is fixed to the magnet housing. The sample holder is mounted on the liquid feethrough, welded to the removable front flange. The liquid feedthrough is a

double walled tube. The liquid flows in through the inner tube and returns through the outer one. care should be taken so that the cold liquid/vapor that comes out does not cause condensation on the optical windows.

A temperature sensor (Pt-resistance thermometer works well in high magnetic field) is sunk into the copper sample holder with Thermal Joint Compound. A heater coil is wrapped around the liquid feedthrough near the sample holder. A Lakeshore 330 Autotuning temperature controller reads and controls the temperature by changing the heater power when necessary.

There are three ports for electrical feedthroughs. One of them has a BNC connector on the outside and an SMA connector on the inside. Another identical one was recently expanded with a T and has a 20-pin feedthrough on one of the flanges. The other port is blanked off and can be used for additional connectors in future. The third one was different from the first two and has a flange designed for the temperature controller, and has 10-pins. This is used for the thermometer (2 pairs), and the heater. Several samples can be mounted simultaneously inside the cryostat and parallel experiments can be conducted.

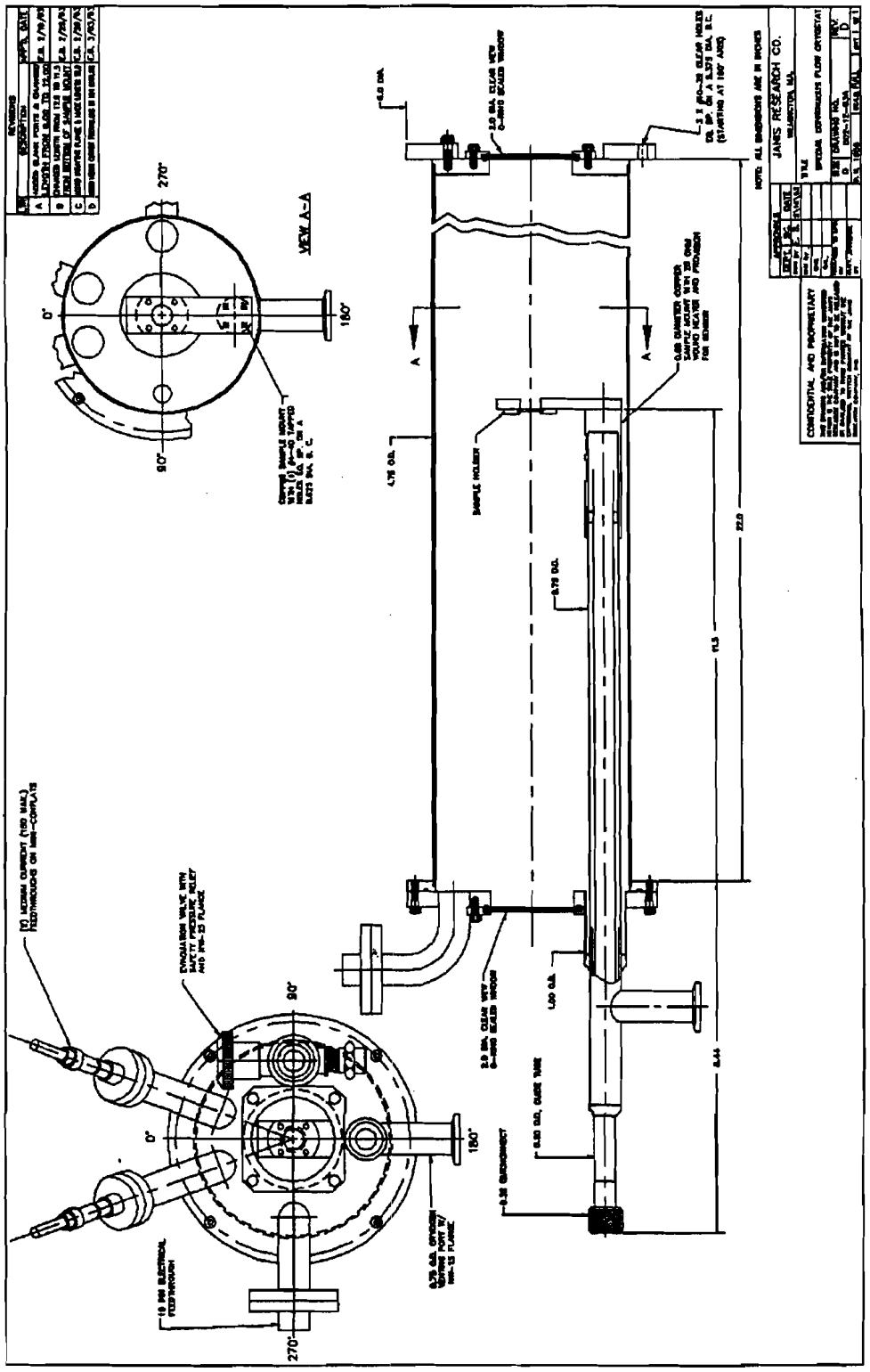

Figure A5.2.1 A drawing of the magnet cryostat. The cryostat was built by Janis Research Co., Wilmington, MA and their drawing number is D02-12-93A.